# Vibrational spectroscopy, quantum state manipulation, and precise tests of QED with cold, trapped molecular ions

Inaugural dissertation

for the attainment of the title of doctor
in the Faculty of Mathematics and Natural Sciences
at the Heinrich-Heine-Universität Düsseldorf

presented by

**Andrii Borodin**
from Novovoronezh

Düsseldorf, July 2014

from the Institute for Experimental Physics
at the Heinrich Heine University Düsseldorf

Published by permission of the
Faculty of Mathematics and Natural Sciences at
Heinrich Heine University Düsseldorf

Supervisor: Prof. Stephan Schiller, Ph.D.
Reviewer: Prof. Dr. Axel Görlitz

Date of the oral examination: 09.07.2014

Dedicated to: my parents, and to my teacher Leonid M. Savchenko

## Abstract

This work describes various novel results of experimental research in the field of ion trapping. One of the most important results - high-resolution spectroscopy of the trapped and cooled molecular ions, and concomitant spectroscopic approaches are described.

The studies were done with different species, trapped in quadrupole ion traps. Several coherent radiation sources (mainly, laser sources) were used to perform laser cooling, optical pumping, excitation of spectroscopic transitions, and photodissociation. Molecular ions were the model systems for comparing the experimental results with theoretical analyses of the ions. Hydrogen deuterated cation ($HD^+$), as one of the most fundamental molecular ions, was a primary object of research: hyperfine-state-resolved spectra are reported. Another study involved polyatomic molecular ions to study the possibilities and limitations of high-resolution spectroscopy. All these studies are performed in extreme conditions - almost collisionless, ions are cooled to translational temperatures well below 1 K.

The advantages of the long storage time of the trapped particles, in combination with translational cooling, were used for detection of weak and narrow transitions in molecular ions, determination of their low transition rates. The detection was performed by way of selective photodissociation and ion counting.

The quantum state preparation, which is an important aspect in quantum optics, quantum information, and precision spectroscopy, is performed to obtain the hyperfine-resolved transitions in $HD^+$, allowing the fundamental theory test, including quantum electrodynamics effects, to be carried out.

To increase the resolution of detected transitions (potentially, including Zeeman-state resolved spectra), an optical magnetometry scheme was proposed. The method utilizes beryllium ions, which are co-trapped and used also as coolant ions, to detect the Zeeman splitting and to determine the magnetic field strength and its direction. The scheme is based on stimulated Raman transition detection; it allows the strength of the magnetic field to be determined at a resolution of approximately 40 mG.

The ion traps can also be used with non-destructive spectroscopy schemes. The preliminary results, and characterisations of the new detection scheme based on non-destructive detection are presented. A new frequency stabilization scheme was implemented for an optical parametric oscillator (OPO), which was used in vibrational spectroscopy of polyatomic molecular ions, for excitation of doubly spin-forbidden transitions in $HD^+$, and can be further used for non-destructive optical force excitation.

# Contents

CHAPTER 1

# Introduction and motivation

In this chapter, the motivation for studying molecular ions will be explained. The internal structure of different molecules will be briefly described. The rotational-vibrational structure will be generally presented, and the relevance of studying hyperfine structure, Zeeman splitting, and QED corrections will be discussed. For an introduction to ion trapping and cooling methods, see Part 1.

## 1.1. General aspects: Rotational-Vibrational Levels

Molecular ions, as well as their corresponding "parent" molecules, possess generally a rotational-vibrational, or in short, rovibrational levels. These levels, on an approximate basis, can be de-coupled from the separate rotational and the vibrational levels. The presence of the rovibrational levels, generally, in addition to the electronic states, complicates the level structure of the molecular ions, compared to the structure of atoms or atomic ions. To determine theoretically the energy levels and transitions in polyatomic molecular ions (with number of nuclei $> 3$), analytical approaches are not applicable, and approximations are used, e.g. based on variational methods, density functional theory, coupled-cluster theory, multi-reference configuration interaction methods and other approaches (see, e.g. Ref. [1, 2]).

An analytical approach is not possible even for the most simple molecular ions, hydrogen deuterated cation ($HD^+$), and dihydrogen cation ($H_2^+$), which consist of two nuclei and one electron. The evaluation of different effects is required to achieve the data for the energy levels, precise enough for validation the theory by comparison with experimentally observable spectra, and determination of fundamental constants (and their possible time variation) .

The basic approach is based on the Schroedinger equation, which contributes to the energy of levels from the non-relativistic theory. An important method of approximation is the Born-Oppenheimer (BO) theory, which describes states of electrons and nuclei as the decoupled states. This approach is quite general, and explains the presence of the rovibrational structure. Fig. 1.1.1 illustrates the rovibrational level structure typical for simple (diatomic) molecular ions with non-harmonic internuclear potential.

The rovibrational structure is also presentin complex molecular ions. Typically, the transition spectrum consists of many vibrational transitions, enriched by rotational transitions.

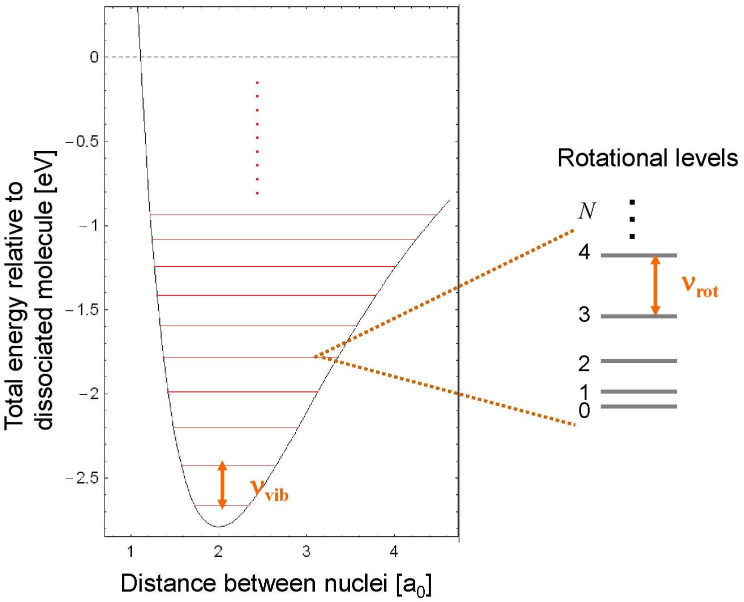

FIGURE 1.1.1. Illustration of rovibrational structure for diatomic molecules and molecular ions [3]. The numerical values are for $HD^+$.

The combined effect of different transition broadening mechanisms is typically large compared to the rotational levels spacing, and may stay large even at low temperatures, achieved for molecular ions trapped and cooled to cryogenic temperatures. The complexity of the structure of polyatomic molecular ions makes it challenging to resolve the details of the rovibrational structure (see, e.g. [4, 5]). The transitions observed in the absorption spectra are usually attributed to the specific groups or radicals constituting the molecular ion. For example, those molecular ions which have a Phenol-OH group, typically exhibit a rovibrational transition at the wavelength 2.7 µm. An example of the transition spectrum is shown in Fig. 1.1.2 for protonated molecular ion $H^+$TyrAla; several distinct lines are associated with certain bonds.

A software is developed (e.g. PGOPHER, see Ref. [6]) that allows the transitions in molecules to be calculated numerically.

Our motivation for studying complex molecular ions was to give us the opportunity to perform IR spectroscopy at a high resolution ($\lesssim$ 200 MHz) in extreme conditions: at a translation temperature below 1 K (see Ref. [5]). This translational temperature is a factor of 8 below the temperature, typically achievable with He buffer gas cooling.

Resolving the details of the rotational structure for the multi-nuclei molecular ions is a challenging task, requiring, for instance, rotational cooling. Using combined traps (with spatially overlapped trapped atoms and ions) can potentially be a good approach. This is already used for studying the interaction of trapped atomic ions with neutral atoms (see

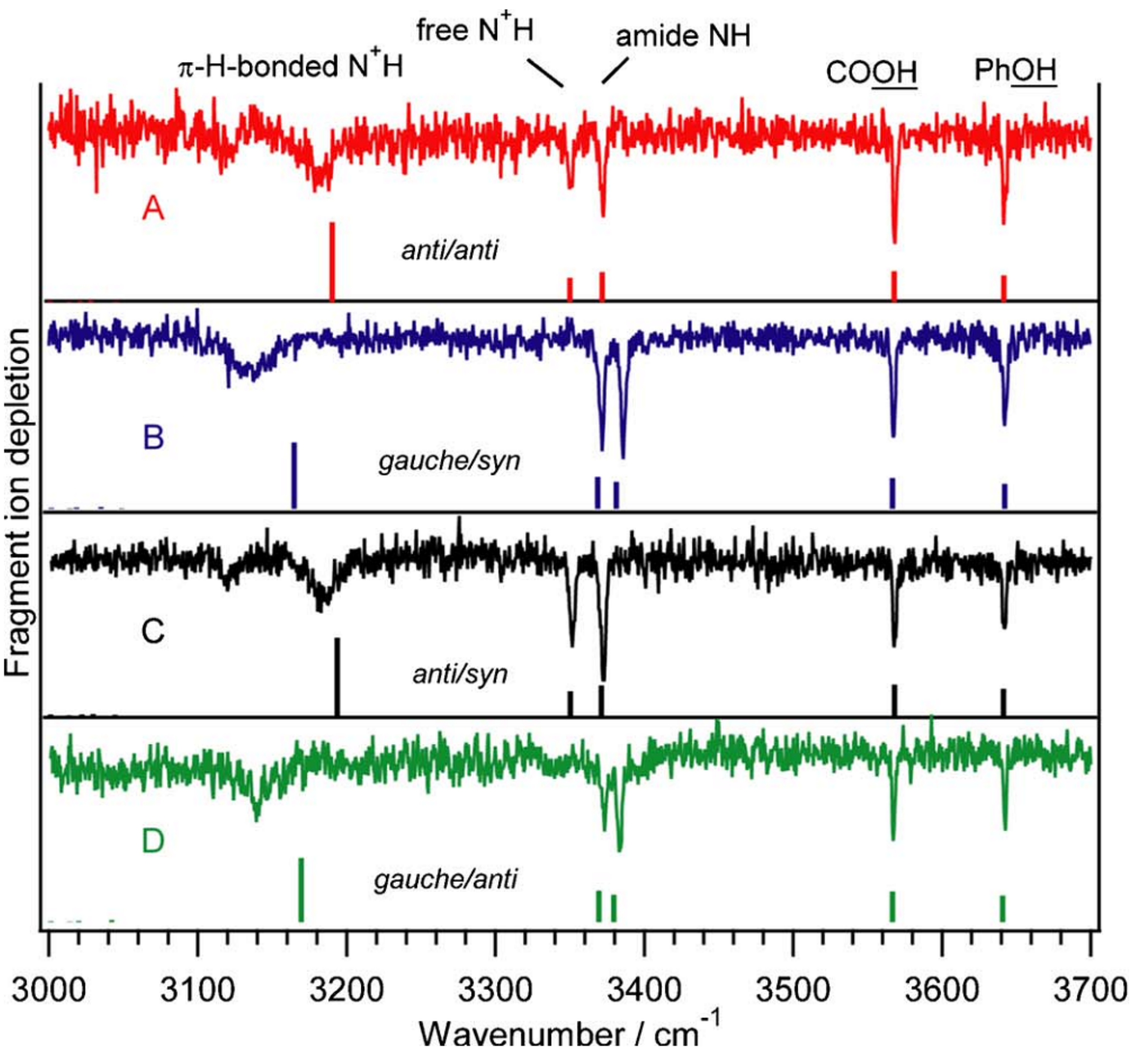

FIGURE 1.1.2. Illustration of the IR spectrum of $H^{+}$TyrAla protonated molecular ions [4]. A to D denotes different conformers. The distinct lines are attributed to the localized vibrational modes, several of them are designated.

Ref. [7, 8]). The interaction of ultracold neutral particles (which are, e.g. trapped and laser-cooled in a magneto-optical or a dipole trap) with molecular ions (trapped in a quadrupole trap) is a promising method, see Ref. [9, 10], and [11, 12] regarding the challenges associated with the role of time-dependent potential (micromotion effect). So far, the method is realized for cooling only certain (mainly, diatomic) molecular ions, see, e.g. Ref. [13]. The interaction of ultracold neutral particles with molecular ions is also of interest for research into kinetics [14], reactive collision [15], and photoassociated or Feshbach molecules (see, e.g. Ref. [16] and the references therein).

Simple molecular ions, consisting of few nuclei, can be effectively cooled by buffer gas cooling (see Ref. [12]). Direct laser cooling of molecules and molecular ions is a challenging task (see Ref. [17]), it is achieved only for some particular molecules (see Ref. [18]).

Sympathetic cooling is widely used in ion traps, it relies on doppler cooling of one of (potentially many) trapped species; the Coulomb interaction allows the other species to be translationally cooled. This way has certain limitations: unlike the case of collisions of cold neutral particles, it does not contribute to rotational cooling of molecular ions. From this point of view, it has similarities with two-photon spectroscopy and saturation spectroscopy, which rely of cancellation the effect of translational motion: the first-order Doppler broadening is eliminated, though molecules are not cooled internally (see e.g. Ref. [19] for molecular iodine, and Ref. [20] for methane molecules).

One method, applicable, mainly, for diatomic molecular ions, utilizes several laser-induced transitions to perform optical pumping (see Ref. [21, 22]). This approach, referred to as “rotational cooling”, is an important step towards achieving the systematic study of the molecular ion structure. In practice, the laser-induced rotational cooling is not applicable for polyatomic molecular ions because of complexity of their structure, requiring many laser sources, and resulting in a small efficiency of the method.

## 1.2. Hydrogen Deuterated cation (HD$^+$): fundamental molecular ion

Spectroscopic measurements where the rovibrational spectrum has a high resolution are typically possible if the molecular ions only consist of a few nuclei, e.g. diatomic molecular ions. Recent developments in narrow-linewidth IR laser sources, stabilized to a frequency comb, make it possible to transfer the precision of the atomic frequency standards to the measurements of transitions in molecules. Very precise theoretical analysis and evaluation of energy states are available for molecular ions with 1 or 2 electrons. This means an in-depth analysis can be made upon comparison of the theoretically-predicted and experimental results, the values of fundamental constants can be defined, their time variations sought, and the applicability of fundamental theories for the description of molecules and molecular ions checked.

There are different reasons behind the motivation for research of hydrogen deuterated cation (HD$^+$). First, HD$^+$, being a diatomic molecular ion, is among the most simple and fundamental molecular ions, like hydrogen cation ($H_2^+$), and tritium hydrated cation (HT$^+$). Second, HD$^+$ consists of stable isotopes and only one electron, has allowed dipole transitions (rovibrational transitions), which have relatively small linewidth ($\sim$ 50 Hz). Third, the variety of rovibrational transitions allows several of these transitions to be used to evaluate different systematical effects (like line shift), thus increasing the accuracy (see Ref. [23]). As a consequence of the first reason, this molecular ion was under consideration in a number of theoretical papers, and high-accuracy theoretical data is available for $HD^+$ [23–28].

An additional motivation is that $HD^+$ possesses hyperfine states, which allows hyperfine splitting constants to be determined.

Theoretical analysis of $HD^+$ ions requires an estimation and calculation of the contribution factors of different effects. The theoretical interest in hydrogen molecular ions was first posed when quantum theory was still in its infancy. The Born-Oppenheimer approximation was applied, see Ref. [29]. Adiabatic corrections [30], and thereafter non-adiabatic, Lamb shift, and relativistic corrections were applied, see [31]. The last decade has ushered in a new epoch, remarkable due to the usage of numerical evaluations of high-order perturbation contributions. So far, the QED calculations of up to the 7th order of the fine structure constant have been performed (see Ref. [28]).

Currently, the hyperfine energies for the lowest rovibrational levels are calculated for $HD^+$ with an uncertainty of about 1 kHz. At this level of precision, the accurate spectroscopic measurements become important. This requires minimization, elimination or taking into account effects of line broadening (residual Doppler broadening, power broadening), line shifts and polarizability (like AC Stark shift, Zeeman effect, RF-trap induced polarization), black-body-radiation induced processes, RF-trap relevant processes (ion heating, micromotion) and other systematic effects (for general information, see e.g. Ref. [32]). This also requires stabilized sources of coherent radiation (mainly, lasers).

A significant part of this work is devoted to experimental spectroscopic studies of $HD^+$. As a result of the comparison of theoretically-predicted and experimentally-observed transitions in $HD^+$ ions, it becomes possible to draw a conclusion about the applicability of the quantum theory for description of real ions, and to derive the value of the mass proton to mass electron ratio (see Ref. [25], and [33] for $CaH^+$ ion).

Theoretical analysis of molecular structure, energy levels, and its discussion is not the aim of this thesis and can be found elsewhere, see e.g. Ref. [26, 28, 34], and the references within these articles. The potential of the hydrogen molecular ion as a molecular ion clock is discussed in Ref. [23, 27].

The focal point of this thesis is the description of experimental approaches, their realizations, and discussion of the results obtained. In the following chapter, the basic approaches for carrying out spectroscopy of molecular ions will be detailed. A more detailed description of the experimental methods and apparatus will be presented in the next chapters.

# Part 1

# Experimental methods and approaches

In this part, an overview of the basic aspects and experimental approaches related to the spectroscopic studies of cold trapped molecular ions will be provided. This includes production, trapping and cooling of different species, and the spectroscopic technique for transition detection. Unless otherwise mentioned, the data is relevant to the experiments with hydrogen deuterated cation ($HD^+$). More detailed information about experiments with polyatomic molecular ions can be found in the attached paper (Ref. [5]).

## CHAPTER 2

# Production, trapping and cooling molecular and atomic ions

The radiofrequency (RF) traps, first proposed in the middle of XX century [35], have been improved over the last few decades to generate excellent conditions which are almost free from external perturbation, so experimental researches can be carried out with trapped ions (for general information, see e.g. [36]). Being operated in vacuum, these traps provide small collision rates with residual background gases and, consequently, long-term storage of trapped ions. Additionally, the trapping technique is frequently combined with laser cooling. The versatile technique of sympathetic cooling, i.e. cooling (molecular) ions by means of Coulomb interaction with laser-cooled ions (usually, atomic ions) proposes extreme conditions for stydying molecular ions - low-temperature, almost collision-free, and applicable for a variety of species.

In our experiments, the setup ulitizes an ultra-high vacuum (UHV) chamber with installed linear ion trap, see Fig. 2.0.1. A Be wire is installed in the chamber and a piezo-driven valve is used to flood the chamber with an HD gas from a gas bottle (see Ref. [37] for details about the trap setup). An electron gun installed in the UHV chamber produces an electron beam with adjustable parameters. Atomic and molecular ions are produced from the corresponding atoms and molecules by an electron impact ionization. The electron beam is directed towards the trap center and is slightly focused. The main parameters which are subject to change are the cathode voltage and the heating wire current, which affects the cathode current. The following are typically used parameters: 750 V for loading $Be^+$ ions and 220 V for loading $HD^+$ ions; the heating wire current is changed to maintain approximately 20 µA cathode current. The UHV chamber has several viewports to allow optical access and fluorescence detection (see also Chap. 4).

The process for trapping the ions starts by loading the coolant $Be^+$ ions. The cooling laser is set to the maximum available power (approximately 3 mW in the trap center, beam diam. $\approx$ 0.3 mm) and the detuning from the corresponding $Be^+$ cooling transition is set up to a few GHz. The Be wire is heated and the electron gun is activated. After a short time the ion being loaded become visible as a result of the increase in fluorescence. An image typical of a “liquid crystal” appears on a CCD camera; this is illustrated by Fig. 2.0.2, (A). Besides the $Be^+$ ions, other species are co-trapped in the linear trap. Typically, these contaminations

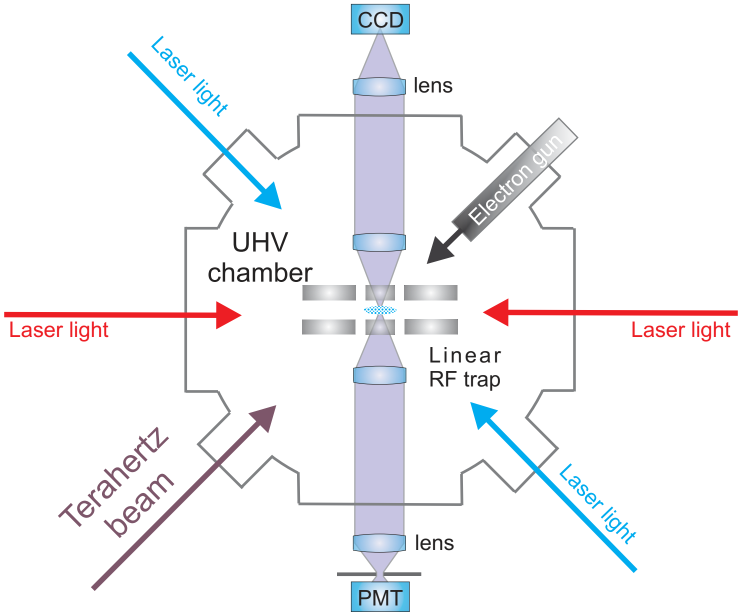

FIGURE 2.0.1. Overview of the trap chamber and laser waves. Dimensions are not to scale.

prevent from the thermodynamical phase change from the "hot cloud" to the Coulomb crystal state (see [38]), and undesired ions must be removed.

This cleaning procedure is done in two steps. First, parametric cleaning is carried out: the constant voltage (typically, a few Volts) is applied for a short time to the two opposite RF electrodes of the Paul trap. This breaks the cylindrical symmetry and reduces the trapping pseudo-potential, resulting in instability of the heavier ions (see Ref. [39]). Typically, after this cleaning it is possible to observe a "hot crystal", shown in Fig. 2.0.2, (B). Second, the transverse secular excitation is applied to the special electrode, which is installed close to the trap. This excitation helps to remove the species which are lighter than $Be^+$ ions. The excitation should have a frequency corresponding to the secular frequency of the ions to be removed. Typically, a wide range scan is performed to remove the undesired species. After cleaning, the $Be^+$ crystallization can be readily achieved. A few hundred to a few thousand $Be^+$ ions are trapped, illustrated by Fig. 2.0.2, (F).

Once the $Be^+$ ions form the Coulomb crystal, $HD^+$ ions can be loaded: the piezoelectric valve is opened to achieve a pressure $\sim 5\ 10^{-11}$ mbar, and an electron gun is activated for a few seconds. After loading, the parametric cleaning described in the previous paragraph can be applied, if required. During the process for loading $HD^+$ ions and the parametrical cleaning, the $Be^+$ ions stay in the form of the Coulomb crystal, which ensures that the $HD^+$ ions are sympathetically cooled by $Be^+$ ions, and this is shown in Fig. 2.0.2, (C).

After nearly 1 hour storage time, the collisions with background gas give rise to chemical reactions with the trapped ions. The products of these reactions can stay trapped, which results in the crystal distortion due to these impurities. The $Be^+$ Coulomb crystal decreases in its size and deformes, and the distortion starts to be clearly visible. Fig. 2.0.2, (D) illustrates the appearance of $BeH^+$, $BeOH^+$ and, possibly, some other species, which form an outer shell. Fig. 2.0.2, (E) illustrates a crystal shape during parametric cleaning (which cannot be visualized immediately after $Be^+$ loading). After removing undesired species, a pure $Be^+$ crystal is obtained, shown in Fig. 2.0.2, (F).

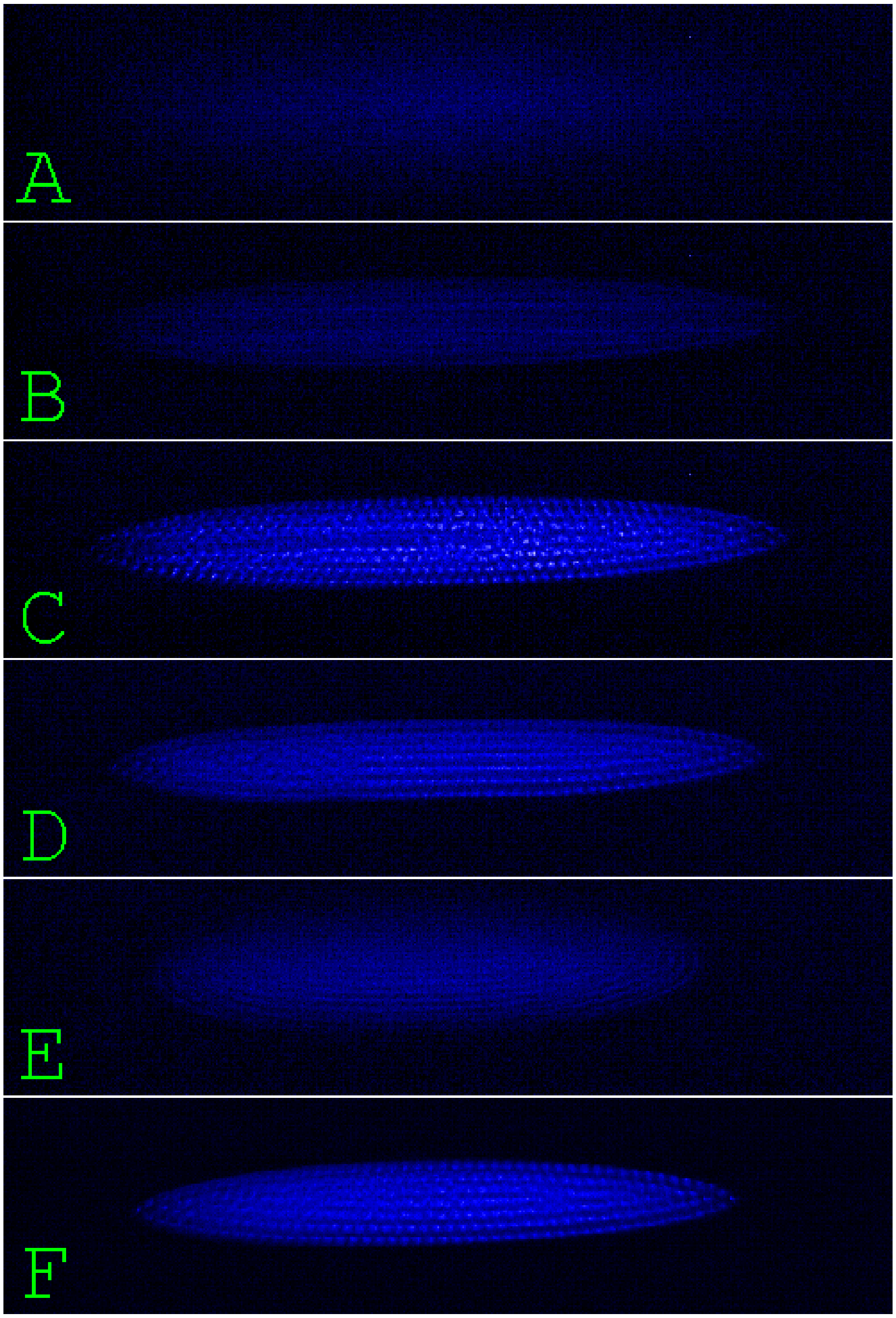

FIGURE 2.0.2. Loading Be$^+$ and removing undesired species. (A) - a "hot cloud" state, whereby impurities are not clearly seen. (B) - "hot crystal" state with a lot of visible impurities in the core. (C) - cold crystal state with HD$^+$ loaded and sympathetically cooled. (D) - cold crystal state after ∼1 hour storage; the crystal is deformed and diminished in size, which is caused by chemical reactions with charge exchange during collision with bachground gases. (E) - parametric cleaning is applied (see the text). (F) - pure Be$^+$ crystal after cleaning. Note the decrease in size compared to (C).

## CHAPTER 3

# Transition detection: selective dissociation, and mass spectroscopy

In our experiments, related to detection of transitions, we used the destructive methods of detection, based on particle counting, and selective photodissociation. Information about the number of ions is obtained by mass spectrometry, performed by the quadrupole trap. Under certain parameters of the trap and the cooling laser, the detected signal is simply proportional to the number or ions of a selected species.

Generally, at the start of the detection procedure, the ion number is detected, giving the initial number of ions. After spectroscopic transition and the following selective photodissociation, the number of particles is detected again; the normalized difference between initial and the final number of particles forms our spectroscopic signal.

Alternatively, the number of ions is counted continuously during the measurement procedure, giving the signal about the number of ions throughout the experimental cycle (in this case, photon counting is performed with a time resolution of 0.1 s). A description of the methods is provided in the following sections. More information about the details of experimental realizations can be found in Ref. [40] and in Appendix 5.

## 3.1. REMPD and R-IRMPD

The selective photodissociation is realized by a resonance-enhanced multi-photon dissociation (REMPD) for $HD^+$ spectroscopy, or by a resonance infrared multi-photon dissociation (R-IRMPD) in the case of the spectroscopy the phenol-OH hydroxyl group in complex molecular ions. In both methods, the goal is to dissociate those molecular ions, for which the spectroscopic transition took place.

REMPD, used in $HD^+$ spectroscopy, is illustrated in Fig. 3.1.1 (A, B) for detection of terahertz and IR transitions, respectively. The selective photodissociation is realized by using at least one narrow bandwidth source of a radiation (comb-stabilized lasers, maser-stabilized THz radiation), and several additional lasers (typically, broadband) to drive transitions to higher rovibrational levels from which a photodissociation takes place. Fig. 3.1.1, (A) illustrates a fundamental rotational (1.3 THz) transition detection: first, a quantum state preparation takes place. It is realized by increasing the fractional population in ($v = 0$, $N = 0$) level; this is a ground level. Two rotational cooling lasers $\lambda_{p1}$ and $\lambda_{p2}$, are used to populate the ($v = 0$, $N = 0$) level. Spectroscopic transition is induced by THz radiation, after which several lasers at $\lambda_{p2} = 2.71\,\mu\mathrm{m}$, $\lambda' = 1565\,\mu\mathrm{m}$ and $\lambda'' = 405\,\mu\mathrm{m}$ perform a photodissociation. Fig. 3.1.1, (B) illustrates a fundamental vibrational transition detection at $\lambda_S = 5.115\,\mu$m. As in previous descriptions, the quantum state preparation is made by increasing the fractional population in the ($v = 0$, $N = 0$) level, which is a ground level. The two rotational cooling lasers $\lambda_{p1}$ and $\lambda_{p2}$, are used to populate the ($v = 0$, $N = 0$) level. Spectroscopic transition is performed by a narrow linewidth lasing radiation at $\lambda_s = 5.115\,\mu\mathrm{m}$, stabilized to an optical comb. Two lasers at $\lambda' = 1475\,\mathrm{nm}$ and $\lambda'' = 266\,\mathrm{nm}$ make a photodissociation of the ions, for which the spectroscopic transition at $\lambda_s = 5.115\,\mu\mathrm{m}$ was realized.

R-IRMPD is illustrated in Fig. 3.1.2. In complex molecular ions, possessing a large number of nuclei, the Intramolecular Vibrational Redistribution (IVR) takes place; this means redistributing the absorbed photon energy among other degrees of freedom. After the redistribution, absorption of another photon on the same transition becomes possible. As IVR occurs on a short time scale (typically, few ten picoseconds), the absorption can be repeated many times during the typical time for a spectroscopy (in our conditions, a few seconds). This results in a cumulation of an amount of energy, enough to break the bond(s).

Counting the ions before, repeating it after performing selective dissociation by REMPD or R-IRMPD, and taking the normalized ratio of the ion loss completes the spectroscopy procedure. This counting technique, realized by the mass spectrometry in the Paul traps, is described in the next section.

## 3.2. Mass-selective detection

The mass spectrometry is carried out in one of the following ways: secular excitation detection (see e.g. [42]) or by trap release with particle counting (see [5]). In both cases, the mass-to-charge selectivity of the trap is used [43].

In the case of trap release, the trap parameter(s) is varied to release first the heavier ions, then lighter ions, see Fig. 3.2.1, (a, b). Fig. 3.2.1 (a) shows the dependence of a release RF voltage (which is a trap parameter) as a function of the particle mass, i.e. the minimum RF voltage for which the ion is still trapped. Fig. 3.2.1 (b) shows an example of the extraction method.

In the case of secular excitation, the heating of the selected species with subsequent fluorescence detection indicates the number of ions of the selected species. The secular excitation method is based on heating the ions using an external oscillating electric field. The heating effect depends on the frequency, and the resonance frequency is referred to as a secular frequency (which, in turn, depends on the mass and charge of the ion to be heated). The method requires the ions trapped to be in the Coulomb crystal state, and this method

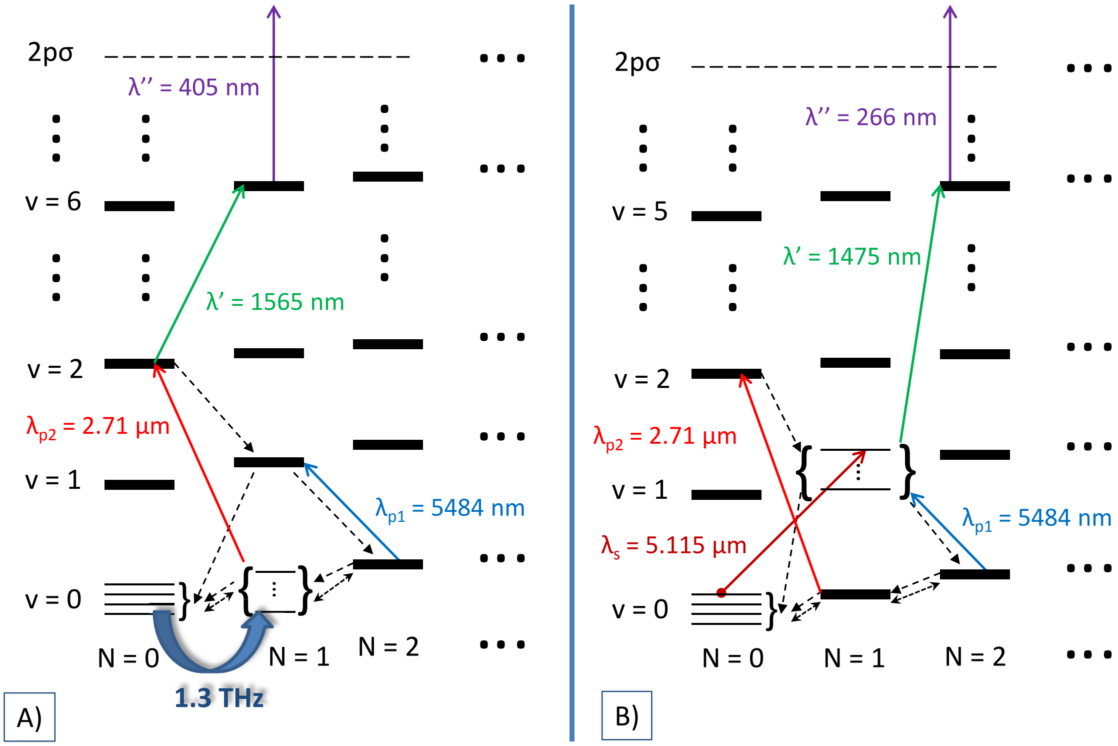

FIGURE 3.1.1. Level schemes and relevant transitions for REMPD in $HD^+$. Levels are shown not to scale. $\lambda_{p1}$ is a rotational cooling laser (see Chap. 6). (A) - detection of pure rotational (1.3 THz) transition. $\lambda_{p2}$ is used for both rotational cooling and transition detection. Quantum state preparation is realized by increasing the fractional population at the$(v = 0,\ N = 0)$ level; this is a ground level. Spectroscopic transition is performed by a THz radiation, after which several lasers at $\lambda_{p2} = 2.71\,\mu\text{m}$, $\lambda' = 1565\,\mu\text{m}$ and $\lambda'' = 405\,\mu\text{m}$ perform a photodissociation. (B) - detection of the fundamental vibrational transition. Both transitions at $\lambda_{p1}$ and at $\lambda_{p2}$ are used for the rotational cooling. Quantum state preparation is realized by increasing the fractional population at the $(v = 0,\ N = 0)$ level; this is a ground level. Spectroscopic transition is made by a narrow linewidth lasing radiation at $\lambda_s = 5.115\,\mu\text{m}$, stabilized to an optical comb. A photodissociation is performed by two lasers at $\lambda' = 1475\,\text{nm}$ and $\lambda'' = 266\,\text{nm}$.

is very sensitive to any change of experimental parameters: cooling laser power, its detuning, trap parameters, presence of any other species. Fig. 3.2.1 (c) shows the secular excitation frequency for several species trapped. An illustration of the secular excitation is shown in Fig. 3.2.1 (d), here the excitation frequency is varied in a wide range to detect a responce from certain (here, $HD^+$) ions.

Obtaining information about the number of ions is of great importance. A narrow-range scan of excitation frequency is typically performed, as its center frequency is known; a

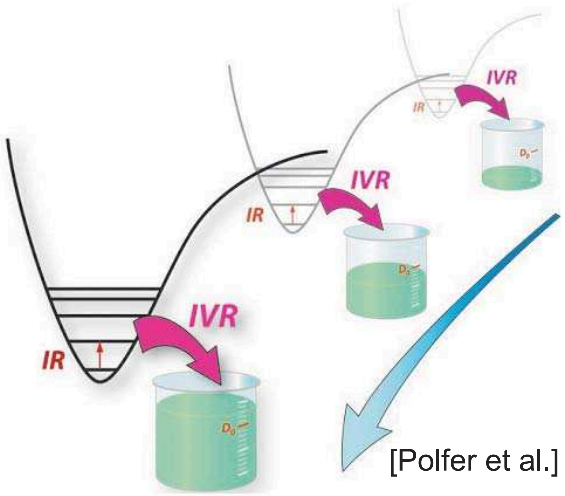

FIGURE 3.1.2. Illustration of R-IRMPD method (from Polfer, Oomens [41]). IR - resonant rovibrational transition in a molecule (molecular ion). IVR - Intramolecular Vibrational Redistribution. The vessel stands for the other degrees of freedom of the molecule. After "filling" the vessel, the molecular bond(s) is broken, thus allowing the photodissociation by IR radiation without UV light.

small frequency deviation is possible due to the effect of motion coupling [42]. The narrow-range scan (typically, ±50 kHz) has the purpose of covering the full range of possible secular frequencies. The experimental realization of ion counting can be generally attributed to one of the following two methods: (1) a "continuous" excitation, or (2) a probe before/after REMPD. In the first method, the secular excitation is applied throughout the measurement cycle, and the fluorescence detection is monitored with a time resolution around 0.1 s. An example of this method is shown in Fig. 5.0.2. In the second method (probe before/after REMPD), the secular excitation is applied for a few seconds before and then repeated after REMPD, giving two signals. Their normalized difference forms the spectroscopic signal. Also, different combinations of methods were used as well. Fig. 3.2.2 shows an example of a method used in experiments.

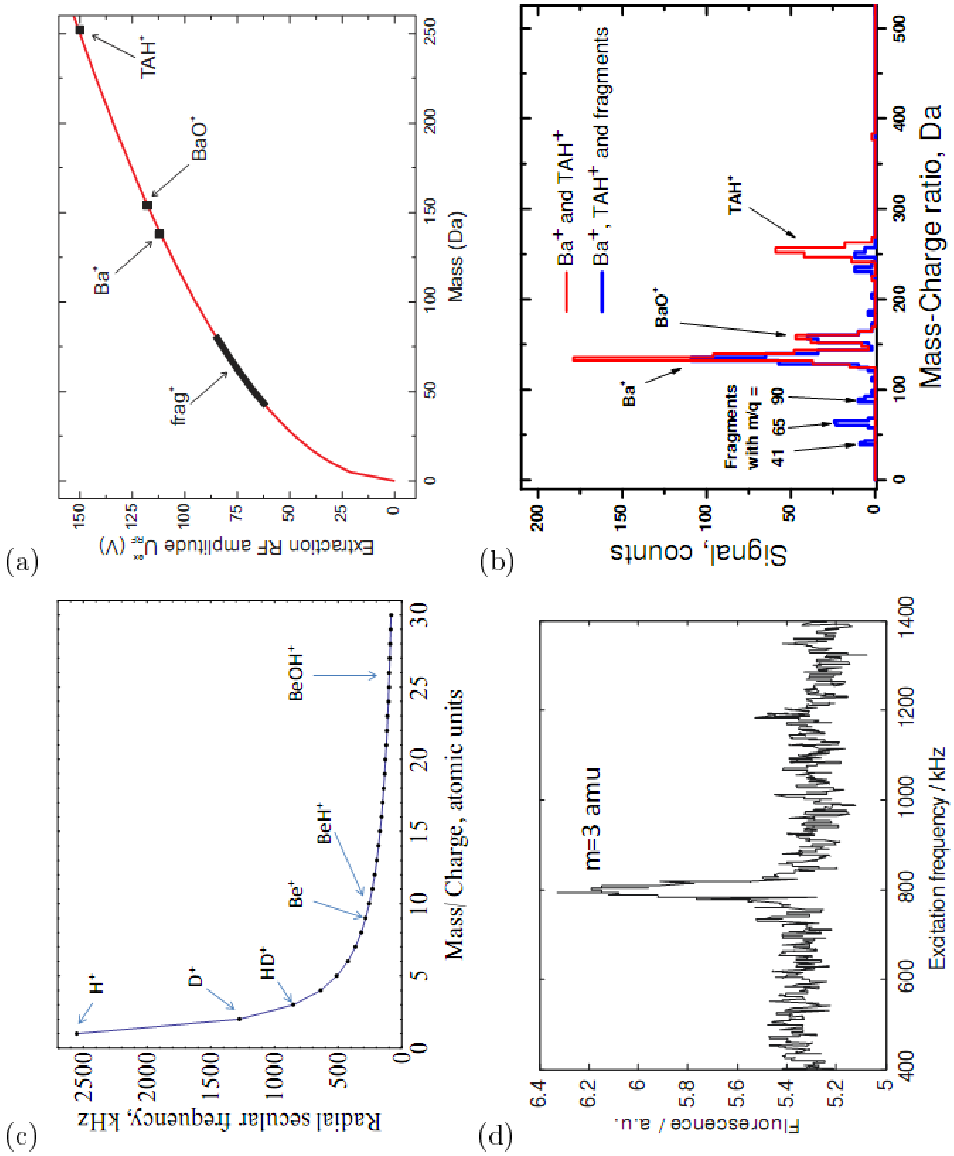

FIGURE 3.2.1. Mass-selective detection with linear quadrupole trap. (a, b): the extraction method, used in vibrational spectroscopy of complex molecular ions (see Ref. [5]). (a) - extraction diagram of different species. (b) - example of results of extraction; several different species are resolved. (c, d): secular excitation method used in $HD^+$ spectroscopy. (c) - secular excitation diagram for different species relevant to the experiments; the light atomic and molecular ions ($H^+$, $D^+$, $HD^+$) have their frequencies, significantly different from those of heavier species ($Be^+$, $BeH^+$, $BeD^+$, $BeOH^+$) and can be resolved. (d) - example of a secular excitation, used in $HD^+$ spectroscopy [S. Schiller et al]; m=3 is the weight of $HD^+$ in atomic units.

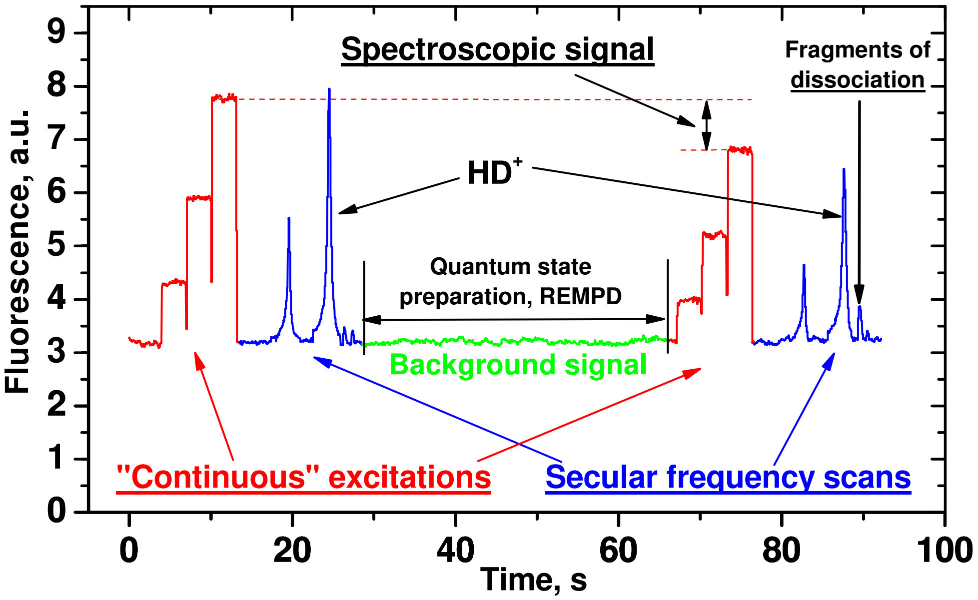

FIGURE 3.2.2. Illustration of a mass-selective excitation of $HD^+$ ions and fragments of their dissociation. The secular excitation is applied at the beginning of the measurement procedure, indicating the number of $HD^+$ ions; this excitation is applied in two ways: fast and slow frequency scans. For the fast scan, the scan rate is $> 10$ Hz, the scan range is relatively small (few tens of kHz), and the fluorescent signal is averaged over excitation frequencies (time constant 0.1 s). This is regarded as “continuous” excitation. For the slow scan, the rate is $< 0.4$ Hz, the scan range is relatively large (about 1 MHz) and it is possible to resolve the issue of different species. This is designated as a “secular frequency scan”. After initial excitations, quantum state manipulation and REMPD is carried out. The secular excitations are applied again after the selective dissociation, providing information about the residual $HD^+$ ions, and about dissociation fragments that may have appeared. A comparison of the initial and residual number of $HD^+$ ions provides a spectroscopic signal.

# Part 2

# Development of the experimental setup

In this section, improvements of the experimental setup, and developments of new apparatus and experimental approaches, will be described. Characterizations, if applicable, will be provided. Most of the developments and results, described in this chapter, are used in the experimental studies of molecular ions (see the following chapters and the papers attached). For information about the setup used in experiments on complex molecular ions, see the attached paper [5].

CHAPTER 4

# Experimental setup

## 4.1. General scheme, imaging optics and fluorescence detection

The experimental setup, developed earlier (see Ref. [37]), was modified by me to fit the new experimental approaches. Fig. 4.1.1 illustrates the setup for high-resolution spectroscopy in HD$^+$ ions. The core of the setup is a linear quadrupole (Paul) trap, installed in an ultrahigh vacuum (UHV) chamber. The vacuum chamber has optical and terahertz access for delivery of the electromagnetic radiation to the trap center in the axial and diagonal directions. The chamber has an electrical access to apply voltages for Be evaporation and to the electron gun for ionization of the atoms and molecules, and an electrical access to the electrodes of the trap. Imaging optics are installed for laser-induced fluorescence detection: one is based on a PhotoMultiplier Tube (PMT) for photon counting, and another is based on a charge-coupled device (CCD) camera for imaging the Coulomb crystal.

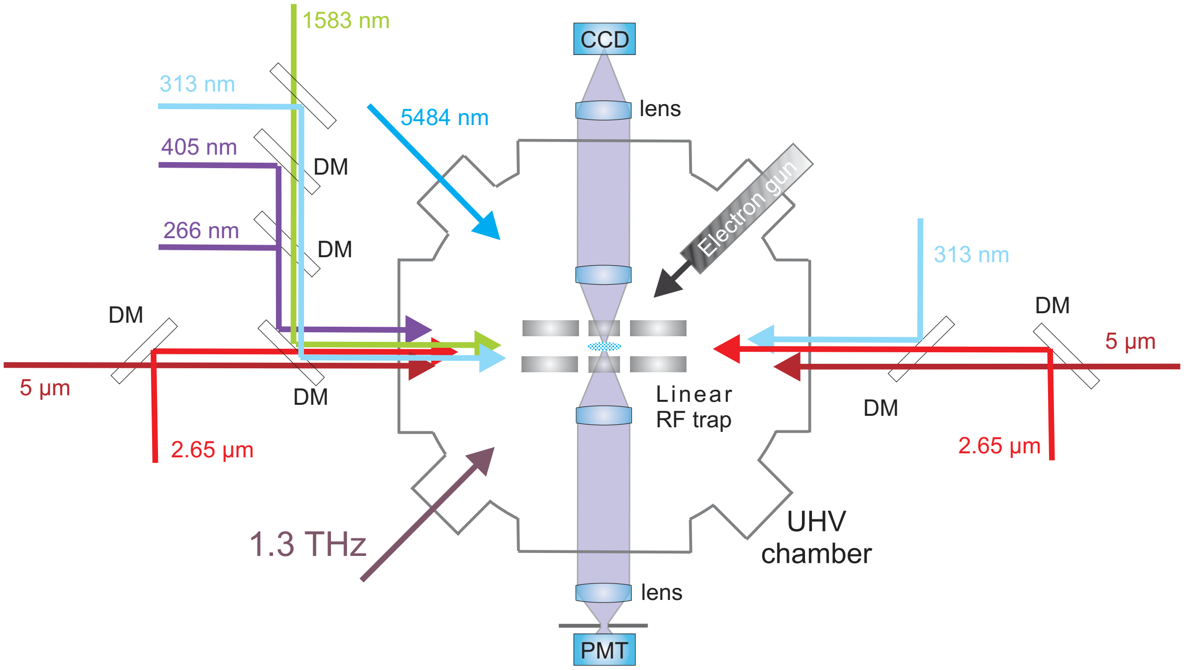

FIGURE 4.1.1. Schematics of the trap system and laser beams for high-resolution spectroscopy in HD$^+$.

In the course of the experiments, the setup was modified to meet changing requirements; these modifications usually concerned the optical part only. The schemes of the setup used in the research of a fundamental rotational and weak spin-forbidden vibrational transition are shown in the attached publications (appendices 4 and 5).

### 4.2. Optical setup

The optical setup, used in the previous experiments (see Ref. [37, 44]), was modified and improved in order to meet the requirements of combining different beams. Minor changes were made to combine the beams as follows: two beams, at 1.4 µm and at 266 nm, were delivered from the left-hand side of the setup; 313 nm beam and 5.1 µm beam were delivered from the right-hand side (see Ref. [45]). The motivation to rebuilt the scheme even further was behind our plan to combine more beams of different wavelengths: 266 nm, 313 nm, 1.4 ... 1.6 µm, 2.7 µm, 5.1 ... 5.5 µm, and later 405 nm. Additionally, the optical mounts used before were not of a good quality, see Fig. 4.2.1, and in the new scheme it was decided to replace the mounts with a new type less sensitive to temperature variations. We planned to use focused beams, and an old scheme of beam alignment, using 2 irises, was not sensitive enough to ensure a proper beam alignment and their overlap. Among the candidates for the new scheme for alignment of the beams, we considered the following: delivering several beams by an optical fiber, and using a "copy point" concept. Regarding the variety of the wavelengths used, ranging from UV to Mid-IR, a "copy point" concept was chosen as a more universal and flexible method. With this concept, a 313 nm laser beam is used as a guide beam, and all other beams are combined with it (see Fig. 4.2.2).

An alignment of the guiding beam can be controlled by imaging optics: from the image in the CCD camera and/or by the fluorescence signal. Inaccuracy involved in this method of alignment can be attributed to the following factors (see Fig. 4.2.3): imprecision of a guiding beam alignment (10 µm), imprecision of a "copy point" with respect to the guiding beam (around 5 µm) and with respect to the position of the trap center (not more than about 3 mm), and imprecision of the alignment to the iris aperture (typically, 0.3 mm, distance from the trap center 250 mm). Totally, inaccuracy is estimated to be 25 µm, providing a good adjustment accuracy for all the beams used. This estimation is valid when the beams are tightly focused to the diameter of about 100 µm and smaller, i.e. when the precise alignment is important. If the beam has larger diameter, the need to be precise becomes less critical.

The main candidates for the new scheme of beam overlapping were: optical elements with a high dispersion, and beamsplitters with high transmission in IR optical domain and reflecting light in UV optical range. The dispersion element, like a prism, required a long separation distance to overlap the beams. This is especially undesirable for the longer wavelength, since

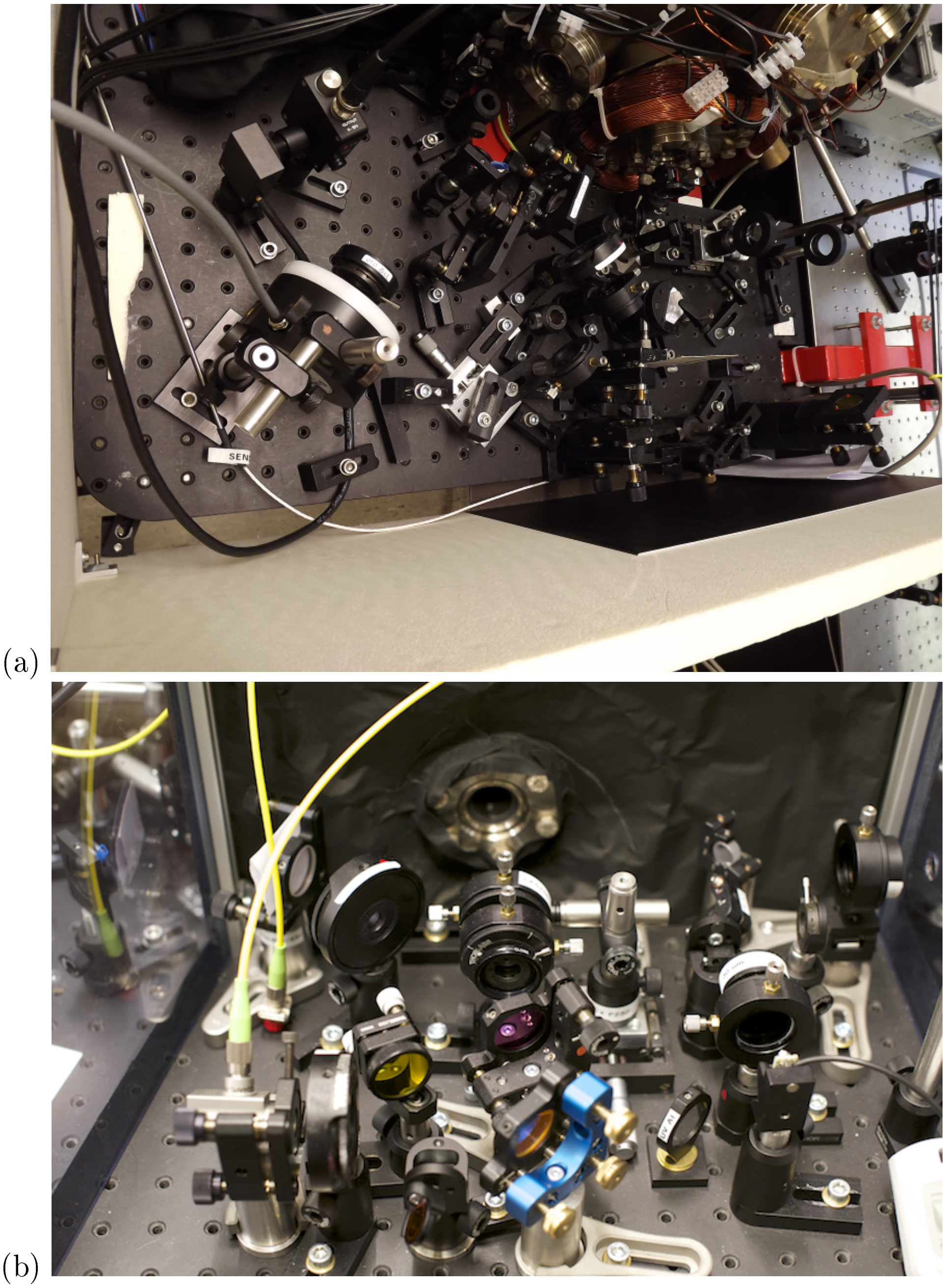

Figure 4.2.1. Optical setup before (a) and after (b) improvement of optical components used.

a collimated beam even with a relatively large diameter of 5 mm starts to diverge quickly, limiting focus spot size. A more compact scheme based on a beamsplitter with high transmission in IR and high reflectivity in UV was considered, but was not available at the time of inquiry.

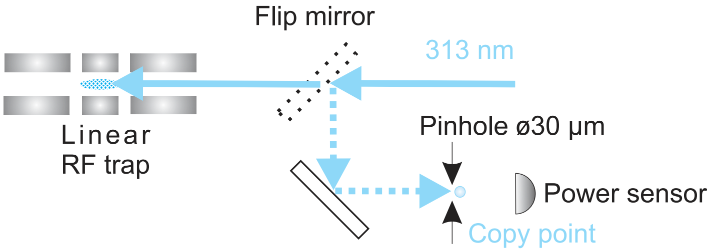

FIGURE 4.2.2. The concept of beam alignment, based on “copy point”. The guiding beam is assumed to be aligned. It is deflected by a flip mirror (shown with a dashed contour), and passes a distance, equivalent to the path from the deflecting mirror to the trap center. At the copy point, which is a mirror image of the trap center, a pinhole is installed. The pinhole represents the trap center and can be used for alignment of any other beam to the trap center.

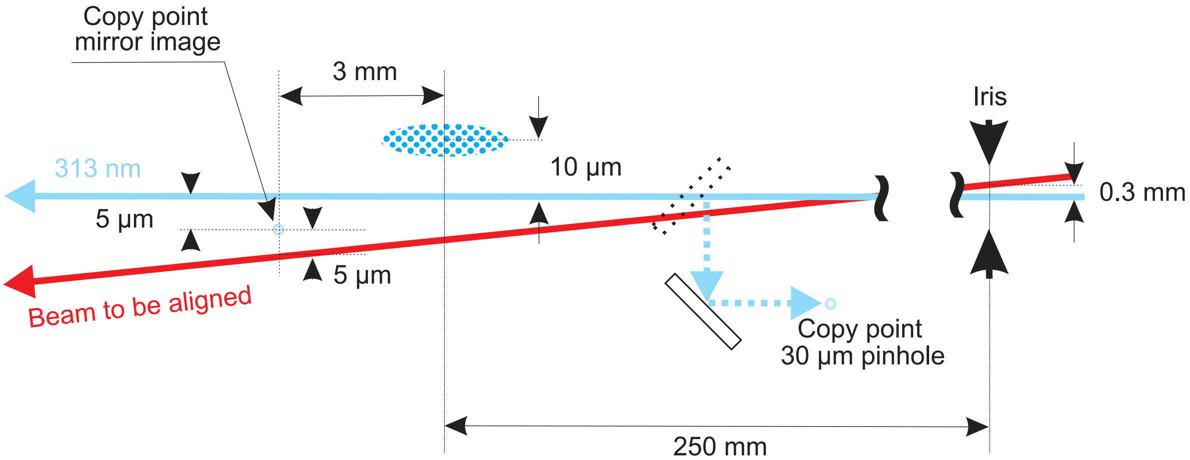

FIGURE 4.2.3. Imprecision of alignment. The dimensions are not to scale, and small misalignments are exaggerated to become visible. Two beams are shown: 313 nm guiding beam (in blue) and all other beams to be aligned (in red). The guiding beam is aligned to the crystal center with 10 µm imprecision. The pinhole is installed close to the copy point, with imprecision of 5 µm relative to the beam center, and with imprecision of 3 mm relative to the crystal center. All beams, except the guiding beam, are assumed to be aligned to the pinhole with imprecision of 5 µm at the copy point position, and with imprecision of 0.3 mm at the iris position. The total imprecision is estimated as a sum of all imprecisions, this being 25 µm.

Several semiconductor materials were considered by me, those which have good transmission in IR, and high, almost metal-like, reflection in UV. Crystalline silicon looked particularly

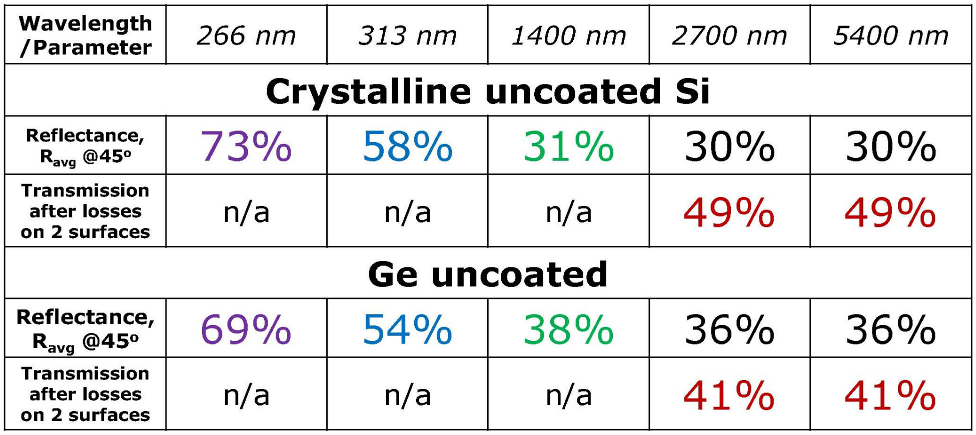

| **Wavelength /Parameter** | *266 nm* | *313 nm* | *1400 nm* | *2700 nm* | *5400 nm* |
|---|---|---|---|---|---|
| **Crystalline uncoated Si** | | | | | |
| **Reflectance, $R_{avg}$ @45°** | 73% | 58% | 31% | 30% | 30% |
| **Transmission after losses on 2 surfaces** | n/a | n/a | n/a | 49% | 49% |
| **Ge uncoated** | | | | | |
| **Reflectance, $R_{avg}$ @45°** | 69% | 54% | 38% | 36% | 36% |
| **Transmission after losses on 2 surfaces** | n/a | n/a | n/a | 41% | 41% |

Table 1. Reflection and transmission of two semiconductor beamsplitter plates, potentially appropriate for combining different wavelengths. Thickness of the beamsplitters is 5 mm. In a UV range, the materials have high reflectivity, and have low transmission losses in IR range. The losses associated with Fresnel reflections are too large for the considered applications. The different colours have a legend: from violet to red, violet means “very useful”, and red means “unsatisfactory”. In black, information which is not relevant to the performance of the beamsplitting, is shown.

interesting for our applications, but the efficiency of transmission IR light was quite low because of the Fresnel reflection of the material with a high refraction index. Transmission and reflection of Si and Ge are shown in Table 1 for different wavelengths.

An inexpensive Si optical window, AR-coated at 3...5 µm, proved to be a good compromise solution. The coating ensures low losses at 2.7 µm and at 5.4 µm, two wavelengths, for which minimal losses are desired as the beams are supposed to apply an optical force and to drive a two-photon transition, respectively. For other wavelengths, a partial reflection is tolerable, because the corresponding beams have high powers, enough to saturate the corresponding one-photon transitions, and to induce high transition rates in $HD^+$. The data of the experimentally measured transition and reflection for AR-coated at 3 ... 5 µm coated crystalline Silicon, are shown in Table 2.

The scheme of beam combining is shown in Fig. 4.2.4 (left-hand side and right-hand side of the vacuum chamber). The new scheme, made of stable mirror mounts on 1-inch pedestal bases, ensures stable beam alignment (see Fig. 4.2.1 (b)); compared to the previously used scheme, only rare re-alignments are required.

The optical scheme contains also wave retarders (not shown in the Figure). Lenses $L1$ ($CaF_2$) are installed to focus the beams towards the trap center. The additional lens $L2$ attached to the flip mount is intended for collimation of a cooling laser beam at 313 nm,

| **Wavelength /Parameter** | *266 nm* | *313 nm* | *1400 nm* | *2700 nm* | *5400 nm* |
|---|---|---|---|---|---|
| **#1. Crystalline Si, AR/AR@3…5 µm, AOI = 15…35°** | | | | | |
| **Reflectance, $R_{avg}$ @45°** | 40% | 38% | 60 % | n/a | n/a |
| **Transmission after losses on 2 planes** | n/a | n/a | n/a | 95% | 94% |
| **#2. Crystalline Si, AR/AR@3…5 µm, AOI = 15…35°** | | | | | |
| **Reflectance, $R_{avg}$ @45°** | n/a | 47% | n/a | n/a | n/a |
| **Transmission after losses on 2 planes** | n/a | n/a | n/a | 95% | 92% |

TABLE 2. Transmission and reflection of Silicon Anti-Reflection coated for 3 to 5 µm. Thickness of the beamsplitters is 5 mm. The colour legend is the same as in Table 1.

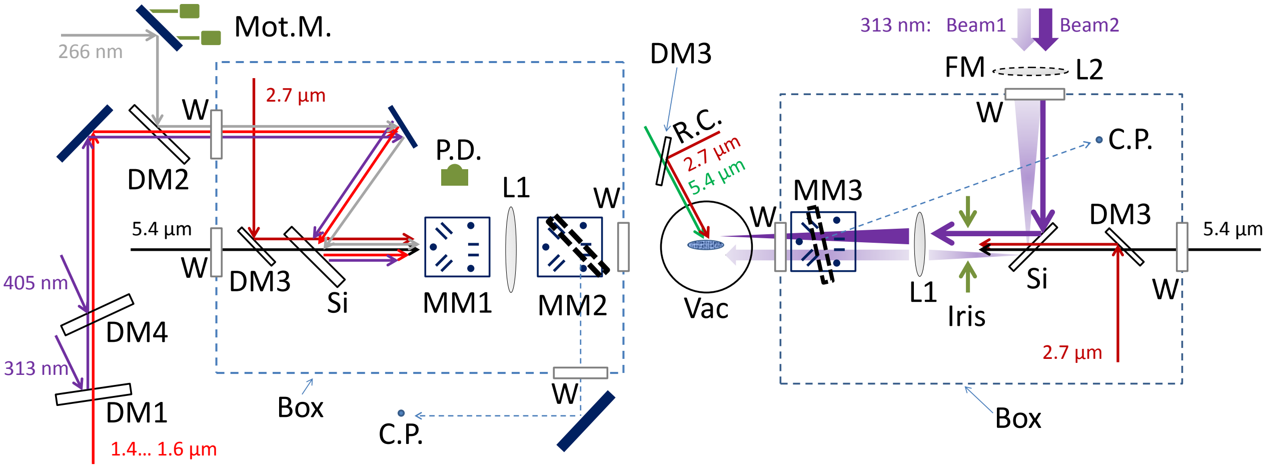

FIGURE 4.2.4. Improved scheme of the experimental setup, used in the experiments requiring combining of different wavelengths. The following abbreviations are used: C.P. - copy point, W - $CaF_2$ optical window, DM - dichroic mirror, Mot.M. - motorized mirror mount, MM - magnetic mount, FM -flip mount, L - lens, P.D. - space reserved for photodetector mount, Si - Silicon optical window AR coated @3...5 µm both sides, Vac - vacuum chamber, R.C. - rotational cooling lasers, Box - sealed enclosure flooded with nitrogen. Two different optical beam paths are shown for 313 nm light, "Beam 1" and "Beam 2". The first one is realized when a lens L2, attached to the flip mount, is inserted in the optical beam; the beam is shown in light violet. In this case a collimated beam is delivered to the trap center. The second optical beam path is realized when a lens L2 is removed from the optical path; the beam propagation is illustrated with dark violet. In this case the focused beam is delivered to the trap center.

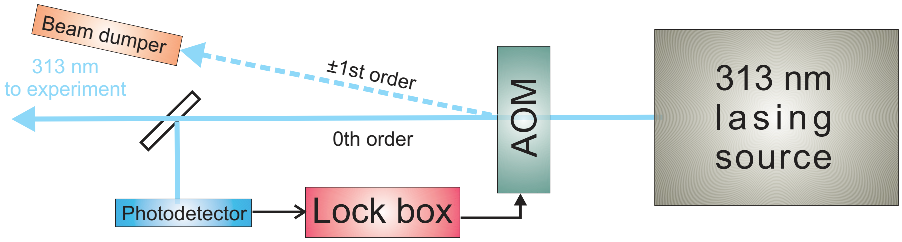

FIGURE 4.2.5. Scheme for stabilization of the cooling laser power at 313 nm. An acousto-optical modulator (AOM) can deflect part of the beam to a beam dumper, and enables the transmitted power to be varied. A stabilization of the transmitted power is realized by locking the system to a certain level of photodetector signal; a feedback from "Lock box" (PID controller) is sent to the AOM for stabilization of the transmitted power.

after propagation through 2 confocal lenses $L2$ and $L1$. Collimated 313 nm beam is more appropriate for cooling a large Coulomb crystal. Alternatively, 313 nm light can be delivered via single-mode fiber, however for the cost of power transmitted at a low level. The beam, delivered via fiber, is useful for small Coulomb crystals and small off-resonance detuning of the cooling beam; the fiber-guided beam has high mode quality, which increases the fluorescent signal and reduces the scattered light, thus increasing a signal-to-noise ratio (see Part 3 on measurements of a weak excitation).

## 4.3. Cooling laser power stabilization

The cooling laser source [46] did not have a special scheme for power stabilization of the 313 nm output radiation, and this power is subjected to fluctuations. To increase the stability of the output power, which is important for precision spectroscopy, the power is actively stabilized in the scheme, shown in Fig. 4.2.5. The AOM deflects part of the incident beam, thus providing a possibility to vary the transmitted power. A beamsplitter, installed after the AOM, reflects a small part of the incident beam to a power detector; the detector provides an error signal for power stabilization, shown as a "Lock box". A typical graph of a stabilized power and a power of a free-running laser source is shown in Fig. 4.3.1. The scheme used provides a good long-term power stabilization with residual long-term instability $< 5\,\%$, which can be an important step towards an increase in the resolution of the spectroscopic schemes we use.

## 4.4. Reduction of water vapor absorption

To reduce the water vapor absorption, which is especially strong for the wavelength of 2.65 µm, that is of particular interest as this wavelength corresponds to $(v = 0, L = 0) \Rightarrow$

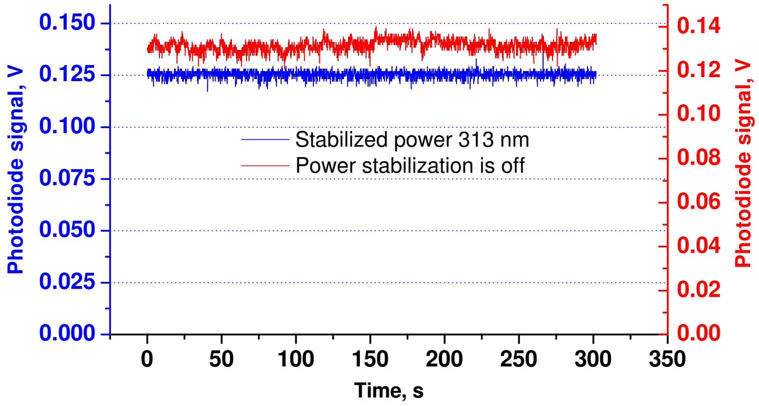

FIGURE 4.3.1. Illustration of stability of the 313 nm laser source with activated power stabilization (blue curve) and without its activation (red curve). The stabilization scheme effectively reduces low-frequency noise, which can be important for many experiments.

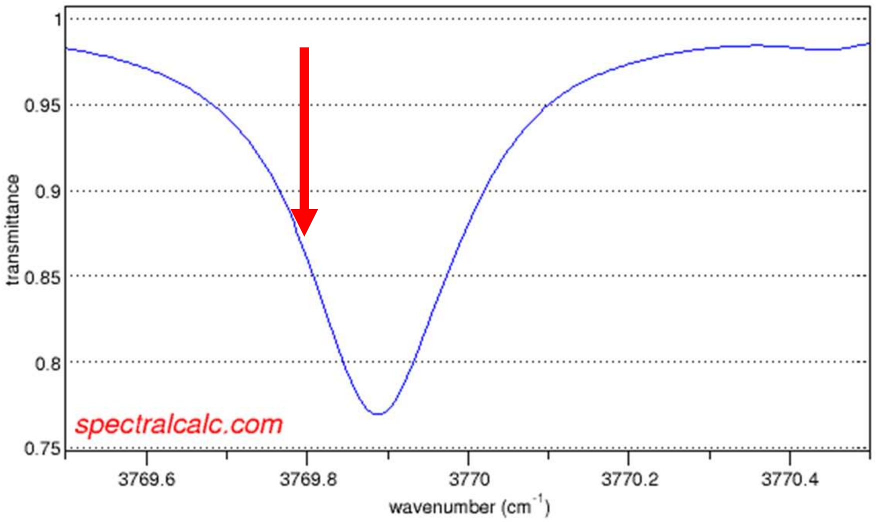

FIGURE 4.3.2. Water absorption at 2.65 µm. The data obtained from Ref. [47]. Parameters used: Database HITRAN2004, gas cell simulator $H_2O$ all isotopes, length 30 cm, 1 bar, 300 K, Volume Mixing Ratio 0.0014 (which corresponds to about 5 % relative humidity at 300 K). The red arrow points to the frequency of the $(v = 0,\ N = 0) \Rightarrow (v = 2,\ N = 1)$ transition of $HD^+$.

$(v = 2,\ L = 1)$ transition in $HD^+$ molecular ion, the optical setup is enclosed by the sealed box, flooded with a water-free nitrogen gas (Fig. 4.2.4). The absorption by the water vapor is illustrated by Fig. 4.3.2, where the spinless $f_{0,theor}$ transition frequency is marked by an arrow. It then follows that relative humidity less than about 5 % is required to transmit

$> 85$ % of power for propagation distance in the air of 30 cm. Experimentally achieved residual humidity $< 3$ % ensures that the residual water vapor absorption is $\lesssim 10$ %.

The optical parametric oscillator (OPO) has also been enclosed with a sealed box. The larger propagation distance, about 1 m, requires even less humidity. Experimentally-achieved residual humidity is beyond the range and resolution of the hygrometer we used; the humidity is estimated to be $< 0.1$ %, which ensures the beam propagation is almost without losses.

The gas absorption modelling was performed using spectralcalc online gas cell simulator [47].

## CHAPTER 5

# Demonstration of an all-diode laser transition detection in $HD^+$

The first experiment performed with one of distributed feedback (DFB) lasers (see sec. 16.7 for the details about the purpose of the lasers), was a demonstration of an all-diode laser transition detection in $HD^+$. Several diode lasers for driving the transitions shown in Fig. 5.0.1 were used to perform REMPD of $HD^+$, cooled by laser-cooled $Be^+$ ions. The scheme of quantum state preparation and of transition detection used here does not require any rotational cooling: the ground state ($v = 0$, $N = 1$) is populated thermally to a sufficient degree, its fractional population is 25 %. The population of the ($v = 0$, $N = 1$) level is decreased during REMPD, and the BBR-assisted pumping redistributes the remaining population of other levels in a few seconds, thus it is also possible to observe strong decay in a few seconds. The DFB1 laser was scanned over the range of about 1 GHz, and it induced, mainly, only the most strong hyperfine transitions between the ($v = 0$, $N = 1$) and ($v' = 2$, $N' = 0$) levels. The tunable telecom laser at the wavelength $\lambda' = 1565$ nm, having linewidth $\sim 50$ MHz, performes population transfer to a higher rovibrational level, ($v = 6$, $N = 1$), from which the $HD^+$ ions are effectively dissociated by 405 nm laser light. We used a "constant" secular excitation scheme (see sec. 3.2) for transition detection, i.e. the secular excitation was applied at the beginning of the measurement cycle and continued to the end of the measurement. The result of this transition detection is shown in Fig. 5.0.2, demonstrating the possibility that $HD^+$ spectroscopy can be carried out with commercially available diode lasers at a moderate-cost.

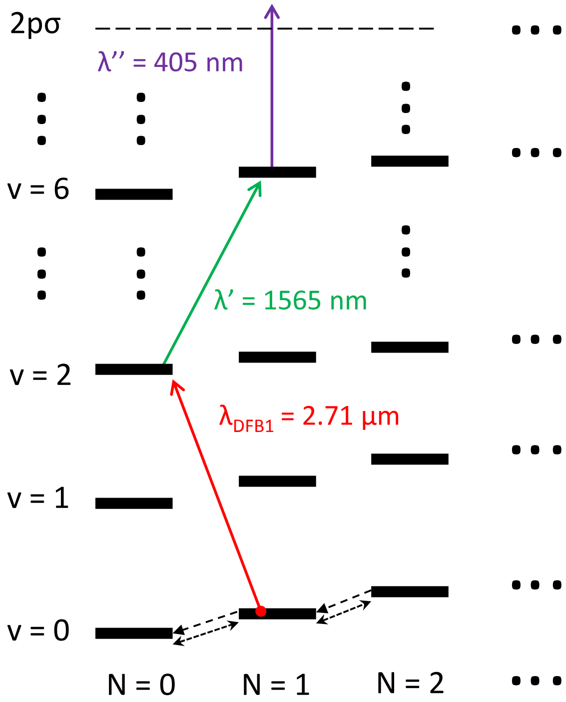

FIGURE 5.0.1. All-diode laser REMPD. Several diode lasers were used: a distributed feedback (DFB) diode laser at 2.71 µm, a commercial telecom diode-based laser at 1565 nm, and a violet diode laser at 405 nm.

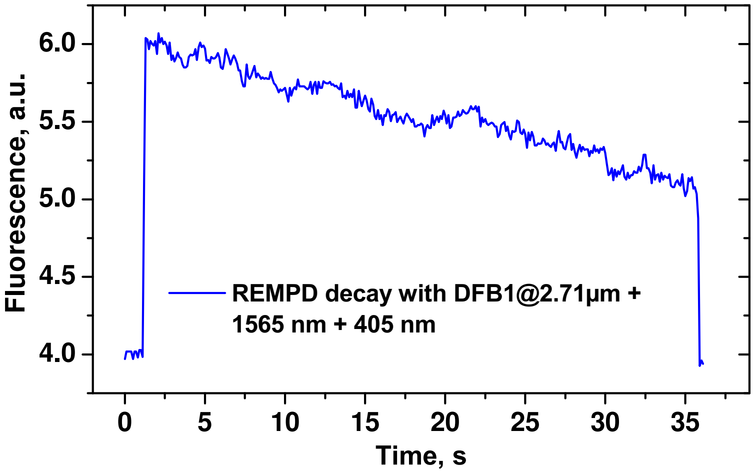

FIGURE 5.0.2. Illustration of the possibility to perform an all-diode laser REMPD spectroscopy. A "continuous" secular excitation method of mass-selective detection is used (see Chap. 3). See the text for the details about lasers and the detection scheme used.

## CHAPTER 6

# Internal state manipulation

Internal state manipulation is a crucial tool in fundamental and applied physics: for spectroscopy and metrology, in quantum computations and quantum information storage and transfer, for atom interferometry, and other fields [48–51].

Quantum state preparation is of importance for high-resolution spectroscopy of $HD^+$ as well. The $HD^+$ molecular ions, loaded in the trap, are cold vibrationally, since the rovibrational transitions are strong and higher vibrational levels are quickly de-populated (after, e.g. excitation by electron impact, or optical pumping) via spontaneous emission. The population is distributed among several of the lowest rotational levels, caused by the interaction with black body radiation (BBR), see Fig. 6.0.1. It was found (see Ref. [21, 22]) that using a few lasers helps to increase significantly the population in the lowest rovibrational level ($v = 0$, $N = 0$), see Fig. 6.0.2. Several experimental results took advantage of the high population and, consequently, higher signal detected, see e.g. Ref. [40, 45].

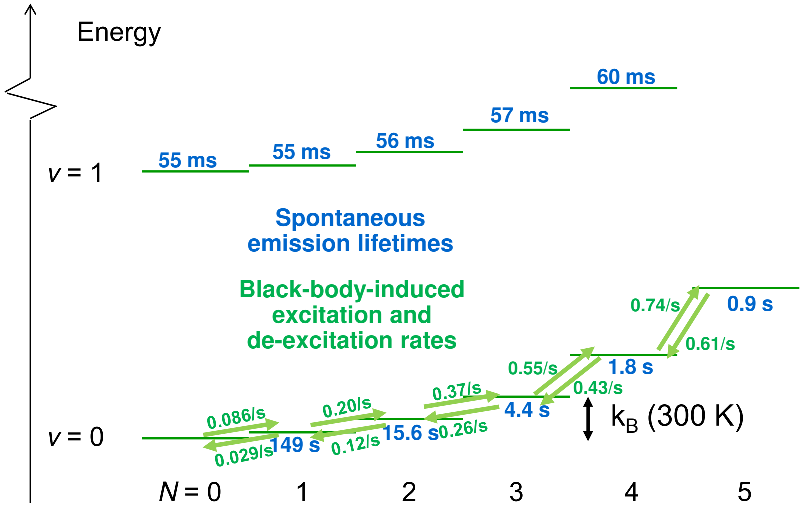

Figure 6.0.1. Rovibrational levels of $HD^+$ ions [3]. Spontaneous emission lifetimes are shown in blue, and black-body-induced transition rates are shown in green for several low-lying rovibrational levels. In the abscence of any other radiation sources, the BBR induces transitions in the rotational structure of the lowest vibrational levels. Several rotational levels are well-populated (up to $N = 4 \ldots 5$), with the highest fractional population at the $N = 2$ level.

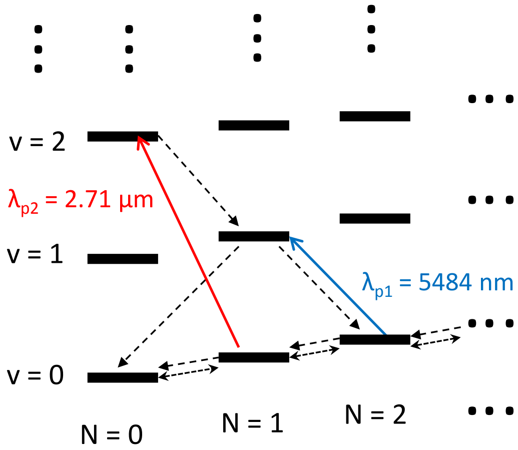

FIGURE 6.0.2. Rotational cooling in $HD^+$. Two lasers are used to perform optical pumping, shown in red and blue. They form an almost-closed transition scheme (upon neglecting BBR), which ensures efficient optical pumping. The $\lambda_{p1}$ light at 5484 nm is delivered from a quantum cascade laser (QCL) source. The distrubuted feedback (DFB) diode laser emits light at $\lambda_{p2} = 2.71$ µm. Spontaneous emission transitions are shown with dashed lines, and BBR induced transitions are shown with dotted lines.

### Hyperfine-state-selective transitions

The important step in the state preparation was carried out in [45]: the optical pumping between different hyperfine (hf) states was realized, see Fig. 6.0.3. In terms of $HD^+$ molecular ions, the hyperfine state is characterized by the three quantum numbers, $F$, $S$ and $J$. The hf-state changing transition is thus a transition (RF or a rovibrational), for which at least one of these quantum numbers is changed. They can be devided into the three classes: (i) allowed, for which $\Delta J = 0, \pm 1$, but $F$ and $S$ remain unchanged, (ii) spin-forbidden, when one of the $F$ or $S$ quantum numbers is changed, (iii) doubly spin-forbidden, for which both $F$ and $S$ are changed.

Transitions between different hyperfine states can be used to increase the population of any of the hyperfine states. This can be accomplished by carrying out optical pumping with involving de-population of the other hyperfine states and transferring their population to the desired state. These hyperfine-state selective transitions result in certain requirements for the lasers used: the frequency must be well controlled, to ensure that only desired transitions are excited. Additionally, the required power to drive the transitions can be relatively high (see Appendix 5), as many of these transitions are forbidden (or doubly-forbidden) and are weak compared to the most strong transitions (as an example in Fig. 6.0.3, the “P4” line is a weak, doubly spin-forbidden transition).

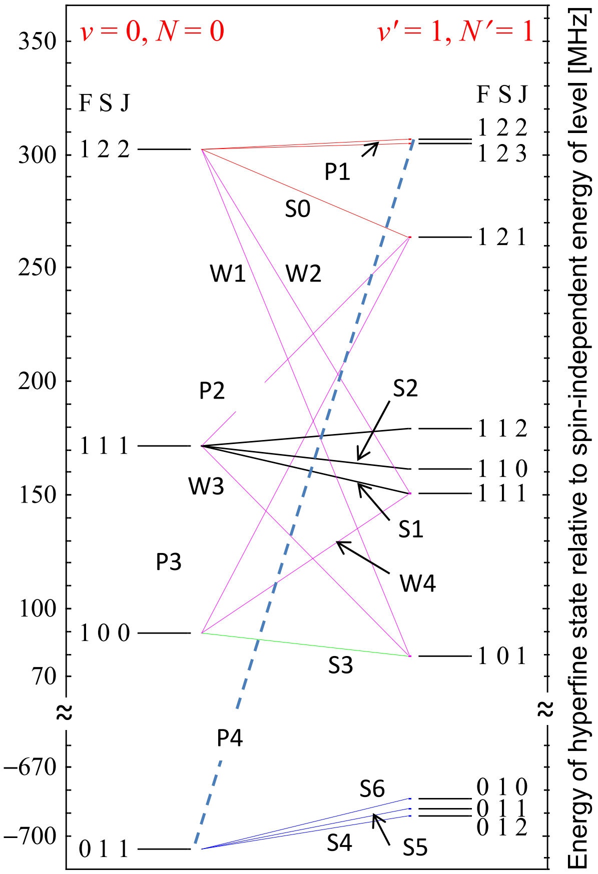

FIGURE 6.0.3. Hyperfine states and some relevant hyperfine transitions ($v = 0,\ N = 0) \rightarrow (v' = 1,\ N' = 1)$ in HD$^+$ [3]. “P, S, W” denotes pump, strong and weak transitions, respectively.

The more detailed information about implementation of rotational cooling and hf-state selective transfer can be found in the attached papers (Ref. [45] and Appendix 5).

CHAPTER 7

# The Optical Parametric Oscillator (OPO)

## 7.1. IR laser souces

Fundamental or low-order overtone vibrational transitions in molecules and molecular ions require light sources in the IR spectral range. Existing laser sources include quantum cascade lasers, diode lasers with distributed feedback, schemes for difference frequency generation and optical parametric oscillators (OPO). The latter, OPO, can provide significant conversion efficiency and high output power. Nowadays OPO systems take advantage of the progress being made in manufacturing non-linear material, including periodically-poled crystals. Different kinds of OPOs are available, including commertially designed ones, with a wide range of specifications: wavelength from UV to mid-IR, CW or pulsed mode. Resonators used to increase conversion efficiency include: single-, double- and triple-wave resonant; mirrorless OPOs also exist. Non-linear materials include bulk or periodically-poled crystals. Methods, developed for frequency and power stabilization, allow OPO to be used as a stable, tunable high-power lasing source for a number of applications in spectroscopy, physical chemistry and other fields (see, e.g. Ref. [52–54]).

A general description of different kinds of OPO can be found elsewhere (see, e.g. [55]). More detailed information about OPO, used in the described experiments, can be found in Ref. [56]. Fig. 7.1.1 illustrates the scheme of the OPO setup.

This singly-resonant OPO is used in: (1) vibrational spectroscopy in polyatomic molecular ions (see Ref. [5]), (2) optical pumping and observation of a weak, doubly spin-forbidden transion in HD$^+$ ion (see Appendix 5), and (3) experimental attempts to observe an optical force.

## 7.2. Frequency stabilization of the OPO

The method of frequency stabilization of the OPO used in vibrational spectroscopy of complex molecular ions (see Ref. [5]), counterdirectional mode coupling, is described in Ref. [56, 57]. This method of frequency stabilization did not result in the required long-term stability of the idler wavelength, and the OPO stabilization scheme was re-built by me to meet the requirements of long-term mode-hop-free operation. The thermal locking mechanism (see, e.g. Ref. [58]) was chosen as a method for providing long-term mode-hop-free

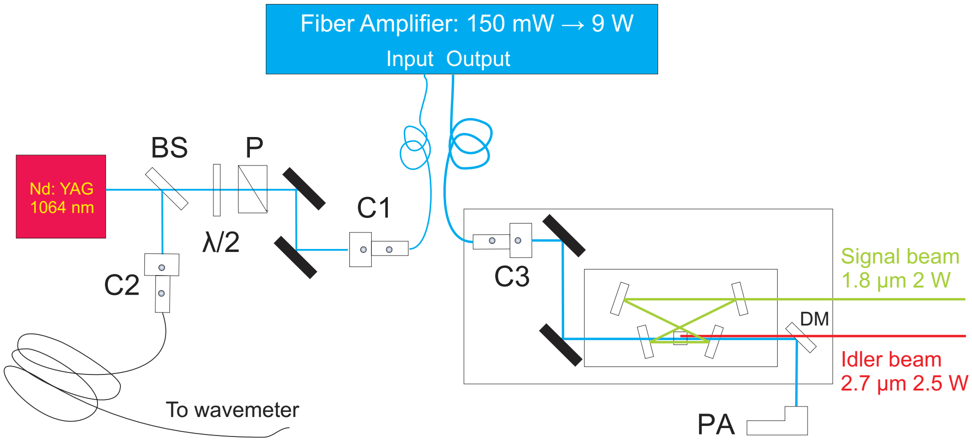

FIGURE 7.1.1. Scheme of the OPO (after [56, 57]). The Nd:YAG laser seeds an optical fiber amplifier, increasing the power to 9 W, used as a pump for the OPO. The OPO consists of collimation unit C3, pump beam alignment mounts, resonator for a signal wavelength (1.8 µm), and a temperature-stabilized oven for MgO periodically-poled lithium niobate, realizing a frequency down-conversion. DM - dichroic mirror for separation pump and idler beam. BS - beam sampler; P - polarizer; PA - power absorber; C1, C2, C3 - fiber collimators.

operation. The most important aspect of the method is its ability to achieve temperature stability of the nonlinear crystal: typically, a tolerable instability is 10 mK. The first thermal control unit used was not able to maintain the required temperature stability, and was improved. The well-shielded second generation temperature control unit met the requirement of 10 mK temperature stability, to provide the long-term mode-hop-free operation.

To realize the frequency stabilization of the idler radiation, the pump frequency is actively tuned to compensate for any drift of the signal (and pump) frequency. The direct measurement of the idler frequency ($\lambda = 2.7\,\mu$m) is difficult to realize; this frequency is obtained by measuring both the pump and signal frequencies alternately using an etalon wavemeter. The illustration of this method is shown in Fig. 7.2.1. The typical residual instability of the output wavelength is illustrated in Fig. 7.2.2, 7.2.3, showing that the idler frequency is stable within about 10 MHz (relative to the wavelength meter), for a duration of several hours. The short-term instability is estimated to be no more than ± 20 MHz, see attached preprint in Appendix 5.

The concept of the active stabilization of the idler frequency is realized by sending the pump and signal beams alternately to the wavelength meter. We use the wavelength meter High Finesse Angstrom WS-7 IR. A PC program controls the shutters, calculates error signals and provides feedback to the pump laser to stabilize the idler frequency in line with a desired detuning. This program is run on the dedicated computer, and the possibility of establishing

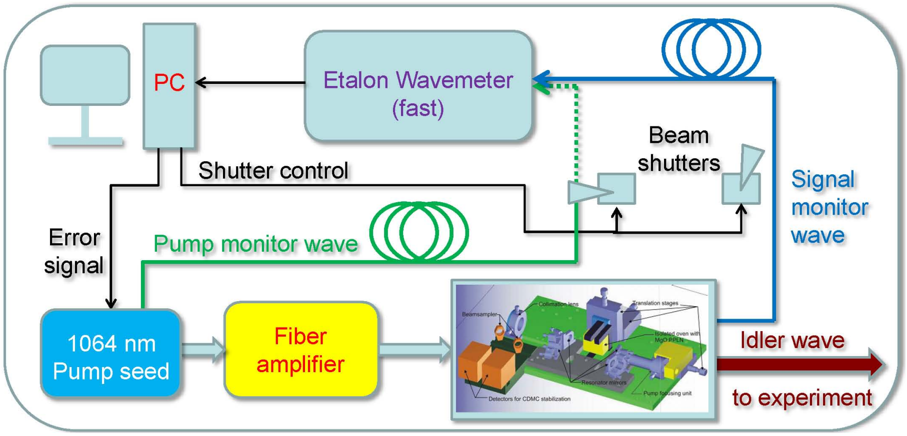

FIGURE 7.2.1. Scheme of OPO idler frequency stabilization. Two wavelengths, for signal and pump waves, are measured by the wavemeter alternately, to obtain the idler wavelength. The PC performs calculus to produce an error signal, sent via DAQ card to the "pump seed" laser.

remote control from the main measurement PC is realized. As the wavelength meter is prone to drifts, a periodical calibration is required. To make a precise calibration, an absolute frequency measurement is carried out with the help of the frequency metrology team from our group [59]. An optical comb, referenced to GPS, was used to calibrate the wavemeter at different wavelengths: the "pump seed" wavelength 1.064 µm, a "reference" wavelength 1.56 µm, and the "OPO signal" wavelength 1.8 µm. A daily check is carried out using a beam at 1.56 µm (the "reference" wavelength), which is obtained from the 313 nm frequency-stabilized laser source (see Ref. [46] for the details related to frequency stabilization in a 313 nm lasing source).

## 7.3. Application of the OPO

For experimental applications, the OPO idler beam is divided into 2 parts, each beam then passes through the Acousto-Optic Modulator (AOM), and the 1st order diffracted beam for each of the 2 beams is then coupled to ZBLAN fiber, see Fig. 7.3.1. The fibers are single-mode at 2.7 µm wavelength, and provide about 50 % transmission. AOMs are driven independently, by a self-made DDS synthesizer and 2 amplifiers (up to about 16 W each). AOMs are water-cooled, and have center frequencies of 50 MHz. The DDS synthesizer can provide two independent frequencies, $f_1$ and $f_2$, their difference $|f_1 - f_2|$, and its multiple $N\,|f_1 - f_2|$, where $N$ is a natural number (provided that all the frequencies do not exceed 150 MHz); the phase control of the waves is also realized. These phase-locked frequencies are important for time-resolved photon counting, see Chap. 8 and 11.

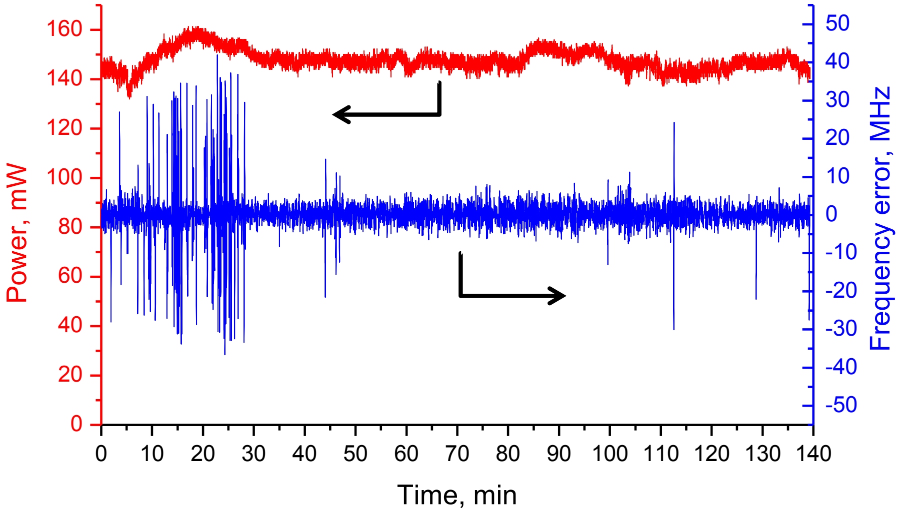

FIGURE 7.2.2. Illustration of the OPO output power (red, left scale) and idler frequency (blue, right scale) instability, while OPO idler frequency is stabilized to the wavemeter. Shown is a typical graph. First 30 min demonstrate higher fluctuations of both power and wavelength, which can be attributed to the heating-up of the OPO setup.

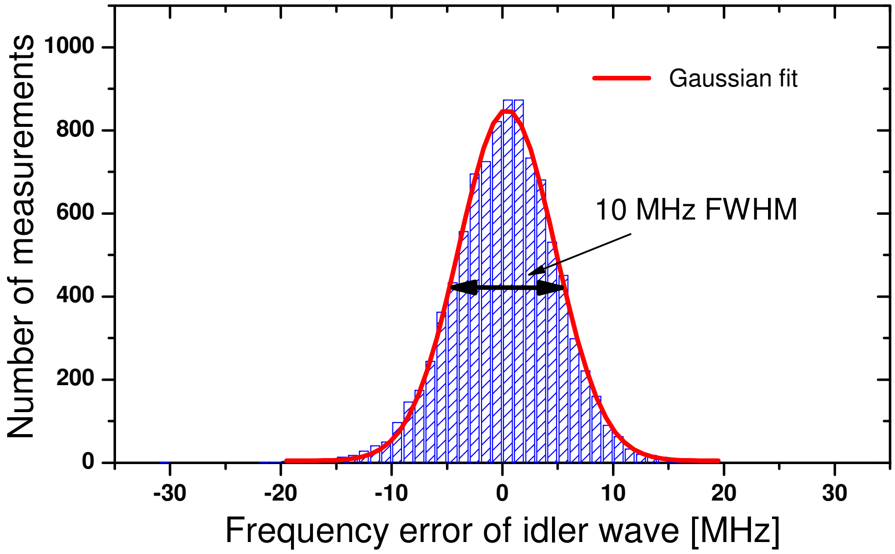

FIGURE 7.2.3. Histogram of the OPO detuning from the lock point. A typical result, obtained during a one-hour period, is shown. The values of error signals are binned with a step of 1 MHz. The Gaussian fit results in 10 MHz linewidth.

Time-resolved photon counting was used in the test experiments to detect an optical force, induced by OPO. The two optical waves, frequency-modulated with AOMs, driven by frequencies $f_1$ and $f_2$, can produce the phase-modulated standing wave. Both $f_1$ and $f_2$ are around 50 MHz and have their difference $|f_1 - f_2|$ in the range from a few ten kHz to

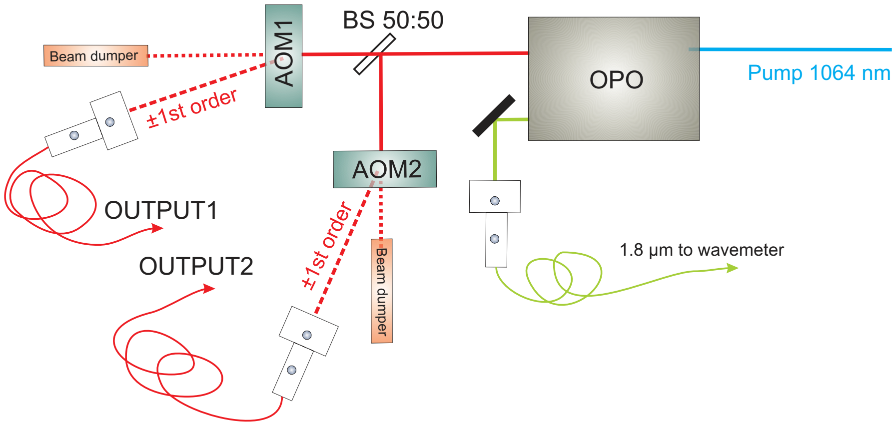

FIGURE 7.3.1. Scheme of employment for OPO idler wave. The beam is devided into two parts (approx. 50:50), each beam passes through independently-driven AOMs, and the ±1st order diffracted beam is coupled to ZBLAN fiber, single-mode at 2.7 µm. The signal beam at 1.8 µm is coupled (small part of the total power) to the wavemeter.

few MHz. The phase-modulated standing wave (also called a running standing wave) can induce an optical force (see Ref. [60]), exciting the ion motion with frequency $|f_1 - f_2|$. If this difference frequency (typical value for our setup is 100 kHz ... 5 MHz) corresponds to the crystal eigen mode, the secular motion is excited, which can be then detected. As the DDS provides an output of $|f_1 - f_2|$, this output can be used as a reference signal for the coherent motion detection.

For experiments, in which the OPO performs optical pumping, and which do not require optical force excitation, the difference frequency $|f_1 - f_2|$ is usually chosen to be a few tens of kHz. Setting this frequency to zero is not desirable, as this will produce a standing wave, and consequently, space-modulated intensity distribution, and may affect the experimental results. Using a slight modulation makes averaging of the intensity distribution on the time scale of seconds, used in the experiments.

The two AOMs can be set to produce the opposite orders of diffracted beams: one of them is the 1st order, and another is the “-1st” order. This scheme can be useful, for example, for excitation of Raman transitions. The difference frequency can be up to $\sim 120$ MHz, which allows excitation, for example, of certain hyperfine transitions of $HD^+$.

CHAPTER 8

# Field Programmable Gate Array (FPGA) for time-resolved photon counting

For the mass spectroscopy in the Paul trap, i.e. species-selective detection, the electric field-induced secular excitation can be applied with an amplitude of many volts and even larger, to induce a strong enough motion of specific ions, with subsequent heating of the crystal and measuring the change in fluorescence. This method was implemented in several of our experiments (see Ref. [40, 45] and Appendix 5).

The strong excitation becomes unavailable with, for example, excitation exerted by an optical force. In this case, a more sophisticated method of detection is required. One of the most sensitive methods is Doppler velocimetry based on time-resolved photon counting. With this method, a (periodic) motion of a laser-cooled fluorescing ion leads to a time-dependent (also periodical) fluorescence, which can be detected, see Fig. 8.0.1. In our approach we followed a method used in Ref. [60] (and also private communications [61]). For typical parameters of the setup, the time-resolved detection necessitates certain requirement: taking into account a low photon flux detected, the excitation should be repeated many times (many periods of excitation), and "folded" with a period of excitation. Experimentally this can be realized using a field-programmable gate array (FPGA) as a basis.

## 8.1. Time-resolved photon counting for a coherent motion detection

A FPGA can be configured to work as a counter of short pulses, which can be a photon flux, see Fig. 8.1.1. A fluorescent signal from PMT, after preamplifier and a discriminator (together, a "pulse shaper"), is sent to the event counter FPGA input ("Stop" port). Time-resolved counting can be realized, when the gate time for the incident count is small enough; practically, it should be less than the inverse of a photon flux.

Generally, for the counter incident event an arrival time is written to the file. If a periodic signal is to be detected, as in the case of a coherent motion excitation, an additional FPGA input, "Start" port, can also be used. When a "Start" signal arrives, the time is reset. Thus, any incident event has a "folded" arrival time, having a form of $T_{folded} = T_{real} \bmod T_{excitation}$, where mod is a modulo operation.

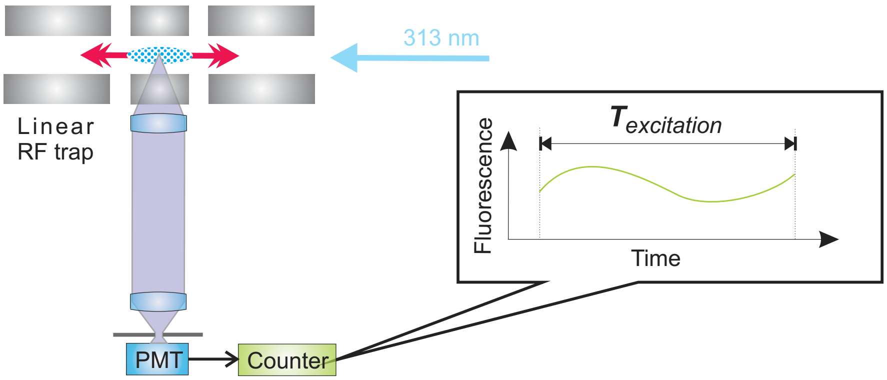

FIGURE 8.0.1. Illustration of a Doppler velocimetry. An AC voltage is applied to one, or several electrodes of the linear RF trap. A periodic electric excitation (with a period $T_{excitation}$) is then applied to the laser-cooled fluorescing ions in the trap, is shown as a red double-arrowed line. This excitation induces ion motion and results in periodic changes in fluorescence, shown as a green wavy line. $1/T_{excitation}$ is typically of the order of many tens kHz or more. The corresponding rapid fluorescence variation can be detected with time-resolved photon counting.

An FPGA is driven with an external clock frequency. The external clock frequency, as well as an ion excitation frequency, is derived from the same external RF source (here, a multi-channel DDS source); this ensures the phase coherence of the waves. The external clock defines the time resolution of the time-resolved counting: the signal is sorted in groups by its time stamp $T_{bin} = \text{Int}\left({}^{T_{folded}}/_{T_{clock}}\right)$ , where "Int" denotes an integer part. In other words, the "folded" arrival time $T$ is binned; typically ten to a few hundred bins are used.

For the typical parameters of the setup, the photon flux is of the order of a few thousand counts per second, and an excitation frequency is of the order of many hundred kHz. To have a reasonable signal to noise ratio, one would like to have at least more than one incident event per every bin, with the number of bins being more than 10. Additionally, excitation must be applied during, at least, its full period. Thus, the minimal time to detect a signal is in the order of millisecond. Practically, to achieve a good resolution, especially when a weak excitation is to be detected, the reasonable time to detect a signal can amount to many seconds.

An FPGA-based counter was built by U. Rosowski in our group for the purpose of performing the Doppler velocimetry (see Chap. 11).

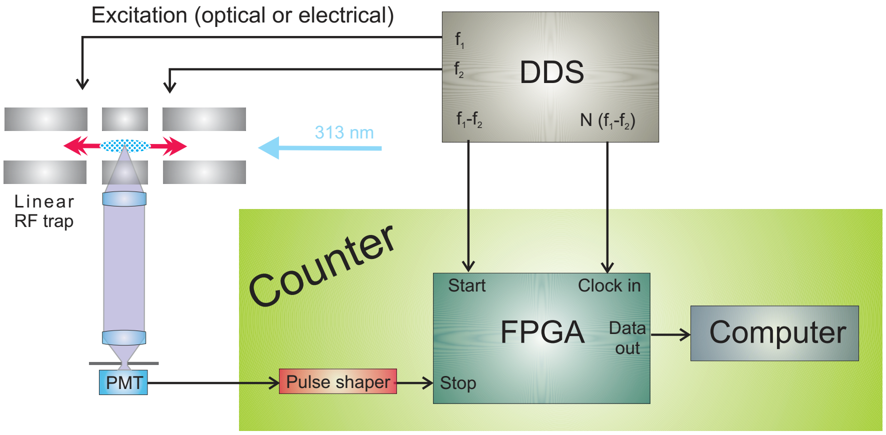

FIGURE 8.1.1. Principle of time-resolved photon counting. Two frequencies, $f_1$ and $f_2$ (or any of them) from the DDS synthesizer, are used to excite the ion motion. Optical excitation assumes applying an optical force and a running standing wave concept (see Chap. 14); electrical excitation can be applied using trap electrodes. The fluorescent signal is written to the data file: a time stamp is made for the detected photon event (when signal arrives at the STOP port). The time is counted in units of clock frequency units and is reset when the signal arrives at the START port.

## CHAPTER 9

# Optical magnetometry with $\mathrm{Be}^+$ ions

One of the important aspects of the precision measurements of the transitions in $\mathrm{HD}^+$ molecular ions is an information about the magnetic field experienced by the ions in the trap. The magnetic field defines the Zeeman splitting of the hyperfine levels, and this splitting becomes important for measurements of hyperfine transitions (in RF domain), rotational transitions (in THz domain), and for high-resolution measurements of rovibrational transitions (mainly, in IR domain).

The magnetic field in the trap also affects the transitions in $\mathrm{Be}^+$, which have to be taken into account to make an optimal choice of cooling radiation parameters. Of importance is also the possibility to vary the magnetic field in 3 orthogonal directions, making it feasible to reduce the magnetic field or to apply the magnetic field in any desired direction. One straightforward approach, applicable to the experimental setup for $\mathrm{HD}^+$ spectroscopy, is making use of $\mathrm{Be}^+$ ions as a precise magnetic field sensor.

The optical cooling scheme for 313 nm and relevant transitions in $\mathrm{Be}^+$ are shown in Fig. 9.0.1. As well known, [44, 62, 63] , use of $\sigma^+$ or $\sigma^-$ light polarization provides an almost close-cycle transition, giving rise to efficient laser cooling of $\mathrm{Be}^+$ ions. In this case, the population is distributed between the excited $2\,^2P_{3/2}$, $F = 3$, $m = \pm 3$ and the ground $2\,^2S_{1/2}$, $F = 2$, $m = \pm 2$ state, and does not decay into the $2\,^2S_{1/2}$, $F = 1$ state, as this would require the transition with $|\Delta m| \geqslant 2$, impossible with the dipole-allowed transitions. In practice, because the polarization state is not ideal, magnetic field is not stable in its amplitude and direction, and because of a Larmor precession, a $F = 1$ state of $2\,^2S_{1/2}$ level becomes populated. An optical sideband is generated in a 313 nm laser source, with the purpose of depleting this level and increasing laser cooling efficiency.

Fig. 1 of Appendix 6 illustrates the general coupling scheme. The case $\Delta_S = 0$ corresponds to an optical repumping scheme; $\Delta_S \simeq \Delta_C \gg \Gamma_{21}$, $\Gamma_{23}$, $\Omega_C$, $\Omega_S$ is the case, when the two-photon transition is important to consider.

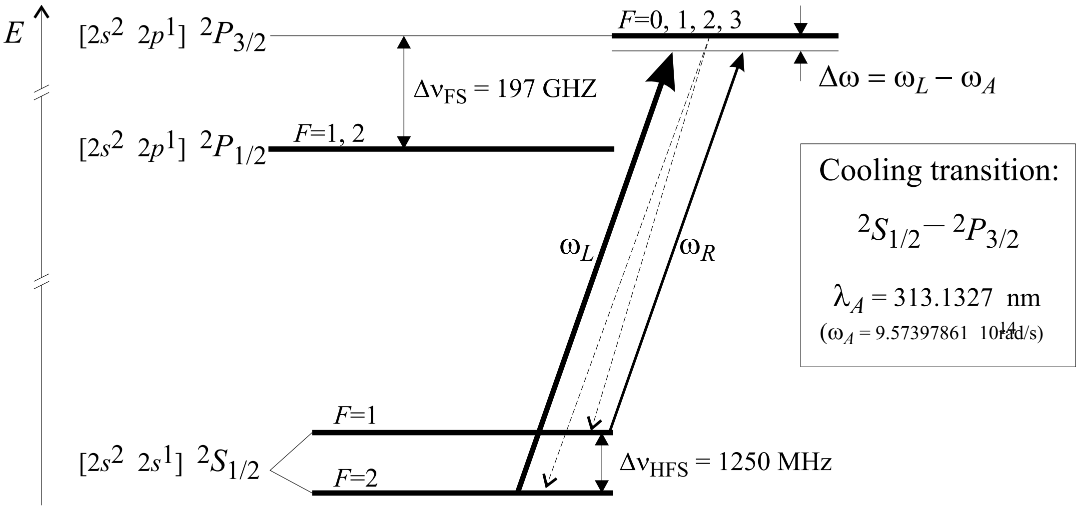

FIGURE 9.0.1. The optical transitions relevant to the laser cooling [44]. $\omega_L$ - carrier frequency; $\omega_R$ - a red-detuned sideband produced by an EOM.

### Determination of magnetic field in the trap center

I proposed the use of a two-photon, Doppler-free stimulated Raman transition to precisely measure the Zeeman splitting and to determine the magnetic field. With a $\Lambda$-scheme transition, two beams, pump and Stokes, should be co-propagating to eliminate or significantly reduce (the wavelengths are not equal) the Doppler broadening. An amplitude- or a phase-modulating EOM allows both the carrier and the sideband to be produced simultaneously, which is important for the stimulated two-photon transition.

I suggested the following parameters: carrier detuning in the order of a few tens MHz, Rabi frequency of the carrier up to a few MHz, detuning of the sideband is scanned to detect the resonance transition, and the Rabi frequency of the sideband is 10...100 times lower than the Rabi frequency of carrier. With these parameters, the one-photon transitions induced by a sideband, are $10^{-4} \ldots 10^{-2}$ weaker than those induced by a carrier, the effective Rabi frequency for a Raman transition is up to a few tens kHz. The Stark shift can also reach a few tens of kHz. The larger intensities with lower detunings are convenient for preliminary determination of the resonance, and reduction of intensity is necessary to increase the precision and reduce systematical shifts.

Another scheme, which allows to compensate for the Stark shifts and to measure unshifted (only broadened) transitions, was also proposed by me: it requires the equality of the Rabi frequencies of the carrier and the repumper.

More information about experimental realization performed by my colleague J. Shen is provided in Appendix 6.

# Part 3

# Measurement of an ion motion excitation

In this part, the results of an experimental detection of an externally induced ion motion will be described. Of special interest is detection of a relatively weak excitation. Measurement of a weak excitation becomes important, for example, to detect an optical force applied to the ions. Our motivation for using an optical force-based detection arises from the state-selectivity of the optical force applied to the ions (in addition to the species-selectivity, used in the mass spectroscopy detection method, which is applied before and after REMPD; see Chap. 3), and the non-destructive nature of the method. The optical force applies only to the ions in a specific state, thus providing a powerful tool for non-destructive spectroscopic measurements.

Most of the experiments, described here, were carried out for excitations, induced by an electric field, applied to the endcap (EC) electrodes of the Paul trap, thus inducing an axial excitation. Unlike an optical force, which is periodical in space with a period of just a few micrometers for the infrared optical domain, the periodic alternating (AC) electric field, applied to the endcap electrodes, creates an almost uniform electric field in the region close to the trap center. This allowed relatively large (up to many hundreds of ions) Coulomb crystals to be used in the test experiments for characterization of an ion motion excitation with a good signal-to-noise ratio. The results are strongly correlated with a case of only one ion in the trap, because the center-of-mass (COM) mode is excited (see Ref. [64–66]). In addition, the magnitude of electric field excitation can easily be controlled by a voltage applied to the EC electrodes, whereas an amplitude of optical force is limited by the power available from the OPO.

CHAPTER 10

# Determination of an electric field in the trap center

An alternating voltage, applied to EC electrodes, creates an electric field in the trap center, which is significantly screened by the presence of RF electrodes. It was experimentally determined that the electric field in the trap center, induced by the AC voltage, applied to the EC electrodes, obeys the relation:

$$E_{center}[{}^{V}\!/{}_{cm}] \approx {}^{V_{EC}[V]}\!/{}_{10}\,, \tag{10.0.1}$$

where $V_{EC}$ is a double amplitude (peak-to-peak) of the alternating voltage, applied to EC electrodes, and $E_{center}$ is the electric field, induced in the trap center. Fig. 10.0.1, (images on the right side) illustrates experimental determination of the electric field: two CCD images are taken, one before applying the shift voltage, and one after that. The shift voltage is chosen to move the ion crystal, so that it is moved by half of its length, and the outside ion takes a central position. In this case it is possible to evaluate the electric field experienced by the outside ion, and thus to estimate the electric field induced by EC electrodes. The ion-ion distance is taken from the image, and is estimated to be 30 µm. The electric field, corresponding to this ion-ion distance, is then multiplied by a factor of 1.65, which models for a string of a large number of equidistantly spaced ions (here, 7 ions), and is a sum of a series:

$$1.65 \approx \sum_{x=1}^{\infty} \frac{1}{x^2}$$

The voltages applied to the EC electrodes were: $\mathrm{EC}_1 = 4.3$ V, $\mathrm{EC}_2 = 5.82$ V before the ion crystal move, and $\mathrm{EC}_1 = 4.42$ V, $\mathrm{EC}_2 = 5.70$ V after the ion crystal move. The result of this experimental data analysis is represented by the Eq. 10.0.1. It is in reasonable agreement with the modelling results, made in Ref. [37], see Fig. 10.0.1 (left graph), according to which the relation has a form $E_{center}[{}^{V}\!/{}_{cm}] \approx {}^{V_{EC}[V]}\!/{}_{3.2}$ . The deviation of the two results can be related to experimental or modelling errors and uncertainties, the presence of other sympathetically cooled ions (which are invisible in the CCD image), degrading or coating of the electrode surfaces, stray electric fields (see Ref. [67]), and other effects, which limit the RF trap performance.

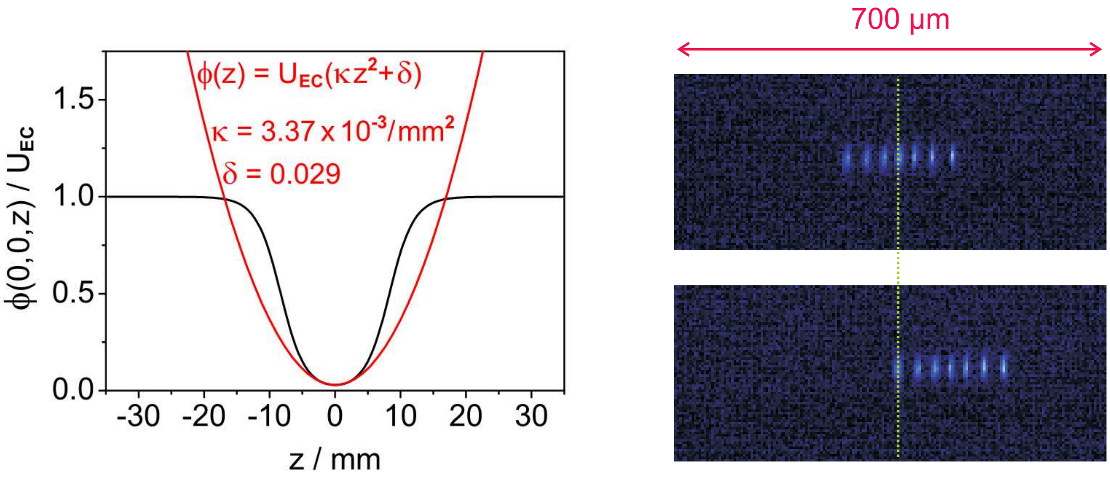

FIGURE 10.0.1. Determination of the axial electric field in the trap center as a function of the EC voltage. Left image - modelling results from U. Froehlich dissertation [37]. Images on the right are taken from a CCD camera for experimental determination of the electric field in the trap center.

The detailed study of the distribution of the electric field in the ion trap was not a focus of this work. The approximate evaluation of the electric field in the trap center as a function of the excitation voltage applied to the EC electrodes is implemented to determine the sensitivity of the ion excitation detection.

This part consists of two chapters, describing different methods of an ion motion detection: by a coherent motion detection, based on a FPGA time-resolved photon counting scheme, and a lock-in detection of an amplitude-modulated excitation, and discussion of the results.

CHAPTER 11

# Coherent motion detection by FPGA-based time-resolved photon counting

The basic concept of FPGA-based time-resolved photon counting is described in Chap. 8. For characterization of this method, a series of experiments were done with axial secular exitation of $Be^+$ and $HD^+$ ions by electric field, applied to the endcap electrodes. Fig. 11.0.1 shows dependence on the applied excitation frequency, when the amplitude of excitation is kept constant. The frequency, at which the highest fluorescence variation occurs, corresponds to the excitation at the secular frequency for the specific ions, in this case for an ensemble of $Be^+$ ions. The maximum variation was detected at a frequency of around 85 kHz, which is the center-of-mass (COM) axial mode of the ensemble of $Be^+$ ions (see Ref. [64–66], and also Ref. [68]). The resonance frequency determined accords well with the results obtained with other methods: lock-in detection (see Chap. 12) and by heating the crystal (which requires much higher excitation amplitude and is not appropriate for detecting weak excitation). The endcap voltages were 4.34 V and 5.28 V, and were chosen to move the Coulomb crystal to the center of the trap.

The graphs in Fig. 11.0.2 allow the sensitivity of the method to be determined: the amplitude of excitation was varied, while the excitation frequency was kept constant and was close to the COM mode of the ensemble of $Be^+$ ions. The sensitivity is determined to be about 0.8 $mV_{pp}$ , applied to the endcap electrodes.

For a quantitative, more detailed characterization of the ion motion and the sensitivity of the method, a discrete fast Fourier transform (FFT) of a folded binned signal is obtained (see also Chapter 8 regarding the signal processing). To characterize the induced motion, the FFT spectral component, having a frequency of the externally applied excitation, is divided by the average FFT spectral density (omitting the DC component for increased sensitivity), to obtain the "FFT contrast factor":

$$FFT\,Contrast\,Factor = \frac{\widetilde{F}_{exc}}{\sum_{\omega\neq 0}\widetilde{F}_{\omega}} \tag{11.0.2}$$

where $\widetilde{F}_{\omega}$ is a FFT component of frequency $\omega$. That is, the "FFT Contrast Factor" reflects the spectral density, having the frequency of external excitation, with respect to the averaged

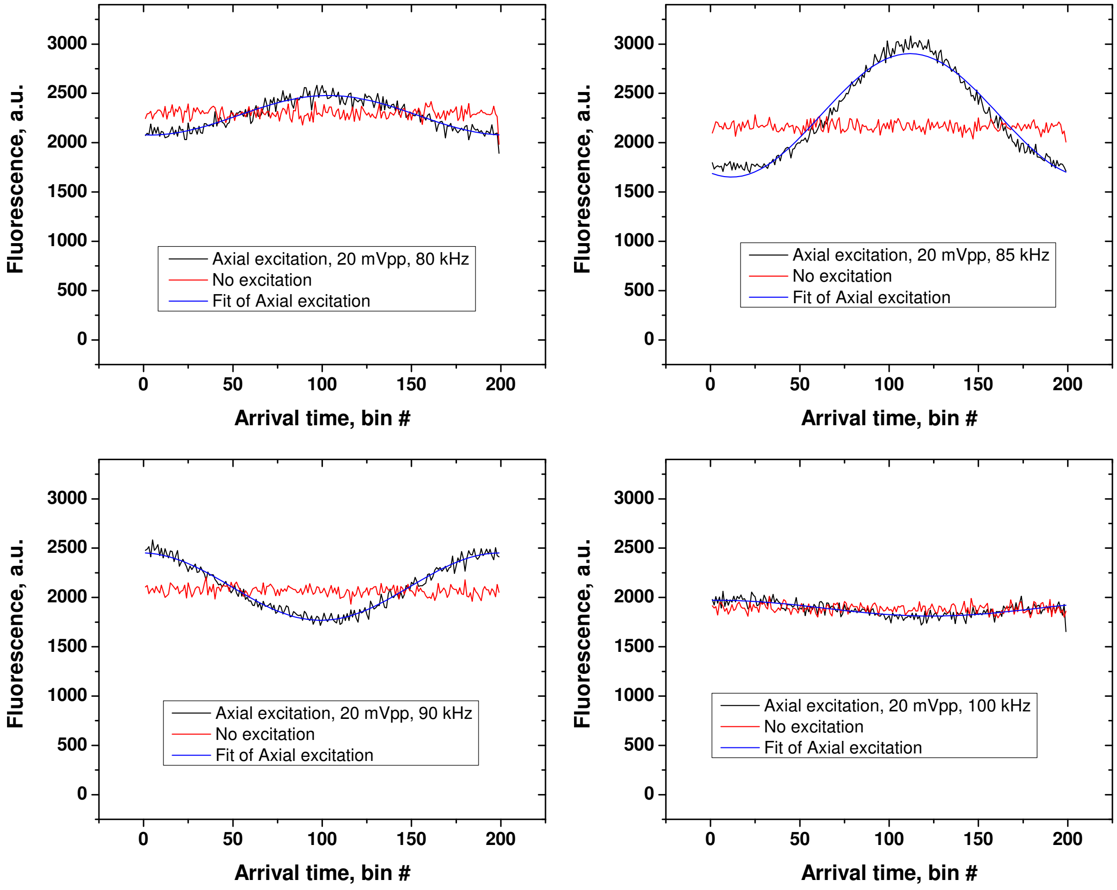

FIGURE 11.0.1. Determination of the frequency for axial oscillation of the ensemble of $Be^+$ ions. The excitation frequency is varied, while its amplitude is kept constant. The maximum variation of fluorescence occurs at a frequency of around 85 kHz. Endcap voltages are 4.34 V and 5.28 V.

noise spectral density. This ratio is approx. equal to 1, if no induced motion is applied, and is more than 1 if there is an excited motion. For a practical application, a Mathematica© program is written to calculate this parameter from the experimental data. The reason for introducing this parameter is to characterize the ion's motion in general cases, when several ions are excited with a periodic force of the same frequency, but having different phases, e.g. the case of an optical force applied to several ions. In a case of a single ion or a coherent (in-phase) motion of many ions, an analytical approach to describe their motion is also possible.

Fig. 11.0.3 illustrates the dependence of the "FFT Contrast Factor" as a function of a frequency applied to endcap electrodes, for two different amplitudes of excitation, applied to $Be^+$ ions. Endcap voltages are 4.34 V and 5.28 V. The largest value of the "FFT contrast factor" corresponds to the highest excitation and occurs, here, at COM mode.

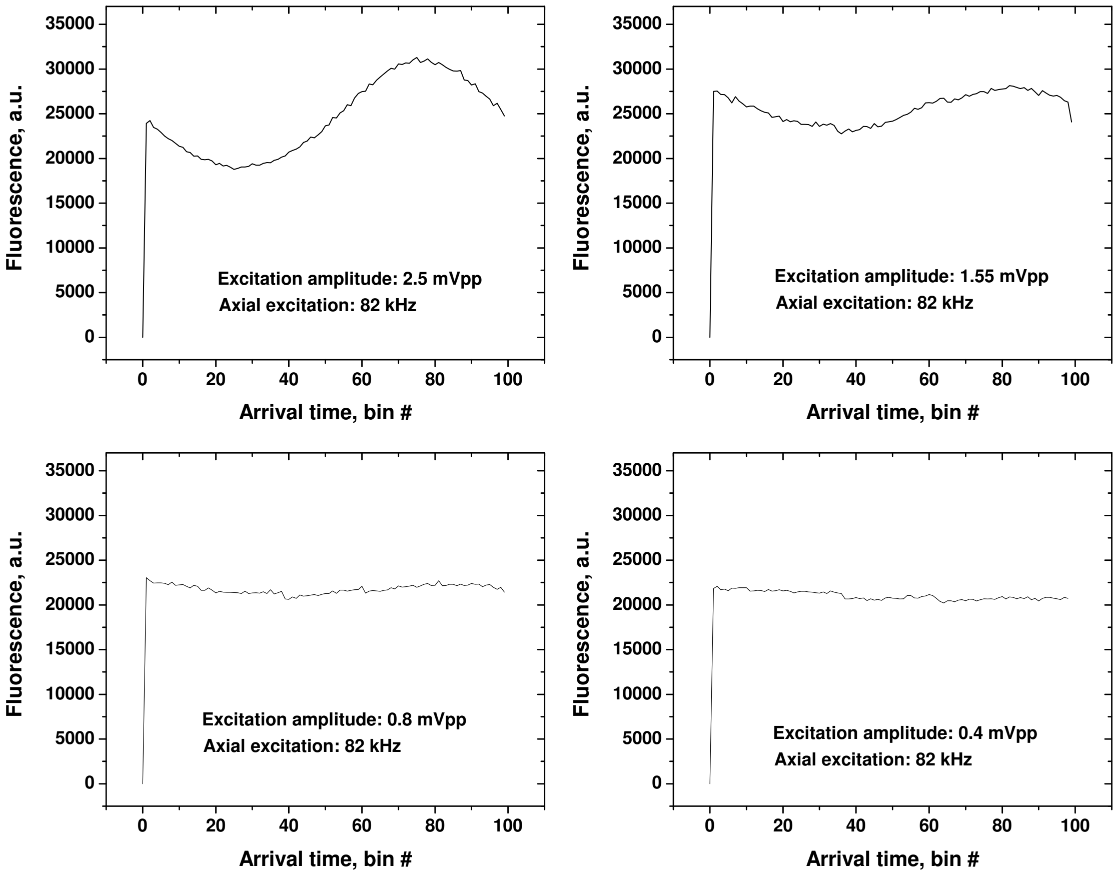

FIGURE 11.0.2. Illustration of a sensitivity determination for a Be$^+$ secular excitation detection by FPGA-based doppler velocimetry. The amplitude of an excitation was varied, while the frequency of the excitation was kept constant. The fluorescence variation is large for higher amplitudes of excitation (two upper graphs), and the variation decreases for smaller excitation amplitudes (two lower graphs). The lowest detectable excitation is determined to be about 0.8 mV$_{pp}$, demonstrating the high sensitivity of the dopplerometry method of motion detection.

If there are 2 different species loaded in the trap, their motion becomes, generally, coupled. Typically in the case of a large Coulomb crystal, this gives rise to frequency shifts (see Ref. [42]). The frequencies can be significantly modified in case of a few-ion system with strong coupling (see, e.g. Ref. [68, 69]). The expected HD$^+$ resonance frequency for a Coulomb crystal, typically used by us, is close to a theoretical one-ion secular frequency (the COM mode), and subjected to a minor variation, depending on the crystal parameters like size, shape, ratio of HD$^+$ to Be$^+$ trapped ions. The wide-range scan was carried out in an attempt to find the resonance of HD$^+$ molecular ions, shown in several examples in Fig. 11.0.4, and repeated with different parameters, but no one revealed reliable excitation

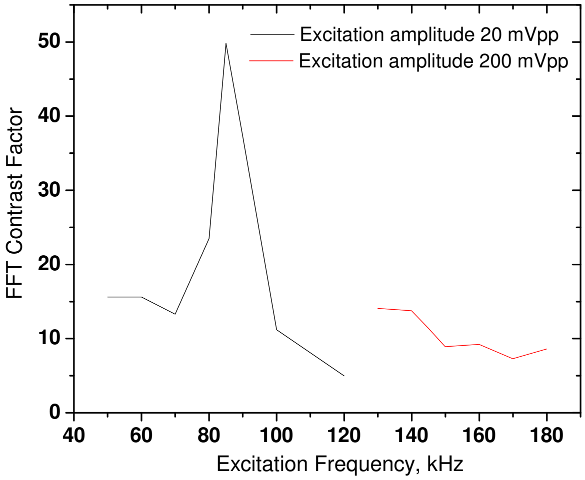

FIGURE 11.0.3. "FFT contrast factor" (see eq. 11.0.2) as a function of excitation frequency and amplitude. The highest value of the factor corresponds to the excitation at the axial secular COM mode frequency, here ≈ 85 kHz. The excitation using higher amplitude makes it possible to observe the wing of the excitation curve, shown as a red line.

of $HD^+$ ion motion. As seen from the graphs, for a high amplitude of excitation, a coherent motion is detected, which is associated with an off-resonance excitation of $Be^+$ ions (proven by excitation of a pure $Be^+$ ion crystal).

An attempt was made to detect optical force excitation, but the results also did not show any signal of excitation (see Part 4). The main reason is considered to be the insufficient coupling between $Be^+$ and $HD^+$ in the trap used, proved by results in Fig. 11.0.4. One of the reasons for insufficient coupling is a lack of loading control for $Be^+$ and $HD^+$ ions. Typically, electron impact loading makes it practically impossible to load fewer than a few hundred $Be^+$ ions, and less than a few tens of $HD^+$ ions. As a consequence, a Coulomb crystal formed of many tens of ions, has a weak ion-ion coupling; the eigen modes have a complex structure and, typically, exhibit only a broad (and shifted) resonance near the COM mode, for each species in the trap.

Another possible reason, preventing the detection of the optical force, can be attributed to the limitation of the coherent motion detection: this method allows the detection of only a motion of a certain frequency, which is equal to the excitation frequency, and is not able to detect an excited motion in the case of a weak coupling of different species (when the excited motion of $Be^+$ ions has a frequency, different from the excitation frequency of $HD^+$ ions). Besides this, different $HD^+$ ions experience different phases of the optical force that may mutually reduce contribution to the fluorescence signal.

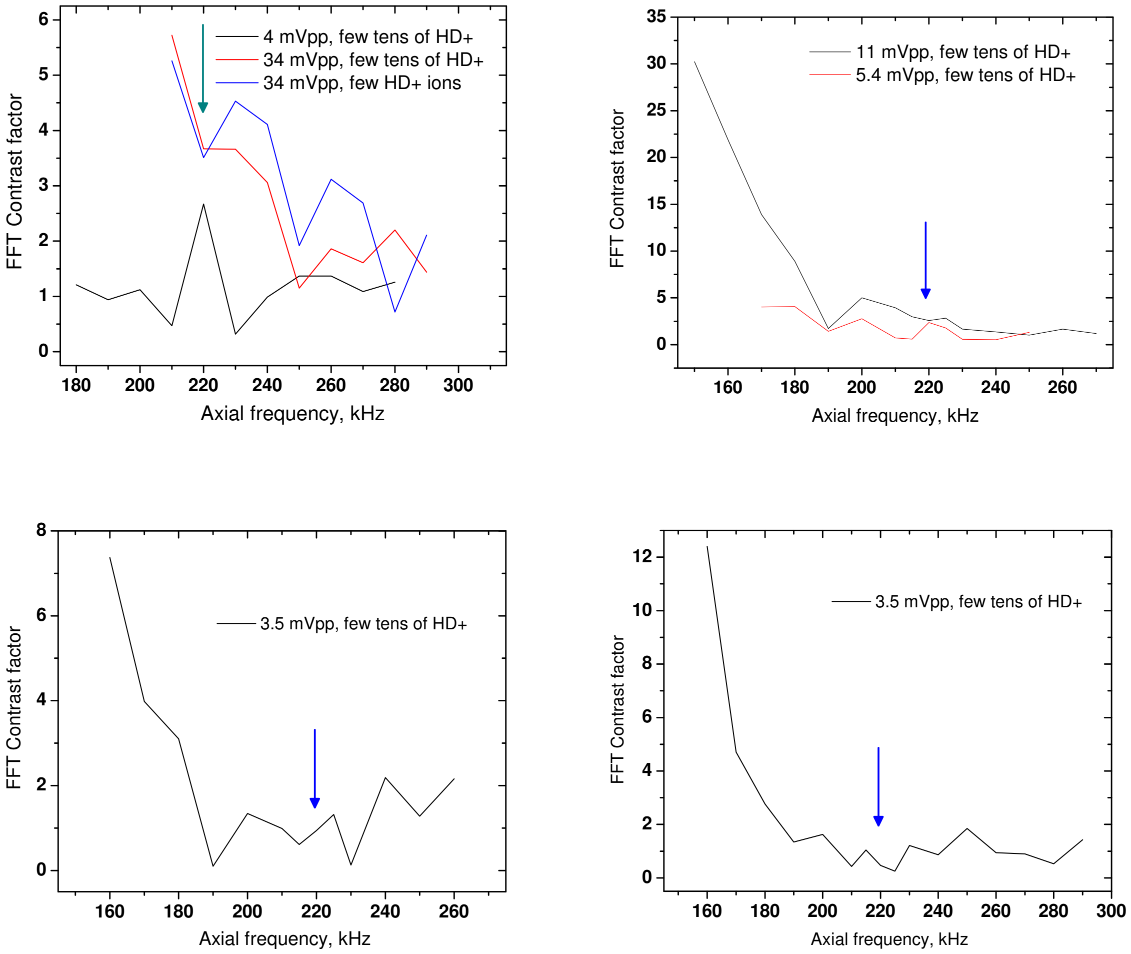

FIGURE 11.0.4. Search for the $HD^+$ secular motion excitation. The arrowed lines show the theoretically predicted frequencies of COM mode of $HD^+$ axial motion for an ensemble of $Be^+/HD^+$ ions. The excitation was not detected.

All these arguments were the reasons to apply another technique for weak excitation detection and to compare the results; another method will be described in the following chapter.

## CHAPTER 12

# Lock-in detection of an amplitude-modulated excitation of the ion motion

Lock-in detection of an amplitude-modulated (AM) excitation of an ion motion is based on detection of a Coulomb crystal heating. This method naturally has a lower sensitivity, compared to the coherent motion detection (which performes a time-resolved detection of a periodic variation of the fluorescent signal). In comparison with a standard mass spectroscopy detection approach, the described method has higher sensitivity thanks to the lock-in detection technique used. As in the case of coherent motion detection, the origin of AM excitation can be of a different kind. An electric-field-induced and an optical-force-induced excitation is of interest in this work; the first one was used in the test experiments to gain easy control over the amplitude of excitation.

The general scheme of the test experiment is shown in Fig. 12.0.1. The amplitude-modulated sine wave is applied to the endcap electrodes: $A = A_0 \sin(\Omega_m t) \sin(\omega_{exc} t)$ , where $\Omega_m$ is a modulation frequency, and $\omega_{exc}$ is an excitation frequency. This excitation

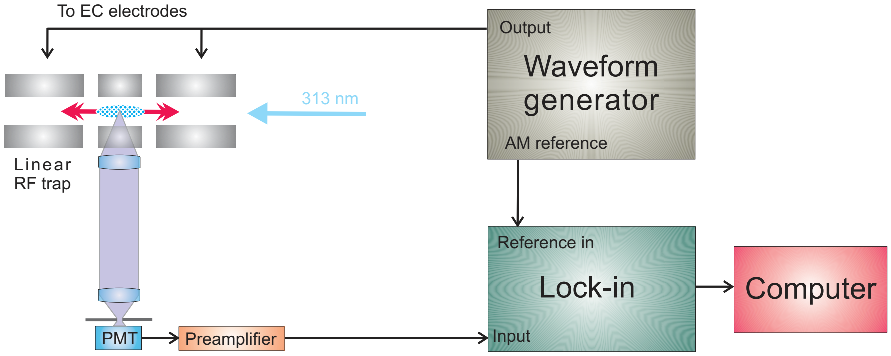

FIGURE 12.0.1. The scheme of the detection of the amplitude-modulated excitation. The waveform generator produces the AM modulated (few tens of Hertz, 100 % modulation depth) sine wave at the frequency of secular excitation. This waveform is applied to the endcap electrodes of the trap and induces the periodic heating of the ion crystal. The corresponding increase in the fluorescence signal is detected by the lock-in detector, which has the reference signal from the waveform generator and the input from the photomultiplier (PMT) with a low-noise bandpass preamplifier.

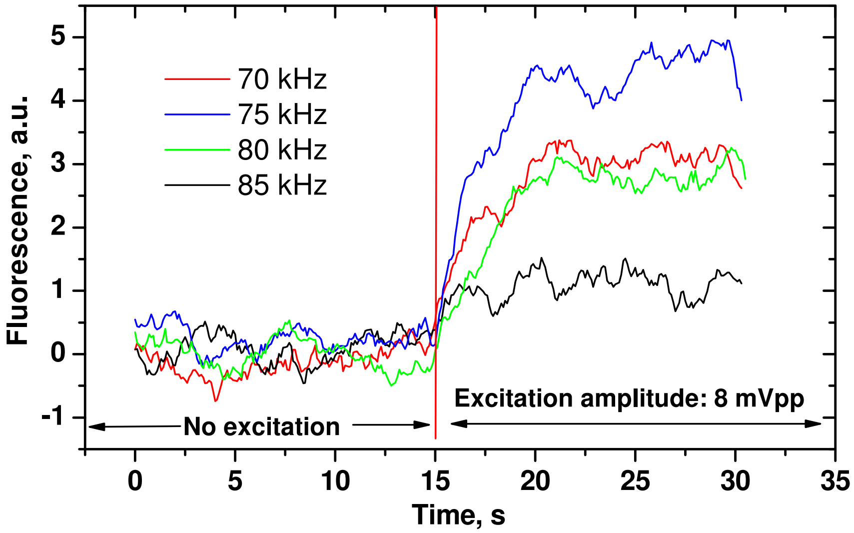

FIGURE 12.0.2. Determination of the axial secular excitation frequency for $Be^+$ ions, using the lock-in detection of the AM excitation applied to EC electrodes. The resonance frequency is determined to be 75 kHz ± 5 kHz. The EC voltages applied are: $EC_1 = 4.34\,V$ and $EC_2 = 5.75\,V$.

results in heating, modulated in time, provided that $\Omega_m$ is significantly smaller than $\omega_{exc}$, and $\omega_{exc} \approx \omega_{sec}$ is close enough to an eigen frequency of the ions in the trap, for excitation of the ion motion. Fluorescence signal is then modulated with $\Omega_m$; this signal is amplified and sent to the lock-in detector, with the reference signal delivered to the lock-in from the synthesizer.

Fig. 12.0.2 illustrates the electric field excitation of $Be^+$ ions. The value of $\Omega_m$ was a few tens of Hertz. For the first 15 seconds in each graph the secular excitation amplitude was not applied, and the detected fluctuations originate from a technical noise. During the next 15 seconds the excitation amplitude is set to a higher constant value. From the graphs, the secular excitation frequency $\omega_{exc}$ is determined to be 75 kHz.

Fig. 12.0.3 allows the sensitivity of the method to be determined: it is 3 ... 4 $mV_{pp}$, applied to endcap electrodes. This sensitivity is lower than the sensitivity of the coherent motion detection method, by a factor of $\sim 5$.

Fig. 12.0.4 shows the determination of a maximum excitation amplitude, which can be applied to search for $HD^+$ secular frequency. The reason for determining this value is that $Be^+$ motion starts to be excited when the amplitude is high enough, and this excitation should be avoided. The maximum amplitude is defined as 40 $mV_{pp}$, applied to EC electrodes. For a higher amplitude of excitation, the signal increases, which is associated with a strong excitation of $Be^+$ ions, and the result is similar to that obtained in the coherent motion excitation method.

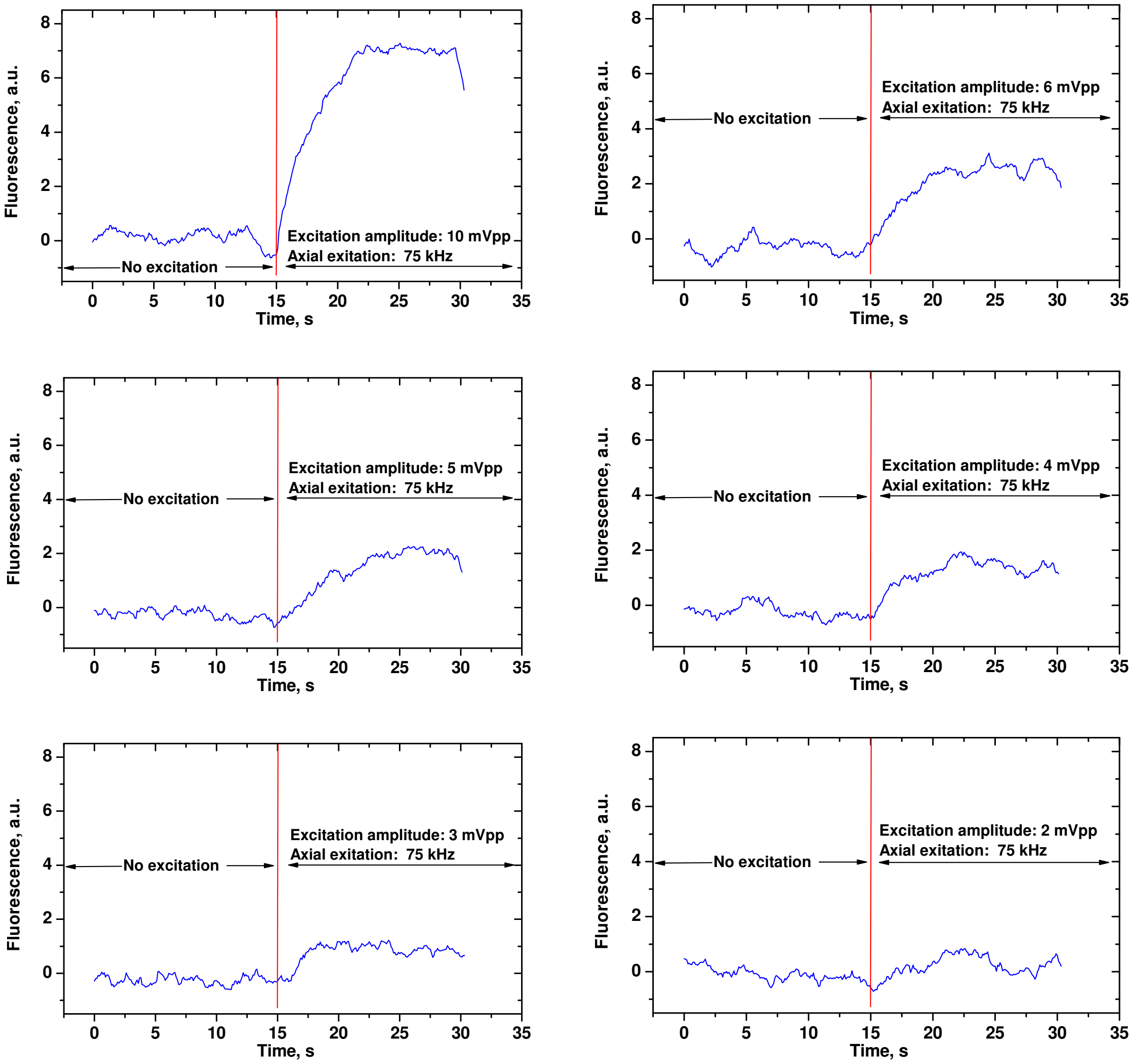

FIGURE 12.0.3. Determination of the sensitivity of detection, using lock-in method. $Be^+$ axial motion was excited at the COM mode, the excitation amplitude was varied to determine the minimal value, for which the detection is still possible. The minimum amplitude is seen to be 3 $mV_{pp}$ applied to the EC electrodes.

Fig. 12.0.5 shows the wide-range scan near the theoretically predicted $HD^+$ secular excitation frequency, with the maximum appropriate amplitude of excitation. As in the method for coherent excitation detection, no response was detected.

Optical force excitation was attempted to be observed using the method of the lock-in detection of the amplitude-modulated excitation, and no excitation was detected. As in the method of the coherent motion detection, this is associated with a weak coupling between $Be^+$ and $HD^+$ motion in the case of a large Coulomb crystal.

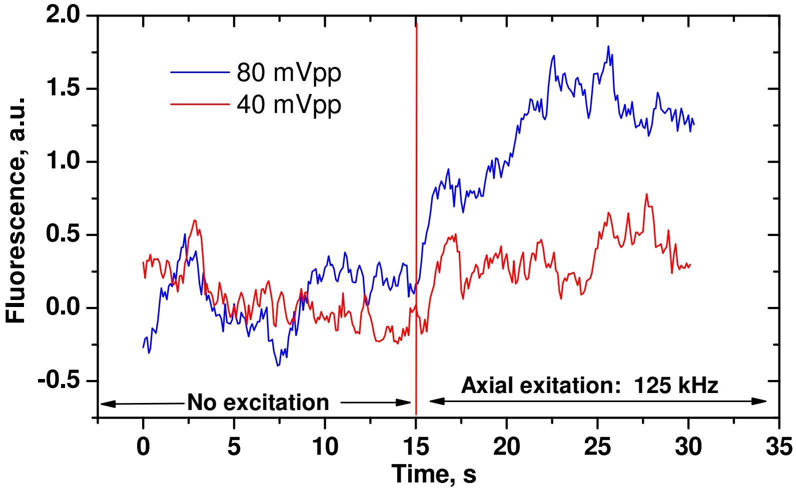

FIGURE 12.0.4. Detection of the far off-resonant excitation of $Be^+$ ions during excitation at the frequency, corresponding to the $HD^+$ eigenmode. The lock-in detection method is used. From the graph it follows that the amplitude for $HD^+$ excitation should not exceed 40 $mV_{pp}$ applied to endcap electrodes. Higher values of excitation amplitude will induce off-resonant $Be^+$ motion. The experiment was done for pure $Be^+$ ions, without $HD^+$. The excitation frequency was 125 kHz, the lowest value of the theoretically predicted range of secular frequencies for $HD^+$, and is chosen to maximize the contribution of $Be^+$ excitation (the excitation becomes stronger for lower frequencies, down to $Be^+$ secular frequency which is about 75 kHz).

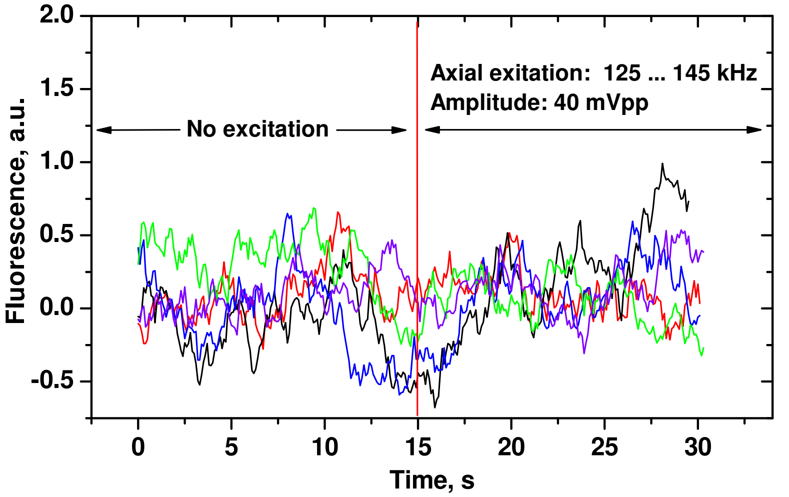

FIGURE 12.0.5. Attempt to resolve $HD^+$ excitation with a lock-in detection of amplitude-modulated excitation applied to endcap electrodes. The amplitude of the excitation was 40 $mV_{pp}$ applied to endcap electrodes, the maximum value, for which an excitation of $Be^+$ motion is not detectable. The scan was carried out in a wide range.

CHAPTER 13

# Summary and conclusions

Characterization of two methods, coherent motion detection and the lock-in detection of the amplitude-modulated excitation, was given. Their limitations and sensitivities were determined. Both methods demonstrated high sensitivity, the coherent motion detection sensitivity is higher and reaches $10^{-21}$ N (applied to $Be^+$ ions). Coherent motion detection requires phase-coherence of excitation and, being used to detect the optical force, is limited mainly to the configuration of strongly-coupled 1 $Be^+$ with 1 $HD^+$ ion. Upon comparison of the results of the test experiments, and on the attempts of optical force detection, the main conclusion can be drawn: the measurement of an optical-force-induced excitation of $HD^+$ ions requires stronger coupling of $Be^+$ and $HD^+$ motion.

It is worth noting that only axial excitation was considered here. The transverse excitation would require an optical force excitation, which is much weaker than considered in this work (see Part 4). For an axial excitation, the two counter-propagating beams can be tightly focused, with the assurance that the beams propagate in the axial direction. This is not the case for the transverse excitation: the beams should propagate in the radial direction, and focusing in only one dimension (e. g. by a cylindrical lens) can be used; alternatively, an optical tweezer can be applied [70]. In both cases, the optical force is significantly reduced compared to the axial excitation. Detection of the transverse excitation will also require the direction of the cooling laser beam, being non-purely axial.

The OPO, described in Chap. 7, can emit the power, which meets the minimum requirement for a detectable excitation, provided that the strongest rovibrational transition $(v = 0, N = 0) \rightarrow (v = 2, N = 1)$ is used, and OPO detuning from this transition is not more than a few hundred MHz.

The setup currently used has several limitations, making it challenging from the point of view of detecting a weak excitation of $HD^+$ molecular ions. First, a photoionization loading of $Be^+$ is highly desirable for loading a well-controlled, few-ion $Be^+$ Coulomb crystal, free of any other species. Second, a tighter trap confinement is required for a doppler-free spectroscopy in a Lamb-Dicke regime and for detection of the optical force. The trap currently used does not allow for a further increase of endcap voltages, as this would require an increase of RF trap voltage to keep a linear form of crystal; a significant increase of RF trap voltage is now

---

limited for technical reasons. And the third reason is related to the design of the vacuum chamber: it does not allow for flexible optical access (a large numerical aperture for tight light focusing is especially important, including focusing of OPO beams), and its baking temperature is limited to $160^{o}$C, which limits an ultimate vacuum and the storage time of the ions trapped.

# Part 4

# Non-destructive transition detection

The spectroscopic methods, used in the several experiments we have carried out on rotational and rovibrational spectroscopy in HD$^+$ ions (see Ref. [5, 40, 45] and Appendix 5), require photodissociation of the molecular ions for transition detection. The methods of REMPD and R-IRMPD, followed by mass spectroscopy, are described in Chapter 3. These methods, being relatively simple and robust, have the significant disadvantage of a low measurement rate: almost every measurement cycle requires re-loading of HD$^+$ ions, which requires manual control over many experimental apparatus and their parameters. We used this method for large Coulomb crystals, with the typical number of HD$^+$ reaching a few hundred. However, even this relatively large number of ions, and with the quantum state preparation (see Ref. [45]), demonstrates a significant fluctuation of the number of ions in the desired quantum state. As a consequence, the measurements must be repeated many times to achieve a better signal-to-noise ratio.

A completely different approach to detect the transition is based on the state-selective probe of the ion. To do this, different methods can be used, based on the light-matter interaction, e.g. applying light pressure (see Ref. [71]), or an interferometry-based detection of a phase shift for the beam propagating through the ion cloud (see Ref. [72]), or based on excitation and detection of an ion motion by the optical force (see Ref. [60]). All the methods are non-destructive (though they are not guaranteed to be quantum non-demolition), and allow to resolve the ion state. The last one, optical force-based, is of a particular interest, as it allows experiments to be performed in extreme conditions - with several or, ultimately, with just one ion in the trap. The optical force excitation allows an individual ion to be addressed, thus resulting in unsurpassed precision and control over systematical effects.

In this part, the general description of the non-destructive method will be given, and modelling results will be shown.

## CHAPTER 14

# Phase-modulated standing wave for an optical force excitation

In our experiments, we followed the method used in Ref. [60]. The origin of the optical dipole force comes from interaction of non-uniformly distributed laser intensity, and the polarizability of the matter. We regard the case of an optical wave which is near-resonant, but far-detuned, i.e. the excitation frequency is approximately the same as the transition frequency and the detuning is significantly larger than the level linewidth, Rabi frequency, and the laser bandwidth or its instability. This case is associated with a strong AC Stark shift.

The two counter-propagating beams from the same laser source, having linear polarizations that are parallel to each other, form a standing wave, see Fig. 14.0.1. This standing wave can induce an optical force to the medium (in our case, trapped molecular ions), provided that the frequency is reasonably far detuned from the transition of the media to suppress any one-photon transition. This detuning should not be too large, as the optical force will reduce. The optical force will act only if a light radiation can interact with the correspondent internal state, meaning that the targer state must be populated.

Typically, the optical force is weak, and high optical powers with focused beams are used to increase it. If one of the counter-propagating beams has its frequency, different from another beam, the phase- (or frequency-) modulated standing wave can be achieved. If the frequency difference is constant, the term "running standing wave" is also used. The "running standing wave" concept allows to apply an optical force excitation, which can be detected by coherent motion detection (see Chapter 11).

Fig. 14.0.2 (a, b) illustrates the state-selectivity of the optical force, when the optical force is created by the radiation with a frequency, close to $(v = 0, N = 0) \Rightarrow (v = 2, N = 1)$ transition (shown in blue). In case (a) the population in $(v = 0, N = 0)$ level is high (depicted by a large red circle) and the optical force exerted to the ion is also high; in case (b) the population in $(v = 0, N = 0)$ level is decreased (e.g. depleted by a spectroscopic transition $(v = 0, N = 0) \Rightarrow (v = 1, N = 1)$, shown as a red solid line), and the optical force is reduced. This state-selective excitation is a powerful tool for a non-destructive detection.

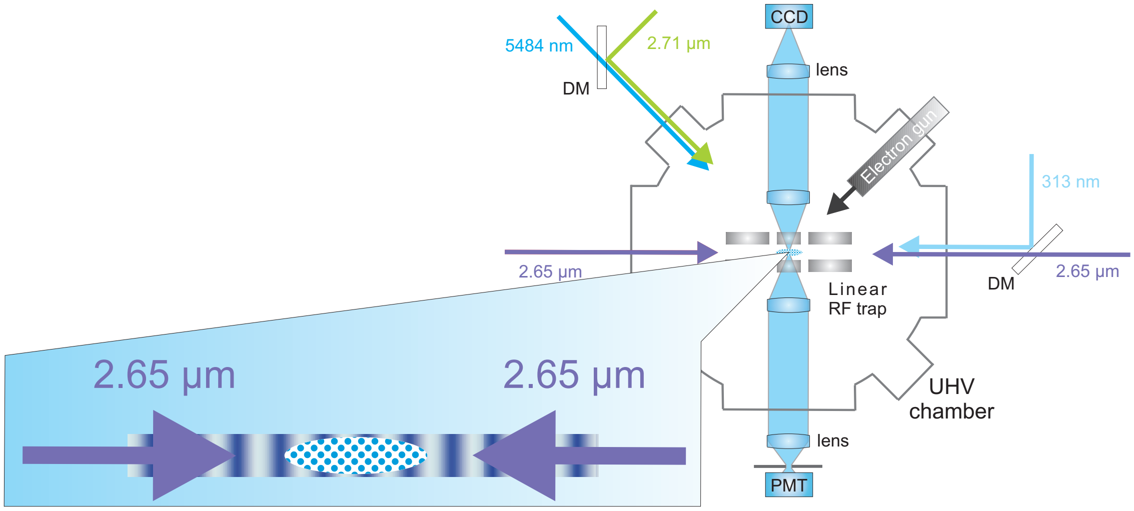

FIGURE 14.0.1. Illustration of the optical force, applied to the molecular ions in the quadrupole trap. Two counter-propagating beams form a standing wave, provided that light is linearly polarized, and polarizations are parallel to each other. These beams are overlapped with a Coulomb crystal of $Be^+$ and $HD^+$ ions, and the optical force is applied to $HD^+$ ions.

The running standing wave produces an optical force, periodical in time: $E_\Sigma = E_1 + E_2 = E \sin(\omega t + 2kz)$, where $\omega = |\omega_1 - \omega_2|$ is the difference frequency for the two counter-propagating beams, $k = {}^{2\pi}/_{\lambda}$ is the wavenumber. Being applied to the ion in the trap and having its periodicity, correspondent to the ion eigen mode, the optical force induces a periodic excitation. As shown in Ref. [60], this excitation can be detected in the 1 + 1' configuration of the ions trapped. One of the ions is examined for a spectroscopic transition, and the optical force performes state-selective excitation: the excitation is high when the ion is in the ground state (this case is shown in Fig. 14.0.2, (a)), and is low if the ion is in the excited state (case b). The optical-force-induced excitation of the spectroscopic ion is transferred to the additional logic ion; this ion performes sympathetic cooling and is used to detect excitation.

One of the most sensitive methods for detecting excitation is based on the Doppler velocimetry of the ion motion, another is based on detection of heating the ions; both methods and their realizations are described in Part 3. Attempts to detect the optical force excitation were carried out for a relatively large number of both spectroscopic (not less than 5) and cooling ions (not less than a few tens), with no evidence of any reliable signal detection. The OPO described in Chapter 7 was used as a tunable frequency-stabilized source of a high power; its frequency corresponds to a first overtone transition in $HD^+$, having relatively strong dipole moment. The spatial overlap of the beams was performed by the method,

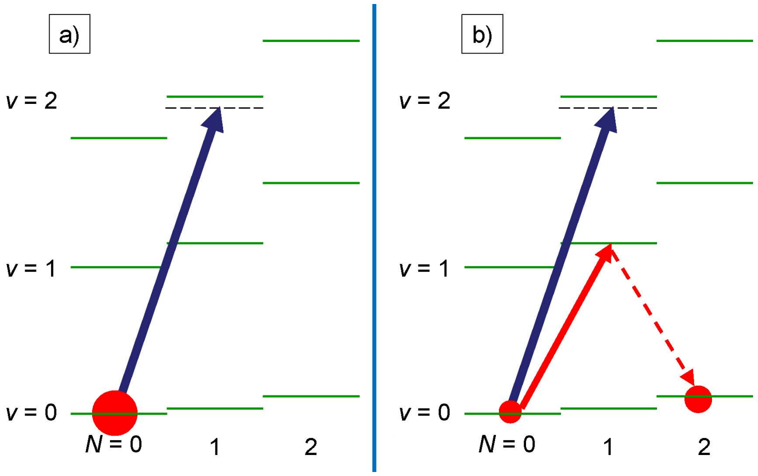

FIGURE 14.0.2. Illustration of a state-selectivity of the optical force excitation [3]. The (phase-modulated) standing wave (shown in dark blue) exerts an optical force, which is dependent on the species, and on the internal state of the species in the trap. The optical force becomes prominent only if the laser radiation is tuned not too far away from the allowed transitions, as shown for $HD^+$ ions in ($v = 0$, $N = 0$) state: optical radiation at 2.65 µm corresponds to a ($v = 0$, $N = 0$) $\rightarrow$ ($v' = 2$, $N' = 1$) transition in $HD^+$, thus making a rovibrational-state selective excitation, dependent on the population of ($v = 0$, $N = 0$) level. The excitation is high when the ($v = 0$, $N = 0$) level is well populated, as shown in case a), and excitation decreases after, e.g. spectroscopic transition ($v = 0$, $N = 0$) $\rightarrow$ ($v' = 1$, $N' = 1$) (shown in red), which decreases population in ($v = 0$, $N = 0$) level, shown in case b).

described in section 4.2, and checked by observation of a beat signal between the two linearly polarized, counter-propagating waves. The following parameters of the laser radiation from OPO at 2.65 $\mu$m were used: beams had 200 mW optical power from each side, focused to approx. 200 $\mu$m, detuning was varied in the range (±) 100 ... 1000 MHz from the spinless ($v = 0$, $N = 0$) $\rightarrow$ ($v = 2$, $N = 1$) transition frequency, and the difference frequency was scanned near theoretically predicted COM mode frequency. The equivalent excitation voltage, applied to endcap electrodes, is estimated to be $\sim 0.5$ mV$_{pp}$.

It should be noted that this excitation is applied to $HD^+$ ions, and is then transferred to the coolant $Be^+$ ions. As discussed in Chapter 13, this indirect excitation, in the case of a weak coupling where a large number of ions have been trapped, gives rise to difficulties with regard to excitation detection. Actually, it was not possible to determine the sensitivity of $HD^+$ excitation because of a strong background signal from the off-resonant excitation of $Be^+$ ions.

The new quadrupole trap with more stiff ion confinement, and lasers for an optical photoionization (optical loading) are being designed to realize the optical force excitation.

CHAPTER 15

# Modelling of the optical force excitation

Optical force excitation of the secular motion of the trapped single ion was modelled numerically. The axial secular motion of the single trapped ion was considered. The following Newton equation of motion describes the motion of the trapped ion, excited by the phase-modulated standing wave ("running standing wave"):

$$m_{\text{ion}}\ddot{z} = F_{trap} + F_{dipole} + F_{damping}\,,$$

where

$$F_{trap} = -\frac{dU_{trap}}{dz}, \quad F_{dipole} = -\frac{dU_{dipole}}{dz}\,,$$

the damping force is, according to [73]:

$$F_{damping} = -\eta\hbar k_C^2\dot{z}\frac{s}{(s+1)^2}\frac{\Delta\,\Gamma}{\Delta^2+{}^{\Gamma^2}\!/\!_4}\,, \tag{15.0.3}$$

and

$$U_{trap} = \kappa z^2 U_{EC}, \quad U_{dipole} = \frac{\hbar\Omega_R^2(t,\,z)}{4\delta}\,,$$

(the dipole trap potential see, e.g. in Ref. [74]), so that the forces can be expressed as

$$F_{trap} = -2\kappa z U_{EC}, \quad F_{dipole} = -\frac{\hbar k\Omega_R^2}{4\delta}\sin(\omega t + 2kz)\,.$$

Generally, the ion is heated by different processes which take place in the trap. I neglect these effects as they are spontaneous, and not coherent with the optical force-induced motion, and give rise to an appearance of a random motion of the ion. Thus, the equation of motion is written in the form

$$m_{\text{ion}}\ddot{z} + \eta\hbar k_C^2\dot{z}\frac{s}{(s+1)^2}\frac{\Delta\,\Gamma}{\Delta^2+{}^{\Gamma^2}\!/\!_4} + 2\kappa z U_{EC} + \frac{\hbar k\Omega_R^2}{4\delta}\sin(\omega t + 2kz) = 0\,,$$

the numerical value for Rabi frequency (in rad/s) can be expressed in a form, convenient for practical calculations [74]:

$$\Omega_R \approx 2\pi\times 10^6\times 27\,d\,\sqrt{I}\ {}^{\text{rad}}\!/\!_{\text{s}}.$$

In these equations, $m_{\text{ion}}$ is the mass of HD$^+$, equal to $4.98\times10^{-27}$ kg, $\kappa = 3.4\times10^{-3}\,\text{mm}^{-2}$ is the trap parameter, $U_{EC}$ is the endcap voltage, $k = {}^{2\pi}\!/\!_{\lambda}$ is the wave vector of the optical force light, $k_C$ is a wave vector of the cooling light wave, $\omega$is the excitation frequency (equal to the difference frequency for the two counter-propagating waves), $\Omega_R$ is the Rabi frequency of the one-photon transition, $\delta$ is the detuning from the one-photon resonance of the laser used for optical force excitation, $\lambda = 2.65\ \mu m$ is the wavelength of this laser radiation, $d$ is the transition dipole moment in Debye, $I$ is the intensity in Watts per cm$^2$ of the light used for optical force excitation, $s$ is the saturation parameter of the cooling light, $\Delta$ is the detuning of the cooling light from the resonance, $\Gamma$ is the linewidth of the cooling transition, $\eta$ is a coefficient of the cooling efficiency (see the further description). After substitution the parameters typical in our experiments (assuming $I = 500\,{}^{\mathrm{W}}/_{\mathrm{cm}^2}$, $d = 0.01\,\mathrm{D}$, and $\delta = 100$ MHz), we obtain an equation

$$\ddot{z} + 2\,\eta\,\dot{z} + 10^6 z + 10^{-7}\sin(10^{12}t + 4\times 10^{12}z) = 0,$$

where ion position $z$ is expressed in micrometers, and time $t$ is in microseconds.

The ion motion has a resonance-similar responce as a function of the excitation frequency. Here, only the resonance excitation is considered, i.e. the optical force has the frequency, correspondent to the eigen mode of the ion in the trap, as this is the case of the most intensive excitation. Assuming $U_{EC} = 5$ V, $s = 1$, $\Delta = \Gamma \sim 10$ MHz, the optical force is $\approx 6\times 10^{-22}$ N (cf. to the value of the sensitivity from Chapter 13).

The equation can be solved numerically. Fig. 15.0.1 shows the summary of the modelling obtained for the parameters, which can be experimentally realized. Three values of $\eta$ were considered: for the upper graph it is equal to 1, in the middle graph it is set to 0.1, and the limit case of $\eta$, set to 0, is shown in the lower graph. The upper case demonstrates a small variation of the ion position in space, and in this case the cooling efficiency is strongly reduced (ions are in the Lamb-Dicke regime). The smaller values for $\eta$ are chosen to take this effect into account and to model the situation of a 1 + 1' ion configuration in the trap, for which the indirect cooling (by means of motion coupling) reduces the cooling force. Further decrease of $\eta$ demonstrates only a minor increase of the ion motion amplitude.

The simplified model, regarded here, allows a conclusion to be drawn, that the optical force excitation, applied to HD$^+$ ion, can be detected in the configuration of 1 HD$^+$ + 1 Be$^+$ ion, loaded in the trap with a stiff enough potential. The more detailed description of the optical force applied to the 1 HD$^+$ ion, sympathetically cooled by 1 Be$^+$ ion, should include the parameters of the new trap, which is being designed. Additionally, light-matter interaction should be replaced by the pure-quantum-mechanical description of the photon absorption (density matrix equation). In the case of transverse excitation, the time-varying potential may need to be regarded. A comprehensive description of this is not included in this thesis.

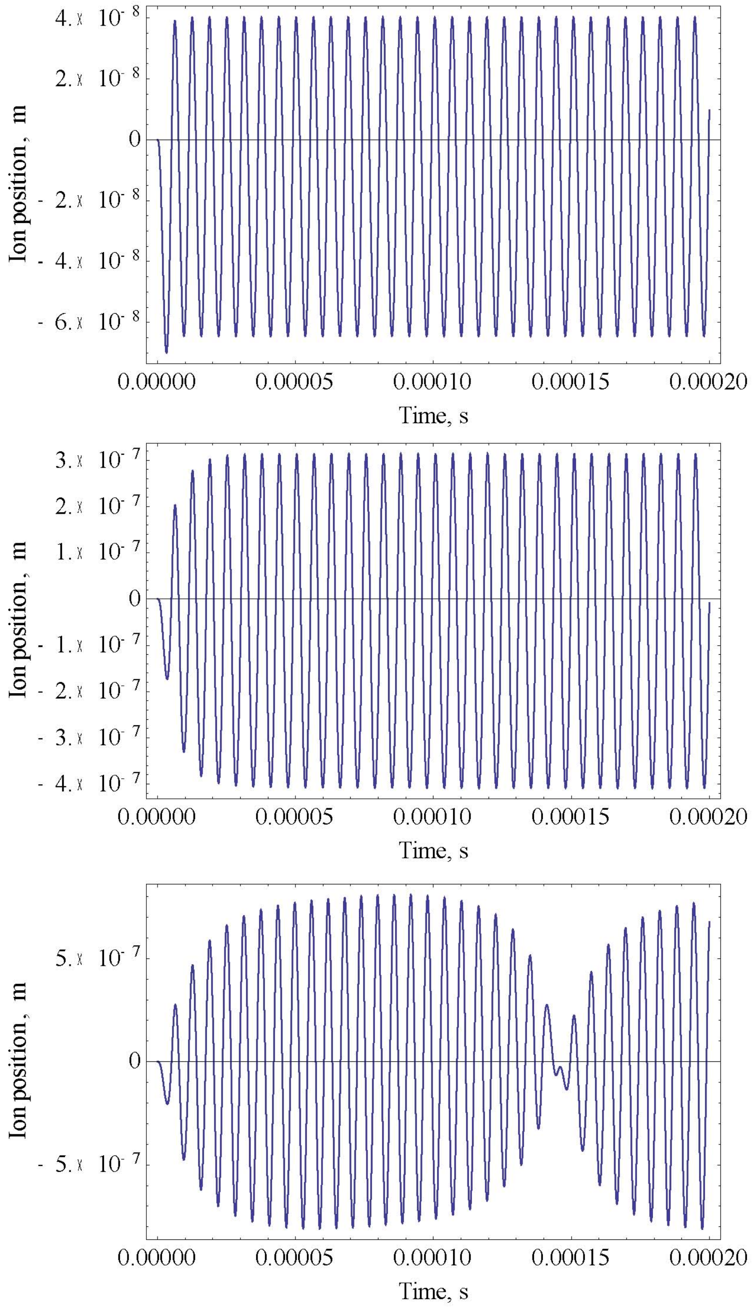

FIGURE 15.0.1. Modelling of the optical force acting on the single ion in the trap. The oscillations are the optical force-induced ion motions. Upper graph - case $\eta = 1$, middle graph - case $\eta = 0.1$, lower graph - case $\eta = 0$ (see the text for description).

# Summary and outlook

## CHAPTER 16

# Summary

Different results and approaches in the field of experimental ion trapping are described in this work. The thesis is based on three publications, two preprints, and additional, so far unpublished materials, which include a detailed description of the setup, and methods used.

Mainly, the results are related to the spectroscopy of molecular ions, trapped and sympathetically cooled by atomic ions in the linear Paul trap. This technique is known to be versatile and appropriate for trapping and cooling different species. Thus, one of the results is obtained for a protonated tyrosine-alanine – polyatomic molecular ion, which was cooled translationally to a secular temperature below 1 K.

Different laser sources play an important role in the described experimental research: they are used to cool the atomic ions, to perform rotational cooling and quantum state manipulations, dissociate molecular ions and perform spectroscopic transition. The most important laser sources, developed for the experiments, are described.

A significant part of this thesis is devoted to the spectroscopy of $HD^+$, one of the most fundamental molecular ions, having dipole-allowed transitions. The spectroscopy is carried out for pure-rotational, for rovibrational transitions, and hyperfine-resolved transition detection is perfomed. To increase the detected signal, the hyperfine-state selective pumping schemes were used to implement a quantum state preparation.

The resolution of the rotational spectroscopy, used in the experiments, approached the limitations related to an uncertainty of the magnetic field experienced by the ions. A simple method of optical magnetometry, based on detection of stimulated Raman transition, was proposed for determination of the acting magnetic field.

In the searches for non-destructive methods of transition detection, applicable to the experiments, an apparatus for time-resolved photon counting was used and characterized. The test experiments and numerical simulations for an optical dipole force, acting on the molecular ions, were performed; the limitations of the setup, preventing an observation of the ion motion excitation, were described.

Possible further developments and approaches are discussed.

### 16.1. Vibrational spectroscopy of cold molecular ions

In this work (Ref. [5]) we observed a photodissociation of cold molecular ions using only IR laser radiation, unlike several previous experiments in our group, in which UV light was required for dissociation of the ions. A continuous-wave optical parametric oscillator (OPO) was implemented in the spectroscopy of polyatomic ions. Protonated tyrosine–alanine ($HTyrAla^+$) was used as a model system. Molecular ions were trapped and sympathetically cooled by laser-cooled atomic ions to less than 800 mK secular temperature. The dissociation rate was proved to be a linear function of the IR photon flux. Resonant IR multiple-photon dissociation spectroscopy (R-IRMPD) generated charged molecular fragments, which are sympathetically cooled and trapped, and subsequently released from the trap and counted.

We measured the cross section for R-IRMPD under conditions of low intensity, and found it to be approximately two orders smaller than the vibrational excitation cross section. The observed rotational bandwidth of the vibrational transition is larger than the one expected from the combined effects of 300 K black-body temperature, conformer-dependent line shifts, and intermolecular vibrational relaxation broadening (J. Stearns et al., J. Chem. Phys., 2007, 127, 154322–154327). This indicates that as the internal energy of the molecule grows, an increase of the rotational temperature of the molecular ions well above room temperature (up to 1000 K), and/or an appreciable shift of the vibrational transition frequency (approx. 6–8 $cm^{-1}$) occurs.

Further studies of cold molecular ions are limited without implementation of rotational cooling (or, generally, quantum state preparation). The rotational cooling is a challenging process to perform for polyatomic ions by way of optical pumping, and collisions with cold neutral particles are required.

### 16.2. High-resolution spectroscopy of the fundamental transition in $HD^+$

Based on the development of a 5.1 µm spectrometer (see Ref. [75, 76]), stabilized to the frequency comb, referenced to H-maser and GPS, it became possible to perform high-precision measurements in $HD^+$. The developed spectrometer has the advantage that it is quick to tune and can carry out hyperfine-state-selective pumping. These important options were used to increase the population in the target state, thus improving the resolution of the experiments.

The laser source has a linewidth of 0.7 MHz, smaller than approx. 3 MHz - an estimation of a Doppler broadening for the secular temperature of 15 mK, used in our experiments.

The ($v = 0$, $N = 0$)$\Rightarrow$($v = 1$, $N = 1$) transition was addressed as a test system, for comparison with theoretical data on $HD^+$. Precise measurements of level spacing as well as their absolute frequency was performed. The achieved resolution is, based on our current knowledge, better than any other measurements for molecular ions. The results obtained demonstrate the higher spectroscopic possibility for ion storage method compared with, for example, molecular (ion) beam experiments.

We determined the "spinless" frequency to be 58 605 051 MHz, with a relative experimental uncertainty of $1.1 \times 10^{-9}$. To our knowledge, this is the most precise test of *ab initio* theory of any molecule done so far. This constituted an improvement to the previous measurements carried out in our group in 2007 (see Ref. [77]).

## 16.3. Pure rotational transition at 1.3 THz in $HD^+$

After improvement of the optical setup, and utilizing the stability and performance of the second-generation cooling laser (see Ref. [46]), it became possible to resolve the pure rotational transition in $HD^+$. This transition at 1.3 THz, being the most fundamental dipole-allowed rotational transition of any molecule, is of particular interest to high-resolution spectroscopy. One of the advantages is the ability to apply the spectroscopic transition in the Lamb-Dicke regime, thus eliminating the Doppler broadening to achieve improved resolution. However, the fractional population of the individual state is low, and for high-resolution spectroscopy the hyperfine-state preparation is required.

In this work, we took initial steps towards achieving high-precision measurements: several transitions were simultaneously excited. To obtain the spectroscopic signal, the excitation frequencies were simultaneously tuned.

To further improve resolution, we plan to carry out further separate transition excitation.

## 16.4. Weak spin-forbidden transition

Rovibrational transitions in diatomic molecules with non-zero nuclear spin exhibit a rich hyperfine structure. The angular momentum couplings lead to selection rules that classify the rovibrational transitions into allowed, spin-forbidden and doubly spin-forbidden transitions. In this work a laser excitation of a doubly spin-forbidden rovibrational transition in $HD^+$ was demonstrated. $HD^+$, the most fundamental heteronuclear molecular ion, was a model system. The experiments were performed with molecular ions which had been sympathetically cooled to a temperature of approximately 10 mK. The weak transition is driven by a continuous-wave optical parametric oscillator. To increase the excitation signal, rotational cooling was employed. We described implementation of the doubly-forbidden transitions for a quantum state preparation.

## 16.5. Optical magnetometry with $\text{Be}^+$ ions

A simple method for the determination of the magnetic field in an ion trap using laser-cooled $\text{Be}^+$ ions was developed and demonstrated. The method is not based on magnetic resonance and thus does not require delivering radiofrequency (RF) radiation to the trap. Instead, stimulated Raman spectroscopy is used, and only an easily generated optical sideband of the laser cooling wave is required. The d.c. magnetic vector, averaged over the $\text{Be}^+$ ion ensemble, is determined. Furthermore, the field strength can be minimized and an upper limit for the field gradient can be determined. The resolution of the method is 0.04 G. The relevance for precision rovibrational spectroscopy of $\text{HD}^+$ is discussed.

## 16.6. Perspectives

The results achieved with trapped atomic ions in the laboratories around the world, and our results with trapped molecular ions provide strong motivation for carrying out further research in the field of cold trapped particles.

The success achieved for IR spectroscopy, and demonstration of the hyperfine-state-selective spectroscopy encouraged our team to create the scheme for a complete state preparation, using several laser sources. The REMPD scheme, used before, was modified to improve its robustness. The new scheme opens more possibilities for state-selective dissociation by excitation of the correspondent transitions not only in the spectroscopic, but also in one of the sequential transitions.

However, the ultimate method for improving the measurement efficiency and increasing the precision and resolution of spectroscopy is to utilize the non-destructive detection method. For this, the configuration of 1 spectroscopic and 1 logic ion seems to be the best solution. The superiority of this $1 + 1'$ ion configuration for carrying out spectroscopy of atomic ions is proved by the recent Nobel Prize award to D. Wineland in 2012.

One of the most important aspects is the resolution of the detected transition. The ion's motion in the $1 + 1'$ ion configuration can be confined to less than the light wavelength, thus providing the Doppler-free regime already for optical transition (not only terahertz transition). Another way of eliminating the Doppler broadening is to implement the 2-photon spectroscopy: in the ladder or Raman configuration, accordingly. We continue our development of different setups for Doppler-free spectroscopy.

Building an ion trap, appropriate for operation in the sideband-resolved regime, can open up new possibilities for precision spectroscopy of molecular ions. It can also provide a strong confinement for ions, important for the optical force excitation. In addition, for loading the $1 + 1'$ ion configuration, good control over the loading parameters is desirable. The photoionization lasers could provide a good spatial resolution, and species selectivity. The modelling performed and the preliminary experiments show that the power of the optical parametric oscillator used will be enough to excite the detectable ion motion.

### 16.7. Further developments in quantum state preparation

A new setup for a hyperfine-state-selective optical pumping is currently being developed. It will allow the $HD^+$ ions to be prepared in a desired hyperfine state in one of several lowest rovibrational levels, namely in ($v = 0$, $N = 0$), or ($v = 0$, $N = 1$), or ($v = 0$, $N = 2$) (see Fig. 16.7.1). The setup uses three lasers, two of them are distributed feedback (DFB) diode lasers, which induce transitions ($v = 0$, $N = 0$) → ($v' = 0$, $N' = 1$) (DFB0) and ($v = 0$, $N = 1$) → ($v' = 2$, $N' = 0$) (DFB1), and one is a quantum cascade laser (QCL) to drive ($v = 0$, $N = 2$) → ($v' = 1$, $N' = 1$). To increase the efficiency of the hyperfine-state-selective optical pumping, tuning of all these lasers should be precisely controlled to drive only desired hyperfine transitions. To enable precise control of the QCL laser, a new stabilization scheme is built on the base of the QCL laser used so far, see Fig. 6.0.2. To drive other transitions, a new compact optical setup is built on the base of two DFB lasers in our group [78]; the frequency stabilization schemes allow the output frequencies of the lasers to be tuned with approx. 10 MHz accuracy.

An example of the advanced hyperfine state preparation, utilizing the 3 lasers, is shown in Fig. 16.7.1. The target state is ($v = 0$, $N = 0$, $J = 2$, $F = 1$, $S = 2$). The DFB0 laser is tuned to deplete all, except for the selected hyperfine state, e.g. ($J$, $F$, $S$) = (2, 1, 2). DFB1 and QCL drive the hyperfine transitions with the upper state ($J'$, $F'$, $S'$) = (2, 1, 2). This ensures that the most probable hyperfine state, occupied after spontaneous emission, will have the same quantum numbers. After several cycles of pumping, the population will be collected in the ($v = 0$, $N = 0$, $J = 2$, $F = 1$, $S = 2$) state, thus making it possible to increase the resolution of hyperfine-state-selective spectroscopy. This state preparation also increases the fractional population in the Zeeman states, thus opening up the possibility of performing Zeeman-state-selective spectroscopy, which is important, for example, in THz spectroscopy.

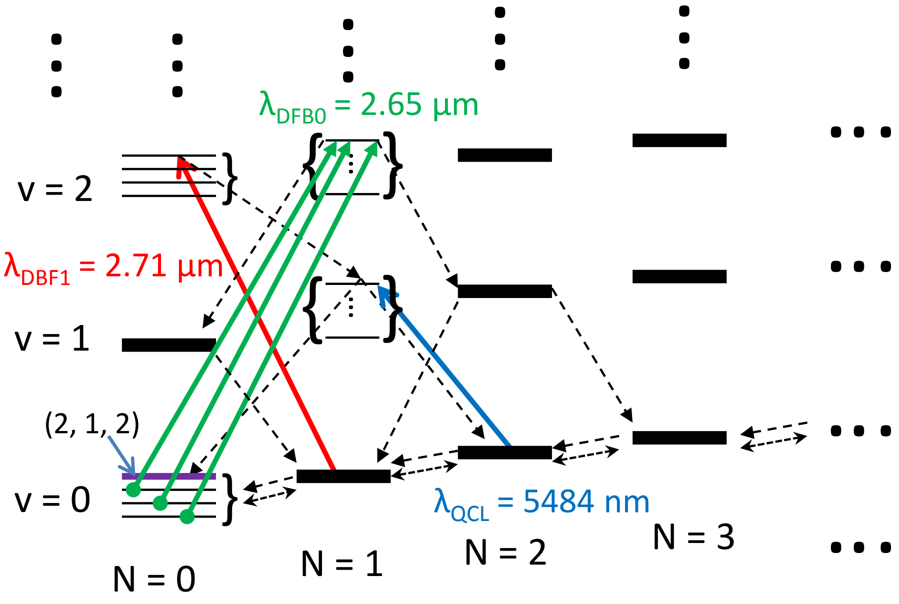

FIGURE 16.7.1. Simplified scheme for complete hyperfine state preparation. DFB0 ($\lambda = 2.65\,\mu$m), DFB1 ($\lambda = 2.71\,\mu$m), and QCL lasers ($\lambda = 5484\,n$m) drive the hyperfine transitions to perform optical pumping to the ($v = 0$, $N = 0$, $J = 2$, $F = 1$, $S = 2$) state, shown as a thick violet line.

# Appendices

# Appendix 1. Impossibility of forbidden transition excitation

In this appendix, the scheme of cross-coupled levels is considered, and formulae for forbidden transition excitation shows that the coupling is prohibited. The motivation behind this work was a publication about the possibility of inducing a forbidden transition, see Ref. [79]. The erratum, stating that this type of transition is not possible, was published later (see Ref. [80]), and modelling of the considered task was carried out by myself in the meantime.

The scheme of relevant levels and transitions is shown in Fig. 16.7.2. The level scheme is typical for diatomic molecules, for example, in HD$^+$ molecular ions. In the scheme considered, a direct transition from the initial state (1) to the final state (3) is impossible because of transition selection rules applied for diatomic molecules (molecular ions), prohibiting the Q-branch transition. Thus, a possibility of a non-linear coupling through the interaction with the intermediate levels is considered.

Typically applied for a two-photon transition, like Raman or a two-photon Doppler-free transition, the adiabatic elimination technique is applied here with the aim of deriving the formulae for the light-matter interaction. Allowed transitions are far-detuned from the frequency of the applied laser radiation ($\Delta_2$, $\Delta_4 \gg \Omega_R$). The interaction is considered in interaction (Dirac) representation, rotating wave approximation (Rabi frequency being much less than $\omega$ - transition frequency) and adiabatic eliminations of intermediate states are applied.

In this appendix I followed an approach from Ref. [74].

Consider the Schroedinger equation

$$i\hbar\frac{\partial}{\partial t}\Psi = \hat{H}\Psi\,,$$

where full Hamiltonian $\hat{H}$ consists of two parts, $\hat{H}_0$ - unperturbed part and $\hat{V}$ - perturbation, described with electric-dipole interaction:

$$\hat{H} = \hat{H}_0 + \hat{V}\,.$$

In the basis, associated with eigenstates, $\hat{H}_0$ has a form of diagonal matrix with elements, equal to the energies of corresponding levels:

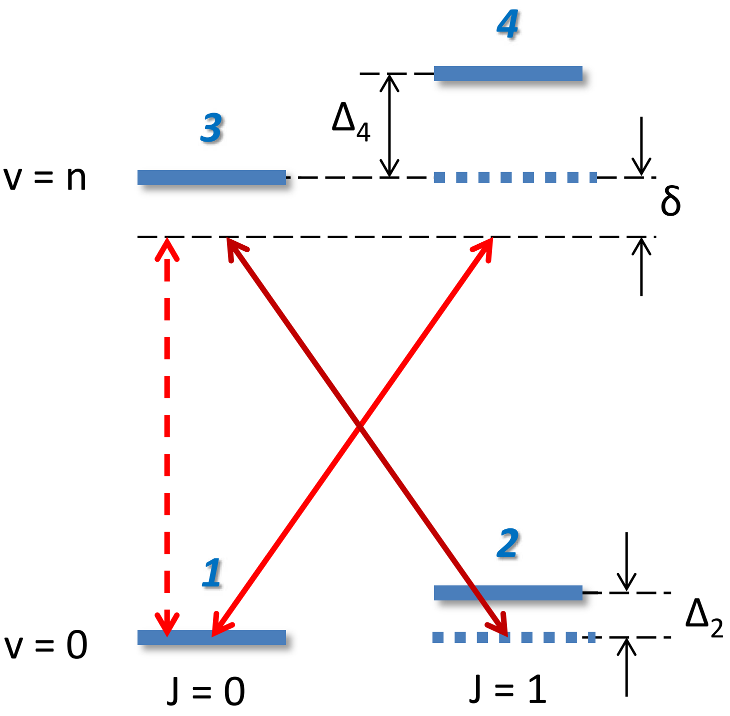

Figure 16.7.2. Scheme of level coupling. Initially level ($v = 0$, $J = 0$) (marked as 1) is populated, level 2 is slightly populated, and levels 3 and 4 are not populated. $\Delta_4$ is large enough to suppress transition between levels 1 and 4. $\delta$ is a detuning of the forbidden transition. $\Delta_2$ is in the order of $\Delta_4$.

$$\hat{H}_0 = \hbar \times \begin{pmatrix} E_0/\hbar & 0 & 0 & 0 \\ 0 & E_0/\hbar + \Delta_2 & 0 & 0 \\ 0 & 0 & E_0/\hbar + \omega_0 + \delta & 0 \\ 0 & 0 & 0 & E_0/\hbar + \omega_0 + \Delta_4 + \delta \end{pmatrix},$$

where $\omega_0$ is a laser frequency, $\delta$ is a detuning from the frequency of the forbidden transition and $E_0$ is the energy of a ground level. $\hat{V}$ incorporates interaction between the following levels: 1 and 4, 2 and 3, 1 and 2, 3 and 4, described with the corresponding Rabi frequencies:

$$\hat{V} = \frac{\hbar}{2} \times \begin{pmatrix} 0 & \Omega_{12}\left(e^{i\omega_0 t} + e^{-i\omega_0 t}\right) & 0 & \Omega_{14}\left(e^{i\omega_0 t} + e^{-i\omega_0 t}\right) \\ \Omega_{12}\left(e^{i\omega_0 t} + e^{-i\omega_0 t}\right) & 0 & \Omega_{23}\left(e^{i\omega_0 t} + e^{-i\omega_0 t}\right) & 0 \\ 0 & \Omega_{23}\left(e^{i\omega_0 t} + e^{-i\omega_0 t}\right) & 0 & \Omega_{34}\left(e^{i\omega_0 t} + e^{-i\omega_0 t}\right) \\ \Omega_{14}\left(e^{i\omega_0 t} + e^{-i\omega_0 t}\right) & 0 & \Omega_{34}\left(e^{i\omega_0 t} + e^{-i\omega_0 t}\right) & 0 \end{pmatrix}.$$

A solution is found in the form:

$$\Psi = c_1 e^{-i\zeta_1}\psi_1 + c_2 e^{-i\zeta_2}\psi_2 + c_3 e^{-i\zeta_3}\psi_3 + c_4 e^{-i\zeta_4}\psi_4 \,,$$

where $\zeta_1 ... \zeta_4$ are time-dependent phases, which will be specified later. Substituting will give a set of equations:

$$\begin{aligned}
i\tfrac{dc_1}{dt} &= c_1\left(\omega_1 - \dot{\zeta}_1\right) + \tfrac{c_2}{2}\Omega_{12}e^{i(\zeta_1-\zeta_2)}\left(e^{i\omega_0 t} + cc\right) + \tfrac{c_4}{2}\Omega_{14}e^{i(\zeta_1-\zeta_4)}\left(e^{i\omega_0 t} + cc\right) \,, \\
i\tfrac{dc_2}{dt} &= \tfrac{c_1}{2}\Omega_{12}e^{i(\zeta_2-\zeta_1)}\left(e^{i\omega_0 t} + cc\right) + c_2\left(\omega_1 + \Delta_2 - \dot{\zeta}_2\right) + \tfrac{c_3}{2}\Omega_{23}e^{i(\zeta_2-\zeta_3)}\left(e^{i\omega_0 t} + cc\right) \,, \\
i\tfrac{dc_3}{dt} &= \tfrac{c_2}{2}\Omega_{23}e^{i(\zeta_3-\zeta_2)}\left(e^{i\omega_0 t} + cc\right) + c_3\left(\omega_1 + \omega_0 + \delta - \dot{\zeta}_3\right) + \tfrac{c_4}{2}\Omega_{34}e^{i(\zeta_3-\zeta_4)}\left(e^{i\omega_0 t} + cc\right) \,, \\
i\tfrac{dc_4}{dt} &= \tfrac{c_1}{2}\Omega_{14}e^{i(\zeta_4-\zeta_1)}\left(e^{i\omega_0 t} + cc\right) + \tfrac{c_3}{2}\Omega_{34}e^{i(\zeta_4-\zeta_3)}\left(e^{i\omega_0 t} + cc\right) + c_4\left(\omega_1 + \omega_0 + \Delta_4 + \delta - \dot{\zeta}_4\right) \,,
\end{aligned}$$

where $\omega_1 = E_0/\hbar$ and "cc" denote complex conjugate. We specify $\zeta_1 ... \zeta_4$ with a view to further analysis in the following way:

$$\begin{aligned}
\dot{\zeta}_1 &= \omega_1 \,, \\
\dot{\zeta}_2 &= \omega_1 + \omega_0 \,, \\
\dot{\zeta}_3 &= \omega_1 \,, \\
\dot{\zeta}_4 &= \omega_1 + \omega_0,
\end{aligned}$$

which leads to a complete set of equations for amplitudes of wave functions, taken without approximations:

$$\begin{aligned}
i\tfrac{dc_1}{dt} &= \tfrac{c_2}{2}\Omega_{12}\left(1 + e^{-2i\omega_0 t}\right) + \tfrac{c_4}{2}\Omega_{14}\left(1 + e^{-2i\omega_0 t}\right) \,, \\
i\tfrac{dc_2}{dt} &= \tfrac{c_1}{2}\Omega_{12}\left(1 + e^{2i\omega_0 t}\right) + c_2\left(\Delta_2 - \omega_0\right) + \tfrac{c_3}{2}\Omega_{23}\left(1 + e^{2i\omega_0 t}\right) \,, \\
i\tfrac{dc_3}{dt} &= \tfrac{c_2}{2}\Omega_{23}\left(1 + e^{-2i\omega_0 t}\right) + c_3\left(\omega_0 + \delta\right) + \tfrac{c_4}{2}\Omega_{34}\left(1 + e^{-2i\omega_0 t}\right) \,, \\
i\tfrac{dc_4}{dt} &= \tfrac{c_1}{2}\Omega_{14}\left(1 + e^{2i\omega_0 t}\right) + \tfrac{c_3}{2}\Omega_{34}\left(1 + e^{2i\omega_0 t}\right) + c_4\left(\Delta_4 + \delta\right) \,.
\end{aligned}$$

Rotating wave approximation (RWA) is applied to eliminate fast-changing (with $\pm 2\omega_0$) component, thus simplifying the equations. Typically, the rotating wave approximation is valid, except in the event when the time scale of change for Rabi frequencies is comparable to the optical frequency. In terms of actual practice, the limitation can be reached for the short laser pulses, like powerful picosecond or femtosecond lasers. In the case of almost-CW laser radiation used in the experiments, RWA is a valid approximation.

The approximation allows the full Hamiltonian to be considered, associated with a new basis, in the form:

$$\hat{H}_0 = \hbar \times \begin{pmatrix} 0 & \Omega_{12}/2 & 0 & \Omega_{14}/2 \\ \Omega_{12}/2 & \Delta_2 + \delta - \omega_{13} & \Omega_{23}/2 & 0 \\ 0 & \Omega_{23}/2 & \omega_{13} & \Omega_{34}/2 \\ \Omega_{14}/2 & 0 & \Omega_{34}/2 & \Delta_4 + \delta \end{pmatrix},$$

where $\omega_{13}$ corresponds to a frequency of a forbidden transition and $\delta$ is a detuning from this transition (being positive for red detuning). Adiabatic elimination is applied for the 2nd and 4th levels, $\frac{dc_2}{dt} = 0$ and $\frac{dc_4}{dt} = 0$, which gives:

$$c_2 = -\frac{\Omega_{12}c_1 + \Omega_{23}c_3}{2(\Delta_2 - \omega_0)},$$
$$c_4 = -\frac{\Omega_{14}c_1 + \Omega_{34}c_3}{2(\Delta_4 + \delta)}.$$

Substitution to the equations will give:

$$i\frac{dc_3}{dt} = c_3\left(\omega_0 + \delta - \frac{\Omega_{23}^2}{4\left(\omega_0 - \Delta_2\right)} - \frac{\Omega_{34}^2}{4\left(\Delta_4 + \delta\right)}\right) - c_1\left(\frac{\Omega_{12}\Omega_{23}}{4\left(\omega_0 - \Delta_2\right)} + \frac{\Omega_{14}\Omega_{34}}{4\left(\Delta_4 + \delta\right)}\right).$$

This equation corresponds to non-linear interaction, with an effective Rabi frequency and a modified detuning. The modified detuning is associated with an AC Stark shift. The coefficient in the brackets after $c_1$ is a coupling coefficient; it consists of two parts, the first being significantly smaller than the second part because of the large denominator. Thus, the effective Rabi frequency can be written as $\Omega_{eff} = \frac{\Omega_{14}\Omega_{34}}{4(\Delta_4+\delta)}$; it has a quadratic dependence on the applied electric field and depends on the transition dipole moments and detuning from the one-photon transition. The coupling efficiency is however very small because of large detuning from the resonance: it is described by the coefficient after $c_3$, which is only marginally different from $\omega_0$. The reason for this is the very unefficient coupling between levels 3 and 4: they are coupled via far-detuned optical transition. The role of the intermediate state 2 is very small, and it makes almost no contribution to the population transfer.

Generally, from the presented consideration it follows that the effective forbidden transition is impossible with the optical transition only, i.e. without applying RF or THz radiation.

# Appendix 2. Vibrational spectroscopy of Phenol-OH Hydroxyl group in molecular ions

In this work we demonstrate vibrational spectroscopy of polyatomic ions that are trapped and sympathetically cooled by laser-cooled atomic ions. We use the protonated tyrosine–alanine ($HTyrAla^+$) as a model system, cooled by barium ions to less than 800 mK secular temperature. The spectroscopy is performed on the fundamental vibrational transition of a local vibrational mode at 2.74 $\mu$m using a continuous-wave optical parametric oscillator (OPO). Resonant IR multiple-photon dissociation spectroscopy (R-IRMPD) (without the use of a UV laser) generates charged molecular fragments, which are sympathetically cooled and trapped, and subsequently released from the trap and counted. We measured the cross section for R-IRMPD under conditions of low intensity, and found it to be approximately two orders smaller than the vibrational excitation cross section. The observed rotational bandwidth of the vibrational transition is larger than the one expected from the combined effects of 300 K black-body temperature, conformer-dependent line shifts, and intermolecular vibrational relaxation broadening (J. Stearns et al., J. Chem. Phys., 2007, 127, 154322–154327). This indicates that as the internal energy of the molecule grows, an increase of the rotational temperature of the molecular ions well above room temperature (up to on the order of 1000 K), and/or an appreciable shift of the vibrational transition frequency (approx. 6–8 $cm^{-1}$ ) occurs.

The author contributed to: repair and modification of the setup, performing experiments, data analyses, discussion of the results, writing the paper.

**Corrigendum:**

1. The phrase in the abstract “We use the protonated dipeptide tryptophan–alanine...” should be read: “We use the protonated dipeptide *tyrosine*–alanine”.

2. The phrase in the abstract “... conformer-dependent line shifts, and intermolecular vibrational relaxation broadening...” should be read: “... conformer-dependent line shifts, and *intra*-molecular vibrational relaxation broadening...”.

PCCP

View Online
Dynamic Article Links

Cite this: DOI: 10.1039/c1cp22428j

www.rsc.org/pccp

PAPER

# Resonant IR multi-photon dissociation spectroscopy of a trapped and sympathetically cooled biomolecular ion species

**Ch. Wellers,† A. Borodin,*† S. Vasilyev, D. Offenberg and S. Schiller**

***Received 27th July 2011, Accepted 20th September 2011***
**DOI: 10.1039/c1cp22428j**

In this work we demonstrate vibrational spectroscopy of polyatomic ions that are trapped and sympathetically cooled by laser-cooled atomic ions. We use the protonated dipeptide tryptophan–alanine ($HTyrAla^+$) as a model system, cooled by barium ions to less than 800 mK secular temperature. The spectroscopy is performed on the fundamental vibrational transition of a local vibrational mode at 2.74 μm using a continuous-wave optical parametric oscillator (OPO). Resonant IR multi-photon dissociation spectroscopy (R-IRMPD) (without the use of a UV laser) generates charged molecular fragments, which are sympathetically cooled and trapped, and subsequently released from the trap and counted. We measured the cross section for R-IRMPD under conditions of low intensity, and found it to be approximately two orders smaller than the vibrational excitation cross section. The observed rotational bandwidth of the vibrational transition is larger than the one expected from the combined effects of 300 K black-body temperature, conformer-dependent line shifts, and intermolecular vibrational relaxation broadening (J. Stearns *et al.*, *J. Chem. Phys.*, 2007, **127**, 154322–154327). This indicates that as the internal energy of the molecule grows, an increase of the rotational temperature of the molecular ions well above room temperature (up to on the order of 1000 K), and/or an appreciable shift of the vibrational transition frequency (approx. 6–8 $cm^{-1}$) occurs.

## 1 Introduction

In the field of cold, trapped molecules, one topic under current study is the development and refinement of suitable spectroscopic methods. Concerning more specifically translationally cold molecular ions, often produced *via* sympathetic cooling by laser-cooled ions, a few studies have been performed recently, on diatomic molecular ions. Ro-vibrational spectroscopy is one example, applied in particular to $HD^+$ and $MgH^+$. Fundamental ($\Delta v = 1$),[1–4] first ($\Delta v = 2$),[1] and third overtone ($\Delta v = 4$)[5,6] vibrational spectroscopy, with resolution of the rotational structure, has been described. In the simplest case, the spectroscopy consisted in a simple variant of resonance-enhanced multiphoton dissociation ($1 + 1'$ REMPD), where a vibrational transition is driven by one photon and a second, UV photon dissociates the molecule by exciting it from the vibrationally excited level to a non-binding electronically excited state. The reduction of the number of intact molecular ions is then detected in an appropriate way. More recently, in our group we have also employed $1 + 1' + 1''$ REMPD on $HD^+$, where the first photon performed a rotational or vibrational excitation, followed by a vibrational excitation and then dissociation by a UV photon.[7] It is of interest to explore if and how spectroscopy can be extended to sympathetically cooled molecular ions other than diatomic ones.

This work is devoted to a first methodological study of vibrational spectroscopy of a sympathetically cooled polyatomic molecular ion. Vibrational spectroscopy of complex molecular ions is a very important method for gaining information on structures of molecules, including biomolecules (see, *e.g.* ref. 8 and references therein), and for studying the energetics of fragmentation.[9] Apart from implementing vibrational spectroscopy, we investigate the question whether the rotational degrees of freedom of the molecules couple, *via* the ion–ion collisions between the molecules and other ions in the trap, to the translational ones, which are sympathetically cooled to less than 800 mK (secular motional temperature). The molecular ion species used, protonated tyrosine–alanine ($HTyrAla^+$), is a test case appropriate for the present purposes since a previous study by Stearns *et al.*[10] has shown that it exhibits a spectrally narrow vibrational transition. The vibrational linewidth observed in that work included the width of the rotational band, whose details were unresolved, due to experimental reasons, but also because of the small rotational constant exhibited by this relatively large molecule.

We found in the course of our studies that resonant IR multi-photon dissociation (R-IRMPD) can be applied to sympathetically cooled $HTyrAla^+$ ion ensembles. Here, only

---

*Institut für Experimentalphysik,*
*Heinrich-Heine-Universität Düsseldorf, 40225 Düsseldorf, Germany.*
*E-mail: andrii.borodin@uni-duesseldorf.de*

† First authorship shared.

photons of energy resonant with a vibrational transition of a specific vibrational mode are used. Upon absorption of the photon, the vibrational energy is distributed on a time scale of less than a nanosecond[11] to other internal degrees of freedom, by intramolecular vibrational relaxation (IVR). After that, another photon of the same energy can be absorbed on the same transition.[12,13,14] (This is not possible with sympathetically cooled diatomic ions, since there are no other internal degrees of freedom, nor sufficient collisional vibrational relaxation because UHV conditions are maintained.) The photon absorption process is repeated, allowing the molecule to collect internal energy until it will be large enough to break certain molecular bonds, leading to generation of charged fragments, and a reduction in the number of parent molecules. This technique is used in spectroscopy of trapped complex molecular ions, but has so far been applied only to uncooled molecules, to our knowledge. It is used in conjunction with large-scale, pulsed infrared laser systems, *e.g.* free-electron lasers, which allow a very wide spectral coverage[8,15] and therefore a rather complete study of the vibrational spectrum. For other methods of spectroscopy of polyatomic molecular ions, using buffer gas cooling, see *e.g.* ref. 32.

The present laboratory experiment is an example that such studies are becoming possible with laboratory laser sources only, even continuous-wave ones. Indeed the IR spectral coverage with cw sources such as OPOs, quantum cascade lasers and difference frequency generators[16] is rapidly increasing.

## 2 Experimental apparatus

In this work, a previously developed, general-purpose apparatus for sympathetic cooling of a large variety of complex molecular ions is employed.[17] Fig. 1 shows an overview of the apparatus. The molecular ions travel from left, the ion source, to the right, the ion trap. Mass-to-charge selected molecular ions are trapped in the ion trap and are sympathetically cooled *via* Coulomb interaction with a laser-cooled atomic ion ensemble species. Depending on their mass and charge, polyatomic ions can be cooled to translational temperatures well below 1 K.[20] The long storage time of few tens of minutes combined with the well-defined and nearly collisionless environment in the ion trap provides very particular conditions for spectroscopy.

As the electrospray ionization takes place at atmospheric pressure, while the achievement of sub-Kelvin temperature using laser cooling requires ultra-high vacuum conditions, high demands are made on the vacuum system. Both conditions are fulfilled using a differentially pumped vacuum setup that provides a pressure gradient of more than 13 orders of magnitude, sustained by in total 11 vacuum pumps.

The molecular ion source is a modified commercial mass spectrometer Finnigan SSQ 700, based on electrospray ionization (ESI). A large variety of neutral molecules can be protonated (*i.e.* one or more proton(s) attach(es) to the neutral molecule by polarization interaction) in the ESI molecular ion source,

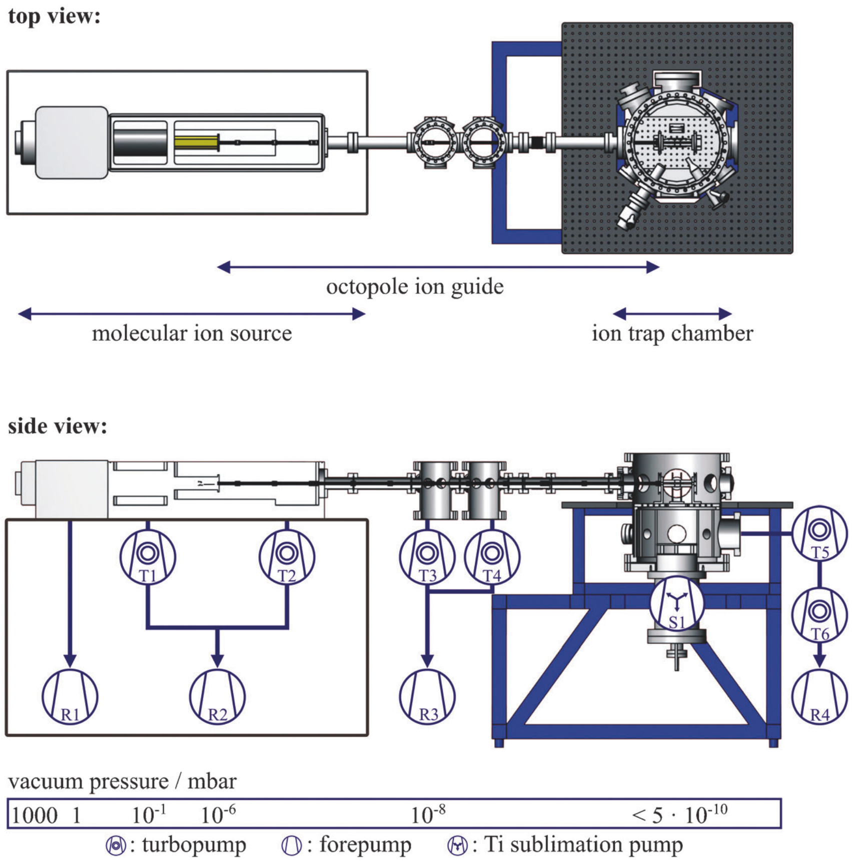

**Fig. 1** Overview of the vacuum setup. Top and side views of the vacuum setup consisting of the electrospray ionization (ESI) molecular ion source, the octopole ion guide, and the ion trap vacuum chamber in which the molecular ions are trapped, cooled and manipulated in a linear quadrupole ion trap. The vacuum pressure in the differential vacuum setup decreases from atmospheric pressure at the molecular ion source inlet (where a solution is fed into the ion source) to ultra-high vacuum values in the ion trap chamber.[18,19]

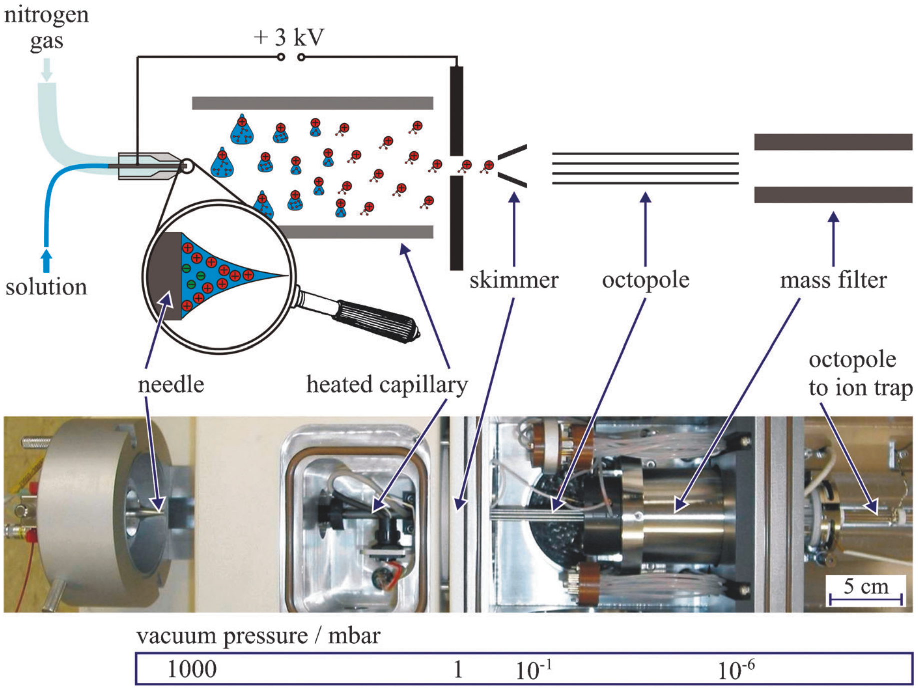

**Fig. 2** Principle and setup of the molecular ion source. The upper schematic diagram (not to scale) illustrates the principle of electrospray ionization as described in the text. The lower photo shows the uncovered molecular ion source, with the needle through which the solution with the molecular ions is sprayed, the heated capillary in which the solvent evaporates, the skimmer (covered by housing components) which serves as aperture, a short octopole used as ion guide, the quadrupole mass filter for selection of the ion species to be transferred to the ion trap, and the beginning of the 2 m long octopole which transfers the molecular ions to the ion trap. The pressures given below the photograph are approximate values for the atmospheric pressure region (1000 mbar), the skimmer region (1 mbar), the octopole region ($10^{-1}$ mbar), and the following high vacuum region ($10^{-6}$ mbar).

including molecules with masses exceeding 10 000 atomic mass units (amu). As Fig. 2 shows, the molecular ions are produced from a solution, which is sprayed as droplets into a vacuum chamber, where the solvent is evaporated until individual protonated molecular ions remain.

In the present study, a solution of 70 pmol $l^{-1}$ dipeptide tyrosine–alanine in a solution of methanol + water (1 : 1 relative concentration) + 0.1% formic acid is prepared, in which protonated tyrosine–alanine forms ($\mathrm{HTyrAla}^+$, mass 251 amu). The protons are supplied by the formic acid. The solution is filled into a syringe, from which it is sprayed at atmospheric pressure (1000 mbar) through a thin metal needle to which a positive high voltage is applied. The emerging solution is shaped by a streaming nitrogen gas into a so-called Taylor cone. Solution droplets break away from the Taylor cone and are accelerated towards a heated capillary (200 °C). The solvent evaporates and the droplets shrink until a critical size, known as Rayleigh stability limit, is reached. The droplets then break apart into smaller ones until bare molecular ions remain. The stream of molecular ions is transferred through the skimmer region at 1 mbar to the quadrupole mass filter with a short octopole ion guide. This mass filter is placed in the high-vacuum section of the apparatus, at about $10^{-6}$ mbar pressure. The quadrupole mass filter parameters are controlled by a computer, allowing purification of the ion stream and delivery of a species with a particular mass-to-charge ratio to the following apparatus section. After the mass filter, the molecular ions are coupled into a 2 m long radio frequency octopole ion guide which transfers the ions to the linear quadrupole ion trap placed in a cylindrical vacuum chamber at $<10^{-9}$ mbar, shown in Fig. 3. Details about the octopole guide can be found in ref. 18 and 21.

The RF trap consists of four cylindrical stainless steel rods with a diameter of 10 mm, which are divided into the middle electrodes of 20 mm length and the two endcap electrodes of 30 mm length. The smallest distance of the electrode surface to the trap axis is $r_0 = 4.36$ mm. With this geometry, the axial electric potential of the trap,[22,23]

$$\Phi_z = \kappa U_{\mathrm{EC}} z^2,$$

has the coefficient $\kappa = 1500\ \mathrm{m}^{-2}$. The RF voltages for radial ion confinement are applied to the middle and the endcap electrodes with an RF frequency of $\Omega = 2\pi \times 2.5$ MHz and a maximum amplitude of $U_{\mathrm{RF,max}} = 500$ V. dc voltages of $-20$ to $+20$ V can be individually applied to the four middle electrodes to compensate external electric fields for exact symmetrization of the quadrupole field. Typical operation parameters are $200\ \mathrm{V} < U_{\mathrm{RF}} < 500\ \mathrm{V}$ and $5\ \mathrm{V} < U_{\mathrm{EC}} < 7\ \mathrm{V}$.

The magnetic field that is necessary for laser cooling of $^{138}\mathrm{Ba}^+$ ions is produced by two coils centered around the trap axis and mounted beyond the endcap electrodes (see Fig. 4). The coils produce a magnetic field in the trap center which is parallel to the trap axis and has a strength of approximately 5 G.

To count the trapped ions, they are released from the trap and led to a channel electron multiplier (CEM) mounted below the trap, serving as an ion detector (Fig. 4). When the

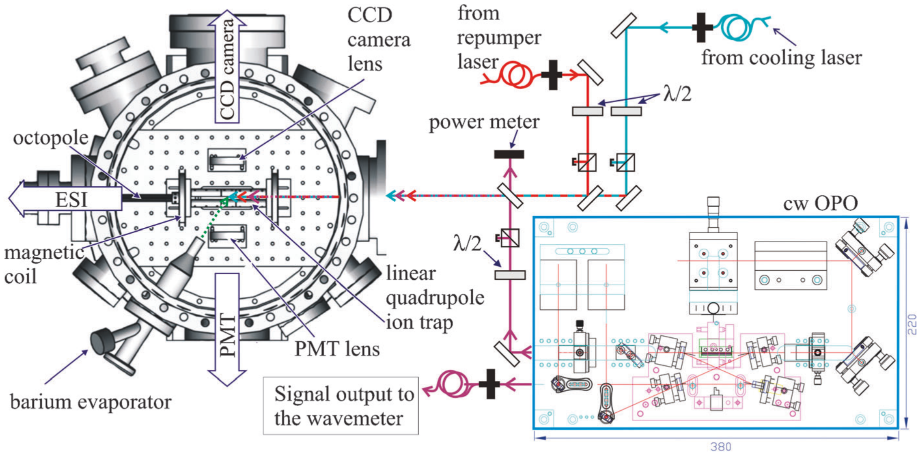

**Fig. 3** Overview of the ion trap vacuum chamber. Molecular ions from the ESI ion source are transferred to the linear quadrupole ion trap *via* the octopole ion guide. The barium ions are produced with an ultra-high-vacuum suitable evaporator directed to the trap center (dashed green arrow). Cooling (493 nm), repumping (650 nm) and vibrational spectroscopy laser light (2.7 μm) (blue, red and violet arrows, respectively) enter the vacuum chamber through an axial sapphire viewport. The fluorescence light emitted by the laser-cooled $^{138}\mathrm{Ba}^+$ ions is collimated by radially arranged lenses to direct it through glass viewports to a CCD camera and a photomultiplier (PMT), both located outside the vacuum chamber.[18] The dimensions of the OPO base plate are in mm.

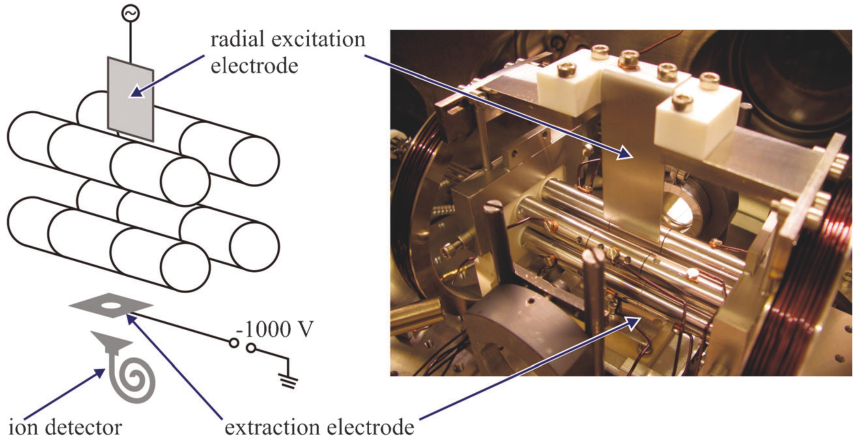

**Fig. 4** Trap setup with cleaning and detection components. With an ac voltage scan applied to the radial excitation electrode, molecules with a specified mass-to-charge ratio can be removed from the trap. The identification of the stored ion species is *via* their mass-to-charge ratio, and is obtained *via* a controlled decrease of the ion trap RF amplitude and a simultaneous detection of the escaping ions. Detection is achieved by directing the ions by an extraction electrode to an ion detector mounted below the trap.

trap RF voltage $U_{\mathrm{RF}}$ is decreased, ions of mass $m$ and charge $q$ are not stably trapped any more once the value reaches

$$U_{\mathrm{RF}}^{\mathrm{ex}} = a r_0^2 \Omega \sqrt{2\kappa U_{\mathrm{EC}} \frac{m}{q}}.$$

Here $a$ is a numerical factor describing the influence of the electric field of the extraction electrode. This simple expression holds in the limit of a single trapped ion and zero kinetic energy.

The escaping ions will be accelerated by an extraction electrode at a dc voltage of about −1000 V and counted. The number of detected ions *versus* the RF voltage represents a mass spectrum of the trapped ion ensembles ($q = e$ is assumed for all ions, as we have no evidence for higher charge states having been produced, trapped and sympathetically cooled). In the spectra shown below, the largest detectable mass (850 amu) corresponds to the RF amplitude used for normal trapping operation, $U_{\mathrm{RF}}^{\mathrm{ex}} = U_{\mathrm{RF}} = 300$ V. By comparing the ion number detected by the counter with the number of ions initially contained in the Coulomb crystals (this number is obtained by Molecular Dynamic (MD) simulations on the basis of CCD images), we found that the ion detection efficiency is between 10 and 20%.

For the laser cooling of $^{138}\mathrm{Ba}^+$ ions, a cooling laser at 493 nm (generated by sum-frequency mixing of a 920 nm diode laser wave and a 1064 nm Nd:YAG laser wave) and a repumper diode laser at 650 nm are required. Both cooling and repumping laser frequencies are locked to transfer cavities, which, in turn, are locked to the Nd:YAG laser, itself stabilized to a ro-vibrational transition of molecular iodine *via* Doppler-free saturation spectroscopy.

## 3 Preparation, cooling and analysis of ion ensembles

First, a barium ion crystal is prepared in the trap by an electron gun bombarding and ionizing metallic barium (ref. 24, Fig. 5(a)).

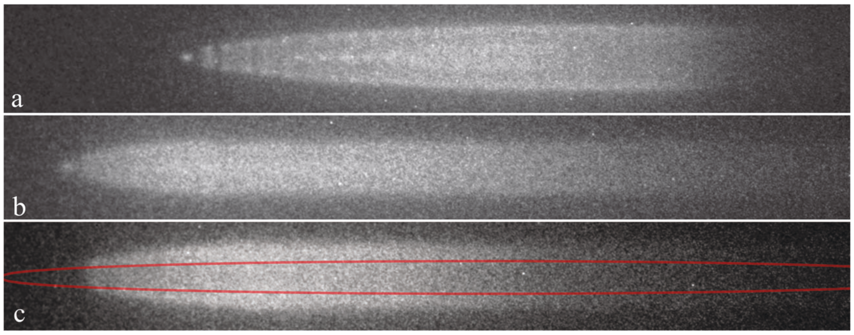

**Fig. 5** Experimental CCD images of ion crystals. (a) A barium ion crystal, containing laser-cooled $^{138}Ba^+$ ions and sympathetically cooled ions of other Ba isotopes. The relative abundance of $^{138}Ba^+$ is 72%. The cooling laser's light pressure acts only on $^{138}Ba^+$, not on sympathetically cooled barium isotopes. The laser cooled ions are therefore pushed to the left with respect to the other isotopes, which are located on the right, in the dark region. Molecular impurity ions ($BaO^+$, $CO_2{}^+$) have been previously removed. (b) A crystal, radially compressed and axially prolonged by the (non-fluorescing) surrounding sympathetically cooled HTyrAla$^+$ ions. (c) The crystal after partial photodissociation of HTyrAla$^+$ ions by R-IRMPD. Sympathetically cooled ionized molecular fragments lighter than $Ba^+$ ions are trapped close to the trap axis, forming a dark region in the center of the crystal (marked in red). Compare with Fig. 8.

Some of these ions react with residual $H_2O$ gas molecules to produce barium oxide ions. The electron gun also ionizes residual $CO_2$ gas. These molecular ion species are also trapped in the ion trap. In order to load molecular ions delivered *via* the octopole ion guide, the dc potential of the entry endcap is decreased and the ion guide is activated for several seconds. In addition, room temperature helium buffer gas (at (4–6) $\times$ $10^{-6}$ mbar) is injected into the trap using a piezoelectric valve. This acts as a buffer gas, in which collisions with the molecular ions reduce their kinetic energy sufficiently for capture in the trap (Fig. 6). The ions in the crystal also collide with the He atoms, causing its melting. The continued action of the cooling laser leads to a steady state corresponding to a cold gas. After restoring the entry electrodes' potential the valve is closed and the pressure of the buffer gas decreases within several seconds due to pumping. Then the barium cloud crystallizes again and sympathetically cools the trapped molecular ions (Fig. 5(b)). For species-selective cleaning we apply a suitably strong ac electric field to a radial excitation electrode (see Fig. 4). It induces a radial secular motion of sufficiently large amplitude so that the resonant ions are ejected from the trap. The frequencies of the excitation are made to cover the secular resonance frequencies of undesired ions. The cleaning is used in particular to remove $CO_2{}^+$ and $BaO^+$.

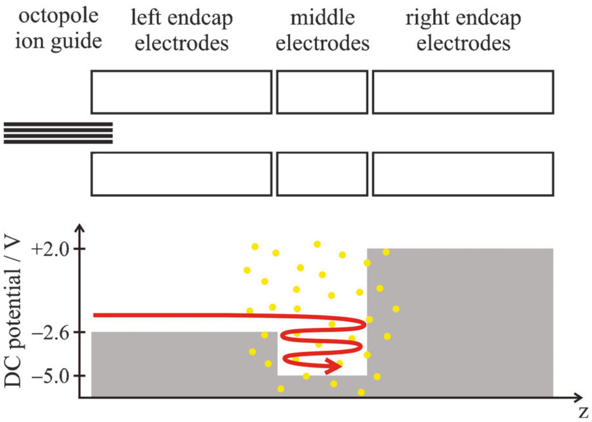

**Fig. 6** Schematic principle of loading of the ion trap with molecular ions coming from the ion source. The dc potential of the left endcap electrodes is temporarily lowered, allowing entrance of the ions. Their kinetic energy (red arrow) is reduced by collisions with helium buffer gas (yellow dots), leading to trapping.

Two ion extraction spectra obtained as described in Section 2 are compared in Fig. 7(a) to show the significant influence of laser cooling and sympathetic cooling. The ensembles contained $Ba^+$, $BaO^+$ and HTyrAla$^+$ and had kinetic energies corresponding to room temperature (red), achieved by collisions with He buffer gas (lasers were off), and below 1 K (blue), achieved by laser cooling. In the 300 K case, the peaks in the extraction spectrum are broadened, indicating a larger distribution in the energy of the trapped ions. For the cooled ensemble, not only the peak of the laser-cooled $Ba^+$ ions is narrower, allowing us to resolve the peak of the sympathetically cooled $BaO^+$ ions, but also the one of HTyrAla$^+$. This latter peak narrowing is a qualitative proof of the sympathetic cooling of complex molecular ions.

The action of R-IRMPD on the ion ensemble is seen in Fig. 5(c), where a $Ba^+$/HTyrAla$^+$ ion crystal was exposed comparatively long to continuous-wave light at 2.74 μm. Fig. 7(b) shows the ion extraction spectra, which give detailed information about the contents of the ensemble. The HTyrAla$^+$ ions were nearly completely destroyed and fragments of different masses have appeared. For comparison, the red curve is the extraction spectrum of a crystal acquired directly after the preparation phase (no R-IRMPD), showing only the two ion species as expected (this spectrum is the same as the blue curve in Fig. 7(a)).

The information contained in the ion extraction spectrum together with the CCD images of the barium ions' fluorescence before and after extraction of the ions can be used to characterize the initial ion ensemble (initial numbers of ions of different species and their temperatures) and the final state (number of fragments and final temperature of different species).[20] MD simulations are performed for this purpose. Fig. 8 shows an example of the final state of an ensemble where R-IRMPD has partially photodissociated the HTyrAla$^+$ ions. A comparison with experimental CCD images reveals that the typical temperature of HTyrAla$^+$ is less than 800 mK. This value is

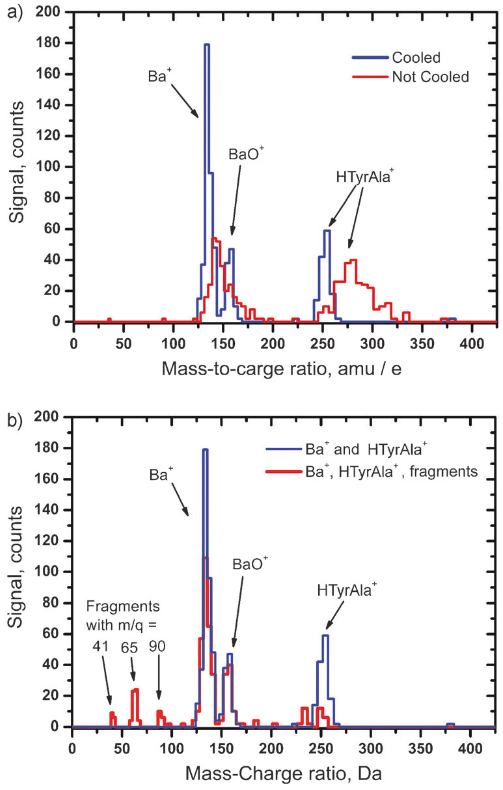

**Fig. 7** (a) Mass spectrum of extracted ions, when the trapped ensemble was laser-cooled (blue) and buffer-gas cooled (300 K, red), respectively. The wider peaks in the 300 K case are due to the correspondingly larger kinetic energy distribution of the ions inside the trap. Note also that in the 300 K case, ions are extracted from the trap already at higher RF amplitudes as compared to cold ions. (b) Mass spectrum of a cold ion ensemble without R-IRMPD (blue) and with R-IRMPD (red).

the thermal energy associated with the secular motion. In addition, all ions perform micromotion. The micromotion energy of the $HTyrAla^+$ ions can be calculated from the trap parameters and the distance from the axis, and amounts to $k_B$ (11.5 K) per ion.[25]

## 4 IR laser source

$HTyrAla^+$ molecular ions have a complex absorption spectrum, with many lines corresponding to fundamental and overtone excitation of local vibrational modes, complicated by the presence of a rotational structure.[10] The single line studied here is the fundamental vibration of the OH group bound to the phenol ring in the $HTyrAla^+$ dipeptide (Fig. 9). We used the idler wave of a continuous-wave OPO for the spectroscopy, since its high power and tunability provides experimental flexibility. The device is home-built, see Fig. 3.[16] It uses a ring cavity containing a periodically poled lithium niobate crystal, and is pumped by an independent Nd:YAG master laser (1064 nm), amplified by a fiber amplifier, with a maximum output of 9.5 W. Typically, 5 W are delivered *via* a fiber to pump the OPO ring cavity located next to the UHV chamber (Fig. 3). This OPO is tunable over a wide spectral range (2500–3000 nm) by changing the temperature of the nonlinear crystal. The typical output spectral linewidth is a few ten kHz, the output power is up to 2.5 W for the idler wave and up to 3 W for the signal wave (at the highest pump power). In order to prevent mode-hops, the OPO is stabilized using back reflections from the gratings in the crystal. The output wavelength of the idler radiation is determined by measuring the wavelength of the signal radiation, which is sent to a high-resolution wavemeter. The master laser is intrinsically frequency-stable on the time scale of interest here, its wavelength being 1064.49 nm. The idler wave of the OPO is sent into the trap axially, by an uncoated $CaF_2$ beam sampler. The power is adjusted by a combination of a polarizer and a rotated $\lambda/2$ wave retarding plate. The diameter of the idler beam inside the trap was measured as 0.86 mm.

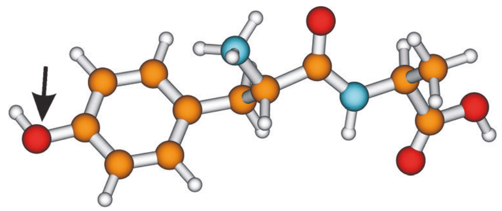

**Fig. 9** 3D view of the structure of $HTyrAla^+$ (conformer A). Atoms: carbon (orange), oxygen (red), nitrogen (blue) and hydrogen (white). The arrow indicates the phenol OH group in which the vibrational excitation studied here takes place.

## 5 Calibration

The molecular ion flux from the ESI source is not stable, showing both short-time fluctuation and longer-term trends, the overall flux variation being on the order of 25%. As a consequence, the number of trapped $HTyrAla^+$ ions varied from one loading to the next. In order to characterize the

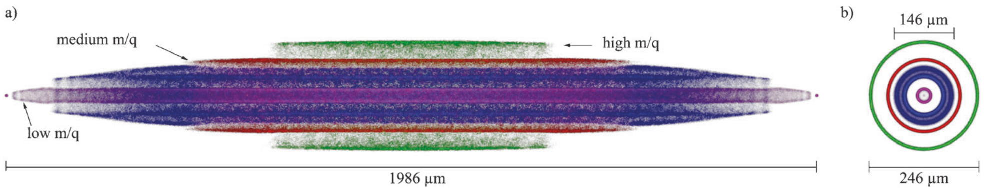

**Fig. 8** Radial mass separation in a multi-species Coulomb crystal. Simulated images for the experimental trap parameters of a Coulomb crystal containing 440 molecular fragments (pink, mass 65 amu), 1190 $Ba^+$ ions (blue, all isotopes), 460 $BaO^+$ ions (red, 154 amu), and 230 $HTyrAla^+$ ions (green, 251 amu). The image shows the crystal as it would appear if all ions were fluorescing. In this simulation the cooling laser radiation pressure force is not taken into account. Compare to the experimental CCD images in Fig. 5, where only $^{138}Ba^+$ ions fluoresce and the radiation pressure force acts. (a) Side view. (b) Cross sectional view. Ions of lower mass arrange close to the trap axis, heavier ions arrange in shells around the lighter ions.

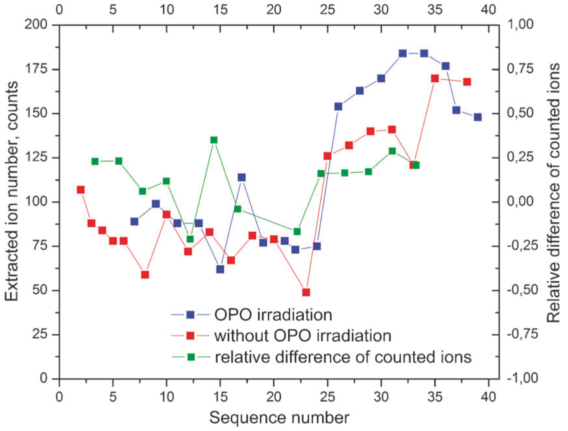

**Fig. 10** Ion flux check and ion number conservation. Red: counts of extracted HTyrAla$^+$ without OPO irradiation. Blue: total counts of extracted HTyrAla$^+$ and its fragments. Green: relative difference of counted ions (right ordinate). The comparison of the two cases shows that the total count is equivalent to the number of loaded HTyrAla$^+$.

variations, the extraction spectra were recorded during a series of repeated HTyrAla$^+$ loadings without Ba$^+$. Interleaved procedures were used, alternating between OPO irradiation on and off. Also, the OPO power and its idler wavelength were changed within a wide range. Fig. 10 shows the measurements, taken over the course of 20 min. Here, the barium ion crystal remained the same, laser cooling was always on. The red points show the variation of the number of counts of extracted HTyrAla$^+$ ions. For comparison, the blue points show the interleaved measurements where after loading and buffer gas cooling, the HTyrAla$^+$ was partially photodissociated. Here, the number of counts of the fragments and of the undissociated HTyrAla$^+$ in the mass spectrum was added. The relative deviation (green) of this total number with respect to the average number of HTyrAla$^+$ detected in the previous and subsequent loadings is moderate, less than 25%. Thus, this total number of counts is used as a measure of the initial number of HTyrAla$^+$ after loading, which is not measurable in a nondestructive way, and also determines the effect of a spectroscopic excitation in terms of the relative photodissociation efficiency of the initial (parent) HTyrAla$^+$ ions. This procedure is quite useful, and more practical than extracting the initial number from MD simulations, which would be very time-consuming.

The typical ion extraction spectrum in Fig. 7 shows an advantage of having sympathetically cooled ions rather than uncooled ions: this method allows a quantitative characterization of the fragment ions. It is seen that there are at least three different types of products of photodissociation, having mass/charge ratios 41, 65 and 90 amu/e. Fragments with atomic mass close to $\frac{m}{q} = 138$ amu/e are hard to distinguish from $^{138}$Ba$^+$. We assume that there is no fragment with this mass which is proved by experiments with room-temperature ions.

A series of R-IRMPD experiments was made for room-temperature and sympathetically cooled ions, for different Coulomb crystal sizes and numbers of HTyrAla$^+$ ions trapped, for different OPO wavelengths, irradiation times and OPO powers. The extraction spectra were sorted into groups corresponding to different power ranges, OPO frequencies and irradiation times.

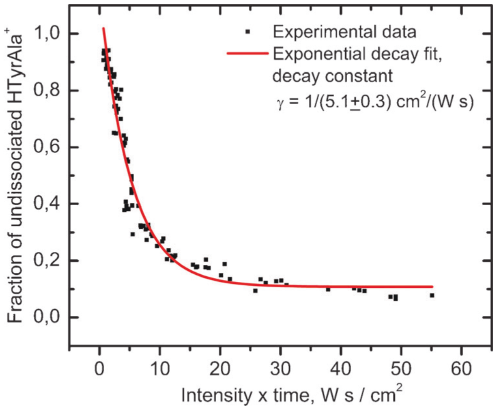

**Fig. 11** Fraction of undissociated uncooled HTyrAla$^+$ ions as a function of irradiated energy. In this series of experiments, only HTyrAla$^+$ ions were trapped and cooled by 300 K He buffer gas, and irradiated for different times and at different OPO power levels. As the measurements were done on uncooled ions, significant broadening of the extraction spectra occurs (see Fig. 7). This limits the resolution of this method and gives rise to an additive noise. Therefore, a fit function with an offset has been used to model the data.

## 6 Results and discussion

Fig. 11 shows the fraction of undissociated HTyrAla$^+$ ions as a function of irradiated energy, given by the product of power and irradiation time, normalized to the beam cross sectional area. In this series of experiments, only HTyrAla$^+$ ions were trapped (in the presence of He buffer gas), irradiated for different times and powers (at the fixed bean diameter), while the OPO wavelength was close to the central wavelength of the observed spectrum. The fraction decreases exponentially with irradiated energy, indicating that a linear process is occurring, where a one-photon process dominates. Note that the dissociation rate is very small. At a typical power of 10 mW and the beam cross section used here, it is 0.34 s$^{-1}$, much smaller than spontaneous or IVR rate (see below). Taking into account the beam cross section and correcting for the non-uniform intensity distribution of the Gaussian OPO beam, we can deduce a (peak) R-IRMPD dissociation cross section of at least $\sigma_{\mathrm{diss,min}} = 1.5 \times 10^{-20}$ cm$^2$ under our conditions. As the buffer gas ion cloud may have had a larger diameter than the laser beam, thus reducing the effective intensity experienced by the ions, this value is a lower limit. On sympathetically cooled ions, which are all located within the OPO wave, only a few measurements of dissociation as a function of irradiation time were performed at low intensity. The obtained decay constant is consistent with that given in Fig. 11, within the errors. Thus, $\sigma_{\mathrm{diss}}$ is similar to $\sigma_{\mathrm{diss,min}}$.

As phenol is that part of HTyrAla$^+$ that carries the OH group excited by R-IRMPD, we can compare $\sigma_{\mathrm{diss}}$ with the peak absorption cross section deduced from a measurement of the same mode on phenol molecules, $\sigma_{\mathrm{PhOH,abs}} = 7.4 \times 10^{-19}$ cm$^2$.[26] Here we have used the experimental oscillator strength value $f = 7.9 \times 10^{-6}$, and assumed a Lorentzian band shape with a FWHM of 6 cm$^{-1}$, obtained from a rotational band simulation at 300 K (see below). We can also consider the theoretical absorption cross section for our particular vibrational transition, obtained from the transition dipole moment of the mode as

**Table 1** Low-energy conformers of $HTyrAla^+$: theoretical and experimental properties from ref. 10. The transition dipole moment components are given in the principal axis system. The experimental spectrum of ref. 10 was taken in steps of 0.5 $cm^{-1}$, thus the differences between the conformers' frequencies are only known with this resolution. The linewidth values are approximate. The observed vibrational frequency has a systematic uncertainty of 2 $cm^{-1}$. The theoretical vibrational frequencies were obtained from quantum chemical computations and corrected by a factor 0.954 in order to take into account anharmonicities of hydride frequencies. This factor has previously given a good fit for protonated amino acids

| | Theoretical | | | | | | Experimental | |
|---|---|---|---|---|---|---|---|---|
| | | | | Rotational constants/GHz | | | | |
| Conformer | Energy rel. to ground [kJ $mol^{-1}$ = $k_B$ (121 K)] | Vibr. freq. of PhOH mode/$cm^{-1}$ | Transition dipole moment ($d_x$, $d_y$, $d_z$) [0.0104 D] | A | B | C | Vibr. freq./$cm^{-1}$ | Line-width/$cm^{-1}$ |
| A | 0 | 3641.2 | (9.96, 2.42, 3.59) | 1.0902 | 0.1442 | 0.1347 | 3641.5 | 2 |
| B | 4 | 3642.2 | (3.15, 8.60, 5.06) | 0.6949 | 0.2018 | 0.1792 | 3642 | 2 |
| C | 0.1 | 3641.8 | (−8.55, 4.35, 5.12) | 1.0912 | 0.1444 | 0.1346 | 3642 | 2 |
| D | 4.1 | 3642.8 | (10.6, 1.16, 1.56) | 0.6911 | 0.2022 | 0.1795 | 3642.5 | 2 |

calculated using Gaussian03[27] (see Table 1), and assume the same FWHM. For the four conformers the values are similar, $\sigma_{abs} = 2 \times 10^{-18}$ $cm^2$ (peak value), approx. three times the phenol value. Thus, $\sigma_{abs}$ is approximately a factor $10^2$ larger than the R-IRMPD cross section $\sigma_{diss}$. A simple interpretation of this ratio is that the molecule must absorb on the order of $10^2$ photons in order to dissociate. Note that the corresponding total energy is approximately one order of magnitude larger than the UV dissociation energy ($E_{diss}$ approx. 35 000 $cm^{-1}$)[10]. Two effects may contribute to this factor. First, the excited molecule may fluoresce, either from the excited state, or from states that it evolves into as a consequence of IVR. In a very simple model, the ratio of decay rate $\Gamma$ from the excited state *via* single or multiple photon emission and the total decay rate $A + \Gamma$, where $A$ is the fluorescence rate, determines the actual energy deposition rate, $dE_{int}/dt = \sigma_{abs} I\Gamma/(\Gamma + A)$, where $I$ is the intensity (stimulated emission is neglected). The ratio may be distinctively smaller than unity and contribute to a reduction of $\sigma_{diss} = (\Gamma/(A + \Gamma))(h\nu/E_{diss})\sigma_{abs}$. The fluorescence rate $A$ for the excited vibrational state is calculated to be approximately 95 $s^{-1}$, using the transition dipole matrix elements given in Table 1. (The calculated stimulated emission rate at the OPO intensity shown in Fig. 12 (blue curves) is approximately 50 $s^{-1}$, smaller than $A$.) Second, the molecules, internally heated by energy deposition, will also "cool" by emission of black-body radiation.[28] Since the time scale over which dissociation is obtained under our experimental conditions is long (of order 1 s) this could be a process of relevance. Such a cooling process would also increase the number of IR photons necessary to be absorbed until sufficient energy is accumulated that leads to dissociation. A detailed explanation of the ratio $\sigma_{diss}/\sigma_{abs}$ is beyond the scope of this work, requiring extensive additional measurements.

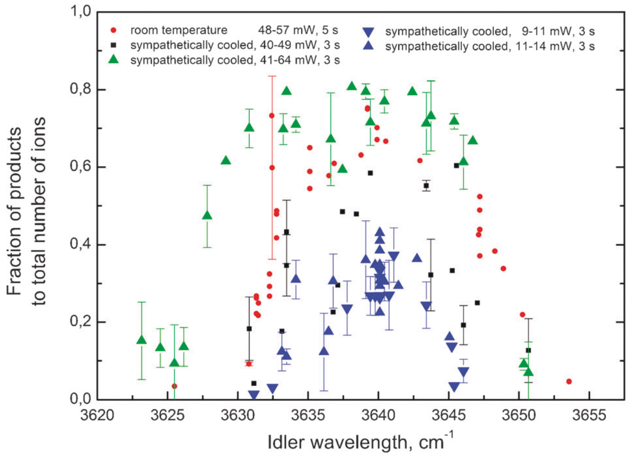

**Fig. 12** Spectra of room-temperature (buffer-gas cooled) and laser-cooled photodestructed $HTyrAla^+$. The error of the room temperature (red) fraction of products is significantly larger than for the sympathetically cooled cases (green, black, blue). Total time to obtain the data shown here was about 2000 min.

The experimentally observed photodissociation spectra are shown in Fig. 12. It comprises data from several hundred individual measurements. The fundamental transition of the phenol-OH mode has the central wavelength of approx. 3640 $cm^{-1}$, within a few wavenumbers both for buffer-gas and sympathetically cooled ions. The measurements shown in blue are taken at the lowest intensities, and the maximum dissociation fraction is below 0.4. This implies that saturation effects are not important in this case. The full width of this line (for sympathetically cooled ions) is approx. 10 $cm^{-1}$ and will be discussed in the following.

The measurements taken with buffer gas cooled molecules show a larger linewidth. This is likely due to both saturation (a larger OPO intensity was used) and to an increase of internal energy (rotational temperature) caused by partial transformation of micromotion energy, which is much larger for buffer-gas cooled ions than for sympathetically cooled ones, to internal energy during collisions with He atoms.

The observed transition linewidths contain information about the internal rotational temperature. However, this information cannot be extracted straightforwardly, as several unknowns contribute to it. First, the preparation step of our cold molecules is not sensitive to a conformer[10] having overall energies close or below the level $k_B \times$ (room temperature), so any ensemble of ions loaded into the trap is expected to contain various conformations and these will contribute to our spectroscopic signal. Different conformations have different rotational constants and vibrational transition frequencies (see Table 1). This introduces a broadening and shape change of the vibrational line. Second, in R-IRMPD, the molecule absorbs many photons before dissociating. The increasing internal energy may lead to an increasing distortion of the molecular structure. As this occurs, the vibrational frequency of the local mode may shift, yielding another cause of broadening. Third, the molecule may be heated rotationally. Fourth, the IVR process leads to line broadening of each ro-vibrational transition line in the band, washing out the fine structure of the rotational band.

The measurements by Stearns *et al.*[10] on HTyrAla$^+$ provide important information on these issues. In their work, vibrationally cold ions were obtained by collisions with cold He buffer gas atoms in a cryogenic trap. The vibrational temperature was measured to be 10–11 K and the rotational temperature was presumed to be in equilibrium. Their measurements include information on the relative shift of the vibrational lines for four conformers and also on the rotational band linewidths (see Section 1). It should be emphasized that their spectroscopic method was not R-IRMPD but vibrationally depleted electronic (UV) spectroscopy, in which only a single IR photon is absorbed, therefore a distortion-induced lineshift cannot contribute to their observed linewidths. As their work was focused on determining a wide IR spectrum rather than precisely measuring one particular line, a frequency step size of 0.5 cm$^{-1}$ was sufficient. Their measurements indicate that the frequency shift between conformers is not more than about 1 cm$^{-1}$ roughly consistent with the theoretical relative shifts. The FWHM linewidth of individual conformer species is about 1.7 cm$^{-1}$, after subtracting the contribution of the spectral linewidth of the pulsed OPO (linewidth *ca.* 1 cm$^{-1}$). Importantly, this linewidth includes the effect of IVR. Our 10 cm$^{-1}$ linewidth (in the sympathetically cooled case) is substantially larger than both the "cryogenic" linewidth and the upper limit for the conformer shift. Therefore, in our sympathetically cooled case conformation variations and IVR broadening cannot be dominant effects. Instead, either our rotational temperature is significantly higher than 10 K or there is a substantial internal-energy-induced line shift, or both.

In order to discuss the influence of temperature on the band linewidth, simulations of the rotational band for different rotational temperatures were made. As input parameters the rotational constants as well as the vibrational transition dipole moments in the molecular frame, as computed by ref. 10 and reported in Table 1, were used. The rotational constants of the vibrational ground state are also used for the excited state, due to lack of any further information. The rotational band structure was computed using the program *PGOPHER*,[29] including transitions between rotational levels with quantum number up to $J = 510$. This high value was required in order to obtain a sufficiently complete band shape even at the highest considered temperature, $T = 1000$ K, at which a very large number of rotational levels in the ground state are thermally populated. The individual ro-vibrational transitions were broadened by a Lorentzian line shape function of 0.9 cm$^{-1}$ full width at half maximum, in order to obtain a smooth band. A value smaller than the contributions from IVR and from the presence of more than one conformer(s) was chosen, in order not to smooth too much any thermal features. Fig. 13 shows the simulated spectra for different rotational temperatures. The resulting line shapes are not Gaussian. The simulated spectrum for 10 K (where a reduced broadening of 0.067 cm$^{-1}$ has been used in order to show the structure of the band more clearly) has a width of 1 cm$^{-1}$, which can be compared with the measurements of ref. 10 (approx. 1.7 cm$^{-1}$). The simulated width is smaller, but an additional contribution coming from IVR broadening must be considered as well. Yamada *et al.*[30,31] have measured the lifetime of the upper vibrational state of the OH vibration in phenol as 14 ps, which corresponds to a linewidth of 0.4 cm$^{-1}$. It is conceivable that the lifetime is shorter in HTyrAla, due to its larger density of states as compared to that of phenol, which may provide more doorway states. The IVR rate strongly depends on such states, as has been shown by Yamada *et al.*, who found, *e.g.* a six times smaller rate when the phenol ring is deuterated (phenol-$d_5$), which significantly changes the vibrational frequencies of the molecule, and a three times higher rate in the case of the OH vibration. Such effects may explain the slightly larger linewidth value observed by Stearns *et al.*

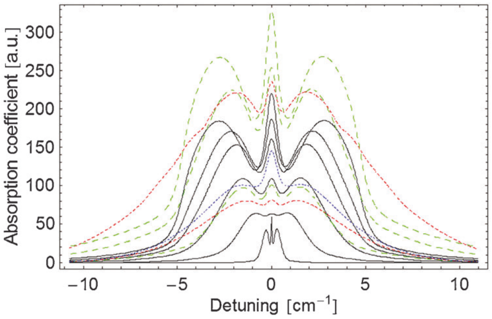

**Fig. 13** Simulated rotational bands of the phenol OH vibration of HTyrAla$^+$. Full lines: conformer A. The temperatures are, increasing from the smallest line, 10 K, 100 K, 300 K, 450 K, 600 K, 1000 K. The red/medium-long-dashed (green/long-dashed, blue/short-dashed) lines are for the B (C, D) conformer. The FWHMs are as follows. Conformer A: 1 cm$^{-1}$ (10 K), 3.9 cm$^{-1}$ (100 K), 6.2 cm$^{-1}$ (300 K), 7.3 cm$^{-1}$ (450 K), 8.1 cm$^{-1}$ (600 K), 9.2 cm$^{-1}$ (1000 K); conformer B: 8.5 cm$^{-1}$ (300 K), 11 cm$^{-1}$ (600 K); conformer C: 6.5 cm$^{-1}$ (300 K), 8.4 cm$^{-1}$ (600 K), 9.2 cm$^{-1}$ (1000 K); conformer D: 6.5 cm$^{-1}$ (300 K). The vertical scale is arbitrary for all curves, also for different temperatures of a single conformer.

For rotational temperatures from room temperature on, the simulated linewidths increase only slowly with temperature, *e.g.* at $T = 100, 300, 450, 600, 1000$ K the simulated FWHMs are approximately 3.9, 6.2, 7.3, 8.1, 9.2 cm$^{-1}$ for conformer A. Thus, in principle the FWHM can be correlated with rotational temperature, but obtaining a high temperature resolution would require an accurate measurement of the bandshape. This was not possible in our work, due to variations in the ion flux and the limited signal-to-noise ratio achieved with the low trapped ion number. For comparison, conformers B, C, D were also simulated, which have linewidths 8.5, 6.5, 6.5 cm$^{-1}$ at 300 K, respectively. Conformer B has a significantly larger FWHM at room temperature and above than conformers A and C. This variability further makes an accurate determination of rotational temperature difficult in the case of a mixture of conformers. The observed FWHM of 10 cm$^{-1}$ corresponds to an effective rotational temperature in the range from above 600 K to above but near 1000 K, significantly above 300 K that the molecules are expected to have after collisions with 300 K helium buffer gas.

## 7 Conclusion

Vibrational spectroscopy of a local mode of a sympathetically cooled polyatomic molecular ion was demonstrated, for the first time to our knowledge. The vibrational excitation of polyatomic HTyrAla$^+$ ions was induced by irradiation with continuous-wave infrared light at 2.74 μm and led to photodissociation *via* the R-IRMPD process. For comparison, experiments were also performed on uncooled ions. The kinetic energy of the ions was significantly different in these two cases. After loading of the ions into the trap, room-temperature He gas was introduced as a first translational cooling step. In the case of subsequent sympathetic cooling, the rotational temperature may be assumed to have reached a value on the order of 300 K, since interaction with the 300 K black-body radiation is dominant. Without sympathetic cooling, the ion micromotion energy may have been partially converted to internal energy, leading to an increased rotational temperature.

For the lower IR intensities used, a photodissociation rate was observed that is linearly dependent on intensity, and allowed determination of the approximate R-IRMPD cross section. It is significantly (approx. two orders) lower than the vibrational absorption cross section, indicating that a significantly larger number of IR photons must be absorbed before dissociation can take place, than that corresponding to a typical bond energy. The R-IRMPD spectral lines exhibited modest signal-to-noise ratios, limited by the fact that the individual dissociation experiments are performed with small number of ions and this number fluctuates from one loading to the next. By comparison with measurements by Stearns and coworkers on HTyrAla$^+$ cooled by cold He buffer gas, we deduce that the observed linewidth of the vibrational transition (10 cm$^{-1}$) is not dominated by IVR from the upper vibrational state, nor by the small frequency shifts among conformers that are present as a mixture in our molecular samples. Instead, it is due to a combination of rotational temperature imposed by the initial preparation, the interaction with black-body radiation of the environment, a possible increase of rotational temperature in the course of absorbing the approx. 80 IR photons, and a shift of the vibrational frequency with increasing internal energy in the molecule. The latter would be caused by cross-coupling anharmonicities of the molecule's modes (and is probably a dominant effect). Phenomenologically, the effective temperature to be assigned to the line is significantly above room temperature, approximately 1000 K. Further studies (experimental and *ab initio* calculations) should allow disentangling the mentioned effects.

Future investigations could be aimed at (i) an accurate determination of the IVR-induced broadening, by performing measurements as in ref. 10, but using an injection-seeded pulsed OPO with reduced linewidth, (ii) determining more precisely the influence of internal-energy-induced broadening, by performing R-IRMPD on rotationally cold HTyrAla$^+$ in a cryogenic trap apparatus as used by Stearns *et al.* in order to reduce the effects of high rotational temperature on the spectral line shape, and measuring with high signal-to-noise ratio the rotational band shape. As for (i), the measurements should be performed on samples containing a single conformer, which can be obtained by selectively UV-dissociating other conformers. Moreover, a combination IR-multiphoton absorption and IR-depletion spectroscopy could be applied: the vibrational lineshape is measured by IR-depletion spectroscopy using an injection-seeded pulsed OPO with reduced linewidth, but preceding the interrogation by multi-photon IR excitation for a fixed but variable time, under conditions that the molecules mostly remain undissociated. In this way, one could determine the line shift as a function of internal energy. One could also measure the vibrational temperature as a function of internal energy, using hot band intensities as indicators. In such measurements, the cryogenic buffer gas should first be removed from the trap in order not to continue rotational cooling. Under such conditions, the molecules would still be rotationally and vibrationally cooled by IR emission, but with a reduced rate. A determination of this cooling rate is itself an interesting aim.

## Acknowledgements

The authors are grateful to H. Gollnick for collaboration on the experiment, to T. Schneider for helpful discussions and to B. Roth for his contributions in the initial phase of this project. We especially acknowledge T. Rizzo, J. Stearns, and T. Wassermann for important suggestions, discussions and communication of unpublished results. This work was funded by the DFG under grant SCHI 431/12-1.

## References

1 T. Schneider, B. Roth, H. Duncker, I. Ernsting and S. Schiller, All-optical preparation of molecular ions in the rovibrational ground state, *Nat. Phys.*, 2010, **6**, 275–278.
2 P. Staanum, K. Højbjerre, P. Skyt, A. Hansen and M. Drewsen, Rotational laser cooling of vibrationally and translationally cold molecular ions, *Nat. Phys.*, 2010, **6**, 271–274.
3 I. Vogelius, L. Madsen and M. Drewsen, Blackbody-Radiation-Assisted Laser Cooling of Molecular Ions, *Phys. Rev. Lett.*, 2002, **89**, 173003.
4 S. Nielsen, J. Andersen, P. Hvelplund, L. Liu and S. Tomita, Biomolecular ions in accelerators and storage rings, *J. Phys. B: At., Mol. Opt. Phys.*, 2004, **37**, 25–56.
5 B. Roth, J. Koelemeij, H. Daerr and S. Schiller, Rovibrational spectroscopy of trapped molecular hydrogen ions at millikelvin temperatures, *Phys. Rev. A: At., Mol., Opt. Phys.*, 2006, **74**, 040501–040504.
6 J. Koelemeij, B. Roth, A. Wicht, I. Ernsting and S. Schiller, Vibrational Spectroscopy of HD$^+$ with 2 ppb Accuracy, *Phys. Rev. Lett.*, 2007, **98**, 173002–173004.
7 U. Bressel, *et al.*, Heinrich-Heine-Universität Düsseldorf, priv. communication.
8 C. Correia, C. Clavaguera, U. Erlekam, D. Scuderi and G. Ohanessian, IRMPD spectroscopy of a protonated, phosphorylated dipeptide, *ChemPhysChem*, 2008, **9**, 2564–2573.
9 T. Dienes, S. Pastor, S. Schürch, J. Scott, J. Yao, S. Cui and C. Wilkins, Fourier transform mass spectrometry—advancing years (1992–mid. 1996), *Mass Spectrom. Rev.*, 1996, **15**, 163–211.
10 J. Stearns, M. Guidi, O. Boyarkin and T. Rizzo, Conformation-specific infrared and ultraviolet spectroscopy of tyrosine-based protonated dipeptides, *J. Chem. Phys.*, 2007, **127**, 154322–154327, and private communication.
11 G. Gregoire, M. P. Gaigeot, D. C. Marinica, J. Lemaire, J. P. Schermann and C. Desfrançois, Resonant infrared multi-photon dissociation spectroscopy of gas-phase protonated peptides. Experiments and Car–Parrinello dynamics at 300 K, *Phys. Chem. Chem. Phys.*, 2007, **9**, 3082–3097.
12 J. Black, P. Kolodner, M. Shultz, E. Yablonovitch and N. Bloembergen, Collisionless multiphoton energy deposition and dissociation of SF$_6$, *Phys. Rev. A: At., Mol., Opt. Phys.*, 1979, **19**, 704–716.
13 N. Polfer and J. Oomens, Vibrational spectroscopy of bare and solvated ionic complexes of biological relevance, *Mass Spectrom. Rev.*, 2009, **28**, 468–494.

14 J. Oomens, B. Sartakov, G. Meijer and G. von Helden, Gas-phase infrared multiple photon dissociation spectroscopy of mass-selected molecular ions, *Int. J. Mass Spectrom.*, 2006, **254**, 1–19.

15 N. Barnes, S. Benson, F. Duarte, C. Freed, D. Harris, R. Sze and P. Zorabedian, *Tunable Lasers Handbook*, Academic, 1995.

16 S. Vasilyev, H. Gollnick, A. Nevsky, A. Grisard, E. Lallier, B. Gerard, J. Jimenez and S. Schiller, Counterdirectional mode coupling in ring resonators with QPM nonlinear crystals and effects on the characteristics of cw optical parametric oscillation, *Appl. Phys. B: Lasers Opt.*, 2010, **100**, 737–747.

17 A. Ostendorf, C. Zhang, M. Wilson, D. Offenberg, B. Roth and S. Schiller, Sympathetic Cooling of Complex Molecular Ions to Millikelvin Temperatures, *Phys. Rev. Lett.*, 2006, **97**, 243005.

18 A. Ostendorf, *Sympathetische Kühlung von Molekülionen durch lasergekühlte Bariumionenin einer linearen Paulfalle*, *PhD dissertation*, Heinrich-Heine-Universität Düsseldorf, 2006 (http://docserv.uni-duesseldorf.de/servlets/DocumentServlet?id = 3404).

19 D. Offenberg, *Studies of trapped, cooled ion ensembles*, *PhD dissertation*, Heinrich-Heine-Universität Düsseldorf, 2009 (http://docserv.uni-duesseldorf.de/servlets/DocumentServlet?id = 13566).

20 D. Offenberg, C. Zhang, Ch. Wellers, B. Roth and S. Schiller, Translational cooling and storage of protonated proteins in an ion trap at subkelvin temperatures, *Phys. Rev. A: At., Mol., Opt. Phys.*, 2008, **78**, 061401.

21 C. B. Zhang, *Production and sympathetic cooling of complex molecular ions*, *PhD Dissertation*, Heinrich-Heine-Universität Düsseldorf, 2008 (http://docserv.uni-duesseldorf.de/servlets/DocumentServlet?id = 9606).

22 L. Hornekær, *Single- and multi-species Coulomb ion crystals: Structures, dynamics and sympathetic cooling*, *PhD dissertation*, University of Århus, 2000.

23 M. Drewsen and A. Brøner, Harmonic linear Paul trap: Stability diagram and effective potentials, *Phys. Rev. A: At., Mol., Opt. Phys.*, 2000, **62**, 045401.

24 B. Roth, A. Ostendorf, H. Wenz and S. Schiller, Production of large molecular ion crystals *via* sympathetic cooling by laser-cooled $Ba^+$, *J. Phys. B: At., Mol. Opt. Phys.*, 2005, **38**, 3673–3685.

25 D. Berkeland, J. Miller, J. Bergquist, W. Itano and D. Wineland, Minimization of ion micromotion in a Paul trap, *J. Appl. Phys.*, 1998, **83**, 5025–5033.

26 S. Ishiuchi, M. Fujii, T. Robinson, B. Miller and H. Kjaergaard, Vibrational overtone spectroscopy of phenol and its deuterated isotopomers, *J. Phys. Chem. A*, 2006, **110**, 7345–7354.

27 M. J. Frisch, G. W. Trucks, H. B. Schlegel, G. E. Scuseria, M. A. Robb, J. R. Cheeseman, J. A. Montgomery, Jr., T. Vreven, K. N. Kudin, J. C. Burant, J. M. Millam, S. S. Iyengar, J. Tomasi, V. Barone, B. Mennucci, M. Cossi, G. Scalmani, N. Rega, G. A. Petersson, H. Nakatsuji, M. Hada, M. Ehara, K. Toyota, R. Fukuda, J. Hasegawa, M. Ishida, T. Nakajima, Y. Honda, O. Kitao, H. Nakai, M. Klene, X. Li, J. E. Knox, H. P. Hratchian, J. B. Cross, V. Bakken, C. Adamo, J. Jaramillo, R. Gomperts, R. E. Stratmann, O. Yazyev, A. J. Austin, R. Cammi, C. Pomelli, J. W. Ochterski, P. Y. Ayala, K. Morokuma, G. A. Voth, P. Salvador, J. J. Dannenberg, V. G. Zakrzewski, S. Dapprich, A. D. Daniels, M. C. Strain, O. Farkas, D. K. Malick, A. D. Rabuck, K. Raghavachari, J. B. Foresman, J. V. Ortiz, Q. Cui, A. G. Baboul, S. Clifford, J. Cioslowski, B. B. Stefanov, G. Liu, A. Liashenko, P. Piskorz, I. Komaromi, R. L. Martin, D. J. Fox, T. Keith, M. A. Al-Laham, C. Y. Peng, A. Nanayakkara, M. Challacombe, P. M. W. Gill, B. Johnson, W. Chen, M. W. Wong, C. Gonzalez and J. A. Pople, *GAUSSIAN 03 (Revision C.02)*, Gaussian, Inc., Wallingford CT, 2004.

28 R. Dunbar, Infrared radiative cooling of gas-phase ions, *Mass Spectrom. Rev.*, 1992, **11**, 309–339.

29 C. M. Western, , *PGOPHER, a Program for Simulating Rotational Structure*, University of Bristol, http://pgopher.chm.bris.ac.uk, retrieved May 9, 2011. We used the parameter *Intensity Units* = Arbitrary.

30 Y. Yamada, T. Ebata, M. Kayano and N. Mikami, Picosecond IR–UV pump–probe spectroscopic study of the dynamics of the vibrational relaxation of jet-cooled phenol. I. Intramolecular vibrational energy redistribution of the OH and CH stretching vibrations of bare phenol, *J. Chem. Phys.*, 2004, **120**, 7400.

31 Y. Yamada, Y. Katsumoto and T. Ebata, Picosecond IR-UV pump–probe spectroscopic study on the vibrational energy flow in isolated molecules and clusters, *Phys. Chem. Chem. Phys.*, 2007, **9**, 1170–1185.

32 I. Compagnon, J. Oomens, G. Meijer and G. von Helden, Mid-Infrared Spectroscopy of Protected Peptides in the Gas Phase: A Probe of the Backbone Conformation, *J. Am. Chem. Soc.*, 2006, **128**(11), 3592–3597.

# Appendix 3. Fundamental vibrational transition at 5.1 $\mu$m in HD$^+$

Advanced techniques for manipulation of internal states, standard in atomic physics, are demonstrated for a charged molecular species for the first time. We address individual hyperfine states of rovibrational levels of a diatomic ion by optical excitation of individual hyperfine transitions, and achieve controlled transfer of population into a selected hyperfine state. We use molecular hydrogen ions (HD$^+$) as a model system and employ a novel frequency-comb-based, continuous-wave 5 $\mu$m laser spectrometer. The achieved spectral resolution is the highest obtained so far in the optical domain on a molecular ion species. As a consequence, we are also able to perform the most precise test yet of the ab initio theory of a molecule.

The author contributed to: repair, improvement of the setup, perform experiments, data simulation, discussion of the results, writing the paper.

PRL **108,** 183003 (2012) PHYSICAL REVIEW LETTERS week ending 4 MAY 2012

# Manipulation of Individual Hyperfine States in Cold Trapped Molecular Ions and Application to $\mathrm{HD}^+$ Frequency Metrology

U. Bressel, A. Borodin, J. Shen, M. Hansen, I. Ernsting, and S. Schiller
*Institut für Experimentalphysik, Heinrich-Heine-Universität Düsseldorf, Universitätsstr. 1, 40225 Düsseldorf, Germany*

(Received 20 November 2011; published 3 May 2012)

Advanced techniques for manipulation of internal states, standard in atomic physics, are demonstrated for a charged molecular species for the first time. We address individual hyperfine states of rovibrational levels of a diatomic ion by optical excitation of individual hyperfine transitions, and achieve controlled transfer of population into a selected hyperfine state. We use molecular hydrogen ions ($\mathrm{HD}^+$) as a model system and employ a novel frequency-comb-based, continuous-wave 5 $\mu$m laser spectrometer. The achieved spectral resolution is the highest obtained so far in the optical domain on a molecular ion species. As a consequence, we are also able to perform the most precise test yet of the *ab initio* theory of a molecule.

DOI: 10.1103/PhysRevLett.108.183003 PACS numbers: 37.10.Pq, 33.15.Mt, 33.15.Pw, 42.50.Xa

Cold trapped molecules [1,2] currently represent an intense field of activity relying on sophisticated methods of molecule production, translational and internal cooling, spectroscopy and sensitive detection. Many applications, such as chemical reaction studies [3,4], tests of molecular quantum theory [5], fundamental physics [6,7] and quantum computing [8] would benefit strongly from the availability of advanced manipulation techniques, already standard in atomic physics. These are not straightforward for molecules, and for charged molecules have not been demonstrated yet. Production methods for molecular ions (usually, e.g., by electron impact ionization) and, if heteronuclear, their interaction with the blackbody radiation of the surrounding vacuum chamber, usually lead to significant population of a substantial number of internal states. A first, important step in the manipulation of internal states of molecular ions is population transfer between rotational states (heteronuclear molecules usually being cold vibrationally, i.e., are all in the $v = 0$ ground vibrational state). It has been demonstrated that a significant fraction (ca. 75%) of an ensemble of diatomic molecular ions can be pumped into the vibrational and rotational ground level ($v = 0$, $N = 0$) [9,10]; see Fig. 1.

For a general diatomic molecule, however, this pumping is usually not capable of preparing molecules in a single quantum state, because spin interactions generate a hyperfine structure with several states in each rovibrational level. For example, a diatomic molecule with one unpaired electron ($s_e = 1/2$), and nuclei with nuclear spins $I_1 = 1/2$ and $I_2 = 1$ (such as $\mathrm{HD}^+$) has 4 hyperfine states in zero magnetic field if the rotational angular momentum is $N = 0$, but 10 if $N = 1$, and 12 if $N \geq 2$; see Fig. 2(a). The ability to address selectively molecules in one particular hyperfine state (or even in a single quantum state with a particular magnetic quantum number $J_z$) and to transfer molecules from one hyperfine state to another are clearly important tools of a molecular quantum toolbox that can be part of a full quantum state preparation procedure.

Complicating the addressing, the number of strong transitions between two given rovibrational levels ($v$, $N$), ($v'$, $N'$) is equal to the larger of the two numbers of hyperfine states, i.e., potentially high, and with only small differences in transition frequency. Figure 2(b) shows as an example the case of the fundamental vibrational transition $(v = 0, N = 0) \rightarrow (v' = 1, N' = 1)$ in $\mathrm{HD}^+$, where 10 strong transitions occur over a range of about 60 MHz ([11,12]). Addressing a single hyperfine state in a multispin molecule thus requires a spectroscopy that can resolve individual hyperfine lines in the spectrum.

In this work, our approach is based on one-photon laser excitation of the fundamental vibrational transition $(0, 0) \rightarrow (1, 1)$ at the wavelength $\lambda_f$, see Fig. 1. The relatively low transition frequency, $\lambda_f > 2.5$ $\mu$m for diatomics, in combination with the low secular kinetic energy $k_B T_{\mathrm{sec}}$ achievable by sympathetic cooling, yields a Doppler broadening $\Delta\nu_D$ of the transitions that is smaller than many line spacings. This provides the desired quantum state selectivity for addressing some of the hyperfine states, using strong transitions. For our test case $\mathrm{HD}^+$, $\lambda_f = 5.1$ $\mu$m, $T_{\mathrm{sec}} \simeq 10$ mK, $\Delta\nu_D \simeq 3$ MHz. Additionally, excitation of weak transitions [which violate the approximate selection rules $\Delta F = 0$, $\Delta S = 0$, see Fig. 2(b)], provides selectivity for all hyperfine states, since for these transitions the frequency spacings are larger. Compared to the use of a pure rotational excitation $(0, 0) \rightarrow (0, 1)$ [13] or a microwave transition within a rovibrational level, the use of a vibrational transition has the advantage that the excitation may be followed by a much faster spontaneous decay from (1,1), either back into the ground rovibrational level (rate approx. 6 $\mathrm{s}^{-1}$) or into the relatively long-lived rotational level ($v'' = 0$, $N'' = 2$) (rate approx. 12 $\mathrm{s}^{-1}$). This allows reasonably rapid pumping of the molecule (possibly after repeated absorption and spontaneous emission events) into

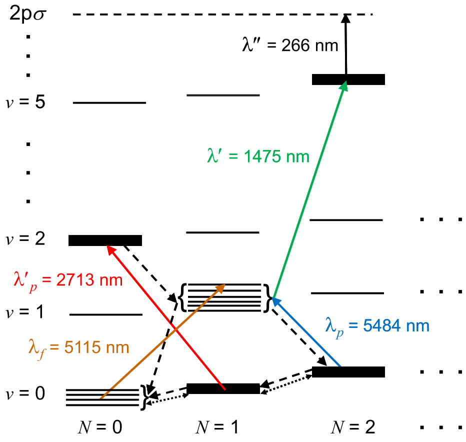

FIG. 1 (color online). Schematic energy level scheme of $HD^+$ with transitions relevant to this work. Hyperfine structure is shown schematically only for the $(v = 0,\ N = 0)$ and (1,1) levels as lines, but is implied for all other levels as well (thick bars). Full lines: laser-induced transitions, dashed lines: some relevant spontaneous emission transitions; dotted lines: some blackbody induced transitions. The spectrally narrow wave $\lambda_f$ selectively excites molecules from a particular hyperfine state $(v = 0, N = 0, F, S, J)$ to a single hyperfine state $(1,1, F', S', J')$ Quantum state preparation is performed by irradiating alternately the appropriately tuned waves $\lambda_f$ and $\lambda_p$, in conjunction with spontaneous emission from the level (1,1). Resonant laser radiation at $\lambda'$ and nonresonant radiation at $\lambda''$ is used to detect that hyperfine-state-selective excitation to the (1,1) level has occurred, by transferring the excited molecules to the electronically excited molecular state $2p\sigma$ from which they dissociate. Initially, rotational cooling is performed by radiation at $\lambda_p$ and $\lambda'_p$. The level energy differences are not to scale. The waves at $\lambda'$, $\lambda''$, $\lambda_p$, $\lambda'_p$, have large spectral linewidths and do not excite hyperfine state selectively.

another long-lived state, a necessary condition for efficient quantum state preparation, as shown below.

The experiment is performed on ensembles of $HD^+$ ions trapped in a linear quadrupole radio-frequency trap (14.2 MHz), sympathetically translationally cooled by co-trapped, laser-cooled Beryllium atomic ions [14] and rotationally cooled by lasers. The $HD^+$ molecule is of interest since it is a fundamental quantum system that allows precision measurements of QED effects and fundamental constants [5]. Our laser system consists of four subsystems: a $\lambda_f = 5.1\ \mu$m laser spectrometer referenced to an atomic frequency standard [15] (see Supplemental Materials [16]), a reliable, frequency-stabilized fiber-laser-based 313 nm laser for cooling of Beryllium ions [17], a rotational cooling laser system (a $\lambda_p = 5.5\ \mu$m quantum cascade laser and, for part of the measurements, a $\lambda'_p = 2.7\ \mu$m diode laser), and a pair of lasers $(\lambda, \lambda')$ for resonance-enhanced multiphoton dissociation (REMPD); see Fig. 1. Rotational cooling [9] is a crucial tool here, as it significantly increases the fractional population of molecules in the lower rovibrational level $(v = 0, N = 0)$, from ca. 10% to 60%–75%. The possibility provided by our laser system to measure the $HD^+$ fundamental vibrational transition frequency $f = c/\lambda_f$ also allows us to perform a precise comparison with the *ab initio* theory of the molecular hydrogen ion.

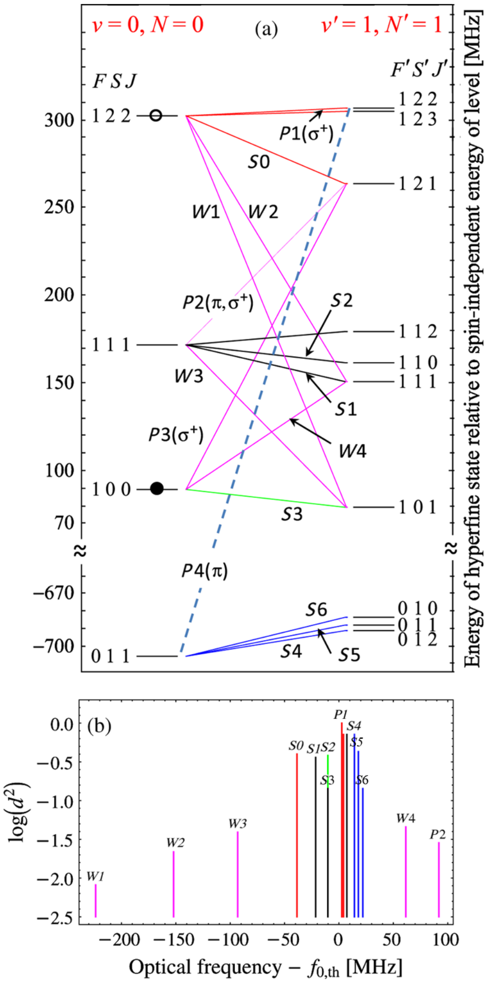

FIG. 2 (color online). (a) Energy diagram of the hyperfine states and main electric-dipole transitions in zero magnetic field. (b) Stick spectrum of the transitions (in zero magnetic field; values of the squared transition moment $d^2$ are normalized to the strongest transition). The states are labeled by the quantum numbers $(F, S, J)$. Weak transitions are shown in pink [12]. Very weak transitions are not shown, except for $P4$ (dashed). The "spin-independent" transition frequency $f_{0,\mathrm{th}}$ is the value if nuclear and electron spin were zero. $S0$, $S1$, $S2$, $S3$, $S4$, $S5$, $S6$, $W1$, $W2$, $W3$, $W4$, $P2$ are transitions studied here ("$W$, $S$, $P$" mean "weak", "strong", and "pumping", respectively). All were observed except $S4$. $W1$, $W3$ are the transitions used here to achieve population transfer from the hyperfine states $(v = 0,\ N = 0,\ F = 1,\ S = 2,\ J = 2,\ J_z)$ (empty circle) and $(0,0,1,1,1,J'_z)$ into the hyperfine state $(0,0,1,0,0,J''_z)$ (filled circle). $P1$, $P2$, $P3$, and $P4$ are proposed optical pumping transitions (with indicated polarizations) for preparation of the molecule in the single quantum state $(0, 0, 1, 2, 2, J_z = +2)$ (one of the Zeeman states in the open circled hyperfine state).

Hyperfine-resolved rovibrational transitions are induced by the $\lambda_f = 5.1$ $\mu$m radiation tuned precisely to individual transitions. We then detect (without hyperfine-state selectivity) the population of the goal vibrational level ($v' = 1, N' = 1$), by $1 + 1'$ resonance-enhanced multiphoton dissociation (REMPD) [18]; see Fig. 1. Together, this represents a three-photon ($1 + 1' + 1$”) REMPD process. The reduction of the HD$^+$ number by the REMPD process is our spectroscopic signal [18].

Figure 3 shows the obtained hyperfine-state resolved spectrum. All theoretically predicted and addressed hyperfine transitions were observed; only the (nominally strong) transition *S*4 is barely detected, for unknown reason. Transition *W*4, which originates from a lower hyperfine state with only a small fractional population ($J = 0$, thus statistically containing only 5%–6% of all molecules), could only be made clearly evident using a preceding hyperfine pumping step (see below). Each of the 4 hyperfine states of the lower level was selectively addressed, and 5 of the 12 upper level hyperfine states were selectively populated. We also observed the line at −10.2 MHz, which contains two nearly coinciding transitions *S*2 and *S*3, but originating from different ground hyperfine states. The remaining strong transitions (including the line marked *P*1 in Fig. 2) were also observed, but their small spacing prevents complete resolution, and they are not reported in the Fig. 3.

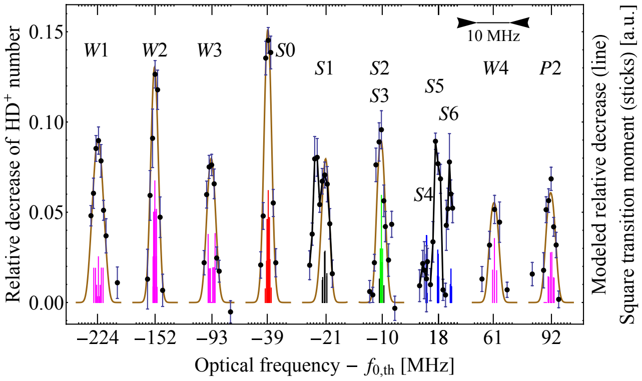

FIG. 3 (color online). Observed hyperfine spectrum of the ($v = 0, N = 0$) → (1, 1) fundamental rovibrational transition in cold trapped HD$^+$ ions. The effective intensity times irradiation duration product of the 5.1 $\mu$m radiation varied from line to line, and was adapted to avoid saturation. Brown lines are the result of fitting $f_{0,\text{exp}}$, the individual line amplitudes, the Doppler temperature (9.5 mK) and the average magnetic field (0.8 G). The sticks are for illustration purpose and show the theoretical squared transition dipole moments for the Zeeman components at 0.8 G, assuming exciting radiation polarized at 45° to the magnetic field. They are scaled by different factors for presentation purpose. Color coding is as in Fig. 2. *S*4, *S*6 were taken at high intensity-irradiation time product, *S*5 at a lower value. The side peak of *S*1 is probably due to an ion micromotion sideband of *S*2/*S*3. The *W*4 line required hyperfine-state optical pumping for its detection (see Fig. 4).

We demonstrate hyperfine-state manipulation by optical pumping of individual hyperfine-state populations into a goal state. As a goal state we choose ($v = 0$, $N = 0$, $F = 1$, $S = 0$, $J = 0$, $J_z = 0$) which is nondegenerate ($J = 0$) and thus a single quantum state (filled circle in Fig. 2). After rotational cooling, we apply the following sequence twice: *W*1 line (3 s), rotational repumping ($\lambda_p$ and $\lambda_p'$ simultaneously for 5 s), *W*3 line (3 s). A final 10 s of rotational repumping is performed before the spectroscopic excitation. The *W*1 and *W*3 transitions excite population from two initial hyperfine states (0, 0, 1, 2, 2, $J_z$), (0, 0, 1, 1, 1, $J_z'$) (without $J_z$ selectivity) into the state (1, 1, 1, 0, 1, $J_z''$). This state has dominant spontaneous decay to the goal state (green line *S*3 in Fig. 2). We find clear evidence that this hyperfine-state preparation is taking place by observing the transition *W*4 starting from the goal state by REMPD; see Fig. 4. This transition is not observable in our experiment without the preparation procedure, since then the population in the lower hyperfine state is too low.

Our hyperfine-state resolved spectrum represents the highest-resolution optical spectrum of any molecular ion so far [5,19,20]. This enables an accurate comparison of experimental frequencies with *ab initio* theory. We

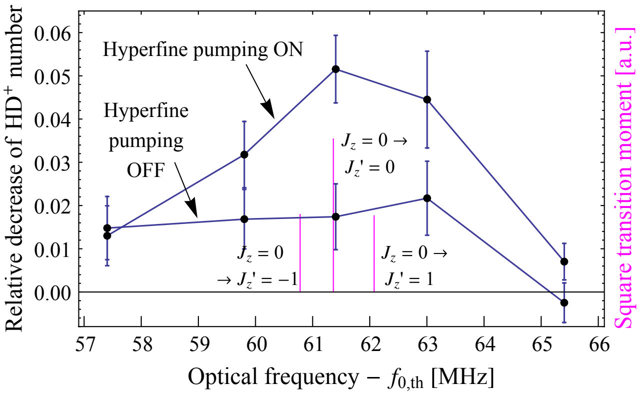

FIG. 4 (color online). Demonstration of hyperfine-state manipulation. The transition *W*4 shown here is observed only when hyperfine optical pumping is implemented. This transition represents the excitation from a single quantum state, (0,0,1,0,0,$J_z = 0$). Data shown were taken alternating measurements preceded by hyperfine optical pumping (upper data points joined by line) and not (lower data points). The intensity of the 5.1 $\mu$m laser radiation was set to its maximum both during hyperfine pumping on the *W*1 and *W*3 transitions and subsequent detection of the *W*4 transition. Irradiation time on the *W*4 transition was 3 s. Rotational cooling by the 2.7 $\mu$m and 5.5 $\mu$m laser was used. The zero level corresponds to the relative decrease measured when the 5.1 $\mu$m spectroscopy laser was blocked. The three sticks show, for illustration purposes, the theoretical transition frequencies and strengths in a 0.8 G magnetic field and radiation polarized at 45° to the magnetic field. The shift of the central component is −0.05 MHz relative to the zero-field frequency.

obtain two hyperfine-state separations in the ground state, $\Delta f_{0,0,a} = (E(0,0,1,2,2) - E(0,0,1,1,1))/h$ and $\Delta f_{0,0,b} = (E(0,0,1,1,1) - E(0,0,1,0,0))/h$, from the measured transition frequency combinations $f(S1) - f(W2)$, $f(W3) - f(W1)$, $f(P2) - f(S0)$, and from $f(W4) - f(S1)$, $f(P3) - f(P2)$, respectively. In addition, two excited state splittings, $\Delta f_{1,1,c} = (E(1,1,1,2,1) - E(1,1,1,1,1))/h$ and $\Delta f_{1,1,d} = (E(1,1,1,1,1) - E(1,1,1,0,1))/h$ are similarly obtainable by suitable frequency combinations. A fit of these hyperfine-state separations to the data (fitting also the spin-independent frequency) yields agreement with the *ab initio* results $(\Delta f_{0,0,a}, \Delta f_{0,0,b}, \Delta f_{1,1,c}, \Delta f_{1,1,d}) = (130.60(1), 82.83(1), 113.33(1), 71.68(1))$ MHz [11,21], with deviations (experimental minus theoretical) of $(-0.22(0.13), 0.28(0.38), -0.13(0.15), 0.27(0.19))$ MHz. The values in inner parentheses being the experimental uncertainties. The two measured hyperfine separations of the ground state also allow determining the two hyperfine constants $E_4(0,0)$, $E_5(0,0)$ [11] which fully describe the hyperfine structure of the ground state [12]. Our fit yields $(E_4(0,0), E_5(0,0)) = (906(17), 142.33(25))$ MHz, whereas the theory values are $(925.38(1), 142.29(1))$ MHz [11,21].

Assuming instead that the hyperfine energies are given by the theoretical values (this assumption being strengthened by the agreement of hyperfine theory and experiment for large-$v$ levels [11,22]), we can fit an overall frequency correction to the spectra $W1$, $W2$, $W3$, $S0$, $S1$, $S2 + S3$, $W4$, $P2$. We obtain the spin-independent frequency $f_{0,\mathrm{exp}} = 586\,050\,52.00$ MHz, with combined statistical and systematic error of 0.064 MHz (see Supplemental Material [16]). The theoretical value is $f_{0,\mathrm{th}} = 586\,050\,52.139(11)(21)$ MHz, where the first error is due to the uncertainty of the fundamental constants and the second is the theoretical error in the evaluation of the QED contributions [21,23,24]. The difference between experimental and theoretical results is $-2.0$ times the combined theoretical plus experimental error. The relative experimental uncertainty of $1.1 \times 10^{-9}$ represents the most accurate test of molecular theory to date. In particular, our measurement is the first molecular measurement sufficiently accurate to be explicitly sensitive to the QED contributions of order $\alpha^5$ (relative to the nonrelativistic contribution to the transition frequency), calculated as 0.109(21) MHz for the transition studied here [21,24].

Based on the technique demonstrated here, we can propose a realistic optical pumping procedure for preparing most of the population in a single quantum state ($v$, $N$, $F$, $S$, $J_z$), i.e., with well-defined projection of the total angular momentum. Under typical conditions, the relative statistical occupation of any individual quantum state in $(v = 0, N = 0)$ is only $\simeq (1/12) \times (60\%–75\%) \simeq 5\%–6\%$ under rotational cooling by a single laser ($\lambda_p$) or two lasers ($\lambda_p$, $\lambda'_p$). Exciting sequentially the four transitions $P4$ $[(0,0,0,1,1) \rightarrow (1,1,1,2,2)]$, $P3$, $P2$, $P1[(0,0,1,2,2) \rightarrow (1,1,1,2,3)]$ in a weak magnetic field and with polarizations chosen as indicated in Fig. 2(a) will cause transfer of the population of all Zeeman quantum states of (0, 0) to the single Zeeman quantum state $(0, 0, 1, 2, 2, J_z = +2)$, via spontaneous emission processes from $(1, 1, 1, 2, J' = \{1, 2\}, J'_z)$, which dominantly occur on strong transitions [red lines in Fig. 2(a)]. These excitations should be interleaved with rotational cooling (lasers $\lambda_p$, $\lambda'_p$), which also serves as repumper following spontaneous decay into $(v'' = 0, N'' = 2)$. The optical pumping procedure should take a few ten seconds and lead to 60%–70% fractional population in the goal state.

In summary, we have shown that it is possible to address and prepare individual hyperfine states in cold, trapped diatomic molecular ions even in presence of a complex spin structure. A midinfrared laser spectrometer controlled by an atomic standard-referenced frequency comb, and sufficiently low ion kinetic energies were two important aspects. The observed, Doppler-limited, transition linewidths (3 MHz) are the lowest obtained to date on a molecular ion species in the optical domain [note that they scale as (molecule mass)$^{-1/2}$]. We also observed, for the first time to our knowledge, weakly allowed hyperfine transitions using optical excitation. As one application, we were able to directly determine the population fraction of molecules, in particular, hyperfine states. The largest value we found was 19%, clearly indicating the effectiveness of our rotational cooling. We also demonstrated excitation of a transition from a single quantum state. Since our test molecule HD$^+$ is the simplest heteronuclear molecule and is excited from the rovibrational ground state, this study represents the first precision measurement of the most fundamental electric-dipole allowed rovibrational transition of any molecule [19]. A comparison of theory with experiment showed that (i) the hyperfine energies of small-$v$, $N$ rovibrational levels agree within deviations of less than 0.3 MHz and (ii) the spin-independent energy agrees within 2 times the relative error of $1.1 \times 10^{-9}$.

We are grateful to B. Roth, T. Schneider, A. Yu. Nevsky, and S. Vasilyev for help and support, and to V. Korobov for important discussions. Funding was provided by DFG project Schi 431/11-1.

---

[1] *Cold Molecules*, edited by R. Krems, B. Friedrich, and W. C. Stwalley (CRC Press, Boca Raton, 2009).

[2] *Low Temperatures and Cold Molecules*, edited by I. W. M. Smith (World Scientific Publishing, Singapore, 2008).

[3] B. Roth, P. Blythe, H. Wenz, H. Daerr, and S. Schiller, Phys. Rev. A **73**, 042712 (2006).

[4] P. F. Staanum, K. Højbjerre, R. Wester, and M. Drewsen, Phys. Rev. Lett. **100**, 243003 (2008).

[5] J. C. J. Koelemeij, B. Roth, A. Wicht, I. Ernsting, and S. Schiller, Phys. Rev. Lett. **98**, 173002 (2007).

[6] S. Schiller and V. Korobov, Phys. Rev. A **71**, 032505 (2005).
[7] H. Müller *et al.*, Phys. Rev. A **70**, 076004 (2004).
[8] D. DeMille, Phys. Rev. Lett. **88**, 067901 (2002).
[9] T. Schneider, B. Roth, H. Duncker, I. Ernsting, and S. Schiller, Nature Phys. **6**, 275 (2010).
[10] P. Staanum, K. Højbjerre, P. S. Skyt, A. K. Hansen, and M. Drewsen, Nature Phys. **6**, 271 (2010).
[11] D. Bakalov, V. I. Korobov, and S. Schiller, Phys. Rev. Lett. **97**, 243001 (2006).
[12] D. Bakalov, V. I. Korobov, and S. Schiller, J. Phys. B **44**, 025003 (2011).
[13] J. Shen, A. Borodin, M. Hansen, and S. Schiller, Phys. Rev. A **85**, 032519 (2012).
[14] P. Blythe, B. Roth, U. Fröhlich, H. Wenz, and S. Schiller, Phys. Rev. Lett. **95**, 183002 (2005).
[15] U. Bressel, I. Ernsting, and S. Schiller, Opt. Lett. **37**, 918 (2012).
[16] See Supplemental Materials at http://link.aps.org/supplemental/10.1103/PhysRevLett.108.183003 for details.
[17] S. Vasilyev, A. Nevsky, I. Ernsting, M. Hansen, J. Shen and S. Schiller, Appl. Phys. B **103**, 27 (2011).
[18] B. Roth, J. C. J. Koelemeij, H. Daerr, and S. Schiller, Phys. Rev. A **74**, 040501-4 (2006).
[19] The $(0, 1) \leftrightarrow (1, 0)$ transition has been measured in an ion beam experiment, with a linewidth $\geq 7$ MHz and a frequency uncertainty $\simeq 21$ MHz, W. H. Wing *et al.*, Phys. Rev. Lett. **36**, 1488 (1976); J. J. Spezeski, Ph.D. dissertation, Yale University, 1977.
[20] H. C. Miller, M. Al-Za'al, and J. W. Farley, Phys. Rev. Lett. **58**, 2031 (1987).
[21] V. I. Korobov, (private communication).
[22] A. Carrington, I. R. McNab, C. A. Montgomerie-Leach, and R. A. Kennedy, Mol. Phys. **72**, 735 (1991).
[23] V. I. Korobov, Phys. Rev. A **74**, 052506 (2006).
[24] V. I. Korobov, Phys. Rev. A **77**, 022509 (2008).

# Appendix 4. Pure rotational transition at 1.3 THz in $HD^+$

We demonstrate rotational excitation of molecular ions that are sympathetically cooled by laser-cooled atomic ions to a temperature as low as approximately 10 mK. The molecular hydrogen ions $HD^+$ and the fundamental rotational transition $(v = 0,\ N = 0) \rightarrow (v = 0,\ N = 1)$ at 1.3 THz, the most fundamental dipole-allowed rotational transition of any molecule, are used as a test case. This transition has not been observed before. Rotational laser cooling was employed in order to increase the signal, and resonance-enhanced multiphoton dissociation was used as detection method. The black-body-radiation-induced rotational excitation is also observed. The extension of the method to other molecular species is briefly discussed.

The author contributed to: repair and modification of the setup, preliminary experiments, results discussion, writing the paper.

PHYSICAL REVIEW A **85**, 032519 (2012)

# Observation of a rotational transition of trapped and sympathetically cooled molecular ions

J. Shen, A. Borodin, M. Hansen, and S. Schiller
*Institut für Experimentalphysik, Heinrich-Heine-Universität Düsseldorf, 40225 Düsseldorf, Germany*

(Received 16 January 2012; published 29 March 2012)

We demonstrate rotational excitation of molecular ions that are sympathetically cooled by laser-cooled atomic ions to a temperature as low as approximately 10 mK. The molecular hydrogen ions $HD^+$ and the fundamental rotational transition $(v = 0, N = 0) \rightarrow (v' = 0, N' = 1)$ at 1.3 THz, the most fundamental dipole-allowed rotational transition of any molecule, are used as a test case. This transition has not been observed before. Rotational laser cooling was employed in order to increase the signal, and resonance-enhanced multiphoton dissociation was used as detection method. The black-body-radiation-induced rotational excitation is also observed. The extension of the method to other molecular species is briefly discussed.

DOI: 10.1103/PhysRevA.85.032519 PACS number(s): 33.20.Bx

## I. INTRODUCTION

High-resolution laboratory rotational spectroscopy of molecules is an important and very well-developed technique in molecular physics. It has provided extensive data on and insight into the structure and dynamics of molecules and has several applications, including the identification of molecular species in interstellar clouds. In the recent past, the accessible spectral region has been extended from the microwave region to the terahertz (submillimeter wavelength) region, thanks to the development of appropriate terahertz radiation sources attaining useful power levels. Continuous-wave, narrow-linewidth terahertz radiation, suitable for high-resolution molecular spectroscopy, is available from backward-wave oscillators or via frequency upconversion using Schottky diodes [1,2] or semiconductor superlattices [3,4].

The resolution of rotational spectroscopy has been increased beyond the Doppler limit by several techniques, such as molecular beams [5], velocity-class selection [6], Lamb-dip spectroscopy, and two-photon spectroscopy [7]. For example, sub-Doppler spectral lines with widths of approximately 15 kHz around 100 GHz [8] and 30–40 kHz at 0.7–1 THz [9,10] have been reported. However, the resolution of such methods is limited by transition time broadening and/or pressure broadening. In order to eventually overcome these limitations, it is interesting to explore a fundamentally different regime: trapping cold (<1 K) molecules in an interaction-free (ultra-high-vacuum) environment and localization to submillimeter extension. Then, transition time broadening and pressure broadening, as well as Doppler broadening, may be strongly reduced or even eliminated altogether. This regime may be reached with cold neutral molecules stored in e.g. optical traps or with cold molecular ions in radio-frequency traps. The production methods of cold molecules have been reviewed elsewhere; see, for example, Refs. [11,12].

In this work, we take a step toward applying high-resolution rotational spectroscopy on cold molecules: we demonstrate rotational excitation on sympathetically cooled and strongly confined molecular ions, using here secular temperatures as low as 10–15 mK. Our spectroscopic technique is a destructive one, resonance-enhanced multiphoton dissociation (REMPD). The particular implementation used here is $1 + 1' + 1''$ REMPD, where the molecule absorbs sequentially three photons of different energies. In our work, the transitions induced by each photon corresponds to the three main energy scales of a molecule: rotational (here ca. 1 THz), vibrational (here: overtone, ca. 200 THz), and electronic (ca. 1100 THz).

With respect to the temperature of the ions and the detection method, our work is complementary to the recent demonstration of terahertz rotational spectroscopy of trapped, helium-buffer-gas-cooled $H_2D^+$ and $D_2H^+$ ions at kinetic ion temperatures of approximately 24 K, where Doppler broadening is limiting the linewidth to approximately 1 MHz [13].

## II. THE $HD^+$ MOLECULE AND THE SPECTROSCOPIC TECHNIQUE

The molecule we consider here, $HD^+$, is the most fundamental molecule with electric dipole-allowed rotational transitions [14]. Its potential as a test system for molecular quantum mechanics and for novel fundamental physics studies has been described previously [14–19]. Vibrational spectroscopy of sympathetically cooled $HD^+$ with the highest resolution of any molecular ion to date has recently been reported by us [20]. Pure rotational transitions have so far been observed only for the last and penultimate vibrational levels, $v = 21, 22$, close to the dissociation limit [21,22], where their $N = 0 \rightarrow N' = 1$ transition frequencies lie in the microwave range (ca. 50 and 9.4 GHz, respectively). Here we report on the rotational transition in the $v = 0$ ground vibrational level, at much higher frequency. The rovibrational transition frequencies have been calculated *ab initio* with high precision [18,19], greatly facilitating the experimental search. The $(v = 0, N = 0) \rightarrow (v' = 0, N' = 1)$ fundamental rotational transition studied here occurs at $f_{0,\,\mathrm{theor}} =$ 1 314 925.752 MHz ("spinless" value, i.e., excluding hyperfine energy contributions), with an estimated theoretical error of approximately 2 kHz [23]. The $f_{0,\,\mathrm{theor}}$ value includes (among others) a contribution of approximately 48.8 MHz from relativistic effects (order $\alpha^2$) and approximately −9.4 MHz from QED effects of order $\alpha^3$.

An important aspect of this work is the use of laser rotational cooling [24]; see Fig. 1. It is used to transfer most of the molecular population, initially distributed among several rotational levels in $v = 0$, into the rovibrational ground state $(v = 0, N = 0)$ and it also empties the spectroscopy target state $(v' = 0, N' = 1)$. It modifies the difference in fractional population of the lower and upper spectroscopy levels, from

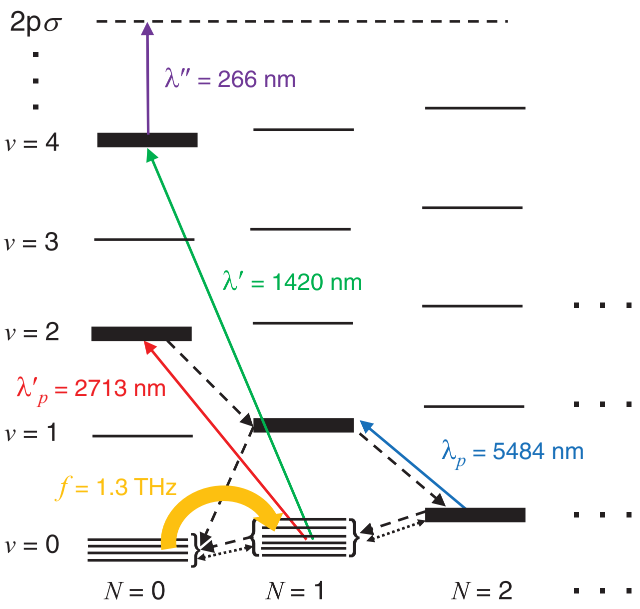

FIG. 1. (Color online) Simplified energy level scheme of HD$^+$ with transitions relevant to this work. Full thin arrows, laser-induced transitions; dashed arrows, some relevant spontaneous emission transitions; and dotted double arrows, some relevant black-body-radiation-induced transitions. The terahertz wave (thick arrow) is tuned so that the four hyperfine states in $(v = 0, N = 0)$ are excited to corresponding hyperfine states in $(v' = 0, N' = 1)$. Resonant laser radiation at $\lambda'$ (1420 nm) and nonresonant radiation at $\lambda''$ (266 nm) transfer the rotationally excited molecules to a vibrationally excited level $(v'' = 4, N'' = 0)$ and then further to electronically excited molecular states (predominantly 2p$\sigma$), from which they dissociate. Rotational cooling is performed by radiation at $\lambda_p$ (5.5 $\mu$m) and $\lambda'_p$ (2.7 $\mu$m). The level energy differences are not to scale. Hyperfine structure is indicated very schematically for the levels $(v = 0, N = 0, 1)$ and as thick lines for some other participating levels. The waves at $\lambda'$, $\lambda''$, $\lambda_p$, $\lambda'_p$ have relatively large spectral linewidths.

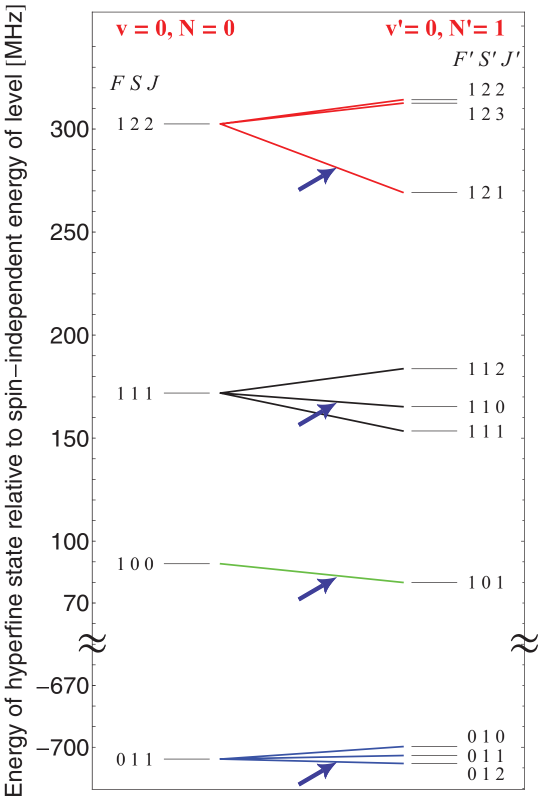

FIG. 2. (Color online) Energy diagram of the hyperfine states and main electric-dipole transitions in zero magnetic field. Left side, rovibrational ground level $(v = 0, N = 0)$; right side, rotationally excited level $(v' = 0, N' = 1)$. The hyperfine states are labeled by the (in part approximate) quantum numbers $(F, S, J)$. The degeneracy factor of each hyperfine state is $(2J + 1)$. Transitions that do not change the quantum numbers $F, S$ are relatively strong and are indicated, starting from the top of the figure, by red, black, green, and blue lines. The four transitions addressed consecutively in this work are indicated by arrows.

approximately −0.15 in thermal equilibrium to approximately 0.7, and thus significantly increases the detectable signal.

The hyperfine structure and the Zeeman effect of the lower and upper rovibrational levels are important aspects in the rotational spectroscopy [25,26]. As Fig. 2 shows, the ground state possesses four hyperfine states and 12 magnetic substates (with magnetic quantum number $J_z$). In the region occupied by the ions in our apparatus, the magnetic field is nonzero, lifting the magnetic degeneracy. The spectrum contains a large number of transitions with relatively large transition dipole moments; see Fig. 3. Most transitions, even the $\Delta J_z = 0$ ones, shift by approximately 100 kHz or more in a field of strength 1 G. Exceptions include five (strong) $J_z = 0 \rightarrow J'_z = 0$ transitions, whose quadratic Zeeman shifts in 1 G are at most 6.2 kHz in absolute value [26]. From each lower hyperfine state there is at least one such transition; the state $(F = 0, S = 1, J = 1, J_z = 0)$ has two. Three of them are indicated by the first, third, and fourth arrows (from the top) in Fig. 2. A fourth is the hyperfine transition $(F = 1, S = 1, J = 1, J_z = 0) \rightarrow (F' = 1, S' = 1, J' = 2, J'_z = 0)$. Its transition frequency $f = f_{0,\,\text{theor}} + 11.78$ MHz is close to other transition frequencies and is therefore not considered suitable for the present work. Instead, we use the $(F = 1, S = 1, J = 1, J_z = 0) \rightarrow (F' = 1, S' = 1, J' = 0, J'_z = 0)$ transition (second arrow from the top in Fig. 2), which, however, exhibits a much larger quadratic Zeeman effect (78 kHz at 1 G). The magnetic field in the trap region is not spatially constant in direction and magnitude, so some line broadening can be expected.

The theoretical Doppler linewidth, considering only secular motion, is approximately 55–70 kHz for the lowest temperatures used here (10–15 mK) and approximately 150–200 kHz if the ion ensemble is in the liquid state (100–200 mK). Note that the values are relatively large due to the low mass of the HD$^+$ ion. At 10–15 mK, the molecular ions are well confined along the axis of the trap and their motion in transverse direction is restricted to a range smaller than the terahertz wavelength (0.23 mm). In the axial direction, the confinement is not as strong, since diffusive motion of the ions is still occurring along the crystal axis, which exceeds in length (ca. 1.5 mm) the terahertz wavelength. Thus, Doppler broadening may still be present in our experiment, even at the lowest temperatures. The terahertz source [27] has a linewidth below

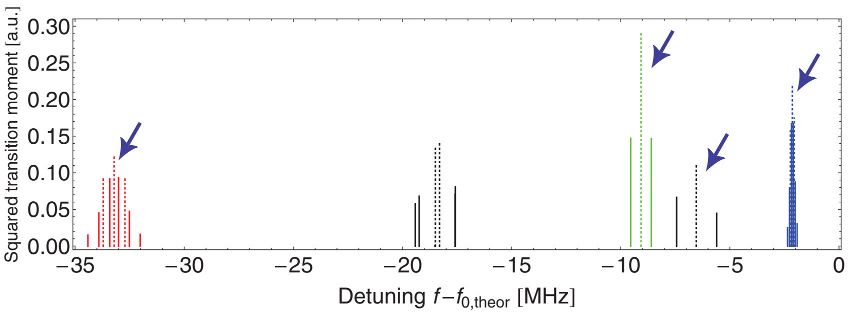

FIG. 3. (Color online) Section of the theoretical stick spectrum of the rotational transition in the frequency range relevant to this work, showing the Zeeman splittings and shifts in a 1 G magnetic field. Dashed lines are $\pi$ transitions; full lines are $\sigma$ transitions. $f_{0,\,\mathrm{theor}}$ is the theoretical "spinless" transition frequency. The four terahertz frequencies of list A (see Table I) are indicated by the arrows. The colors used correspond to those used in Fig. 2.

100 Hz and subhertz absolute frequency stability, values that are not relevant in comparison to other line-broadening effects.

The Doppler linewidth is smaller than the typical spacing between hyperfine transitions originating from different ground hyperfine states, even in the presence of a magnetic field on the order of 1 G. This is in principle advantageous, since it could permit resolution of the hyperfine structure. However, detecting individual hyperfine lines would also lead to a small signal-to-noise ratio: The individual hyperfine levels each contain only a fraction of the total population. If a statistical population distribution were produced by action of the black-body radiation field (BBR) and of the rotational cooling lasers, each substate would contain 1/12 of the total population, this fraction being typically 20 to 30 molecules. The individual populations are likely to vary significantly in time, requiring the collection of substantial data and averaging. We do not attempt to do so here and in order to obtain a sufficiently strong rotational excitation signal we have applied the following strategy.

We irradiate the molecules sequentially on terahertz frequencies corresponding to strong hyperfine transitions. Different frequency sets are used; see Table I. Each frequency from a set is irradiated for 200 ms and is meanwhile frequency-modulated by ±2 kHz at a 5 Hz rate. The list is repeated several times for a total of 3 s or more, depending of the excitation approach used.

The frequency lists include three of the five above mentioned low-Zeeman-shift $J_z = 0 \rightarrow J_z' = 0$ transitions, which originate from three of the four hyperfine states of $(v = 0, N = 0)$, and the respective frequency values have been chosen to correspond to an assumed magnetic field of 1 G. As mentioned above, the chosen transition starting from the fourth hyperfine state $(F = 1, S = 1, J = 1)$ has a substantial quadratic Zeeman effect. We therefore attempt to compensate for the lack of precise knowledge of the magnetic field distribution by exciting at four distinct frequencies, corresponding to the shifts induced by the magnetic field values 0.25, 0.5, 0.75, and 1 G (the detuning for 0 G is −6.617 MHz). Altogether, this list of frequencies (denoted by $A'$; see Table I) should nominally excite four of the twelve Zeeman substates. However, in the presence of a significant Doppler broadening, more substates (with larger Zeeman shifts) will be addressed. Indeed, the frequencies necessary to excite all Zeeman substates of the ground hyperfine states fall into ranges of approximately ±0.5, ±1, 0, ±0.22 MHz at 1 G, relative to the frequencies of the list $A'$. These spreads have a partial overlap with the Doppler broadening at the higher molecular temperatures (100–200 mK) employed here.

In order to obtain information about the detuning dependence of the rotational excitation, we also apply "detuned-frequency lists." Lists labeled $B$ and $C$ are detuned to smaller and larger frequencies, respectively, relative to list $A'$ (relative detunings of list $B$: −1.782, −1.311, −0.704, −0.327 MHz, relative detunings of list $C$: 1.803, 1.443, 0.714, 0.326 MHz). The detunings are larger than the shift induced by the Zeeman effect in a 1 G field. Lists $D$ and $E$ have relative detunings approximately half as large as those of lists $B$ and $C$, respectively (list $D$: −0.891, −0.655, −0.352, −0.163 MHz, list $E$ : 0.901, 0.722, 0.357, 0.163 MHz). Finally, list $A$ is also used, which is a simplified version of list $A'$. Frequency modulation is used in all cases.

## III. EXPERIMENTAL APPARATUS AND PROCEDURE

A schematic of our apparatus [28] is shown in Fig. 4. The ultra-high vacuum (UHV) chamber houses a linear ion trap driven at 14.2 MHz. HD gas is loaded into the chamber by opening a piezoelectric valve, after which it is ionized by an

TABLE I. Frequency lists used for excitation of the rotational transition. $f_i$ is the terahertz frequency.

| | Frequency $f_i - f_{0,\,\mathrm{theor}}$ (MHz) | | | | | | |
|---|---|---|---|---|---|---|---|
| Lower hyperfine level ($F$, $S$, $J$) | (1,2,2) | (1,1,1) | | | | (1,0,0) | (0,1,1) |
| List $A'$ | −33.211 | −6.597 | −6.578 | −6.558 | −6.539 | −9.069 | −2.138 |
| List $A$ | −33.211 | −6.539 | | | | −9.069 | −2.138 |
| List $B$ | −34.993 | −7.850 | | | | −9.773 | −2.465 |
| List $C$ | −31.408 | −5.096 | | | | −8.355 | −1.812 |
| List $D$ | −34.102 | −7.194 | | | | −9.421 | −2.301 |
| List $E$ | −32.310 | −5.817 | | | | −8.712 | −1.975 |
| 500-MHz detuning | 500 | | | | | | |

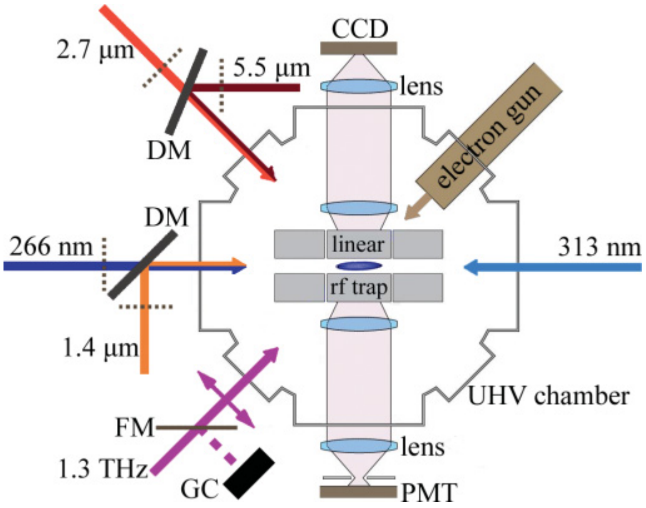

FIG. 4. (Color online) Schematic of the apparatus and beams. GC, Golay cell; FM, flip mirror; DM, dichroic mirror; and dotted lines, electrically controlled laser beam shutters. The double arrow indicates the polarization of the terahertz wave. Not to scale.

electron gun. The laser radiation for REMPD enters from the left and the 313 nm cooling radiation [29] enters from the right. The rotational cooling radiation enters diagonally. The terahertz source is positioned close to the vacuum chamber and its wave is focused into the chamber center by a concave paraboloidal mirror oriented at right angle to the beam. With a manual flip mirror, the wave can be sent to a Golay cell detector for power-monitoring purposes. The terahertz source has been described previously [27]. It is driven at the 72nd subharmonic of the desired frequency, near 18 GHz. This signal is provided by a microwave synthesizer, which is frequency locked to a global positioning system (GPS)-referenced hydrogen maser. The first REMPD laser is a diode laser emitting at the wavelength $\lambda = 1420$ nm and exciting the $(v = 0, N = 1) \rightarrow (v' = 4, N' = 0)$ transition. The second REMPD laser excitation is nonresonant and is provided by a resonantly frequency-doubled 532 nm laser. Initially, a $\mathrm{Be}^+$ ion crystal is produced in the trap. Typically, the same $\mathrm{Be}^+$ ion crystal is used for several hours of experimentation.

The molecular sample preparation routine starts by frequency stabilization of the cooling laser to a frequency a few tens of MHz to the red of the frequency for optimal $\mathrm{Be}^+$ cooling, using a hyperfine transition of molecular iodine as reference. Then, a small amount of HD gas is let into the chamber and ionized by the electron gun. Both $\mathrm{HD}^+$ ions as well as heavy impurity ions are generated, trapped, and quickly sympathetically cooled. In order to remove these impurity ions, the DC quadrupole potential is briefly increased, reducing the quasipotential strength in one transverse direction. The heavy ions then escape from the trapping region. This ends the preparation procedure; the produced cold $\mathrm{HD}^+$ sample contains typically approximately 300 molecules.

The acquisition of one data point proceeds as follows: (i) The terahertz excitation is initially effectively kept off by detuning the frequency by 500 MHz from the rotational resonance, and the REMPD lasers are also blocked. (ii) The rotational cooling laser beams are unblocked, and a repeated secular frequency scan (740–900 kHz) is activated and kept on during the remainder of the measurement cycle (method I). The heating of the molecular ions heats the $\mathrm{Be}^+$ ions sympathetically and spectrally broadens their 313 nm absorption line. This leads to a substantial increase of the cooling-laser-stimulated atomic fluorescence, due to the laser's relatively large detuning from atomic resonance. The fluorescence signal level is indicative of the initial number of $\mathrm{HD}^+$ in the ion ensemble. (iii) For a duration $T_c = 35$ s, the rotational cooling takes place, after which the 2.7 $\mu$m rotational cooling laser is blocked (not the 5.5 $\mu$m laser). (iv) The REMPD lasers are unblocked and simultaneously the terahertz frequency scan is initiated. The resulting molecule loss reduces the heating and thus the atomic fluorescence signal. (v) The change in fluorescence as a function of time is followed until the signal essentially reaches the level in the absence of molecules. (Figure 5 displays the first 60 s only.) The secular excitation is kept on all the time. This concludes acquisition of one data point.

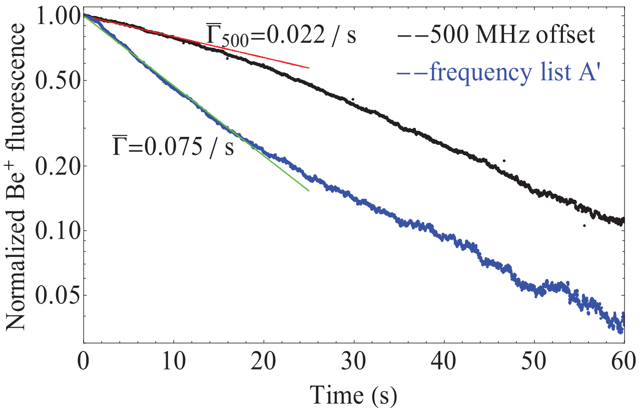

FIG. 5. (Color online) Atomic fluorescence signal during continuous secular excitation of the $\mathrm{HD}^+$ ions (method I, liquid state). The time axis starts after the 2.7 $\mu$m rotational cooling laser is turned off and the two REMPD lasers and terahertz radiation are turned on. The upper (black) trace, where the terahertz radiation is detuned from resonance, shows the molecular ion number decay due mainly to the effect of BBR-induced rotational excitation. Lower (blue) trace is for terahertz radiation on resonance. Each trace is the average of 10 individual decays. The lines are exponential fits to the first 10 s of the data.

In an alternative measurement mode (method II), the secular scan activated in step (ii) to obtain a normalization signal is turned off after a few seconds while the rotational cooling continues. At the end of step (iii), both rotational cooling lasers are blocked. In step (iv), the terahertz source and the REMPD lasers are turned on only for 3 s. Immediately afterward, in step (v) the secular excitation is turned on again and the reduced fluorescence level is recorded during a few seconds. The ratio of the two fluorescence levels defines our signal and gives approximately the relative decrease in $\mathrm{HD}^+$ number after REMPD.

At the end of either procedure, residual $\mathrm{HD}^+$ and product ions are removed from the trap by applying the following cleaning procedure. (In method II, we do not "reuse" the remaining molecules, as we prefer to excite molecular samples prepared in the same way each time.) The cooling laser is detuned by a few 100 MHz to the red of the atomic cooling transition, causing melting of the crystal into a liquid. A secular excitation frequency scan covering the frequencies of $HD^+$ and lighter ions is turned on. The cooling laser is briefly blocked and unblocked several times. Light ions are thereby ejected from the trap. The secular excitation is turned off and the system is ready for a new molecule loading.

## IV. RESULTS AND DISCUSSION

The first set of measurements was taken in the liquid state using method I. Figure 5 shows two atomic fluorescence traces. The upper (black, "background") trace was obtained with the terahertz wave frequency detuned by 500 MHz from $f_{0,\text{theor}}$, a value where no transition line exists. The REMPD only dissociates molecules in the $(v = 0, N = 1)$ level. This level has initially been depopulated by the 2.7 $\mu$m rotational cooling laser, which is favorable for the purpose of the spectroscopy. As soon as the spectroscopy phase starts, the level receives population not only by terahertz rotational excitation (if the frequency is near resonance), but also by BBR-induced excitation from all hyperfine states of the ground rovibrational level (rate ca. 0.09/s at 300 K). In addition, the population still present in the $(v = 0, N = 2)$ level or reaching it from higher-lying rotational levels is transferred into $(v = 0, N = 1)$ by BBR-stimulated emission (rate ca. 0.12/s) and spontaneous emission (rate ca. 0.06/s). Therefore, a REMPD-induced molecule loss is always present.

A rate equation simulation yields a BBR-induced molecule number decay rate that depends on REMPD laser intensities and reaches ca. 0.075/s in the limit of very high intensities. After partial optimization of the UV dissociation laser alignment onto the ion crystal and therefore maximization of its intensity, we observed values of ca. 0.04/s at 25 s after the REMPD laser was turned on. The rate at this time rather than at 0 s is considered since at 0 s the number of molecules present is larger and this may lead to some saturation of the secular excitation signal. We explain the difference compared to the theoretical maximum by the actually available laser power and possibly imperfect REMPD laser beams overlap. With an improved alignment of the UV laser, an increase of the BBR-induced decay rate to ca. 0.060/s was observed.

The lower (blue) trace represents the decay in the presence of resonant terahertz radiation, using frequency list $A'$. We observe a large difference in the initial rate of signal decrease as compared to the background trace. Note that the decay occurring in the presence of resonant terahertz radiation also contains the background decay.

We also performed measurements with the two frequency lists $B$ and $C$, for which the frequencies were detuned from those of list $A'$ by different amounts for the four hyperfine states. As Fig. 6 (top) shows, the decay rates do not differ significantly from the background decay rates, and we can therefore deduce an upper limit for the magnetic field of 1.5 G, as the influence of the Doppler width is not significant here.

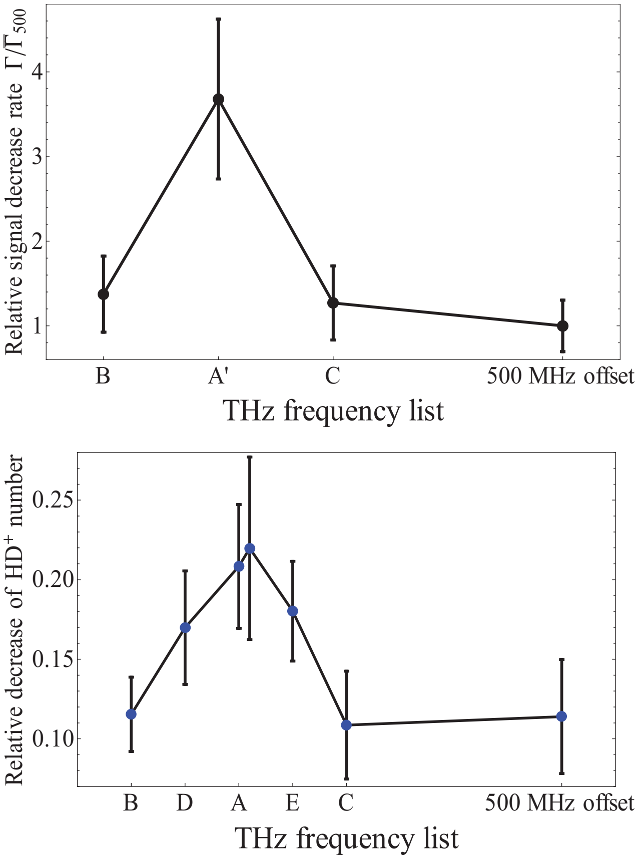

FIG. 6. (Color online) Frequency dependence of the rotational excitation. Top, in the liquid state, at ca. 100–200 mK, using method I. $\Gamma_{500}$ is the average decay rate when the terahertz radiation frequency is detuned by 500 MHz. Each data point results from nine individual decays. Bottom, in the crystallized state, at 10–15 mK, using method II. Each data point represents the mean of nine or ten measurements. The two close points were taken with the same list $A$ on different days and are shown separated for clarity. The error bars in both plots show the standard deviations of the data, not of the mean. The lines are guides for the eye.

A second set of measurements was taken with method II; see Fig. 6 (bottom). Here, the terahertz radiation is applied only when the ion ensemble is well crystallized, at temperatures of approximately 10–15 mK. Data points were taken alternately at 500 MHz detuning, with list $A$, with list $B$ ($D$), and with list $C$ ($E$). Again, a finite (background) signal is observed when the terahertz radiation is far detuned, since BBR excites the rotational transition significantly on the used time scale of 3 s. Irradiation with the frequency list $A$ provides a clear signal that rotational excitation induced by terahertz radiation takes place. We find again no significant difference in the rotational excitation efficiency for the detunings of lists $B$ and $C$, compared to the background measurement. However, reducing the detunings to half the values (lists $D$ and $E$) shows an increase of signal. This increase can be explained by the presence of a magnetic field of ca. 1 G or a Doppler width of several 100 kHz, or a combination of both. However, the Doppler width is at most 70 kHz under the operating conditions, and therefore we conclude that we observed the effect of the magnetic field on the hyperfine transition frequencies.

## V. CONCLUSION

We observed a pure rotational excitation of a sympathetically cooled molecular ion ensemble. In order to facilitate the observation, we applied a scheme adapted to the particularities of the apparatus. As the available detection scheme is a destructive one that employs photodissociation of the rotationally excited molecules, a new molecular ion loading cycle has to be implemented for each data point, and the data acquisition rate is very low. The number of ions sympathetically cooled is also small. Therefore, the preparation of a significant fraction (ca. 70%) of the molecular ions in the lower spectroscopic level was essential. Even so, the detection of a rotational transition originating from a single hyperfine state has too low of a signal-to-noise ratio. This is also due to the concurrent process of BBR-induced rotational excitation, which yields a finite background signal (decay rate) in connection with the photodissociation.

We therefore applied terahertz radiation at four frequencies that nominally excite the four hyperfine states in the lower spectroscopic level. This allowed a clear observation of the rotational excitation, using two different methods. By applying terahertz radiation detuned from the nominal resonance frequencies by amounts varying from 0.16 to 0.9 MHz (absolute) for the four frequencies, we found a significantly reduced but still observable excitation. This can be explained by the presence of a magnetic field with values up to approximately 1 G. In comparison, the contribution of secular ion motion to the linewidth when the ions are at approximately 10 mK and well-confined is negligible.

There is a strong motivation for further development of the method demonstrated here, since a resolution of the hyperfine structure of $HD^+$ and an accurate measurement of the hyperfine transition frequencies would represent a significant test of the *ab initio* calculations of this molecule. Possible improvements are the application of hyperfine state preparation techniques, recently demonstrated [20], and accurate control of the magnetic field in the trap region.

Finally, it is useful to consider the extension of this work to other molecular species. These can be characterized by their mass and their rotational constant, which are to a certain extent related. For many species, the masses will be significantly larger and the rotational constants significantly smaller than in the case of $HD^+$. The smaller rotational constant will lead to a significantly smaller transition frequency, in the microwave regime. It is likely that the Lamb-Dicke regime will then be effective, in particular if the microwave propagation direction is along the narrow width of the molecular ion ensemble, and Doppler broadening would be absent altogether. The smaller rotational constant will also lead to a smaller black-body-radiation excitation rate (at 300 K), which is very favorable, since it will make possible REMPD with near-zero background. The experimentally demonstrated fraction of molecules in the ground state obtained by applying rotational cooling on such heavier molecules is so far significantly below the level used here on $HD^+$ [30], but simulations [31] show that similar levels should be achievable with appropriate laser cooling schemes and laser systems. Hyperfine structure and Zeeman shift coefficients will be molecule-specific. Molecular ions in an electronic spin singlet state are particularly interesting, as they would have a reduced number of hyperfine states, of Zeeman substates, and much reduced linear Zeeman shift coefficients, simplifying and narrowing the spectrum. Thus, the extension of rotational spectroscopy of sympathetically cooled molecular ions to other species appears very promising.

## ACKNOWLEDGMENTS

This work was funded by the DFG (Project Schi 431/11-1) and by an equipment grant of the Heinrich-Heine-Universität. We thank F. Lewen for the loan of equipment and V. Korobov for communication of unpublished results. We are indebted to B. Roth and T. Schneider for their contributions in the initial phase of this study.

---

[1] F. Lewen, S. P. Belov, F. Maiwald, T. Klaus, and G. Winnewisser, Z. Naturforsch. A **50**, 1182 (1995).

[2] A. Maestrini, J. Ward, G. Chattopadhyay, E. Schlecht, and I. Mehdi, Frequenz—J. RF Engineer. **62**, 118 (2008).

[3] F. Klappenberger, K. F. Renk, P. Renk, B. Rieder, Y. I. Koshurinov, D. G. Pavelev, V. Ustinov, A. Zhukov, N. Maleev, and A. Vasilyev, Appl. Phys. Lett. **84**, 3924 (2004).

[4] C. P. Endres, F. Lewen, T. F. Giesen, S. Schlemmer, D. G. Paveliev, Y. I. Koschurinov, V. M. Ustinov, and A. E. Zhucov, Rev. Sci. Instrum. **78**, 043106 (2007).

[5] See, e.g., H. W. Kroto, *Molecular Rotation Spectra* (Wiley, London, 1975).

[6] S. Carocci, A. Di Lieto, A. Menciassi, P. Minguzzi, and M. Tonelli, J. Mol. Spectrosc. **175**, 62 (1996).

[7] L. A. Surin, B. S. Dumesh, F. S. Rusin, G. Winnewisser, and I. Pak, Phys. Rev. Lett. **86**, 2002 (2001).

[8] G. Cazzoli, L. Dore, C. Puzzarini, and S. Beninati, Phys. Chem. Chem. Phys. **4**, 3575 (2002).

[9] G. Winnewisser, S. P. Belov, Th. Klaus, and R. Schieder, J. Mol. Spectrosc. **184**, 468 (1997).

[10] V. Ahrens, F. Lewen, S. Takano, G. Winnewisser, S. Urbana, A. A. Negirev, and A. N. Koroliev, Z. Naturforsch. A **57**, 669 (2002).

[11] R. Krems, B. Friedrich, and W. C. Stwalley, eds., *Cold Molecules* (CRC Press, Boca Raton, FL, 2009).

[12] I. W. M. Smith, ed., *Low Temperatures and Cold Molecules* (World Scientific Publishing, Singapore, 2008).

[13] O. Asvany, O. Ricken, H. S. P. Müller, M. C. Wiedner, T. F. Giesen, and S. Schlemmer, Phys. Rev. Lett. **100**, 233004 (2008).

[14] W. H. Wing, G. A. Ruff, W. E. Lamb, and J. J. Spezeski, Phys. Rev. Lett. **36**, 1488 (1976).

[15] A. Carrington, I. R. McNab, and C. A. Montgomerie, J. Phys. B **22**, 3551 (1989).

[16] J. C. J. Koelemeij, B. Roth, A. Wicht, I. Ernsting, and S. Schiller, Phys. Rev. Lett. **98**, 1730024 (2007).

[17] S. Schiller and V. Korobov, Phys. Rev. A **71**, 032505 (2005).

[18] V. I. Korobov, Phys. Rev. A **74**, 052506 (2006).

[19] V. I. Korobov, Phys. Rev. A **77**, 022509 (2008).

[20] U. Bressel *et al.*, to appear in Phys. Rev. Lett. (2012).

[21] A. Carrington, C. A. Leach, A. J. Marr, R. E. Moss, C. H. Pyne, and T. C. Steimle, J. Chem. Phys. **98**, 5290 (1993).

[22] A. Carrington, I. R. McNab, C. A. Montgomerie, and J. M. Brown, Mol. Phys. **66**, 1279 (1989).

[23] V. I. Korobov (private communication).

[24] T. Schneider, B. Roth, H. Duncker, I. Ernsting, and S. Schiller, Nat. Phys. **6**, 275 (2010).

[25] D. Bakalov, V. I. Korobov, and S. Schiller, Phys. Rev. Lett. **97**, 243001 (2006).

[26] D. Bakalov, V. I. Korobov, and S. Schiller, J. Phys. B **44**, 025003 (2011).

[27] S. Schiller, B. Roth, F. Lewen, O. Ricken, and M. Wiedner, Appl. Phys. B **95**, 55 (2009).

[28] P. Blythe, B. Roth, U. Fröhlich, H. Wenz, and S. Schiller, Phys. Rev. Lett. **95**, 183002 (2005).

[29] S. Vasilyev, A. Nevsky, I. Ernsting, M. Hansen, J. Shen, and S. Schiller, Appl. Phys. B **103**, 27 (2011).

[30] P. Staanum, K. Højbjerre, P. Skyt, A. Hansen, and M. Drewsen, Nat. Phys. **6**, 271 (2010).

[31] See the Supplemental Materials in Ref. [24].

# Appendix 5. Weak spin-forbidden transition detection at 2.7 $\mu$m in HD$^+$

Rovibrational transitions in diatomic melecules with nonzero nuclear spin exhibit a rich hyperfine structure. The angular momentum couplings lead to selection rules that classify the rovibrational transitions into allowed, spin-forbidden and doubly-spin-forbidden transitions. In this work a laser excitation of a doubly-spin-forbidden rovibrational transition in HD$^+$ was demonstrated. HD$^+$, the most fundamental heteronuclear molecular ion, was a model system. The experiments were performed with sympathetically cooled molecular ions to a temperature of approximately 10 mK. The weak transition is driven by a continuous-wave optical parametric oscillatro. To increase the excitation signal, rotational cooling was employed. We described implementation of the doubly-forbidden transitions for a quantum state preparation.

The author contributed to: building the apparatus, modification of the setup, performing experiments, data analyses, discussion of the results, writing the paper.

# Observation of a doubly spin-forbidden rovibrational transition in cold trapped molecular ions

*A. Borodin and S. Schiller*

Institut für Experimentalphysik, Heinrich-Heine-Universität Düsseldorf, 40225 Düsseldorf, Germany

### Abstract

Rovibrational transitions in diatomic molecules whose nuclear spins, total electronic spin and rotational angular momentum are nonzero exhibit a rich hyperfine structure. The angular momentum couplings lead to selection rules that classify the rovibrational transitions into allowed, spin-forbidden and doubly-spin-forbidden transitions. Here, we demonstrate laser excitation of a doubly spin-forbidden rovibrational excitation in HD$^+$, the most fundamental heteronuclear molecular ion having a $^2\Sigma$ ground level. The experiment is performed with molecular ions sympathetically cooled by atomic ions to a temperature of approximately 10 mK. The weak transition is driven by a continuous-wave optical parametric oscillator. We employ rotational cooling in order to increase the excitation signal, and all-diode-laser based resonance-enhanced multiphoton dissociation for detection of the transition. The relevance of doubly spin-forbidden transitions for quantum state preparation of molecular ions is discussed.

## 1 Introduction

Weak (nearly forbidden) transitions in atoms are commonly used for precision quantum-optical experiments. For example, in the field of quantum information the atomic ground state and a long-lived metastable state can be used to encode a qubit, which is manipulated via a weak, e.g. electric quadrupole, transition connecting the two states. In optical atomic clocks, the coherent oscillation of a superposition between, e.g. a singlet $^1S_0$ and a triplet $^3P_0$ state represents the clock oscillation, and its excitation is performed by driving the spin-forbidden transition between the two states. In molecules, such transitions seem to be more rarely observed or considered in laboratory applications. Since the upper state addressed by a weak transition can also decay via allowed transitions into other states, the upper state does not usually have a very long lifetime, making detection of the weak transition more difficult.

In recent years, the field of trapped molecular ions has developed strongly. The trapping, usually in conjunction with translational cooling, allows in principle to achieve long storage time of the molecules. Then, under appropriate conditions (low collision rates, e.g. if cooling is implemented via sympathetic cooling with co-trapped atomic ions), weak transitions become accessible or detectable.

Among the molecular ions which are being studied in ion traps for spectroscopy are $MgH^+$ [1], $AlH^+$ [2], $HfF^+$ [3], $N_2^+$ [4, 5]. These particular species do not possess hyperfine structure, although they possess electron-spin-rotation interaction. A species studied intensely in our group is $HD^+$. It possesses hyperfine structure in its full complexity: proton spin (1/2), deuteron spin (1), electron spin (1/2) and rotational angular momentum ($N$). The lack of inversion symmetry is responsible for a higher complexity of the spectra as compared to the homonuclear $H_2^+$. Notwithstanding its hyperfine structure, the relative simplicity of the 3-body quantum system $HD^+$ allows precise theoretical analysis. Its transition frequencies [6] and their strength [7] can be predicted in detail. The potential for testing quantum theory, and for fundamental physics has been described previously [8, 9]. Different transitions in this molecular ion have already been observed [10–14]. The hyperfine structure of $HD^+$ has been studied extensively theoretically [7, 15] and experimentally observed and characterized [12] in two low-lying rovibrational levels. Every rovibrational level is split into 4, 10, or 12 hyperfine sub-levels, depending on whether the rotational angular momentum is $N = 0$, 1 or $> 1$, respectively. The splitting arises from the electron spin-proton spin interaction, the electron spin-deuteron spin interaction and the electron spin-rotational angular momentum interaction.

The existence of hyperfine structure of the rovibrational levels forces experimenters to consider ways to implement quantum state preparation, as this is helpful as a starting point for precision spectroscopy. The possibility of quantum state preparation was previously demonstrated [12], where it was also shown how this can be useful for rendering detectable transitions which normally exhibit too low a signal-to-noise ratio. The weak transition rendered detectable was a singly spin-forbidden transition, and the quantum state preparation made use of two singly spin-forbidden transitions.

Here we describe how doubly-spin-forbidden transitions are also relevant for quantum state preparation (at least in the case of $HD^+$), since they will eventually enable preparation of a set of molecules or a single molecule with high probability in a single, arbitrary hyperfine state. We then report the observation of a particular doubly spin-forbidden rovibrational transition, ($v = 0$, $N = 0$) $\rightarrow$ ($v' = 2$, $N' = 1$). Note that this is an overtone electric dipole transition, which itself is weak since it becomes allowed by the small anharmonicity of the internuclear potential. In order to observe the doubly spin-forbidden transition, we developed an appropriate frequency-stabilized continuous-wave laser source of 2.7 $\mu$m wavelength, which provides sufficient power.

In the following, we first present the motivation for this work, then the experimental apparatus and the measurement procedures, followed by the results, and terminating with their discussion.

## 2 Motivation

Fig. 1 shows the hyperfine states' energies for the ($v = 0$, $N = 0$) and ($v' = 2$, $N' = 1$) levels. The first level has four hyperfine states, while the second has 10 hyperfine states. This large number gives rise to a large number of hyperfine transitions. Fig. 2 shows the relative strengths and frequencies of the various hyperfine transitions. The strongest ones are shown in red, green, blue and black. In these spin-allowed transitions, the (approximate) quantum numbers $F$ and $S$ do not change value, and $J$ changes by at most one unit. Their detuning from the corresponding "spin-less" frequency $f_{0,theor}$ is comparatively small, less than $\pm 50$ MHz, because the constants of the hyperfine hamiltonian do not vary strongly with vibrational and rotational quantum number, see Ref. [15]. Hyperfine-state changing transitions (where at least one of $F$ and $S$ change value) have detunings as large as $\pm 1$ GHz and strengths as small as $10^{-9}$ relative to the strongest transition. They are shown in pink in Fig. 2. These transitions can be divided into two groups: (i) transitions in which $S$ changes, but not $F$ ("singly spin-forbidden"); these transitions lie inside the coloured boxes

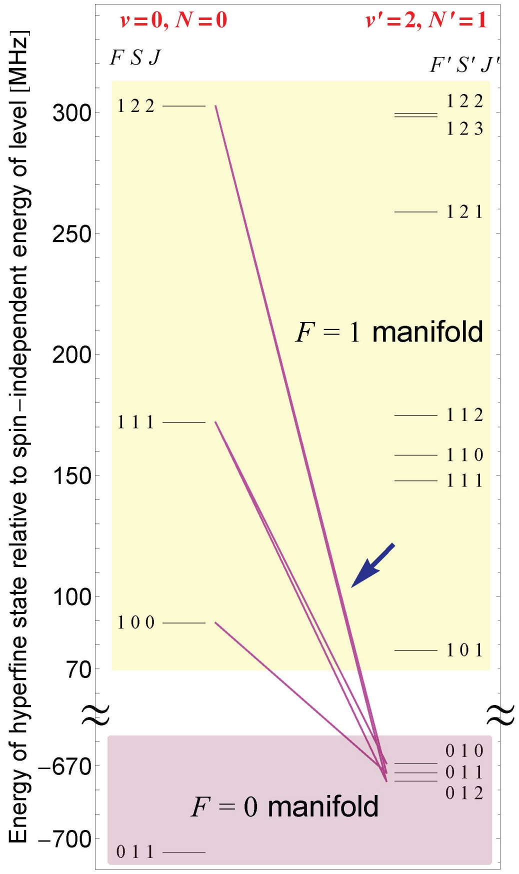

Fig. 1: (Color online) Energy diagram of the hyperfine levels. Inside the frame, on the left side, the hyperfine levels of the rovibrational ground level ($v = 0$, $N = 0$) are indicated; on the right side, those of the rovibrationally excited level ($v = 2$, $N = 1$). The hyperfine states are labeled by the (in part approximate) quantum numbers ($F$, $S$, $J$). The magnetic degeneracy factor of each hyperfine state is $(2J + 1)$ (not shown). The very weak, $F$-manifold-changing doubly-spin-forbidden transitions (where both $F$ and $S$ change their values) having large negative frequencies are shown in pink. The two transitions addressed (simultaneously) in this work are indicated by the arrow.

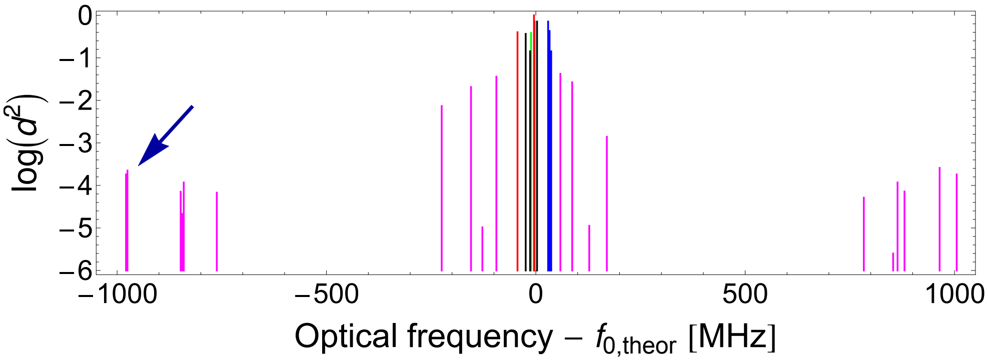

Fig. 2: (Color online) Stick spectrum of all transitions having relative strength exceeding $2 \times 10^{-5}$. $d$ is the transition dipole moment normalized to that of the strongest hyperfine transition. In this panel, all non-strong transitions are shown in pink. The two transitions addressed (simultaneously) in this work are indicated by the arrow. They span 4 MHz and are not resolved.

in Fig. 2. Their detunings are less than ±250 MHz and their strength is a few orders smaller than the strongest transition. (ii) Transitions in which both $S$ and $F$ change ("doubly spin-forbidden"). These have detunings in the range of 750 to 1000 MHz and −750 to −1000 MHz and are a few orders weaker than the singly spin-forbidden transitions. Doubly spin-forbidden transitions with negative detuning are shown in pink in Fig. 1. A subset of these, namely those originating from the state ($v = 0$, $N = 0$, $F = 1$, $S = 1$, $J = 2$) are listed in table 1. The table contains also one transition in which $J$ changes by two units, making it weaker still.

Let us return to the rovibrational ground level ($v = 0$, $N = 0$) of the molecule, which will be the lower (initial) level for a range of possible spectroscopic studies. Counting also the Zeeman sub-states, there are altogether 12 quantum states in the ground level. From our previous work, we know that when rotational cooling by a 5.4 $\mu$m laser is performed, even the hyperfine state with the largest fractional population (the ($F = 1$, $S = 2$, $J = 2$) state) has only approximately 20 % population [12]. This is a small number, and it is very desirable to increase it, since this will lead to stronger signals and shorter overall measurement times. Quantum state preparation is needed for this purpose. We will now discuss that an efficient quantum state preparation requires the ability to excite doubly spin-forbidden transitions.

As a concrete example we consider the task of precision spectroscopy of the pure rotational, fundamental transition ($v = 0$, $N = 0$)→($v' = 0$, $N' = 1$). This transition has already been observed [13], but not with high frequency resolution. Among its many hyperfine transitions, particularly attractive is the transition between the states ($F = 0$, $S = 1$, $J = 1$) and ($F' = 0$, $S' = 1$, $J' = 2$), since it exhibits a small Zeeman shift and a small Zeeman splitting. Its detuning from the "spin-less" pure rotational transition frequency $f_{0,theor}$ is $f - f_{0,theor} = -2.1\,\mathrm{MHz}$. The initial state of this transition is the energetically lowest hyperfine state of the ground level, see Fig. 1. More precisely, the $J_z = 0 \rightarrow J'_z = 0$ Zeeman component exhibits a quadratic Zeeman shift approx. equal to 2.9 kHz in 1 G and whose other metrological properties have been discussed in Ref. [16]. The other two Zeeman sub-states of the lower level, $J_z = \pm 1$, can be excited to $J'_z = \pm 2$, respectively, with nearly opposite linear Zeeman shifts of approx. $\mp 40\,\mathrm{kHz}$, respectively [? ]. Thus, assuming a

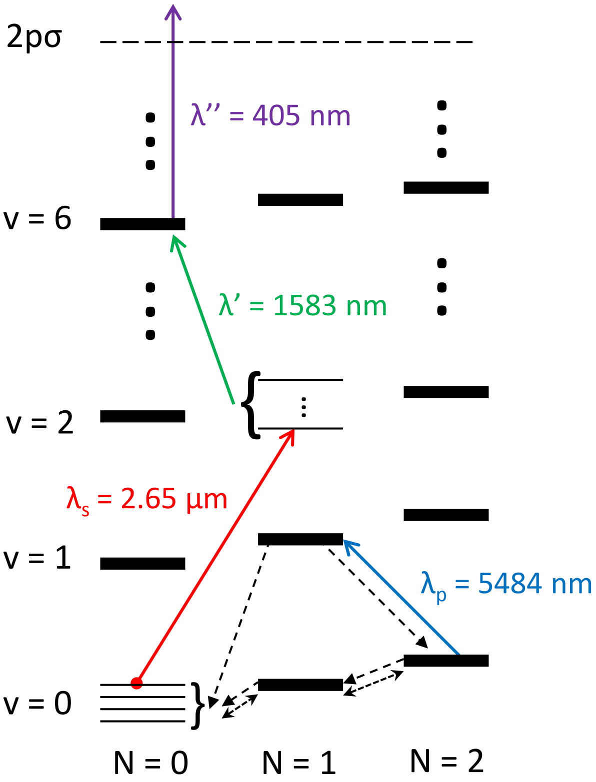

Fig. 3: (Color online) Simplified energy level scheme of HD$^+$ with transitions relevant to this work. Full, colored arrows indicate laser-induced transitions; dashed arrows indicate spontaneous emission transitions; dotted double arrows indicate black-body-radiation-induced transitions. One doubly spin-forbidden hyperfine transition between ($v = 0$, $N = 0$) and ($v' = 2$, $N' = 1$), excited by the optical parametric oscillator, is shown in red. Resonant laser radiation at $\lambda$= 1583 nm and nonresonant radiation at $\lambda$= 405 nm transfer the rovibrationally excited molecular ions from ($v' = 2$, $N' = 1$) first to a higher vibrational level ($v'' = 6$, $N'' = 0$) and then further to electronically excited levels (predominantly $2p\sigma$), from which the ions dissociate. Rotational cooling is via optical pumping at $\lambda$= 5484 nm. The level energy differences are not to scale. The hyperfine structure is shown schematically for the levels ($v = 0$, $N = 0$) and ($v' = 2$, $N' = 1$), and as thick lines for some other levels.

magnetic field $B = 0.035\,\mathrm{G}$, all three sub-levels of the lower hyperfine state can be excited with a 1.3 THz radiation field having full spectral width of approx. $3\,\mathrm{kHz}$. If the spectroscopy occurs in the Lamb-Dicke regime, a spectroscopic line-width of $3\,\mathrm{kHz}$ would be expected. At this resolution level, a precise test of the combined hyperfine energy contribution ($-2.1\,\mathrm{MHz}$) and a test of the QED corrections down to those of order $\alpha^5$ relative to the non-relativistic transition frequency (amounting to $4\,\mathrm{kHz}$ [6]) would be possible.

The task of quantum state preparation would in this case be the transfer of population residing in the upper three hyperfine levels of the ground level (see Fig. 1) to the lowest-energy hyperfine level ($F = 0,\ S = 1,\ J = 1$). This quantum state preparation can be implemented using a tunable laser source that drives the ($v = 0,\ N = 0$)$\rightarrow$($v' = 1,\ N' = 1$) transition (as using in Ref. [12]). Alternatively, the ($v = 0,\ N = 0$)$\rightarrow$($v' = 2,\ N' = 1$) overtone transition can be used.

However, after loading the molecular ions, after thermalization with the black-body radiation environment, the molecular population is distributed among several rotational levels in the ($v = 0$) manifold, only about 10 % residing in the ground level. Therefore as a first step for quantum state preparation, laser rotational cooling would be employed, as mentioned above [11, 17]. This is indicated in Fig. 3 as a blue line. Here, a laser transfers population to the ground level ($v = 0, N = 0$) via optical pumping. After optical pumping approximately 60% of the molecular ions will be in the ground level. Concomitantly, optical pumping also increases the population in each hyperfine state of the ground level. For example, approximately 20% of all ions are then in the ($F = 1, S = 1, J = 2$) hyperfine state [12].

As a second step, hyperfine pumping can be used to increase the population in a particular hyperfine state. Fig. 1 shows as diagonal lines (pink) the transitions which can be used for pumping (after a number of intermediate steps) into the hyperfine state ($F = 0,\ S = 1,\ J = 1$), the lower state of the proposed spectroscopy transition. These transitions, one of which is shown as a red arrow in Fig. 3, have the purpose of de-populating the $F = 1$ manifold of the ($v = 0,\ N = 0$) level. As can be seen from Fig. 1, they include both singly and doubly spin-forbidden transitions. The transitions excite the ions into the rovibrational level ($v' = 2,\ N' = 1$), from which decay by spontaneous emission to the vibrational ground levels ($v'' = 0,\ N'' = 1$) and ($v'' = 0,\ N'' = 3$) takes place. The spontaneous decays will predominantly occur on strong transitions, i.e. on spin-allowed transitions (without change in $F$ and $S$). Black-body stimulated emission and spontaneous emission from these two levels to ($v'' = 0,\ N''' = 0$) and ($v'' = 0,\ N''' = 2$), respectively (short dashed lines in Fig. 3), will again leave $F$ and $S$ unchanged. The rotational cooling laser (operated with near-zero detuning) will mainly induce strong transitions, and the following spontaneous decay (long dashed lines in Fig. 3) will mainly proceed on strong transitions, too. Both types also do not change $F$ and $S$. After several cycles of these transitions, the population of the $F = 0$ state of the ground level ($v = 0,\ N = 0$) is expected to be significantly increased.

A first demonstration of hyperfine pumping, an increase of the population of the ($v = 0,\ N = 0,\ F = 1,\ S = 0,\ J = 0$) hyperfine state was shown, which has only 5 % of total population after rotational cooling, by driving singly spin-forbidden transitions from ($v = 0,\ N = 0,\ F = 1,\ S = 2,\ J = 2$) and ($v = 0,\ N = 0,\ F = 1,\ S = 1,\ J = 1$) [12].

The above discussion shows that doubly spin-forbidden transitions are necessary if one needs to deplete all hyperfine states (except the goal state) and at the same time transfer the population into hyperfine states of appropriate spin structure. Below we show experimentally that such transitions can indeed be driven. In order to provide sufficient intensity for excitation of doubly spin-forbidden transitions, we developed a continuous-wave optical parametric oscillator (OPO) as a suitable laser source.

| $(F,\ S,\ J)$ | | Detuning, $f - f_{0,theor}$ [MHz] | Relative strength |
|---|---|---|---|
| Lower state | Upper state | | |
| (1, 2, 2) | (0, 1, 0) | −971.5 | $2 \times 10^{-7}$ |
| | (0, 1, 1) | −975.4 | $2 \times 10^{-4}$ |
| | (0, 1, 2) | −978.8 | $2 \times 10^{-4}$ |

Tab. 1: Transition strengths (relative to the strongest hyperfine transition) and precise detunings of the hyperfine transitions near -977 MHz detuning from the spin-less frequency of the $(v = 0,\ N = 0) \to (v' = 2,\ N' = 1)$ rovibrational transition. The second and third entries are the doubly spin-forbidden transitions. The first transition has $\Delta J = 2$ and is therefore extremely weak and does not contribute significantly to the detected signal.

For the rovibrational transitions considered here the Zeeman structure is not taken into account, because the splitting of the states induced by a relatively small magnetic field (of order 1 Gauss) present in the trap, is at most a few MHz, smaller than the combined linewidth due to Doppler broadening and frequency instability of the laser.

## 3 Experimental method

### 3.1 Overview

A schematic of the experimental setup is shown in Fig. 4. A linear radio-frequency quadrupole trap is operated in an ultrahigh-vacuum chamber. The trap is driven at 14.2 MHz, and is used for simultaneous trapping of $\mathrm{Be}^+$ and $\mathrm{HD}^+$ ions. $\mathrm{HD}^+$ions are cooled sympathetically by interaction with $\mathrm{Be}^+$ ions [18]. Both $\mathrm{Be}^+$ and $\mathrm{HD}^+$ ions are obtained from the corresponding atoms and molecules by electron impact ionization. Be atoms are generated by evaporation from metallic beryllium wire, and HD molecules are loaded into the chamber from a HD gas bottle with a piezoelectric valve.

We use a REMPD (resonance-enhanced multiphoton dissociation) technique [19] for detection of the ions that have been vibrationally excited to $v' = 2$, see Fig. 3. First, a 1.6 µm tunable diode laser further excites the molecules resonantly to $v'' = 6$. Then, an inexpensive, commercially available, spectrally broad 405 nm diode laser (100 mW) photodissociates the molecules. The three laser beams involved in the OPO+REMPD excitation (2.7 µm (OPO), 1.6 µm, 405 nm) are combined from the left-hand side of the setup. Laser light for cooling of $\mathrm{Be}^+$ is delivered from the right-hand side. The rotational cooling laser (5.4 µm) enters diagonally.

Doppler broadening arises from ion motion in the trap associated with the ion ensemble's secular temperature. We worked at the lowest secular temperature reachable, estimated to be in the range 10 to 15 mK, where the corresponding Doppler broadening is about 5 MHz for 2.7 $\mu$m radiation. Micro-motion along the trap axis, at the trap RF driving frequency (here, 14.2 MHz), can contribute to the line shape of a transition.

### 3.2 The OPO

The rovibrational transition frequency of the $(v = 0,\ N = 0) \to (v = 2,\ N = 1)$ transition is $f_{0,theor} = 113.014969$ THz (2.65 µm). Among continuous-wave laser sources which can generate

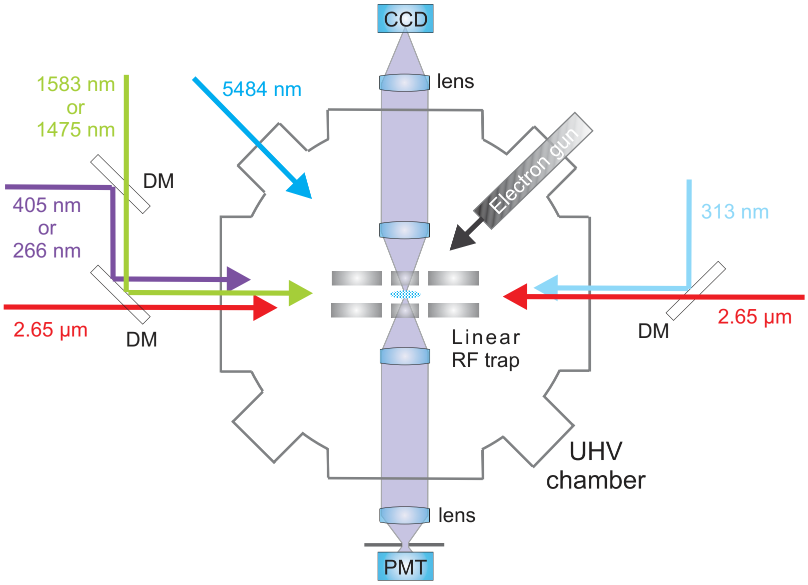

Fig. 4: (Color online) Schematic of the setup and beams. DM: dichroic mirrors, CCD: charge-coupled device, PMT: photomultiplier, both for $Be^+$ fluorescence detection. Dimensions are not to scale.

radiation at this wavelength, OPO sources offer the highest emission power. A DFB-type diode laser with typical output power of a few mW, and previously used by us for driving a $\Delta v = 2$ transition [11] would not have been sufficient for the present purpose. We used a home-made continuous-wave, singly-resonant OPO, pumped with 9 W at 1064 nm. The resonant (signal) wavelength is 1.8 µm, and the idler wavelength is 2.65 µm. This OPO was previously used in experiments on vibrational excitation of complex molecular ions [20], where a transition having a line-width of approx. 5 $cm^{-1}$ was detected. In that work the OPO's wavelength was stabilized using a technique based on counter-directional mode coupling [21].

In the present work, the line-widths of transitions in $HD^+$, cooled to a secular temperature of 10 to 15 mK, are Doppler-limited and amount to approximately 5 MHz at 2.65 µm. In order to achieve excitation rates that are stable in time, an appropriate long-term frequency stabilization of the OPO's frequency to this level was implemented, i.e. it suppresses the frequency drift.

The first task of this stabilization is the achievement of mode-hop-free operation. To this end, a thermal lock method was used (see, e.g. [22]). Additionally, in order to stabilize the idler frequency (at 2.65 µm), its value is continuously measured and a digital feedback system based on LabView adjusts the pump laser frequency accordingly. Because no mid-IR wavemeter was available, we used a near-IR wavemeter (High Finesse Angstrom WS-7 IR). With this wavemeter, we measured alternating the pump (1.06 µm) and signal (1.8 µm) frequencies $f_{pump}$, $f_{signal}$. The LabView program computed in real time the idler frequency as $f_{idler} = f_{pump} - f_{signal}$. Deviations of the idler frequency from the goal frequency $f_{0,theor} - 977\,\mathrm{MHz}$ were converted into an error signal fed back to the frequency tuning element of the pump laser.

The remaining instability of the idler frequency is illustrated by Figs. 5 a, b. As seen from the graphs, the output frequency is stabilized to within ±5 MHz relative to the goal frequency (as measured by the wavemeter). The wavemeter accuracy was checked by comparison with measurements using a frequency comb referenced to a H-maser and GPS, which provided absolute frequency accuracy. Additionally, 1.5 µm radiation from our 313 nm cooling laser source (see Ref. [23]) is used to perform a routine calibration of the wavemeter; this is possible since the 1.5 µm source is frequency-stabilized to an iodine line, providing an adequate frequency reference . The frequency measurements by the wavemeter do not provide full information about the OPO's frequency instability since the wavemeter does not determine the OPO linewidth. We estimate the combination of frequency instability and linewidth to yield an effective linewidth of ±10 MHz.

The OPO's idler radiation is coupled into a single-mode, 3 m long ZBLAN fiber (FiberLabs Inc.) and delivered to the experimental setup. A metal-coated off-axis parabolic reflective collimator (Thorlabs, Inc.) is used to collimate the output beam. About 30 mW power is available at the output of the fiber, and after transmission through air, the power in front of the vacuum chamber window was about 10 mW. The wave is focused into the trap center, where its beam diameter is approx. 200 µm, resulting in an intensity of $I \simeq 30\ \mathrm{W/cm^2}$. The Rabi frequency $\Omega_{R,ab}$ of the doubly spin-forbidden transitions of interest (the two strongest transitions of Table 1) is estimated using [24]

$$\Omega_{R,ab} = (2\pi)\, 27\, d_{ab}\, \sqrt{I/(1\,\mathrm{W\,cm^{-2}})} \times 10^6\ \mathrm{s^{-1}}\ .$$

The value is a few $10^3\,\mathrm{s^{-1}}$, significantly smaller than the combined linewidth due to Doppler broadening (approx. 5 MHz) and the frequency instability of the OPO (estimated to be 20 MHz). The transition rate $R_{ab}$ is obtained as

$$R_{ab} = \frac{\pi\, S\, \Omega^2_{R,ab}}{2\,\Delta\omega}\ ,$$

where $d_{ab}$ is the reduced transition dipole moment in debye, $S$ is a relative line strength, and $\Delta\omega$ is the effective transitions linewidth, $\Delta\omega \simeq 2\pi\times 20$ MHz. The transition rate has contribution from the individual relative line strengths from Table 1 and the reduced dipole moment $d_{ab}$ from [7, 25] (0.011 debye). Taking into account each of the two strongest transitions from Table 1, the excitation rate for each of them is estimated to be $0.35\ \mathrm{s^{-1}}$, and the total excitation rate is about $0.7\ \mathrm{s^{-1}}$. This value indicates that the relatively high power employed here (10 mW) can be regarded as weak.

## 3.3 Procedures

As REMPD is a destructive method, a re-loading of "fresh" $\mathrm{HD^+}$ molecular ions is required after almost every cycle of measurement. Typically, reloading of $\mathrm{Be^+}$ ions is not required, and the atomic ion ensemble (Coulomb crystal) can be used during several hours of experimentation. The measurement cycle starts with loading $\mathrm{HD^+}$ by opening a leak valve for introduction of HD gas and a short (1-3 s long) activation of the electron gun for ionization. The electron impact loading of $\mathrm{HD^+}$ can produce other species, which are then also trapped and sympathetically cooled. In order to remove them from the trap, a DC potential is applied to two opposite RF electrodes of the trap, thus breaking the symmetry and reducing the quasi-potential in one of the transverse directions [26]. After loading and removal, a protocol is run which controls the lasers, secular excitation, and records signals from imaging optics and fluorescence detection. The measurement cycle is completed by removing all ions from the trap (except for the $\mathrm{Be^+}$ ions) by application of appropriate secular excitation produced by an additional electrode.

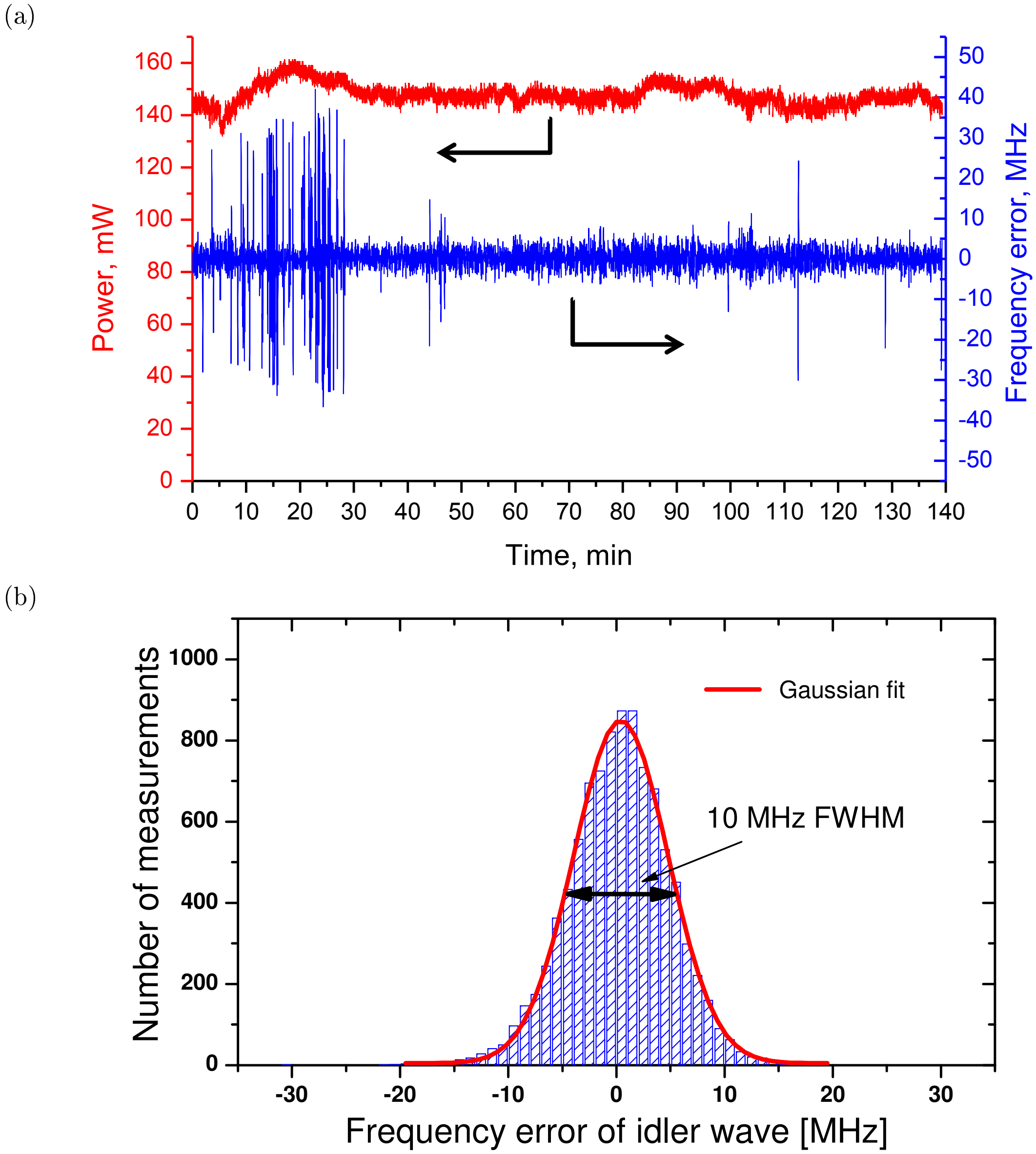

Fig. 5: Frequency stabilization of the continuous-wave OPO. (a) Stability of idler frequency and output power, while the OPO is frequency-stabilized. Two data points per second are measured and plotted; (b) Histogram of the idler frequency error while the OPO is frequency-stabilized. The measurement duration was approximately 60 min.

We used two measurement procedures to detect the laser excitation of the doubly spin-forbidden transition. In the first procedure ("constant excitation"), an excitation of the transverse secular motion of the $HD^+$ ions is kept applied during the simultaneous OPO and REMPD lasers (1.6 µm and 405 nm) irradiation. The secular excitation induces heating of the $HD^+$ molecular ion ensemble, and their energy is transferred to the $Be^+$ ensemble. Its increased energy is then detected as an increase in fluorescence. During REMPD, the number of $HD^+$ ions decreases, and consequently the $Be^+$ fluorescence signal decreases. This method naturally leads to a noticeable increase in the temperature of the ions, which then causes an increased Doppler broadening and is therefore not appropriate for precise transition frequency measurements.

In the second procedure ("before/after excitation"), the secular excitation is applied for a short time before OPO and REMPD lasers irradiation, then doubly spin-forbidden excitation and REMPD are performed, followed by a second secular excitation. As in the first procedure, the fluorescence signals during the secular excitation intervals give information about the number of $HD^+$ ions in the trap. The normalized difference of the two signals recorded before and after OPO+REMPD define our spectroscopic signal.

## 4 Results

### 4.1 OPO frequency instability test

A preliminary characterization of the excitation of the rovibrational transition was performed by attenuating the OPO power significantly, to approx. 10 mW and tuning it close to the spin-less transition frequency, i.e. near 0 MHz detuning from $f_{0,theor}$. The OPO then drives the strong transitions, which are shown as colored lines at the center of Fig. 2. Using the "constant excitation" method, we then observed the fluorescence signals presented in Fig. 6 (a). The ion number decreases with a rate of 0.02 $s^{-1}$ . The relatively low rate is attributed to limitation of the excitation of REMPD laser at 1.6 µm. In case (b), an additional spectral broadening of the OPO radiation by approx. ±30 MHz was applied by sweeping the pump laser frequency which in turn produces a frequency sweep of the 2.65 µm radiation.

Comparing the two cases, we find that the mean decay constant was the same, while its variance differed. The variance was approximately a factor 3 larger in case (a). We interpret this as arising from the residual frequency instability of the OPO: a moderate frequency sweep averages out the residual instability and thus reduces the fluctuations of the measurements.

### 4.2 Detection of the doubly spin-forbidden transition

In our experimental procedure, the detection of a single hyperfine transition intrinsically has a small signal-to-noise ratio (SNR). The number of $HD^+$ ions is low, typically a few hundred, and this population is distributed between several rotational levels. The population in the ground vibrational level is furthermore distributed over four hyperfine states, resulting in only a few ten molecules in the lower spectroscopy state even after rotational cooling. As a consequence, obtaining a detection with sufficient SNR requires repeating the experiment, and averaging over the obtained individual measurements. Fig. 4.2 illustrates the excitation of the two weak doubly-spin-forbidden lines near -977 MHz detuning listed in Tab. 1, referred hereafter as "transition". Detection was made using the "before/after excitation" scheme, which ensures that the $HD^+$ ions remain at low secular temperature, approximately 10 -15 mK. At each detuning value, we performed at least

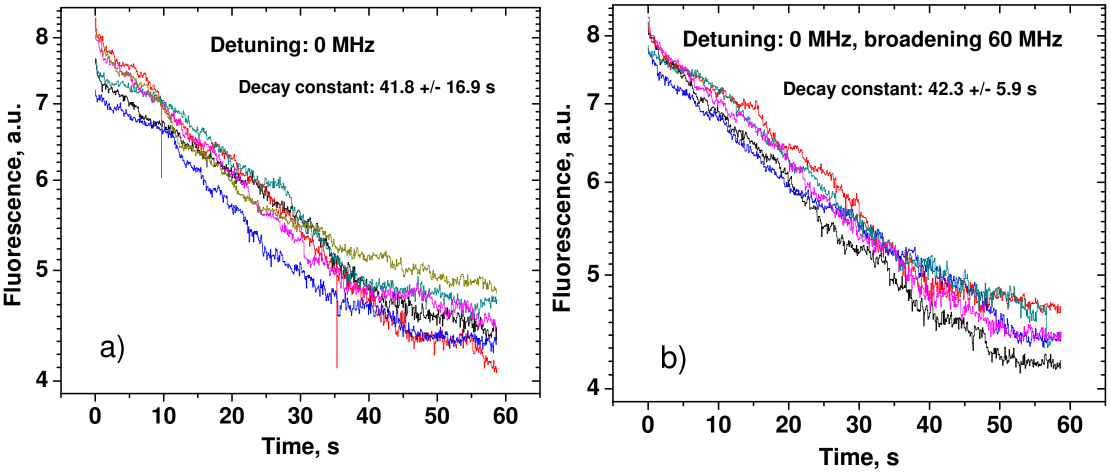

Fig. 6: Excitation and detection of $(v = 0,\, N = 0) \rightarrow (v' = 2,\, N' = 1)$ transition in $HD^+$ molecular ion. (a): the OPO frequency was stabilized to 0 MHz detuning from $f_{0,\,theor}$ . (b): the OPO was additionally broadened by ±30 MHz. Both cases show the same average decay constant, but the fluctuations in case (a) are larger, which is interpreted as resulting from the residual frequency instability of the OPO frequency.

10 measurements. The OPO+REMPD detection time was 5 seconds for each measurement. The OPO frequency was locked to the target frequency without additional broadening. The shown error bars are the standard deviation of the data.

The total time required for data acquisition of the plot of Fig. 4.2 was about 10 hours because of the length of the individual measurement cycle that includes molecular ion loading, cleaning, rotational cooling, transition excitation, REMPD, and ion removal.

The transition is clearly detected. It exhibits a line-width of approximately 40 MHz, that we attribute mostly to the frequency instability of the OPO source. Note that for large enough detuning from the spin-less frequency, e.g. at -1030 MHz, almost no signal is detected. The instability of the decay values is ±5 % and represents the sensitivity of our method. It is due to the power fluctuations of the cooling laser, variation of the number of ions in the lower spectroscopy level, and variation in background ion loss.

According to Fig. 4.2 the maximum fractional decay signal obtained is 10%. This is the fraction of all molecules that is dissociated via the employed transitions. Considering that the lower spectroscopy state contains approximately 20% of all ions after rotational cooling, this means that approx. 50 % of the relevant population was excited during 5 s. This is equivalent to an excitation rate of 0.14 $s^{-1}$ . This value is in a reasonable agreement with the excitation rate calculated above, 0.7 $s^{-1}$ The discrepancy of a factor 4 we attribute mainly to the imperfect spatial overlap of the 2.7 $\mu$m beam focus and the molecular ions, and to to the limitation of the excitation of REMPD laser at 1.6 µm.

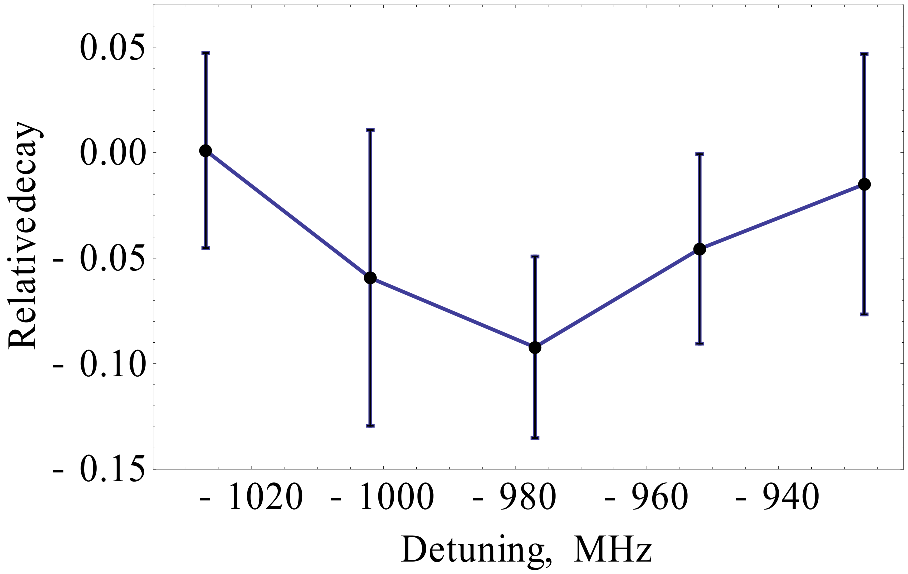

Fig. 7: Spectrum of a pair of doubly-spin-forbidden hyperfine transitions in the $(v = 0, N = 0) \rightarrow (v' = 2, N' = 1)$ overtone transition, at a detuning around -977 MHz with respect to the spin-less transition frequency.

## 5 Discussion and conclusion

We excited and observed a weak, doubly spin-forbidden transition of $HD^+$ in an ensemble of sympathetically cooled molecular ions. In order to achieve a significant transition probability, a high-power continuous-wave optical parametric oscillator was developed. We used a destructive detection method, based on photo-dissociation of the excited molecular ions, that requires re-loading molecular ions after each experimental cycle run.

The fraction of ions addressable by the studied transition determines the maximum achievable signal. In the ideal case of all ions being in the rovibrational ground level, and relative hyperfine state population according to the magnetic degeneracy, a maximum fractional ion number reduction of -0.25 would be possible. The experimentally achieved value of -0.10±0.05 means that about 40% of this maximumwas achieved.

The detected transition pair is of importance for the implementation of a “complete” quantum state preparation, which requires excitation of doubly spin-forbidden transitions to deplete all “undesired” quantum states with concomitant transfer of molecular population to an arbitrary target state. More precisely, the doubly spin-forbidden transitions are required to transfer population between the $F$-manifolds. In the present work, we drove two such transitions. For a full quantum state preparation into the $(F = 0, S = 1, J = 1)$ hyperfine state two additionalhyperfine transitions having detunings of -760 MHz and -844 MHz would have to be excited. These two transitions would be excited after appropriately frequency-tuning the OPO away from the -977 MHz transition pair to each frequency in turn. Our OPO system is in principle capable of doing so, as the output radiation can be tuned within approximately ±100 MHz without mode hop. Work towards implementing such a complete quantum state preparation is currently under way in our laboratory.

## References

[1] O. O. Versolato, M. Schwarz, A. K. Hansen, A. D. Gingell, A. Windberger, L. Klosowski, J. Ullrich, F. Jensen, J. R. Crespo Lopez-Urrutia, and M. Drewsen. Decay Rate Measurement of the First Vibrationally Excited State of $MgH^+$ in a Cryogenic Paul Trap. *Phys. Rev. Lett.*, 111:053002, 2013.

[2] Ch. M. Seck, E. G. Hohenstein, Chien-Yu Lien, P. R. Stollenwerk, B. C. Odom. Rotational State Analysis of $AlH^+$ by Two-Photon Dissociation. *arXiv:1402.0123v1.*

[3] Huanqian Loh, K. C. Cossel, M. Grau, Kang-Kuen Ni, E. R. Meyer, J. L. Bohn, Jun Ye, E. A. Cornell. Precision Spectroscopy of Polarized Molecules in an Ion Trap. *arXiv:1311.3165v1.*

[4] M. Kajita, G. Gopakumar, M. Abe, M. Hada, and M. Keller. Test of $m_p/m_e$ changes using vibrational transitions in $N_2^+$. *Phys. Rev. A*, 89:032509, 2014.

[5] Willitsch et al. 2nd IOTA COST Workshop on Cold Molecular Ions, Arosa, 2 - 5 September 2013.

[6] V. I. Korobov, L. Hilico, J. P. Karr. Complete set of the $m\alpha^7$ order corrections to the rovibrational transition frequencies in $H_2^+$, $HD^+$, and antiprotonic helium. *arXiv:1312.3728*, 2013.

[7] D. Bakalov, V.I. Korobov, S. Schiller. Magnetic field effects in the transitions of the $HD^+$ molecular ion and precision spectroscopy, J. Phys. B: Al. Mol. Opt. Phys., 44, 025003 (2011); Corrigendum: J. Phys. B: Al. Mol. Opt. Phys., 45, 049501 (2012).

[8] B. Roth and S. Schiller. Sympathetically cooled molecular ions: from principles to first applications, Proc. in "Cold Molecules", R. Krems, B. Friedrich, and W. Stwalley, http://arxiv.org/abs/0812.1154. 2009.

[9] B. Roth, J. Koelemeij, H. Daerr, I. Ernsting, S. Jorgensen, M. Okhapkin, A. Wicht, A. Nevsky, and S. Schiller. Trapped Ultracold Molecular Ions: Candidates for an Optical Molecular Clock for a Fundamental Physics Mission in Space. *Proc. in 6th Internat. Conf. In Space Optics, ESTEC, Noordwijk, The Netherlands*, ESA-SP 621, 2006.

[10] J.C.J.Koelemeij, B. Roth, A. Wicht, I. Ernsting and S. Schiller. Vibrational Spectroscopy of $HD^+$ with 2-ppb Accuracy. *Phys. Rev. Lett.*, 98:173002, 2007.

[11] T. Schneider, B. Roth, H. Duncker, I. Ernsting and S. Schiller. All-optical preparation of molecular ions in the rovibrational ground state. *Nature Physics*, 6:275–278, 2010.

[12] U. Bressel, A. Borodin, J. Shen, M. Hansen, I. Ernsting and S. Schiller. Manipulation of Individual Hyperfine States in Cold Trapped Molecular Ions and Application to HD+ Frequency Metrology. *Phys. Rev. Lett.*, 108:183003, 2012. See also Appendix 3.

[13] J. Shen, A. Borodin, M. Hansen, and S. Schiller. Observation of a rotational transition of trapped and sympathetically cooled molecular ions. *Phys. Rev. A*, 86:032519, 2012. See also Appendix 4.

[14] J. C. J. Koelemeij, D. W. E. Noom, D. de Jong, M. A. Haddad, W. Ubachs. Observation of the v=8 to v=0 vibrational overtone in cold trapped HD$^+$. *Appl. Phys. B*, 107, Issue 4:1075–1085, 2012.

[15] D. Bakalov, V.I. Korobov, S. Schiller. High-precision calculation of the hyperfine structure of the HD$^+$ ion. *Phys. Rev. Lett.*, 97:243001, 2006.

[16] D. Bakalov and S. Schiller. The electric quadrupole moment of molecular hydrogen ions and their potential for a molecular ion clock. *Appl. Phys. B*, 114:213–230, 2014.

[17] P. Staanum, K. Hojbjerre, P. Skyt, A. Hansen and M. Drewsen. Rotational laser cooling of vibrationally and translationally cold molecular ions. *Nature Physics*, 6:271 – 274, 2010.

[18] P. Blythe, B. Roth, U. Frohlich, H. Wenz, and S. Schiller. Production of Ultracold Trapped Molecular Hydrogen Ions. *Phys. Rev. Lett.*, 95:193002, 2005.

[19] B. Roth, J. C. J. Koelemeij, H. Daerr, and S. Schiller. Rovibrational spectroscopy of trapped molecular hydrogen ions at millikelvin temperatures. *Phys. Rev. A*, 74:040501, 2006.

[20] Ch. Wellers, A. Borodin, S. Vasilyev, D. Offenberg and S. Schiller. Resonant IR multi-photon dissociation spectroscopy of a trapped and sympathetically cooled biomolecular ion species. *Phys. Chem. Chem. Phys.*, 13:18799–18809, 2011. See also Appendix 2.

[21] S. Vasilyev, H. Gollnick, A. Nevsky, A. Grisard, E. Lallier, B. Gerard, J. Jimenez and S. Schiller. Counterdirectional mode coupling in ring resonators with QPM nonlinear crystals and effects on the characteristics of cw optical parametric oscillation. *Appl. Phys. B*, 100:737–747, 2010.

[22] M. Vainio, J. Peltola, S. Persijn, F.J.M. Harren and L. Halonen. Thermal effects in singly resonant continuous-wave optical parametric oscillators. *Appl. Phys. B*, 94:411–427, 2009.

[23] S. Vasilyev, A. Nevsky, I. Ernsting, M. Hansen, J. Shen, and S. Schiller. Compact all-solid-state continuous-wave single-frequency UV source with frequency stabilization for laser cooling of Be$^+$ ions. *Appl. Phys. B*, 103:27–33, 2011.

[24] B. W. Shore. *The Theory of Coherent Atomic Excitation*. Wiley, 1990.

[25] E. A. Colbourn and P. R. Bunker. Accurate Theoretical Vibration-Rotation Energies and Transition Moments for HD$^+$, HT+, and DT+. *J. Mol. Spectr.*, 63:155, 1976.

[26] U. Froehlich, B. Roth and S. Schiller. Ellipsoidal Coulomb crystals in a linear radio-frequency trap. *Physics of Plasma*, 12:073506, 2005.

# Appendix 6. Optical magnetometry with Be$^+$ ions

A simple method for the determination of the magnetic field in an ion trap using laser-cooled Be$^+$ ions was developed and demonstrated. The method is not based on magnetic resonance and thus does not require delivering radiofrequency (RF) radiation to the trap. Instead, stimulated Raman spectroscopy is used, and only an easily generated optical sideband of the laser cooling wave is required. The d.c. magnetic vector, averaged over the Be$^+$ ion ensemble, is determined. Furthermore, the field strength can be minimized and an upper limit for the field gradient can be determined. The resolution of the method is 0.04 G. The relevance for precision rovibrational spectroscopy of HD$^+$ is discussed.

The author contributed to: proposition and development of the method, modification of the setup, preliminary experiments, data analyses, discussion of the results, writing the paper.

The final publication is available at Springer via http://dx.doi.org/10.1140/epjd/e2014-50360-7.

# A simple method for characterization of the magnetic field in an ion trap using Be$^+$ ions

*Jianwei Shen, Andrii Borodin**, *and Stephan Schiller*

Institut fuer Experimentalphysik, Heinrich-Heine-Universitaet Duesseldorf, 40225 Duesseldorf, Germany

*Correspondence address: andrii.borodin@uni-duesseldorf.de

### Abstract

We demonstrate a simple method for the determination of the magnetic field in an ion trap using laser-cooled $^9$Be$^+$ ions. The method is not based on magnetic resonance and thus does not require delivering radiofrequency (RF) radiation to the trap. Instead, stimulated Raman spectroscopy is used, and only an easily generated optical sideband of the laser cooling wave is required. The d.c. magnetic vector, averaged over the $^9$Be$^+$ ion ensemble, is determined. Furthermore, the field strength can be minimized and an upper limit for the field gradient can be determined. The resolution of the method is 0.04 G at present. The relevance for precision rovibrational spectroscopy of HD$^+$ is briefly discussed.

## 1 Introduction

Methods of magnetic field measurement are of high importance in different fields of fundamental and applied research - for example in quantum optics, quantum information processing, and high-resolution spectroscopic measurements. The large variety of magnetic field sensors, utilizing e.g. microelectromechanical systems (MEMS), the Hall effect, the giant magnetoresistance effect, superconducting quantum interference (SQUID), have different sensitivities and magnetic field ranges. A common natural disadvantage of these sensors is the need to introduce them into the region where the magnetic field is to be determined. Although many sensors are compact, this requirement becomes critical in the case of, e.g., experiments with trapped ions or atoms, where the presence of vacuum complicates sensor deployment and the sensor can not be used in situ while the experiment is operating. In this case, the trapped ions or atoms themselves can serve as sensors, because the magnetic field affects their level energies, and the measurement of transition frequencies (shifts) can be used to deduce the magnetic field. Typically, for atoms in the linear Zeeman shift regime, the line splitting is on the order of Larmor precession frequency, which is 2.8 MHz/G. If a sufficiently large magnetic field can be applied, a RF transition can be used to probe the splitting, see e.g. Ref. [1].

The measurement of a small magnetic field, when the concomitant Zeeman splitting is reduced to on the order of 10 kHz or less, is possible in case of non-zero nuclear magnetic moment and non-zero electronic angular momentum ($J$), because then RF radiation can be used to measure the splitting between hyperfine states. As an example, the hyperfine transition frequency $f_0$ in the ground $^2S_{1/2}$ level of $^9\mathrm{Be}^+$ is 1.25 GHz in zero field. Using RF spectroscopy between hyperfine states, the frequencies can be spectroscopied with kHz resolution or better. Since the Zeeman shifts of the hyperfine states are on the order of MHz per Gauss, then a resolution at milli-Gauss level is in principle possible.

Our approach for determining Zeeman shifts of trapped $^9\mathrm{Be}^+$ ions is based on using stimulated Raman transitions. The $^9\mathrm{Be}^+$ ion is a key element of many quantum logic, spectroscopic, and quantum simulation studies [1–4]. The method utilizes only the cooling light and a modulation sideband and does not require delivering a RF field to the trap center, thus simplifying the overall scheme. In fact, no additional hardware beyond the one used for our experiments on sympathetic cooling was employed.

## 2 Motivation

In our experimental setup, $^9\mathrm{Be}^+$ ions trapped in a linear ion trap are used as coolant ions for sympathetic cooling of co-trapped $\mathrm{HD}^+$ molecular ions. $\mathrm{HD}^+$ is a model system in precision spectroscopy of cold trapped molecules for the purpose of testing quantum theory and the time-independence of fundamental constants. Precise measurements of transition frequencies of $\mathrm{HD}^+$ require information about the magnetic field experienced by the ions in the trap. Therefore, it is natural to consider the coolant $^9\mathrm{Be}^+$ ions as an in-situ magnetic field sensor.

For instance, in pure rotational spectroscopy in $\mathrm{HD}^+$ at 1.3 THz (see Ref. [5]) it is of interest to resolve the Zeeman structure of individual hyperfine lines. As a concrete example we consider the hyperfine transition $(v = 0,\ N = 0,\ F = 0, S = 1, J = 1) \to (v' = 0,\ N' = 1,\ F' = 0, S' = 1, J' = 2)$ at a detuning $f - f_{0,theor} = -2.1$ MHz from the spinless rotational transition frequency $f_{0,theor}$ (see Fig. 3 of Ref. [5]). It is particularly attractive, since it exhibits a small Zeeman shift and a small Zeeman splitting. The $J_z = 0 \to J'_z = 0$ component of this particular transition has a quadratic Zeeman shift that is approx. 2.9 kHz in a field of 1 G. Other metrological properties have been discussed in [6, 7]. Thus, assuming that one can set a magnetic field with the small value $B < 0.05$ G in the trap, and that the ions are in the Lamb-Dicke regime, a shift and transition linewidth (due to a possible magnetic field gradient) of less than 10 Hz should be achievable. At this resolution level, a precise measurement of the hyperfine energy contribution ($-2.1$ MHz) and a test of the QED corrections including those of order $\alpha^6$ relative to the nonrelativistic transition frequency would become possible (see Ref. [8]). Note that the closest two Zeeman components arise from transitions $J_z = \pm 1 \to J'_z = \pm 2$, with nearly opposite linear Zeeman shifts of approx. $\mp 40$ kHz/G, respectively, and would be clearly removed from the $J_z = 0 \to J'_z = 0$ transition [9]. This example shows the utility of reducing the strength of the magnetic field in an ion trap for a particular application.

## 3 Experimental scheme and setup

The optical transitions in $^9\mathrm{Be}^+$ relevant to laser cooling are shown in Fig. 1. The use of $\sigma^+$ or $\sigma^-$ transitions provides an almost closed-cycle level scheme, allowing efficient laser cooling of $^9\mathrm{Be}^+$ ions. In this case, the atomic population is almost completely distributed between the excited $^2P_{3/2}$, $F'' = 3$, $m_{F''} = \pm 3$ and the ground $^2S_{1/2}$, $F = 2$, $m_F = \pm 2$ state; decay into $^2S_{1/2}$, $F' = 1$ state is forbidden, as this would require transitions with $|\Delta m| \geqslant 2$, which are not allowed in electric-dipole transitions. However, because of non-ideality of the laser polarization state, instability of the magnetic field and its direction, and Larmor precession, the $F' = 1$ state of the $^2S_{1/2}$ level

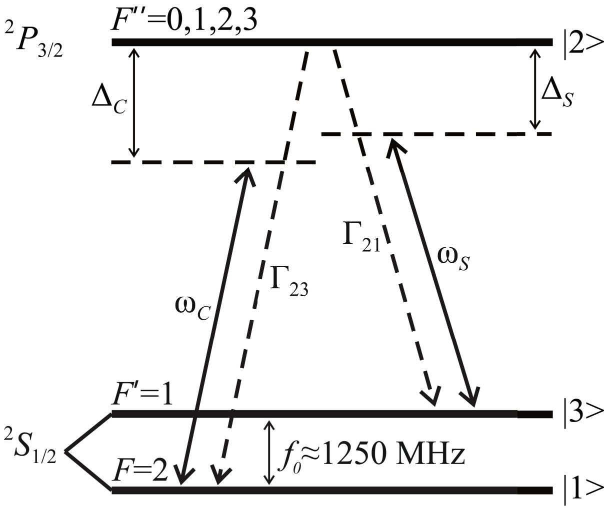

Fig. 1: The optical transitions relevant to the stimulated Raman spectroscopy. $\omega_C$: carrier frequency; $\omega_S$: a red-detuned sideband produced e.g. by an amplitude or phase modulator.

becomes populated. An optical sideband ($\omega_s$ in Fig. 1) of the 313 nm wave used for laser cooling, at 1.25 GHz offset, may be irradiated onto the atoms with the purpose of depleting this state and increase the laser cooling efficiency (repumper).

In this work, we used a two-photon, Doppler-free Raman transition to precisely measure the Zeeman splitting and to determine the magnetic field. In a $\Lambda$-scheme transition, two beams, pump and Stokes ($\omega_c$ and $\omega_s$), are co-propagated in order to significantly reduce the effect of Doppler broadening, by a factor $\simeq 10^6$, so that the residual Doppler linewidth is about $10^2$ Hz.

A phase modulator inserted into the laser beam allows the simple generation of the Stokes wave as a sideband; the fact of simultaneous carrier and sideband generation is important for the stimulated Raman transition. Thus, the waves used for the Raman transition are the same as for the purpose of laser cooling and repumping. The stimulated Raman transition becomes strong for a case of the two-photon resonance, i.e. when $\Delta_C = \Delta_S$, according to the notation in Fig 1. The latter condition is strict for the case of $\Delta_C$, $\Delta_S \gg \Omega_C$, $\Omega_S$, where $\Omega_C$ and $\Omega_S$ are the corresponding one-photon Rabi frequencies. Generally, the two-photon transition is spectrally broadened, which is characterized by the effective Rabi frequency for a Raman transition. For our typical conditions, the sideband intensity is varied in the range of few percent to few ten percent of the carrier power, and also the total power is varied, and thus the effective Rabi frequency is in the range of few kHz to many hundred kHz. The a.c. Stark shift is of similar value. Large absolute sideband intensities are conveniently used for preliminary determination of the Raman resonance. Subsequently, a reduction of intensity is necessary for increasing the measurement precision by reducing systematic shifts.

## 4 Transitions and level splitting in $^9$Be$^+$

Stimulated Raman transitions take place between Zeeman states of the hyperfine levels $F = 2$ and $F' = 1$ of the $^2S_{1/2}$ electronic ground state, with intermediate states being $F''$ =0, 1, 2 or 3 of the electronically excited $^2P_{3/2}$ level. The Zeeman splitting within one hyperfine state is (in the following $F$ refers to any state)

$$E_Z = g_F m_F \mu_B \, B \simeq 1.4 \frac{\mathrm{MHz}}{\mathrm{G}} \, g_F m_F \, B \ ,$$

where the $g_F$ factor is

$$g_F \simeq g_J \frac{F(F+1) - I(I+1) + J(J+1)}{2F(F+1)} \ ,$$

and the $g_J$ factor is

$$g_J \simeq \frac{3}{2} + \frac{S(S+1) - L(L+1)}{2J(J+1)} \ .$$

For $^9$Be$^+$ the values are

$$\begin{array}{lll} g_F = +{}^2\!/_3 & \text{for } P_{3/2}, & \text{all } F \\ g_F = -{}^1\!/_2 & \text{for } S_{1/2}, & F = 1 \\ g_F = +{}^1\!/_2 & \text{for } S_{1/2}, & F = 2 \end{array}$$

The selection rules for dipole-allowed optical transitions are:

$$\begin{array}{ll} \Delta F = 0, \ \pm 1 & \\ \Delta m_F = -1, \ 0, \ +1 & \text{for a } \sigma^-, \ \pi, \ \sigma^+ \text{ transition, respectively.} \end{array}$$

The possible Zeeman components of the Raman transition $F' = 1 \rightarrow F = 2$ and the corresponding Zeeman shifts (i.e. magnetic-field shift of $\hbar(\omega_c - \omega_s)$) are:

$$\begin{array}{lll} \Delta E_Z = ({}^3\!/_2, \ 1, \ {}^1\!/_2, \ 0) \times 1.4 \frac{\mathrm{MHz}}{\mathrm{G}} \times B & \text{for} & m_{F'} = -1 \rightarrow m_F = (-2, \ -1, \ 0, \ +1) \\ \Delta E_Z = (1, \ {}^1\!/_2, \ 0, \ -{}^1\!/_2, \ -1) \times 1.4 \frac{\mathrm{MHz}}{\mathrm{G}} \times B & \text{for} & m_{F'} = \phantom{+}0 \rightarrow m_F = (-2, \ -1, \ 0, \ +1, \ +2) \\ \Delta E_Z = (0, \ -{}^1\!/_2, \ -1, \ -{}^3\!/_2) \times 1.4 \frac{\mathrm{MHz}}{\mathrm{G}} \times B & \text{for} & m_{F'} = +1 \rightarrow m_F = (-1, \ 0, \ +1, \ +2) \end{array}$$

for $\sigma^-$, $\pi$, and $\sigma^+$ transitions. Summarizing, the possible Zeeman shifts of the Raman resonance at 1.25 GHz are:

$$\Delta E_Z = (0, \ \pm{}^1\!/_2, \ \pm 1, \ \pm{}^3\!/_2) \times 1.4 \frac{\mathrm{MHz}}{\mathrm{G}} \times B \tag{1}$$

and a maximum of 7 different Zeeman shifts may be observed.

The excitation spectrum depends on strength of the magnetic field, its direction with respect to the propagation direction of the cooling laser beam and its sideband, on their polarization, and on their intensities. However, we do not attempt to give a complete model, since it is not necessary to do so for the present purpose.

It is important to note that a particular transition from the above list Eq. (1) is observed only if the corresponding initial $m_{F'}$-state of the $F' = 1$ hyperfine level is populated. Generally, all $m_{F'}$ states can be populated and thus all 7 lines can be detected. There are special cases of $\sigma^-$ (and $\sigma^+$)-induced transitions (carrier and sideband), for which only $m_{F'} = -1$ $(+1)$ states of the $F' = 1$ hyperfine level have significant population in consequence of the interaction with the radiation. As mentioned before, this is caused by Larmor precession, non-ideality of light polarization state, and misalignment of magnetic field vector or field strength fluctuation. The observed Zeeman splittings are then limited to:

$$\begin{array}{l} \Delta E_{Z,\sigma^+} = -1.4 \frac{\mathrm{MHz}}{\mathrm{G}} \times B \, , \ \text{for } \sigma^+ - \text{induced transition} \, , \\ \Delta E_{Z,\sigma^-} = +1.4 \frac{\mathrm{MHz}}{\mathrm{G}} \times B \, , \ \text{for } \sigma^- - \text{induced transition} \, . \end{array} \tag{2}$$

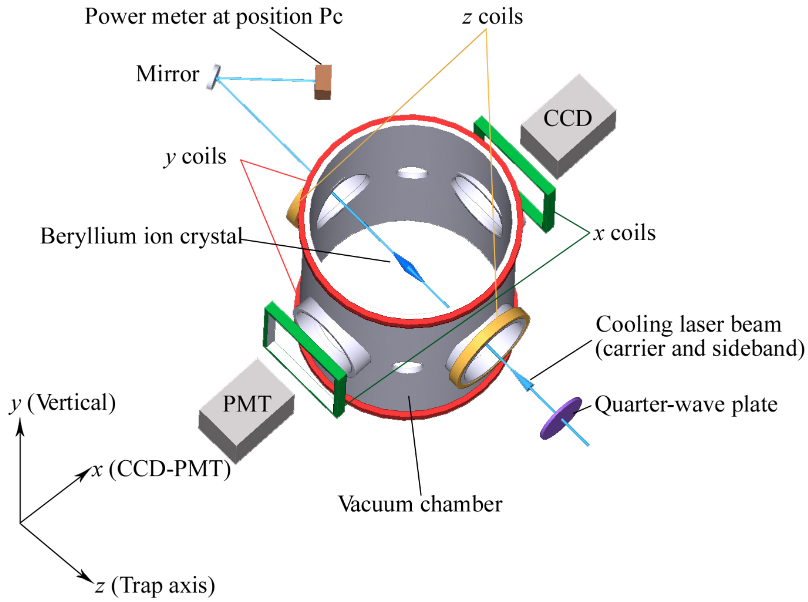

Fig. 2: Geometry of the ion trap apparatus and its magnetic field coils.

## 5 Apparatus

Fig. 2 illustrates the setup used for sympathetic cooling and in which stimulated Raman spectroscopy of $^9\mathrm{Be}^+$ ions has been studied. The cooling laser beam at 313 nm propagates along the symmetry axis of the linear quadrupole trap ($z$-direction). We denote the horizontal and vertical directions in the laboratory as $x$ and $y$, respectively. The $^9\mathrm{Be}^+$ fluorescence is partially collected by a CCD camera and by a photomultiplier tube (PMT) operating in the photon counting regime. The latter is used to define the signal. The power of the cooling beam (carrier plus sidebands) is measured after passing the vacuum chamber, at position Pc.

For compensation of the external magnetic field, and for applying a desired magnetic field, three pairs of Helmholz coils are mounted around the vacuum chamber; the directions of the respective fields are nearly orthogonal to each other.

The cooling laser is frequency-tunable and lockable in a detuning range of a few hundred MHz relative the $^9\mathrm{Be}^+$ cooling transition. Our laser (see Ref. [10]) includes internally a waveguide electro-optic phase modulator driven at a frequency $f_{mod} \simeq 1250\,\mathrm{MHz}$ that generates a phase modulation sideband pair. The "red" sideband is used as a repumper (wave $\omega_s$ in Fig. 1).

$^9\mathrm{Be}^+$ ions are loaded and other species are removed from the trap [11]. During this step, the 313 nm carrier wave is red-detuned by a few hundred MHz from the cooling transition line, and the sideband power is set to a few ten percent of the carrier power. In order to cool the $^9\mathrm{Be}^+$ ion ensemble and any additional molecular ions to the lowest temperature, or to perform measurements as the ones described below, the carrier detuning is instead kept at a few ten MHz, and the sideband power is typically reduced by a moderate factor.

For performing stimulated Raman spectroscopy measurements, the sideband frequency $f_{mod}$ is

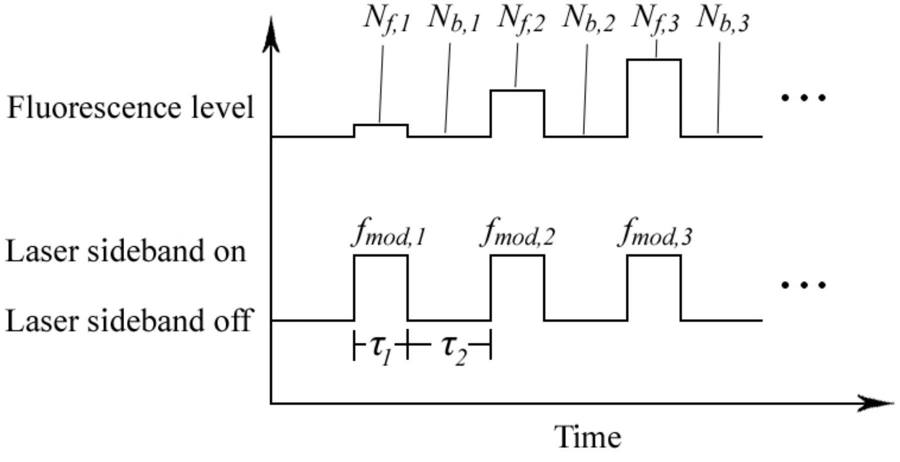

Fig. 3: Measurement time line. See the text for details.

scanned, while all other parameters are kept constant.

The measurement sequence is illustrated in Fig. 3. During each cycle (duration $\tau_1 + \tau_2$) the carrier is always on, while the sideband is turned on and off. During the interval $\tau_1$ (sideband on) the PMT signal $N_{f,i}$ is recorded, and during the interval $\tau_2$ (sideband off), the signal $N_{b,i}$ is recorded. From one cycle to the next, the sideband frequency is changed from $f_{mod,i}$ to $f_{mod,i+1}$, in order to scan the transition. For each sequence $i$ of the frequency scan, we define the background-compensated, normalized signal-to-noise ratio as the relative fluorescence $(N_{f,i} - N_{b,i})/N_{b,i}$. This removes to some extent the influence of laser power variations, assuming that the background count $N_b$ is proportional to laser power (i.e. when it is due to scattered laser light).

In order to minimize the magnetic field in the trap region, an iterative procedure was used. The magnetic field generated by one of the Helmholtz coil pairs was modified via its current and the current was optimized so as to produce minimum Zeeman splittings, while the other two field components were kept constant; then the value of the field component of that first coil pair was held constant while the field component generated by the second coil pair was varied, etc. Repeating this procedure several times and also reducing cooling laser power and sideband power in order to achieve higher resolution, we converged to a small magnetic field strength.

## 6 Experimental results and data analysis

In the general case, when all transitions take place, Eq. (1) applies. Fig. 4 illustrates the Zeeman spectrum for a particular, fixed applied magnetic field. Fig. 5 (top) shows the Zeeman splittings for several different values of one magnetic field component, here the $B_x$-component. In this measurement it can be directly seen that the transverse magnetic field $B_y^2 + B_z^2$ is nonzero. For each measurement, the cooling light power was recorded as well.

We also performed measurements similar to the one shown in Fig. 5 but varying the magnetic field component, $B_y$ (data set II) and $B_z$ (data set III). The data sets I, II, III, all taken at the

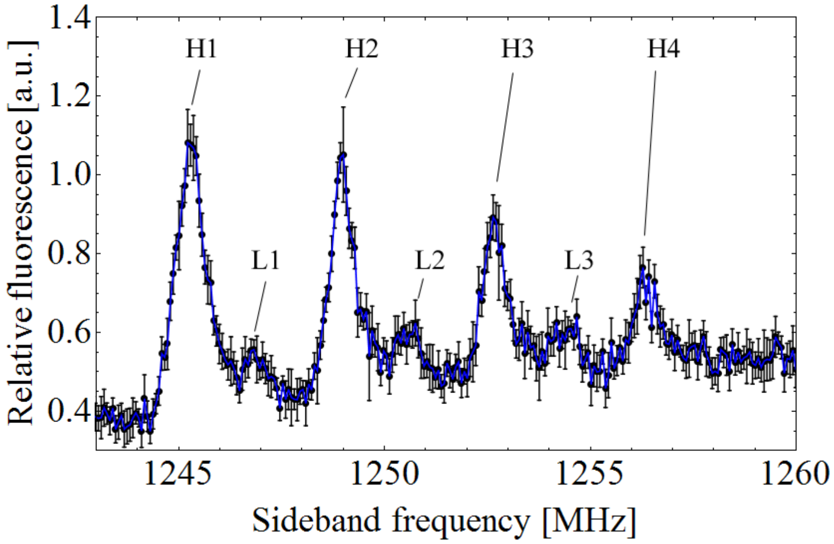

Fig. 4: Zeeman spectrum as a function of sideband frequency $f_{mod}$. All 7 possible transitions are detected. "H" means "high", "L" means "low". The number denotes the line number. Laser power is 70 µW. In this measurement, the current settings are $I_x = -5.74$ A, $I_y = 1.70$ A, $I_z = 0.14$ A, which correspond to $B_x = -2.434$ G, $B_y = 0.008$ G, $B_z = 1.022$ G.

same power (70 $\mu$W at position Pc), were fitted with the functions:

$$\begin{aligned} f_\eta &= \eta\sqrt{B_x^2 + B_y^2 + B_z^2} + f_{offset}\,, \\ B_j &= k_j\, I_j + B_{j,offset}\,, \end{aligned} \tag{3}$$

where $j$ denotes the spatial components $x$, $y$ and $z$. The values of $\eta$ are taken in accordance with the list Eq. (1). The seven coefficients $B_{j,offset}$, $k_j$, and $f_{offset}$ were obtained from a least-squares fit. The result of this fit may be expressed as:

$$\begin{aligned} B_x =&\quad (0.362 \pm 0.003)\ \mathrm{G/A} \times [I_x - (0.985 \pm 0.042)\ \mathrm{A}]\,, \\ B_y =&\quad (0.434 \pm 0.049)\ \mathrm{G/A} \times [I_y - (1.681 \pm 0.065)\ \mathrm{A}]\,, \\ B_z =&\quad (3.586 \pm 0.036)\ \mathrm{G/A} \times [I_z + (0.145 \pm 0.007)\ \mathrm{A}]\,. \end{aligned} \tag{4}$$

From this fit, we obtain the current values that minimize the magnetic field components. After setting the components $B_y$ and $B_z$ close to zero, we recorded data again as a function of $B_x$. The result is shown in Fig. 5 (bottom). The effect of the minimization of $B_y$ and $B_z$ is obvious. Note that in this case, the peaks L1, L2 and L3 are not detected any more.

Subsequently, we set $B_x$ and $B_y$ close to zero, and varied $B_z$. Now the laser wave can be set to $\sigma$ polarization since the magnetic field is then along the direction of propagation. A typical spectrum under a fixed value of $B_z$ is shown in Fig. 6. There is only a single resonance. Varying now $B_z$, we obtain data set IV, which is displayed in Fig. 7. It was taken with a low value of beam power, 6 $\mu$W at position Pc.

We also investigated the light-atom interaction effects. Fig. 8 shows examples of the power dependence of the peak frequency $f_\eta$ and of the line shape of one of the two $\sigma$-transitions under

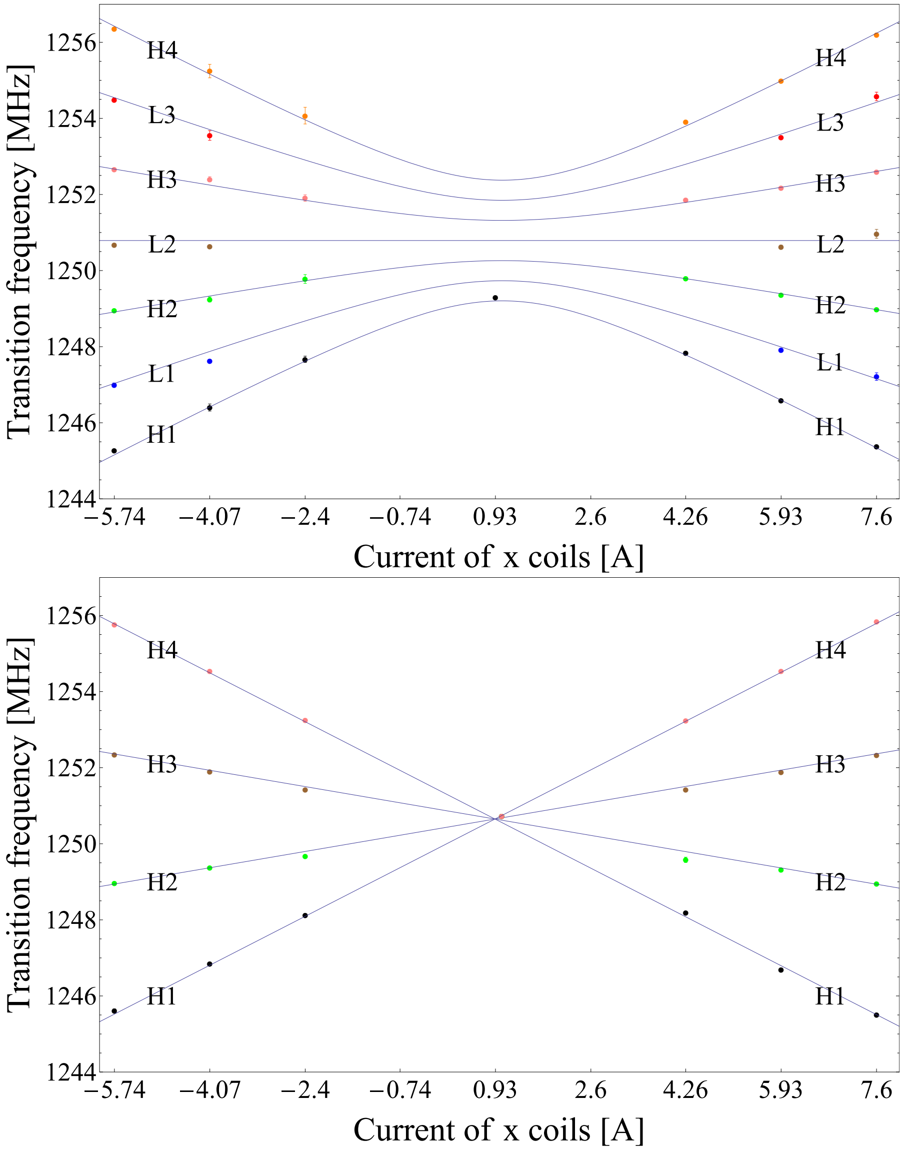

Fig. 5: Zeeman shifts as a function of one magnetic field component, $B_x$. Top: Data set I. The data points are the transition frequencies obtained from individual scans such as Fig. 4, all at 70 µW power. The frequencies of that figure are reported in the present plot as data points for the current $I_x = -5.74$ A. $B_y$ and $B_z$ are not zero: $B_y = 0.008$ G, $B_z = 1.022$ G ($I_y = 1.70$ A, $I_z = 0.14$ A). Bottom: $B_y$ and $B_z$ are set to close to zero ($I_y = 1.681$ A, $I_z = -0.166$ A).

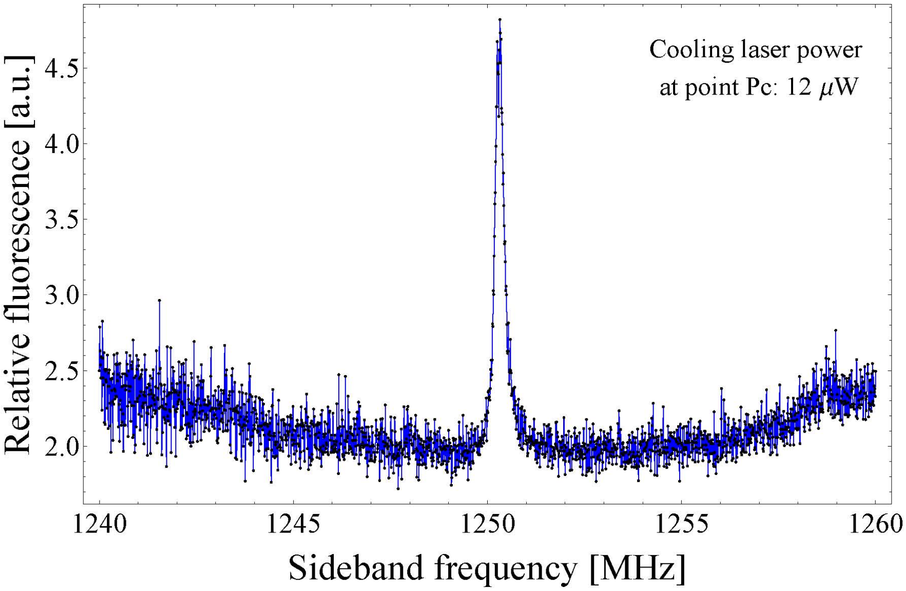

Fig. 6: Spectrum obtained with a $\sigma$-polarized beam. Only one peak is detected. A nonzero magnetic field in the beam propagation direction, $B_z \neq 0$, is applied. The other field components are nearly zero.

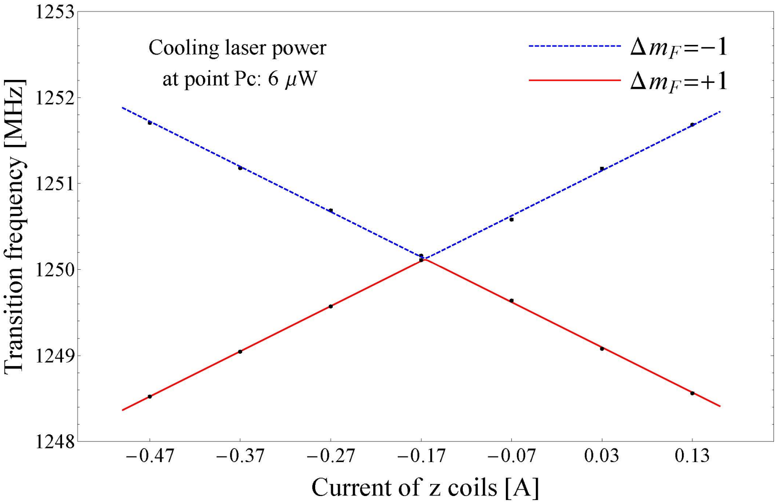

Fig. 7: Zeeman shift of the $\Delta m_F = m_{F'} - m_F = \mp 1$ transitions as a function of $B_z$. The magnetic field components $B_x$ and $B_y$ are minimized.

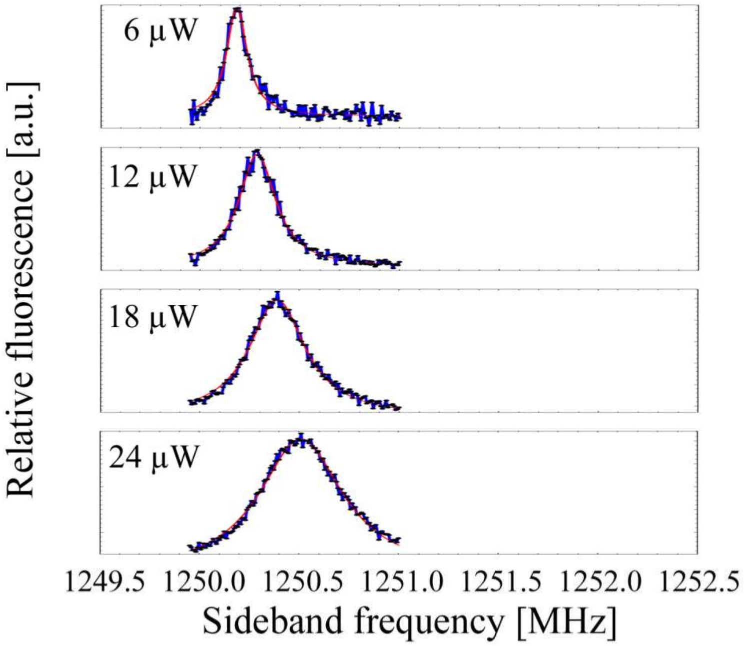

Fig. 8: Light shift and power broadening of a $\sigma$-transition. All spectra were taken under the same conditions, only the beam power was varied. The magnetic field strength is nearly zero.

near-zero field conditions. The peak shift and the linewidth as a function of beam power are summarized in Fig. 9. We find a linear dependence of the frequency shift and linewidth on the light power. Extrapolation of the peak frequency to zero beam power predicts the hyperfine frequency to be $f_0 = 1250.065 \pm 0.013$ MHz. A value of $1250\,017\,670.46 \pm 1.5$ Hz has been obtained by Nakamura et al [1], and a value of $1250\,017\,674.088 \pm 0.024$ Hz has been obtained by Shiga et al [3]; the discrepancy of our measurements from these values ($3.6\,\sigma$) may in part be due to an imperfect polarisation state of the beam or the small residual magnetic field.

## 7 Discussion

In this work, we focus on the ability to minimize the magnetic field. We consider this issue from two points of view. First, the fit of data sets I, II, III allows us to compute the magnetic field uncertainty when the currents are set to minimize the field components. The result is

$$\Delta B = \sqrt{(0.362 \times 0.042)^2 + (0.434 \times 0.065)^2 + (3.586 \times 0.007)^2}\ \mathrm{G} = 0.041\,\mathrm{G}\,.$$

We can also consider the data set IV (Fig. 7). A fit of only this data yields

$$\begin{aligned} B_z &= (3.753 \pm 0.020)\ \mathrm{G/A} \times [I_z + (0.166 \pm 0.001)\ \mathrm{A}] \\ \sqrt{B_x^2 + B_y^2} &= (0.007 \pm 0.031)\ \mathrm{G}\,. \end{aligned} \tag{5}$$

The result for the current value that minimizes $B_z$ lies outside the $2\sigma$ uncertainty range of the result obtained in Eq.(4), but it should be noted that the conditions of data set IV were

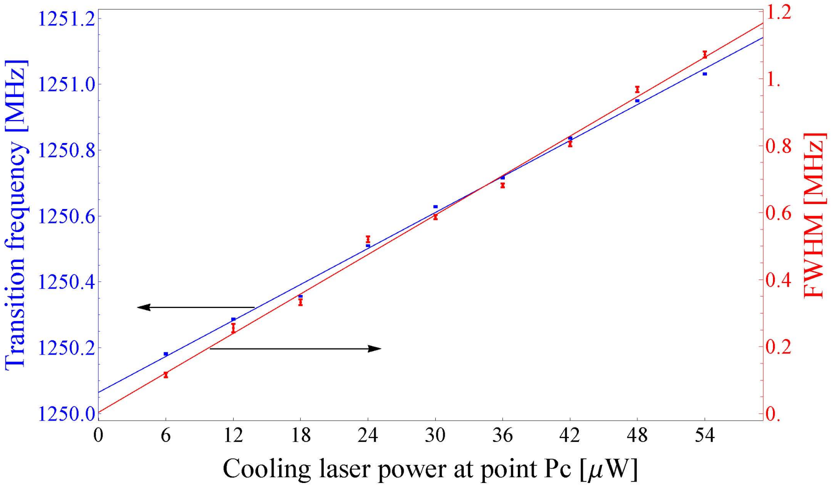

Fig. 9: Light shift and power broadening as a function of laser power, including the cases shown in Fig. 6.

different: lower beam power and smaller range of offsets from the zero-field-component current value. Nevertheless, the field strength uncertainty, $\Delta B' = \sqrt{(3.753 \times 0.001)^2 + (0.031)^2}\,\mathrm{G} = 0.031\,\mathrm{G}$ is comparable to $\Delta B$.

As a third result, we can consider the measurement performed with near-zero field, and consider the difference between the zero-intensity extrapolated resonance frequency of Fig. 9 and the literature experimental value, $\Delta f_0 = 47 \pm 13\,\mathrm{kHz}$. From this we may set an upper limit to the field strength present during that measurement, $(47 + 13)\,\mathrm{kHz}/(1.4\,\mathrm{MHz/G}) \simeq 43\,\mathrm{mG}$.

Finally, we can provide an upper limit for the magnetic field gradient as follows. The narrowest linewidth observed when reducing the laser power as much as possible while keeping the ions cooled (approximately 2 $\mu$W), is approximately 40 kHz. Assigning the linewidth to be due completely to a nonzero magnetic field gradient across the ion ensemble (size: 2 mm in $z$-direction), it would then be equal or less to 40 kHz/(1.4 MHz/G) $\simeq$ 29 mG. This is a conservative upper limit, since Fig. 9 indicates that at this laser power there is still light-induced broadening present.

## 8 Conclusion and outlook

We demonstrated a simple method for measuring the magnetic field in an ion trap that uses beryllium ions. The method is simple since it utilizes only the cooling laser and an optical sideband that is also conventionally present since it serves as a repumper during laser cooling. The magnetic field resolution, approximately 40 mG, is at present limited by power broadening and the Stark shift induced by the cooling wave, imperfect polarization state of the cooling wave, and by the temporal instability of the currents supplied to the Helmholtz coils (here, the instability is of the order of 1 mA). In addition, a non-uniformity of the magnetic field, if present, also limits the resolution of the absolute field strength determination.

The method has been applied here to an ensemble containing a large number of trapped ions (a few thousands), since this is typical for our application of sympathetic cooling. We believe that the method could be applied also in the case of few ions or a single trapped ion. In the case of a moderate number of trapped ions (e.g. an ion string), the use of a tightly focused beam would allow addressing an individual ion and determining the field at its location.

As a further perspective, we propose that it may be possible to eliminate the light shift. This requires equal Rabi frequencies of the sideband and the carrier; then the light shifts induced by the two radiation fields compensate each other. The one-photon transition induced by the strong sideband, can, in principle, hinder from observation the two-photon transition, but an appropriate choice of intensities and detunings can allow for (partial) compensation of the light shifts and for detection of the two-photon signal. A complete compensation of the frequency shifts means equality of sideband and carrier intensities (neglecting for simplicity the issue of branching ratios). Thus, this scheme requires a modulation index of about 0.33, which is available from high-efficiency waveguide modulators.

Acknowledgement: We are indebted to Q.-F. Chen for assistance in the data analysis. We are also very grateful to M. Hansen and U. Bressel for performing a magnetic field characterization using magnetic sensors. This work was done in the framework of project Schi 431/19-1 funded by the Deutsche Forschungsgemeinschaft.

## References

[1] T. Nakamura, M. Wada, K. Okada, I. Katayama, S. Ohhtani, H. A. Schuessler. Precision spectroscopy of the Zeeman splittings of the hyperfine structure for nuclear structure studies. *Optics Communications*, 205:329–336, 2002.

[2] C.W. Chou, D. B. Hume, J. C. J. Koelemeij, D. J. Wineland, and T. Rosenband. Frequency Comparison of Two High-Accuracy $Al^+$ Optical Clocks. *Phys. Rev. Lett.*, 104:070802, 2010.

[3] N. Shiga, W. Itano and J. Bollinger. Diamagnetic correction to the $^9Be^+$ ground-state hyperfine constant. *Phys. Rev. A*, 84:012510, 2011.

[4] M. Biercuk, H. Uys, A. VanDevender, N. Shiga, W. Itano and J. Bollinger. Optimized dynamical decoupling in a model quantum memory. *Nat. Letters*, 458:996–1000, 2009.

[5] J. Shen, A. Borodin, M. Hansen, and S. Schiller. Observation of a rotational transition of trapped and sympathetically cooled molecular ions. *Phys. Rev. A*, 86:032519, 2012.

[6] D. Bakalov and S. Schiller. The electric quadrupole moment of molecular hydrogen ions and their potential for a molecular ion clock. *Appl. Phys. B*, 114:213–230, 2014.

[7] S. Schiller, D. Bakalov, and V. I. Korobov. Phys. Rev. Lett. (accepted). *arXiv:1402.1789*, 2014.

[8] V. I. Korobov, L. Hilico, and J. P. Karr. Theoretical transition frequencies beyond 0.1 ppb accuracy in $H_2^+$, $HD^+$, and antiprotonic helium. *Phys. Rev. A*, 89:032511, 2014.

[9] D. Bakalov, V.I. Korobov, S. Schiller. Magnetic field effects in the transitions of the $HD^+$ molecular ion and precision spectroscopy, J. Phys. B: Al. Mol. Opt. Phys., 44, 025003 (2011); Corrigendum: J. Phys. B: Al. Mol. Opt. Phys., 45, 049501 (2012).

[10] S. Vasilyev, A. Nevsky, I. Ernsting, M. Hansen, J. Shen, and S. Schiller. Compact all-solid-state continuous-wave single-frequency UV source with frequency stabilization for laser cooling of $\mathrm{Be}^+$ ions. *Appl. Phys. B*, 103:27–33, 2011.

[11] P. Blythe, B. Roth, U. Frohlich, H. Wenz, and S. Schiller. Production of Ultracold Trapped Molecular Hydrogen Ions. *Phys. Rev. Lett.*, 95:193002, 2005.

# Bibliography

[1] I. Shavitt and R. J. Bartlett. *Many-body perturbation theory and coupled-cluster theory methods in chemistry and physics.* Cambridge Press, 2009.

[2] P. Szalay, T. Mueller, G. Gidofalvi, H. Lischka, and R. Shepard. Multiconfiguration self-consistent field and multireference configuration interaction methods and applications. *Chem. Rev.*, 112:108–181, 2012.

[3] Prof. S. Schiller, private communications.

[4] J. Stearns, M. Guidi, O. Boyarkin, and T. Rizzo. Conformation-specific infrared and ultraviolet spectroscopy of tyrosine-based protonated dipeptides. *J. Chem. Phys.*, 127:154322–7, 2007.

[5] Ch. Wellers, A. Borodin, S. Vasilyev, D. Offenberg, and S. Schiller. Resonant IR multi-photon dissociation spectroscopy of a trapped and sympathetically cooled biomolecular ion species. *Phys. Chem. Chem. Phys.*, 13:18799–18809, 2011. See also Appendix 2.

[6] C. M. Western et al. PGOPHER, a Program for Simulating Rotational Structure.

[7] A. Grier, M. Cetina, F. Orucevic, , and V. Vuletic. Observation of cold collisions between trapped ions and trapped atoms. *Phys. Rev. Lett.*, 102:223201, 2009.

[8] K. Ravi, S. Lee, A. Sharma, G. Werth, and S. Rangwala. Cooling and stabilization by collisions in a mixed ion-atom system. *Nat. Comm.*, 3:1126, 2012.

[9] W. Smith, O. Makarov, and J. Lin. Cold ion-neutral collisions in a hybrid trap. *J. Mod. Optics*, 52(16):2253–2260, 2005.

[10] Eric R. Hudson. Method for producing ultracold molecular ions. *Phys. Rev. A*, 79:032716, 2009.

[11] K. Chen, S. Sullivan, , and E. Hudson. Neutral gas sympathetic cooling of an ion in a Paul trap. *Phys. Rev. Lett.*, 112:143009, 2014.

[12] A. K. Hansen, O. O. Versolato, L. Klosowski, S. B. Kristensen, A. Gingell, M. Schwarz, A. Windberger, J. Ullrich, J. R. Crespo Lopez-Urrutia, and M. Drewsen. Efficient rotational cooling of Coulomb-crystallized molecular ions by a helium buffer gas. *Nat. Letters*, 508:76–79, 2014.

[13] W. Rellergert, S. Sullivan, S. Schowalter, S. Kotochigova, K. Chen, and E. Hudson. Evidence for sympathetic vibrational cooling of translationally cold molecules. *Nat.*

*Letters*, 495:490–495, 2013.

[14] Ch. Zipkes, L. Ratschbacher, C. Sias, and M. Koehl. Kinetics of a single trapped ion in an ultracold buffer gas. *New J. of Phys.*, 13:053020, 2011.

[15] F. Hall and S. Willitsch. Millikelvin Reactive Collisions between Sympathetically Cooled Molecular Ions and Laser-Cooled Atoms in an Ion-Atom Hybrid Trap. *Phys. Rev. Lett.*, 109:233202, 2012.

[16] A. Haerter. *Two-body and three-body dynamics in atom-ion experiments.* PhD thesis, University Ulm, 2013.

[17] J. Nguyen, C. Ricardo Viteri, E. Hohenstein, C. David Sherrill, K. Brown, and B. Odom. Challenges of laser-cooling molecular ions. *New J. Phys.*, 13:063023, 2011.

[18] E. Shuman, J. Barry, and D. DeMille. Laser cooling of a diatomic molecule. *Nature*, 467:820, 2010.

[19] H. Kato. Doppler-free high resolution spectral atlas of iodine molecule. Technical report, Japan Society for the Promotion of Science, 2000.

[20] M. Gubin, E. Kovalchuk, E. Petrukhin, A. Shelkovnikov, D. Tyurikov, R. Gamidov, C. Erdogan, E. Sahin, R. Felder, P. Gill, S. N. Lea, G. Kramer, and B. Lipphardt. Absolute frequency measurements with a set of transportable He-Ne/$CH_4$ optical frequency standards and prospects for future design and applications. P. Gill, Frequency standards and Metrology, Proc. of the Sixth Symposium, pp. 453-460, Singapore, 2002.

[21] T. Schneider, B. Roth, H. Duncker, I. Ernsting, and S. Schiller. All-optical preparation of molecular ions in the rovibrational ground state. *Nature Physics*, 6:275–278, 2010.

[22] P. Staanum, K. Hojbjerre, P. Skyt, A. Hansen, and M. Drewsen. Rotational laser cooling of vibrationally and translationally cold molecular ions. *Nature Physics*, 6:271 – 274, 2010.

[23] D. Bakalov and S. Schiller. The electric quadrupole moment of molecular hydrogen ions and their potential for a molecular ion clock. *Appl. Phys. B*, 114:213–230, 2014.

[24] L. Wolniewicz and J. Poll. The vibration-rotational energies of the hydrogen molecular ion $HD^+$. *J. Chem. Phys.*, 73:6225, 1980.

[25] S. Schiller and V. Korobov. Test of time-dependence of the electron and nuclear masses with ultracold molecules. *Phys. Rev. A*, 71:032505, 2005.

[26] D. Bakalov, V.I. Korobov, and S. Schiller. High-precision calculation of the hyperfine structure of the $HD^+$ ion. *Phys. Rev. Lett.*, 97:243001, 2006.

[27] S. Schiller, D. Bakalov, and V. I. Korobov. Simplest Molecules as Candidates for Precise Optical Clocks. *Phys. Rev. Lett.*, page 023004, 2014.

[28] V. I. Korobov, L. Hilico, and J. P. Karr. Theoretical transition frequencies beyond 0.1 ppb accuracy in $H_2^+$, $HD^+$, and antiprotonic helium. *Phys. Rev. A*, 89:032511, 2014.

[29] D. Bishop and A. Macias. *Ab initio* Calculation of Harmonic Force Constants. II. Application to Gaussian Wavefunctions for $H_2^+$. *J. of Chem. Phys.*, 51:4997, 1969.

[30] D. Bishop. Properties of the Adiabatic Energy Curves for the Ground States of $H_2^+$, $HD^+$, and $D_2^+$. *J. of Mol. Spectr.*, 51:422–427, 1974.

[31] E. A. Colbourn and P. R. Bunker. Accurate Theoretical Vibration-Rotation Energies and Transition Moments for $HD^+$, HT+, and DT+. *J. Mol. Spectr.*, 63:155, 1976.

[32] Fritz Riehle. *Frequency standards: basics and applications.* Wiley, 2004.

[33] M. Kajita and Y. Moriwaki. Proposed detection of variation in $^{m_p}/_{m_e}$ using a vibrational transition frequency of a $CaH^+$ ion. *J. Phys. B: At. Mol. Opt. Phys.*, 42:154022, 2009.

[34] D. Bakalov, V.I. Korobov, and S. Schiller. Magnetic field effects in the transitions of the $HD^+$ molecular ion and precision spectroscopy. *J. Phys. B: Al. Mol. Opt. Phys.*, 44:025003, 2011. Corrigendum: J. Phys. B: Al. Mol. Opt. Phys., 45, 049501 (2012).

[35] W. Paul and H. Steinwedel. Ein neues massenspektrometer ohne magnetfeld. *Z. Naturforschg.*, 8a:448–450, 1953.

[36] P. K. Gosh. *Ion traps.* Oxford, 1995.

[37] U. Froehlich. *Towards Laser Spectroscopy of Ultracold Molecular Hydrogen Ions.* PhD thesis, HHU Dusseldorf, 2008.

[38] D. Dubin and T. O'Neil. Trapped nonneutral plasmas, liquids, and crystals (the thermal equilibrium states). *Rev. Mod. Phys.*, 71:87–172, 1999.

[39] U. Froehlich, B. Roth, and S. Schiller. Ellipsoidal Coulomb crystals in a linear radiofrequency trap. *Physics of Plasma*, 12:073506, 2005.

[40] J. Shen, A. Borodin, M. Hansen, and S. Schiller. Observation of a rotational transition of trapped and sympathetically cooled molecular ions. *Phys. Rev. A*, 85:032519, 2012. See also Appendix 4.

[41] N. Polfer and J. Oomens. Vibrational spectroscopy of bare and solvated ionic complexes of biological relevance. *Mass Spectr. Rev.*, 28:468–494, 2009.

[42] B. Roth, P. Blythe, and S. Schiller. Motional resonance coupling in cold multispecies Coulomb crystals. *Phys. Rev. A*, 75:023402, 2007.

[43] W. Paul. Electromagnetic traps for charged and neutral particles. *Rev. Mod. Phys.*, 62:531, 1990.

[44] H. Schnitzler. *Development of an experiment for trapping, cooling, and spectroscopy of molecular hydrogen ions.* PhD thesis, University Konstanz, 2001.

[45] U. Bressel, A. Borodin, J. Shen, M. Hansen, I. Ernsting, and S. Schiller. Manipulation of Individual Hyperfine States in Cold Trapped Molecular Ions and Application to HD+ Frequency Metrology. *Phys. Rev. Lett.*, 108:183003, 2012. See also Appendix 3.

[46] S. Vasilyev, A. Nevsky, I. Ernsting, M. Hansen, J. Shen, and S. Schiller. Compact all-solid-state continuous-wave single-frequency UV source with frequency stabilization for laser cooling of $Be^+$ ions. *Appl. Phys. B*, 103:27–33, 2011.

[47] Spectralcalc.com. Hi-resolution gas spectra.

[48] D. Wineland, C. Monroe, D. Meekhof, B. King, D. Leibfried, W. Itano, J. Bergquist, D. Berkeland, J. Bollinger, and J. Miller. Quantum state manipulation of trapped atomic ions. *Proc. R. Soc. Lond. A*, 454:411–429, 1998.

[49] N. Vitanov, T. Halfmann, B. Shore, and K. Bergmann. Laser-induced population transfer by adiabatic passage techniques. *Ann. Rev. Phys. Chem.*, 52:763–809, 2001.

[50] N. Vitanov, M. Fleischhauer, B. Shore, and K. Bergmann. coherent manipulation of atoms and molecules by sequential pulses. *In: Advances of Atomic, Molecular, and Optical Physics*, 46:55–190, 2001.

[51] M. Khudaverdyan, W. Alt, I. Dotsenko, L. Foerster, S. Kuhr, D. Meschede, Y. Miroshnychenko, D. Schrader, and A. Rauschenbeutel. Adiabatic quantum state manipulation of single trapped atoms. *Phys. Rev. A*, 71:031404, 2005.

[52] S. Gaertner, J. Krieg, A. Klemann, O. Asvany, S. Bruenken, and S. Schlemmer. High-resolution spectroscopy of $CH_2D^+$ in a cold 22-pole ion trap. *J. Phys. Chem. A*, 117:9975–9984, 2013.

[53] H. Chadwick, P. Morten Hundt, M. van Reijzen, B. Yoder, and R. Beck. Quantum state specific reactant preparation in a molecular beam by rapid adiabatic passage. *J. Chem. Phys.*, 140:034321, 2014.

[54] Y. Inokuchi, O. Boyarkin, T. Ebata, and T. Rizzo. UV and IR spectroscopy of cold $1,2$-dimethoxybenzene complexes with alkali metal ions. *Phys. Chem. Chem. Phys.*, 14:4457–4462, 2012.

[55] K. Thyagarajan and A. Ghatak. *Lasers: fundamentals and applications.* Springer, 2010.

[56] H. E. Gollnick. Stabilization of a continuous OPO and spectroscopic application. Master's thesis, HHU Dusseldorf, 2010.

[57] S. Vasilyev, H. Gollnick, A. Nevsky, A. Grisard, E. Lallier, B. Gerard, J. Jimenez, and S. Schiller. Counterdirectional mode coupling in ring resonators with QPM nonlinear crystals and effects on the characteristics of cw optical parametric oscillation. *Appl. Phys. B*, 100:737–747, 2010.

[58] M. Vainio, J. Peltola, S. Persijn, F.J.M. Harren, and L. Halonen. Thermal effects in singly resonant continuous-wave optical parametric oscillators. *Appl. Phys. B*, 94:411–427, 2009.

[59] Dr. I. Ernsting, private communications.

[60] D. Hume, C. Chou, D. Leibrandt, M. Thorpe, D. Wineland, and T. Rosenband. Trapped-ion state detection through coherent motion. *Phys. Rev. Lett.*, 107:243902, 2011.

[61] Dr. D. Hume, private communications.

[62] M. Biercuk, H. Uys, A. VanDevender, N. Shiga, W. Itano, and J. Bollinger. Optimized dynamical decoupling in a model quantum memory. *Nat. Letters*, 458:996–1000, 2009.

[63] N. Shiga, W. Itano, and J. Bollinger. Diamagnetic correction to the $^9$Be$^+$ ground-state hyperfine constant. *Phys. Rev. A*, 84:012510, 2011.

[64] J. Cirac and P. Zoller. Quantum computations with cold trapped ions. *Phys. Rev. Lett.*, 74(20):4091–4094, 1995.

[65] A. Steane. The ion trap quantum information processor. *Appl. Phys. B*, 64:623–642, 1997.

[66] D. F. V. James. Quantum dynamics of cold trapped ions with application to quantum computation. *Appl. Phys. B*, 66:181–190, 1998.

[67] A. Haerter, A. Kruekow, A. Brunner, and J. Hecker Denschlag. Long-term drifts of stray electric fields in a Paul trap. *Appl. Phys. B*, 114:275–281, 2014.

[68] G. Morigi and H. Walther. Two-species Coulomb chains for quantum information. *Eur. Phys. J. D*, 13:261–269, 2001.

[69] J. Wuebbena, S. Amairi, O. Mandel, and P. O. Schmidt. Sympathetic cooling of mixed-species two-ion crystals for precision spectroscopy. *Phys. Rev. A*, 85:043412, 2012.

[70] A. Ashkin. Optical trapping and manipulation of neutral particles using lasers. *Proc. Natl. Acad. Sci.*, 94:4853–4860, 1997.

[71] K. Sheridan, N. Seymour-Smith, A. Gardner, and M. Keller. All-optical broadband excitation of the motional state of trapped ions. *Eur. Phys. J. D*, 66:289, 2012.

[72] P. Windpassinger, D. Oblak, P. Petrov, M. Kubasik, M. Saffman, C. Garrido Alzar, J. Appel, J. Mueller, N. Kjaergaard, and E. Polzik. Nondestructive probing of Rabi oscillations on the Cesium clock transition near the standard quantum limit. *Phys. Rev. Lett.*, 100:103601, 2008.

[73] C. Zhang. *Production and sympathetic cooling of complex molecular ions.* PhD thesis, HHU Dusseldorf, 2008.

[74] B. W. Shore. *The Theory of Coherent Atomic Excitation.* Wiley, 1990.

[75] U. Bressel, I. Ernsting, and S. Schiller. 5 $\mu$m laser source for frequency metrology based on difference frequency generation. *Optics Lett.*, 37(5):918–920, 2012.

[76] U. Bressel. *High-resolution vibrational spectroscopy of cold molecular hydrogen ions.* PhD thesis, HHU Dusseldorf, 2011.

[77] J.C.J.Koelemeij, B. Roth, A. Wicht, I. Ernsting, and S. Schiller. Vibrational Spectroscopy of HD$^+$ with 2-ppb Accuracy. *Phys. Rev. Lett.*, 98:173002, 2007.

[78] S. Alighanbari, private communications.

[79] M. Kajita, M. Abe, M. Hada, and Y. Moriwaki. Estimated accuracies of pure $XH^+$ (X: even isotopes of group II atoms) vibrational transition frequencies: towards the test of the variance in ${}^{m_p}/_{m_e}$. *J. Phys. B: At. Mol. Opt. Phys.*, 44:025402, 2011.

[80] M. Kajita, M. Abe, M. Hada, and Y. Moriwaki. Corrigendum. *J. Phys. B: At. Mol. Opt. Phys.*, 44:209802, 2011.

## Acknowledgements

This last page is dedicated to those who helped me to make contributions to this thesis.

I would like to express my sincere thanks to:

- my supervisor Prof. S. Schiller for belief in my willpower and providing challenging, but interesting and exciting tasks, giving me a possibility to visit many scientific conferences and meetings, and making fruitful scientific collaborations,
- Prof. A. Görlitz for helpful discussions and for reviewing my dissertation,
- my colleagues Ch. Wellers, M. Hansen, J. Shen, S. Alighanbari, for contributing to the development of experimental apparatus, and performing the measurements,
- Dr. A. Nevsky and Dr. Q.-F. Chen for helpful suggestions, Dr. I. Ernsting for helping with precision measurements,
- our former institute colleagues U. Bressel, D. Offenberg, Dr. T. Schneider, Dr. B. Roth, Dr. S. Vasilyev, and Dr. A. Chijioke for sharing experience, and for help in the initial stage of the project,
- P. Dutkiewicz, R. Gusek, D. Iwaschko, and U. Rosowski for developing electronic components,
- H. Hoffmann for producing mechanical components,
- Prof. P. O. Schmidt for helpful discussions, and for sharing experience with Be source,
- Prof. J. Hecker Denschlag and his team for helpful suggestions on the single-ion trap.